

Ames

1 W-22073

NASA CONTRACTOR REPORT 177393

Study of Comet Nucleus Gamma-Ray Spectrometer
Penetrator System

(NASA-CR-177393) STUDY OF COMET NUCLEUS
GAMMA-RAY SPECTROMETER PENETRATION SYSTEM
(Martin Marietta Aerospace) 244 p CSCL 03A

N88-27120

Unclas
G3/88 0154784

G.L. Adams
R.J. Amundsen
R.W. Beardsley
R.H. Cash
B.C. Clark
T.C.D. Knight
J.P. Martin
P. Monti
D.A. Outteridge
W.D. Plaster
W.E. Simon

CONTRACT NAS2-12130
March 1986

NASA

Study of Comet Nucleus Gamma-Ray Spectrometer
Penetration System

G.L. Adams
R.J. Amundsen
R.W. Beardsley
R.H. Cash
B.C. Clark
T.C.D. Knight
J.P. Martin
P. Monti
D.A. Outteridge
W.D. Plaster
W.E. Simon
Martin Marietta Denver Aerospace
Denver, Colorado

Prepared for
Ames Research Center
under Contract NAS2-12130
March 1986



National Aeronautics and
Space Administration

Ames Research Center
Moffett Field, California 94035

1. Report No. NASA CR-177393		2. Government Accession No.		3. Recipient's Catalog No.	
4. Title and Subtitle Study of Comet Nucleus GAMMA-RAY SPECTROMETER PENETRATION SYSTEM. Final Technical Report				5. Report Date March 1986	
				6. Performing Organization Code	
7. Author(s) G.L. Adams, R.J. Amundsen, R.W. Beardsley, R.H. Cash, B.C. Clark, T.C.D. Knight, J.P. Martin, P. Monti, D.A. Outteridge, W.D. Plaster, W.E. Simon				8. Performing Organization Report No.	
9. Performing Organization Name and Address Martin Marietta Denver Aerospace, P.O. Box 179, Denver, Colorado 80201				10. Work Unit No.	
				11. Contract or Grant No. NAS2-12130	
12. Sponsoring Agency Name and Address National Aeronautics and Space Administration Washington, D.C. 20546				13. Type of Report and Period Covered Contractor Report	
				14. Sponsoring Agency Code 157-04-80	
15. Supplementary Notes Point of Contact: Technical Monitor, Byron L. Swenson, MS 244-10 Ames Research Center, Moffett Field, CA 94035 (415) 694-5705					
16. Abstract A penetrator system has been suggested as an approach for making in-situ measurements of the composition and physical properties of the nucleus of a comet. This study has examined in detail the feasibility of implementing the penetrator concept. The penetrator system and mission designs have been developed and iterated in sufficient detail to provide a high level of confidence that the concept can be implemented within the constraints of the Mariner Mark II spacecraft.					
17. Key Words (Suggested by Author(s)) Space Sciences Comets Penetrator				18. Distribution Statement Subject Category 88 Unclassified - Unlimited	
19. Security Classif. (of this report) Unclassified		20. Security Classif. (of this page) Unclassified		21. No. of Pages 255	
22. Price*					

Table of Contents

	<u>Page</u>
<u>Summary</u>	0
1.0 <u>Introduction</u>	1
2.0 <u>Discussion</u>	3
3.0 <u>Requirements Discussion</u>	8
3.1 <u>Gamma Ray Detector Design Issues</u>	8
3.2 <u>Alpha-Backscatter Spectrometer Design Issues</u>	10
3.3 <u>Physical Properties Instruments</u>	11
4.0 <u>Baseline Design Summary</u>	12
4.1 <u>Penetrator System Structure and Science Instruments</u>	12
4.1.1 Nose and Shaft Structure	12
4.1.2 Temperature Sensors	13
4.1.3 Accelerometers	14
4.1.4 Alpha Particle Instrument	14
4.1.5 Gamma-Ray Spectrometer	16
4.1.6 Terrabrake Structure	20
4.1.7 Rocket Motor	20
4.1.8 Penetrator Support Module	21
4.1.9 Penetrator Thermal Shield	21
4.2 <u>Thermal Control</u>	21
4.3 <u>Electronics Systems</u>	23
4.3.1 Controller and Data Handling Subsystems	26
4.3.2 Power Subsystem	27
4.3.3 Communication Subsystem	27
4.3.4 Thermal Control Subsystem	28
4.3.5 Interfaces	29
4.3.6 Sensor Electronics	29
4.3.7 Propulsion Electronics	30
4.3.8 Ground Support Equipment	30
4.4 <u>Flight Dynamics</u>	31

	<u>Page</u>
5.0 <u>Design Discussions</u>	34
5.1 <u>Penetrator Configuration</u>	34
5.2 <u>Penetrator Structure</u>	37
5.3 <u>Materials Interference</u>	37
5.3.1 <u>Penetrator Materials</u>	37
5.3.2 Mantle Interference	50
5.4 <u>Thermal Approach</u>	53
5.5 <u>Flight Dynamics Analyses</u>	71
5.5.1 <u>Spin/Eject Phase</u>	73
5.5.2 Coast Phases	79
5.5.3 Delta-V Phase	84
5.5.4 Results and Recommendations	91
5.6 <u>Electronics System</u>	99
5.6.1 <u>PSM Description</u>	102
5.6.1.1 PSM Data Handling	102
5.6.1.2 PSM Thermal	110
5.6.1.3 PSM RF	110
5.6.1.4 PSM Power	113
5.6.1.5 PSM Converter	113
5.6.1.6 PSM Power Management Unit	113
5.6.1.7 PSM Interfaces	116
5.6.1.7.1 PSM/Spacecraft Interfaces	116
5.6.1.7.1.1 PSM/Spacecraft BIU Interface	116
5.6.1.7.1.2 PSM/Spacecraft Power Interface	116
5.6.1.7.2 PSM/penetrator Interfaces	116
5.6.1.7.2.1 PSM/penetrator Power Interface	116
5.6.1.7.2.2 PSM/penetrator Hardline Controller Interface	116
5.6.2 Penetrator Description	119
5.6.2.1 Penetrator Data Handling	120
5.6.2.2 Penetrator Science	120
5.6.2.2.1 Penetrator Alpha-Backscatter Instrument	120
5.6.2.2.2 Penetrator Gamma-Ray Spectrometer Instrument	130
5.6.2.2.3 Penetrator Accelerometers	130
5.6.2.2.4 Penetrator Temperature Probes	130
5.6.2.3 Penetrator Thermal	133
5.6.2.4 Penetrator RF	133
5.6.2.5 Penetrator Power	135
5.6.2.5.1 Penetrator Converter	135
5.6.2.5.2 Penetrator Battery	135
5.6.2.5.3 Penetrator Power Management Unit	138

	<u>Page</u>
5.6.2.6 Penetrator Propulsion	138
5.6.2.7 Penetrator Interfaces	139
5.6.2.7.1 Penetrator/PSM Power Interface	139
5.6.2.7.2 Penetrator/PSM Hardline Controller Interface	139
5.6.3 Parts List	141
5.6.4 Packaging	141
5.6.5 Cabling	145
5.6.6 Ground Support Equipment	145
5.7 <u>Ge Detector Enclosure and Contamination Issues</u>	151
5.7.1 Conventional Laboratory Ge Detector Enclosures	151
5.7.2 Inert Gas Backfill Approach	151
5.7.3 Permanent Vacuum Seal	153
5.7.4 Continuously Pumped Configuration	154
5.7.5 Enclosure Vented to Space	155
5.8 <u>Propulsion System for Penetrator Implant Velocity</u>	156
5.8.1 Rocket Motor Tradeoff	156
5.8.2 Shuttle Safety Requirements	157
 Appendix A: <u>Stress Analysis CNPS Structure</u>	 A 1
A 1.0 <u>Material Properties</u>	A 1
A 2.0 <u>Baseline Assumptions</u>	A 1
A 3.0 <u>Results</u>	A 2
 Appendix B: <u>Additional Delta-V Phase Equations</u>	 B 1
 Appendix C: <u>Electronics Systems Requirements</u>	 C 1
C 1.0 <u>Penetrator Support Module (PSM)</u>	C 1
C 1.1 <u>Interfaces</u>	C 1
C 1.2 Thermal	C 1
C 1.3 Data Handling	C 2
C 1.4 Communications	C 2
C 1.5 Power Converter	C 3
C 1.6 Cabling	C 3
C 1.7 Temperatures	C 3
C 2.0 <u>Penetrator</u>	C 3
C 2.1 <u>Interfaces</u>	C 3
C 2.2 Science	C 3
C 2.3 Thermal	C 4
C 2.4 Electromechanical	C 5
C 2.5 Data Handling	C 5

	<u>Page</u>
C 2.6 RF Communications	C 6
C 2.7 Propulsion	C 6
C 2.8 Power	C 6
C 2.9 Power Management Unit	C 6
C 2.10 Cabling	C 6
C 2.11 Temperatures	C 6
 Appendix D: <u>Software Requirements</u>	 D 1
D 1.0 <u>Penetrator Support Module (PSM)</u>	D 1
D 1.1 <u>Prerelease phase</u>	D 1
D 1.2 <u>Flight and post-impact phases</u>	D 2
D 2.0 <u>Penetrator</u>	D 2
D 2.1 <u>Prerelease phase</u>	D 2
D 2.2 <u>Flight phase</u>	D 3
D 2.3 <u>Post-impact phase</u>	D 3
 Appendix E: <u>CNPS RF Subsystem Design</u>	
E 1.0 <u>Scope</u>	E 1
E 2.0 <u>Subsystem Description</u>	E 1
E 2.1 <u>Operating Frequency Selection</u>	E 2
E 2.2 <u>Link Analysis</u>	E 3
E 2.3 <u>Antenna Design</u>	E 6
E 2.4 <u>Transmitter-Receiver Design</u>	E 7
E 3.0 <u>Conclusions</u>	E 9
 Appendix F - <u>Flight Software Top-level VCLR'S</u>	 F 1
F 1.0 <u>PSM Top-level VCLR</u>	F 1
F 2.0 <u>PSM Pre-release VCLR</u>	F 2
F 3.0 <u>PSM Flight VCLR</u>	F 3
F 4.0 <u>PSM Post-impact VCLR</u>	F 4
F 5.0 <u>Penetrator Top-level VCLR</u>	F 5
F 6.0 <u>Penetrator Pre-release VCLR</u>	F 6
F 7.0 <u>Penetrator Flight VCLR</u>	F 7
F 8.0 <u>Penetrator Post-impact VCLR</u>	F 8

	<u>Page</u>
Appendix G - <u>Microcomputer Memory & Telemetry Estimates</u>	G 1
G 1.0 <u>Groundrules</u>	G 1
G 2.0 <u>PSM PROM Estimate</u>	G 2
G 3.0 <u>Penetrator PROM Estimate</u>	G 3
G 4.0 <u>Penetrator RAM Estimate</u>	G 4
G 5.0 <u>PSM RAM Estimate</u>	G 5
G 6.0 <u>Penetrator Data Length</u>	G 5
 Appendix H - <u>Error Detection & Correction</u>	 H 1
 Appendix I - <u>Penetrator Accelerometer Sampling</u>	 I 1
I 1.0 <u>Sample/Hold Amplifier</u>	I 1
I 2.0 <u>Accelerometer RAM Requirements</u>	I 1
I 3.0 <u>Impact-Detection</u>	I 2
I 4.0 <u>DAS Interrupt Service Routine</u>	I 3
I 5.0 <u>DAS Interrupt Service Routine (Critical Path)</u>	I 3
 Appendix J - <u>Power Consumption</u>	 J 1
J 1.0 <u>CNPS Power Management</u>	J 1
J 2.0 <u>Power Calculation Groundrules</u>	J 1
J 3.0 <u>General</u>	J 2
J 4.0 <u>Penetrator Power</u>	J 2
J 5.0 <u>PSM Power</u>	J 2
J 6.0 <u>Penetrator Battery Requirements</u>	J 4
 Appendix K: <u>Preliminary Parts List</u>	 K 1
 Appendix L: <u>Cable Signals</u>	 L 1
 Appendix M: <u>Preliminary Solid Rocket Motor Data</u>	 M 1

Figures

Figure 2-1a	Baseline Penetrator Design	4
Figure 2-1b	Baseline Penetrator Design	5
Figure 4-1	Configuration of Alpha Particle Instrument	15
Figure 4-2	Gamma Ray Detector Assembly	17
Figure 4-3	Penetrator Electronics, System Block Diagram	24
Figure 4-4	Penetrator Support Module Electronics, System Block Diagram	25
Figure 5.1-1	Maximum Deceleration as a Function of Penetrability Index	35
Figure 5.1-2	Penetration Distance as a Function of Penetrability Index	35
Figure 5.1-3	Energy Dissipation Above Threshold as a Function of Penetrability Index	36
Figure 5.3-1	Gamma Ray Detector Effective Sampling Volumes	40
Figure 5.3-2	Deviation of C/Si Ratio for Various Mantle Thicknesses	51
Figure 5.3-3	Deviation of O/Si Ratio for Various Mantle Thicknesses	52
Figure 5.3-4	Minimum Penetration Depth for 10 Δ Error in Hydrogen	53
Figure 5.4-1	Penetrator Thermal Math Model Nodalization, Radiator Concept	55
Figure 5.4-2	Typical Energy Balance and Temperatures for Steady State Penetrator Operation (Implanted), Radiator Concept	57
Figure 5.4-3	TRASYS Exterior Penetrator Nodes	58
Figure 5.4-4	TRASYS Forward Section of Flare	59
Figure 5.4-5	TRASYS Aft Section of Flare	59
Figure 5.4-6	TRASYS Electronics Section	60
Figure 5.4-7	TRASYS Aft Section	60
Figure 5.4-8	MITAS Nodes for Final Penetrator Design	61
Figure 5.4-9	Temperatures in Crystal Region During Annealing Cycle (17.5 W Heater on Aft Section)	63
Figure 5.4-10	Temperatures in the Crystal for Final Design of Anneal Heater (36 W)	64
Figure 5.4-11	Steady State Node Temperatures during Onboard Cooldown	65
Figure 5.4-12	OnBoard Cooldown After Anneal Cycle	67
Figure 5.4-13	Thermal Performance of Implanted Penetrator for Various Comet Temperatures	69
Figure 5.4-14	Typical Thermal Impacts on Detector While Implanted	70
Figure 5.5-1	Penetrator State vs. Trajectory Sequence of Events	72
Figure 5.5-2	Spin/Eject Phase Geometry	74
Figure 5.5-3	Interface Geometry Between End of Coast Phase and Start of Delta-V Phase	81
Figure 5.5-4	Thrust Misalignment and Offset	85
Figure 5.5-5	Delta-V Phase Euler Angles	86
Figure 5.5-6	Spin/Eject Phase Nutation Angle	93
Figure 5.5-7	Geometrical Interpretation of Delta-V Phase Wobble	96
Figure 5.5-8	Periodic Angle of Attack During Delta-V Phase	96
Figure 5.5-9	Maximum Angle of Attack vs. Delta-V Duration	97

	<u>Page</u>
Figure 5.6-1 Penetrator Support Module Electronics System Block Diagram	100
Figure 5.6-2 Penetrator Electronics System Block Diagram	101
Figure 5.6-3 PSM Data Handling Clock microcomputer, Bus, a Demux	103
Figure 5.6-4 PSM Data Handling Timers	105
Figure 5.6-5 PSM Data Handling Memory	106
Figure 5.6-6 PSM Data Handling Address Decode	107
Figure 5.6-7 PSM Data Handling Interrupts	108
Figure 5.6-8 PSM Data Handling Data Acquisition System	109
Figure 5.6-9 PSM Data Handling I/O Ports	111
Figure 5.6-10 PSM Receiver Diagram	112
Figure 5.6-11 CNPS Power and Grounding Diagram	114
Figure 5.6-12 PSM Power Converter	115
Figure 5.6-13 PSM Data Handling BIU I/F	117
Figure 5.6-14 PSM Data Handling Hardline Controller	118
Figure 5.6-15 Penetrator Data Handling Clock, Microcomputer, Bus Demux	121
Figure 5.6-16 Penetrator Data Handling Address Decode	122
Figure 5.6-17 Penetrator Data Handling Memory	123
Figure 5.6-18 Penetrator Data Handling Timers	124
Figure 5.6-19 Penetrator Data Handling I/O Ports	125
Figure 5.6-20 Penetrator Data Handling Interrupts	126
Figure 5.6-21 Penetrator Data Handling Hardline Controller	127
Figure 5.6-22 Penetrator Data Handling Data Acquisition System	128
Figure 5.6-23 Alpha-backscatter Electronics Diagram	129
Figure 5.6-24 Penetrator Alpha Pulse Height Analyzer (Typ of 2)	131
Figure 5.6-25 Gamma Ray Spectrometer Electronics Diagram	132
Figure 5.6-26 Penetrator Transmitter Diagram	134
Figure 5.6-27 Penetrator LVPS Power Converter Block Diagram	136
Figure 5.6-28 Penetrator HVPS Power Converter Block Diagram	137
Figure 5.6-29 Penetrator Rocket Motor Electrical Interface	140
Figure 5.6-30 Penetrator Electronics Module	142
Figure 5.6-31 Penetrator Support Module	143
Figure 5.6-32 Penetrator Battery Module	144
Figure 5.6-33 Penetrator Cabling Diagram	146
Figure 5.6-34 PSM Cabling Diagram	147
Figure 5.6-35 CNPS Electronics BCE	148
Figure 5.6-36 CNPS Electronics BCE	149
Figure E-1(a) One Way Link	E 1
Figure E-1(b) Two Way Link	E 2

Tables

Table 2-1	Comet Nucleus Model-Parameter Set	3
Table 4-1	Penetrator System Estimated Mass Summary	12
Table 4-2	Penetrator System Link Analysis	28
Table 5.3-1	Gamma Ray Mean Free Paths	39
Table 5.3-2	Nitrogen Response for Various Materials Usage for Penetrator Components and Comet Composition	42
Table 5.3-3	Nitrogen Response for Various Materials Used on the Penetrator Components and Comet Composition with no NH ₃ Ice	43
Table 5.3-4	Response Levels and Comet Fractions for Titanium	44
Table 5.3-5	Response Levels and Comet Fractions for Aluminum	45
Table 5.3-6	Response Levels and Comet Fractions for Chromium Using Alternative Materials	46
Table 5.3-7	Response Levels and Comet Fractionsd for Iorn Using Alternative Materials	47
Table 5.3-8	Material Interferences Analysis for Baseline Penetrator Design	48
Table 5.3-9	Response Levels and Comet Fractions for Chlorine	49
Table 5.4-1	Comet Nucleus Parameter Set	54
Table 5.4-2	Final Crystal Temperatures After Ejection/Cruise Phase	66
Table 5.5-1	Penetrator and Spacecraft Parameter Values	
Table 5.6-1	Penetrator Support Module Subsystems Elements	102
Table 5.6-2	Aydin Vector Model ACC201-1 Receiver Specitication	110
Table 5.6-3	Penetrator Subsystem Elements	119
Table 5.6-4	Aydin Vector Model TM-502/L Transmitter Specifications	133
Table 5.6-5	Lithium Sulphur Dioxide and Lithium Thionul Chloride Battery Comparison	138
Table 5.6-6	Printed Circuit Board Area Requirements	141
Table 5.6-7	HP Personal Computer Features	145
Table 5.8-1	Candidate Rocket Motor for Penetrator	156
Table E-1	Operating Frequency Selection Parameters	E 2
Table E-2	Link Analysis (PSK) 1500 MHz	E 3
Table E-3	Link Analysis (PSK/PM) 1500 MHz	E 4
Table E-4	Link Analysis (PSK/FM) 1500 MHz	E 4
Table E-5	Link Analysis Summary	E 6
Table E-6	Antenna Performance Characteristics	E 6
Table E-7	Transmitter-Receiver Hardware Characteristics	E 7
Table E-8	Transmitter-Receiver Design Selection Trade Study	E 8
Table E-9	Transmitter and Receiver Critical Performance Specifications	E 9
Table J-1	Penetrator Average Power	J-3
Table J-2	PSM Average Power	J-3

ACRONYMS

ac	Alternating Current
Al	Aluminum
AU	Astronomical Unit
B	Boron
BCE	Bench Checkout Equipment
Ca	Calcium
Cl	Chlorine
CM	Center of Mass
cm	Centimeter
CNPS	Comet Nucleus Penetrator System
Co	Cobalt
CRAF	Comet Rendezvous and Asteroid Flyby
dB	Decibell
dc	Direct Current
ed	Editor
eV	Electron Volt
Fe	Iron
FM	Frequency Modulated
FSE	First Stage Electronics
Ge	Germanium
H	Hydrogen
hr	Hour
JPL	Jet Propulsion Laboratory
JSC	Johnson Space Center
kg	Kilogram
km	Kilometer
Li	Lithium
LSB	Least Significant Bit
max	Maximum
MeV	Million Electron Volts
Mg	Magnesium
mg	Milligram
MIL	Military
mil	One Thousandth of an Inch
min	Minimum
MITAS	Martin Marietta Interactive Thermal Analyzer System
mJ	Millijoule
MLI	Multi-Layer Insulation
mm	Millimeter
Mn	Manganese
Mo	Molybdenum
mrad	Milliradians
ms	Millisecond
MTLINF	Material Interferences Software Program
mW	Milliwatt
N	Nitrogen
Na	Sodium

NASA	National Aeronautics and Space Administration
Ni	Nickel
O	Oxygen
PCB	Printed Circuit Board
PHA	Pulse Height Analyzer
ppb	Parts Per Billion
PRA	Penetrator Relay Antenna
PSM	Penetrator Support Module
PTS	Penetrator Thermal Shield
RF	Radio Frequency
rpm	Revolutions Per Minute
s	Second
S	Sulphur
Si	Silicon
Sn	Tin
STD	Standard
STSE	System Test Support Equipment
Th	Thorium
Ti	Titanium
TRASYS	Thermal Radiation Analysis System
V	Volts
Zr	Zirconium

Summary

The purpose of this study was to examine in detail the feasibility of implementing in-situ measurements of the composition and physical properties of the nucleus of a comet using an instrumented penetrator, which will carry the instrumentation beneath the surface mantle into the unaltered material.

The penetrator system and mission designs have been developed and iterated in sufficient detail to provide a high level of confidence that the concept can be implemented within the constraints of the Mariner Mark II spacecraft.

The detailed design activities also included the technology assessments and development plans necessary to enable realistic cost estimates to be made for implementing the penetrator concept.

1.0 Introduction

This is the final report for contract NAS2-12130, "Study of Comet Nucleus Gamma-Ray Spectrometer Penetration System", performed for the NASA/Ames Research Center.

A better understanding of the origins of the solar system and of life on Earth are amongst the major objectives of NASA's program of space exploration. The study of comets is a key element in meeting these objectives since comets are thought to be the most primitive, pristine bodies remaining in our solar system. Comets are believed to be composed of unaltered material from which the planets were formed, including ices, silicates, metals, and complex organic compounds (the 'dirty snowball' model). The planets and satellites that have been explored so far retain only a very severely altered record of their origins, obscured by billions of years of evolution during which their surfaces have been shaped by both external and internal processes. Unlike these larger bodies, comets have spent most of their existence in distant, dimly-lit, cold regions of the solar system (Oort's cloud), and are far too small to have been significantly altered by their own internal heat and gravitational differentiation. It is probable that they alone retain unaltered evidence of the chemical and physical conditions under which the solar system formed. Collisions with comets may have provided the Earth and other planets with a significant fraction of their volatiles (gases and liquids), and may have brought to Earth organic molecules necessary for the origin of life.

The proposed Comet Rendezvous/Asteroid Flyby (CRAF) Mission, to be launched in the early 1990's, will be the first mission to provide an extended and detailed observation of a comet and will be the first mission using the Mariner Mark II spacecraft. The Mariner spacecraft will rendezvous with a short period comet and will fly in co-orbit with the comet, gathering data for a period of more than two years. During this time the comet will pass from a state of low activity when it is far from the sun to maximum activity as it develops its tail and then passes closest to the sun at perihelion.

The purpose of the study discussed in this report was to examine the feasibility of implementing in-situ atomic composition and physical properties measurements for a comet nucleus using a penetrator - a projectile which impacts the surface and is buried by the impact. It was considered necessary that the resulting design should be compatible with anticipated cost and weight constraints associated with the CRAF mission.

The Comet Nucleus Penetrator has been designed to implant an instrument complement into the nucleus of a comet and to provide data on elemental composition and physical properties. It will penetrate beneath the surface mantle into material more representative of the bulk composition of the nucleus. Compositional measurements will be made by a gamma-ray spectrometer with a neutron detection capability and an alpha particle instrument with alpha, proton, and x-ray modes. The gamma ray detector will be a high purity germanium crystal, maintained at a temperature less than 120 K in order to provide excellent energy resolution.

The Penetrator also includes accelerometers and temperature sensors. There are two sets of triaxial accelerometers that will completely describe the motion of the penetrator during the penetration event, plus a highly sensitive axial accelerometer for determination of mantle thickness and density. There are one fixed and three deployable temperature sensors that will allow determination of the temperature gradient and estimation of the thermal diffusivity of the nucleus material. Other measurements were considered, such as incorporation of gas chromatography. However, the impacts of additions to the baseline instrument complement were clearly incompatible with the cost and weight constraints we have assumed for the CRAF mission.

The Penetrator consists of a slender titanium alloy shaft and a flared afterbody, made primarily of Kevlar composite. Materials were selected to provide an optimum combination of strength and ductility at low temperatures, light weight, and minimization of contamination of the induced gamma-ray signal. The Penetrator is spun and released from the Spacecraft, coasts to a point near the nucleus, and is implanted by the firing of a small solid rocket motor. The spin/eject mechanism and rocket motor give a nominal 3σ targeting error on the nucleus of ~ 70 m. The external configuration of the Penetrator has been designed to limit the impact deceleration to no more than a predicted 4120 m s^{-2} (420 g). The thermal design of the gamma-ray detector system provides for rapid radiative cooling to a temperature of about 102 K on the Spacecraft, and then actively uncages the detector after impact, thermally isolating it and allowing it to remain in its low temperature high resolution operating range (less than 120 K) long enough to acquire high quality data.

Composition and thermal data are acquired for five days. The data handling scheme accumulates data in memory and transmits all accumulated data to the Spacecraft during every data transmission.

In designing the penetrator to be fully compatible with current models of cometary nuclei two parameters strongly impacted the design, namely nucleus penetrability and temperature. Initially a range of penetrability index from 2 to 20 (solid ice to a very hard packed snow) was assumed. However, it soon became obvious that this range was totally inadequate and that very much softer materials had to be considered. The penetrator has been designed to operate over a penetrability index range of 2 to 100 (solid ice to soft snow). It also became clear that one could not be certain that it would be possible, or desirable, to select, or be limited to, an emplacement site where the cometary temperature would be within the operating temperature range of the emplaced gamma-ray detector at a subsurface location. Consequently initial cooling and thermal isolation of the gamma-ray detector is an essential part of any viable design. The recently discovered low albedo and irregular shape of Halley's cometary nucleus, which allows higher temperatures in some areas and makes temperature predictions difficult, supports the prudence of this approach.

The Comet Nucleus Penetrator System (CNPS) comprises four elements: the Penetrator (PEN), the Penetrator Support Module (PSM) mounted on the CRAF spacecraft bus, the Penetrator Thermal Shield (PTS), also mounted on the spacecraft, and the Penetrator Relay Antenna (PRA) mounted on the spacecraft low precision scan platform.

2.0 Discussion

Design of a penetrator for the proposed application presents a complex system design and optimization problem. There are a large number of inter-related and competing parameters which drive the design and the design compromises necessary in order to satisfy the initial requirements for the system. In the course of this study many trade-off analyses have been performed which have led to the baseline design presented in this report. It should be noted that a different set of requirements would have resulted in a design that would be somewhat different, but different more in detail than in concept. The results of this study clearly show that the penetrator concept is feasible and can be implemented within a reasonable set of imposed constraints. Obviously, at this stage, problems still remain to be fully solved, but there are no items which would appear to present insuperable difficulties. The baseline design is shown in Figures 2-1a and 2-1b.

A major factor influencing the design of a penetrator is our current lack of knowledge regarding the physical properties of a comet nucleus. Table 2-1 shows the parameter set assumed for the purposes of this study (from Campins, H (ed) Comet Nucleus Modeling Workshop, SAIC (1985)). The range of nucleus hardness is of particular importance for the design of the penetrator since it forces a design which has to operate when buried beneath the surface, if a fixed impact velocity is selected. This precludes, for example, using a radiative cooler on the penetrator to cool the germanium gamma ray detector crystal and also places certain additional requirements on the communication system.

Table 2-1 Comet Nucleus Model—Parameter Set

	Minimum	Expected	Maximum	Comment
Albedo (Geometric)	0.01	0.05	0.5	
Depth of Mantle	0.01 mm	~10 cm	100 cm	
Surface Temperature	100 K*	130 K	170 K (Subsolar Pt)	*Could be Less at Poles
Temperature at Sampling Depth		130 K		Asymptotic Value
Diameter		5 km		Wild 2 Geometric Mean, Axial Ratio 2 : 1
Rotation Period	3 h	10-15 h*		*Wild 2
Gas Production Rate (mol/s)	10 ²⁶		10 ²⁷ (<2 AU)	Wild 2 - Kopff New Values Available When Photometry Reduced
Dust/Gas Mass Ratio	0.4	0.6-0.8	1.0	
Surface Density (gr/cm ³)	0.005*	0.05	1.5	*Top 1-cm Lag Deposit
Density at Depth (gr/cm ³)	0.1	1.0	1.5	
Thermal Conductivity (mW/cm K)	0.02	1-2	100	
Specific Heat (cal/gr K)	0.3	0.5-0.8	1.0	
Cohesiveness (Tensile Strength (dy/cm ²))	10 ²	10 ⁴ -10 ⁵	10 ⁸ *	*Solid Crystalline Ice
Compressive Strength (dy/cm ²)	10 ³	10 ⁵	10 ⁹ *	*Solid Crystalline Ice
Hardness (Penetrability)	2	10	≥ 50	The Range Given is from Block Ice to Fluffy Snow in a Relative Scale
Grain/Particle Size (Number Dist)	< 0.1 μm	0.1 μm-10 cm	> 10 cm	
Porosity (Pore Volume/Total Volume)	0.1	0.3	0.8	
Expected Gravity		~ 10 ⁻⁴ g		

-4-

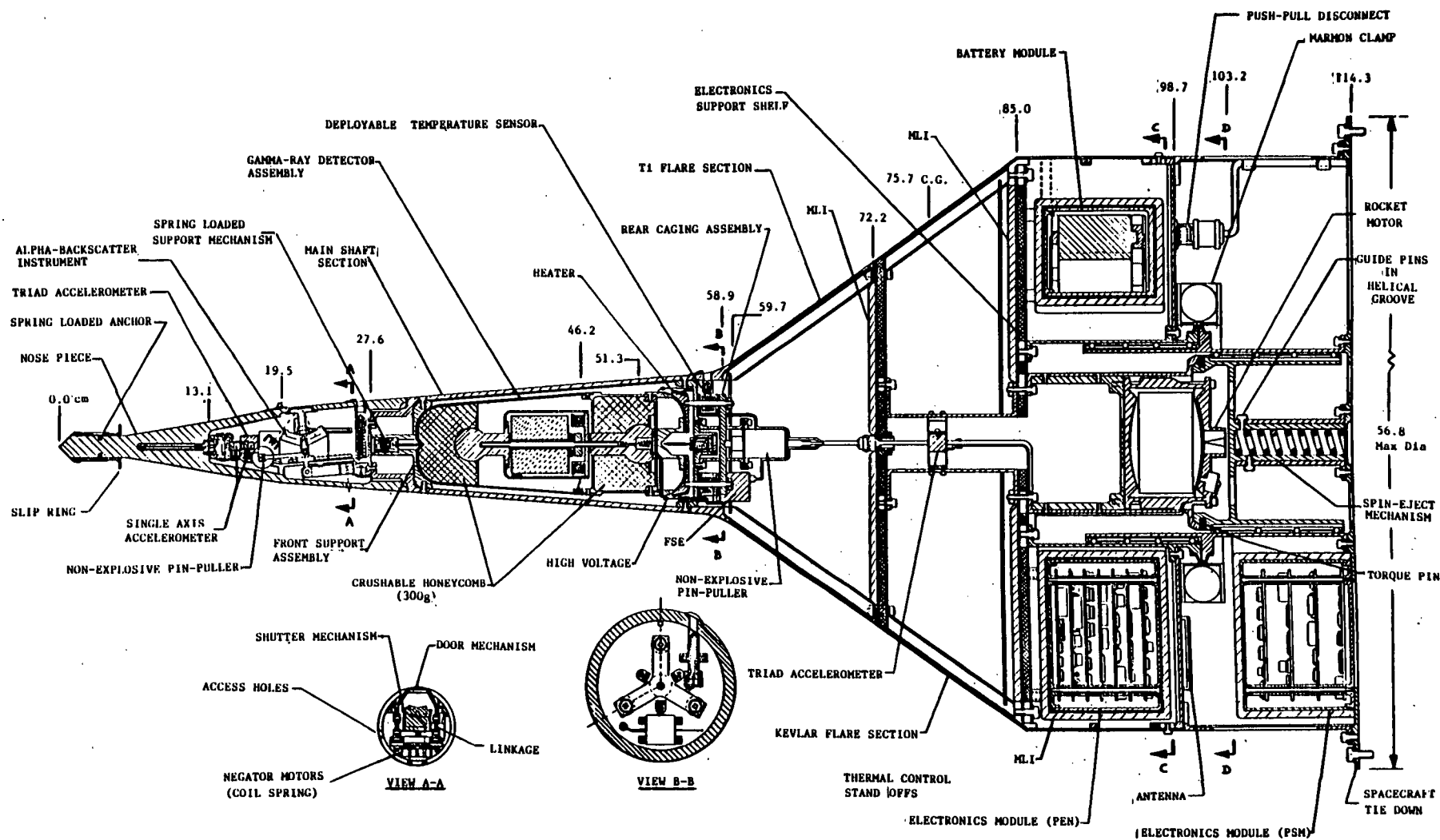
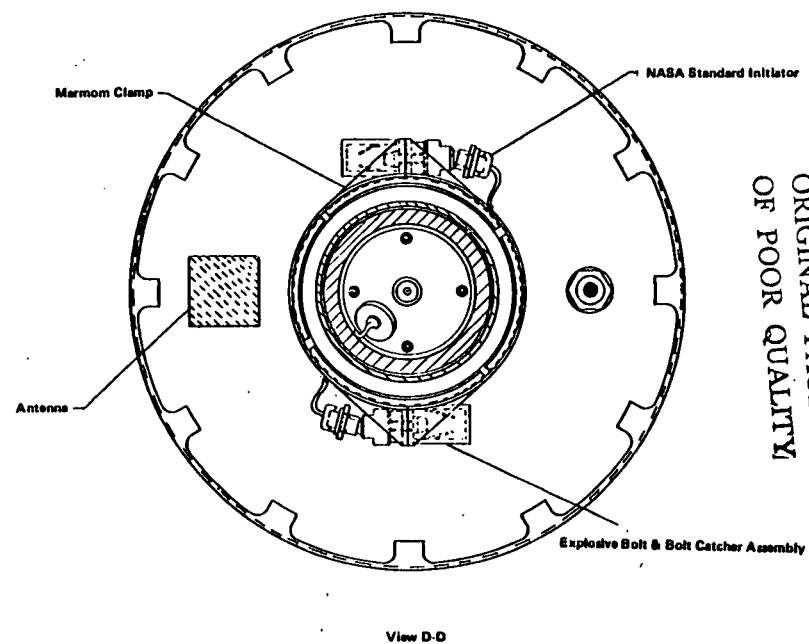
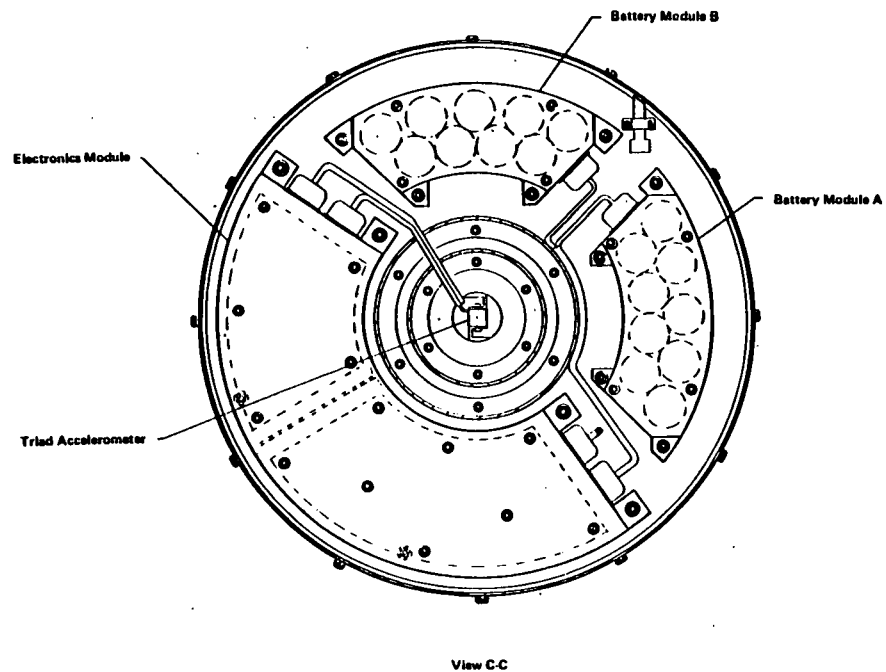


Figure 2-1a Baseline Penetrator Design



ORIGINAL PAGE IS
OF POOR QUALITY

Figure 2-1b Baseline Penetrator Design

A penetrator design with an adjustable velocity has been evaluated. However, it is improbable that remote sensing will provide any information on nucleus penetrability. Consequently, a precursor penetrator would be required to provide a point penetrability measurement, about which allowances for inhomogeneity of the nucleus would be made. However, this approach is incompatible with the CRAF cost constraints and has not been pursued. Other options were examined in an attempt to design a penetrator that would be less sensitive to the uncertainty in surface material strength. These included configurations with detachable afterbodies, which leave the afterbody at the surface to facilitate communications. Such penetrators have been previously developed for arctic applications on Earth. For the comet application, however, this approach is not appropriate for two reasons. First, most of the penetrator weight is in the aft end, and having a detachable afterbody does not either limit the impact loads or the tendency to bury the communications system upon impact with the softest material. Second, a detachable afterbody necessitates development of an umbilicus, which is a development risk and can be a source of significant energy dissipation with an adverse effect on penetrator flight dynamics.

The depth of emplacement of the penetrator is controlled by its mass, the shaft diameter, the nose and afterbody shape, the penetrability (i.e., bearing and tensile strength) of the nucleus material, and the impact velocity. The impact velocity is determined by the minimum penetration depth requirement for the hardest nucleus material. The specification for the minimum penetration depth is determined by proper placement of the instruments (particularly the gamma-ray spectrometer) and loads encountered during impact. The minimum depth of penetration must also be sufficient to eliminate any tendency for the penetrator to slap down during impact. Penetration for a possible soft material must be arrested by a flared afterbody, or "terrabrake". Peak loads occur for materials of intermediate hardness, when the terrabrake strikes the surface and the residual velocity is absorbed by the larger contact area. The shape and size of the terrabrake must be chosen to limit the loads and the depth of penetration for soft material. The depth of penetration into the softest material can be reduced by increasing the diameter of the terrabrake, but this approach results in system weight and integration to the spacecraft problems that are not compatible with the proposed CRAF mission.

The baseline configuration shown in Figures 2-1a and 2-1b is a compromise between the many design factors involved. Starting at the nose, the shape has an overall aspect ratio (i.e., length to diameter) of 3:1 to provide an initial low resistance to penetration. The forward third of the nose has a short cylindrical section 2 cm in diameter that greatly reduces the tendency of the penetrator to slap down when striking at a less-than-normal impact angle. The blunt nose tip also provides better depth resolution from the accelerometer data, which is particularly important for sensing a mantle. The nose segment includes an anchoring mechanism to provide added assurance that the penetrator will remain locked to the nucleus following impact and penetration. The forward diameter of the penetrator shaft is 6.5 cm, at a station 19.5 cm aft of the nose tip, to accommodate the alpha particle instrument as far forward as possible. The shaft tapers to 12.5 cm at a station 58.9 cm aft of the nose tip. This provides the required volume for

the gamma-ray spectrometer and its thermal isolation system. The taper also provides a gradually increasing deceleration that helps alleviate the peak loads encountered for materials of intermediate penetrability. Aft of the shaft is the conical terrabrake, which extends to a station 85 cm aft of the nose tip with a base diameter of 50 cm, designed to arrest and absorb the impact in surface materials of intermediate to high penetrability. At the back end of the terrabrake is sufficient volume to place the data handling, power, and communication subsystems. By positioning these subsystems around the periphery of the base, the spin moment of inertia is maximized (which is desirable for stability purposes). The small solid rocket motor is located on the penetrator centerline at the aft end. The overall length of the penetrator is 103.2 cm.

3.0 Requirements Discussion

3.1 Gamma Ray Detector Design Issues

Extraction of compositional data from the gamma-ray flux in the comet nucleus requires a detector that can accurately determine the energy of gamma rays striking it. Previous planetary investigations used scintillator detectors, but recent developments in semiconductor gamma-ray detectors have substantially improved the achievable energy resolution. Detection of gamma rays in a semiconductor is based on the production of charge carriers (electrons and holes) in the semiconducting material when a gamma ray's energy is absorbed. Its energy can be deposited in the detector by the photoelectric effect, Compton interaction, and pair production. The electrons and holes produced are collected by an electric field in the material to provide a signal that is a direct measure of the energy of the gamma ray. For successful gamma ray detection a semiconductor needs high resistivity, high Z , and needs to be manufacturable in a large size and with current blocking electrical contacts. Germanium is the most suitable semiconductor that has the required characteristics. A minimum detector size of about 5 cm diameter and 5 cm long is necessary to achieve acceptable sensitivity.

In order to collect charge from the whole of a detector, an electric field of about 1000 V cm^{-1} must be applied across it by application of a voltage to electrodes on its opposite faces. Furthermore, the leakage current flowing through the material must be very small so that the signal arising from the gamma ray is detectable. If the detector contacts provided a free exchange of holes and electrons between the semiconductor and the external electrodes, large currents would flow through the detector when a voltage is applied across it. To overcome this, "blocking" contacts must be used - that is, the positive contact must not inject holes, nor the negative contact inject electrons into the material. This can be achieved by forming heavily-doped n and p regions at the detector surfaces. The n^+ surface is used as the positive detector electrode, and the p^+ surface as the negative electrode. The materials used for doping are lithium at the n^+ contact and boron at the p^+ contact. Lithium is diffused into the germanium at high temperatures, forming a fairly thick and rugged layer, whereas, ion implantation is used for the boron, producing a layer that is thin and less rugged.

Minimization of leakage current also dictates that the detector must be operated at low temperature. The large thermal generation rate of hole-electron pairs by excitation of electrons across the $1.12 \times 10^{-19} \text{ J}$ (0.7 eV) band gap makes acceptable operation at temperatures higher than 120 K increasingly dependent on the characteristics of the particular detector used and the design of the electronics, with an absolute limit of roughly 130 K. The requirement that the detector be maintained below 120 K for the duration of the experiment provides design margin and has been a major driver for design of the penetrator.

Another consideration in detector design is susceptibility to radiation damage that may be suffered due to cosmic ray bombardment during the long transit time to the comet. Energetic particles can produce interstitial-vacancy pairs in a germanium crystal by knocking the atoms from their normal positions.

Because the dense regions of damage produced by energetic particles provide trapping sites for holes and electrons, detectors are sensitive to radiation damage. Hole trapping, which is the predominant degrading effect on energy resolution, may be minimized by building a cylindrical coaxial detector with the p^+ contact on the outside. The holes then make only a short traversal from the outer portions of the detector (where most interactions occur) to the contact of collection. To establish high fields at the periphery, we must use n-type germanium. Reverse electrode (n-type) coaxial detectors are thus about 30 times less sensitive to radiation damage than conventional-electrode (p-type) coaxial detectors, and are consequently the proper choice for our gamma-ray spectrometer.

The choice of a reverse-electrode configuration has an important influence on the manner in which the detector is mounted. In this configuration, the more rugged Li-diffused n^+ contact is on the inner hole surface, while the very thin B-implanted p^+ contact is on the outer surface. Given the preference to support the detector on the inner rugged Li-diffused contact, the use of a true coaxial detector is appropriate. To provide as large a load-bearing surface as possible, we will need to determine how far the Li-diffused layer can be extended outward from the inner hole of the coaxial detector while still maintaining good diode characteristics. The detector will need to be mounted in such a way as to prevent the detector surfaces from becoming damaged and to protect the brittle crystal itself from the shock generated by impact with the comet nucleus and from other vibration sources. Another requirement generated by susceptibility to radiation is the need to anneal out any radiation damage prior to emplacement. This generates a requirement to be able to heat the crystal for an appropriate temperature - time profile. The high diffusivity of the lithium dopant limits the temperature of the anneal to about 100°C. Incidentally, having the lithium as the inside contact minimizes the loss of detector volume as a result of lithium diffusion during this annealing cycle since a given thickness of lithium drift corresponds to a smaller volume at the inner radius than it would at the outer radius.

Another decision in detector design is the selection of ac or dc coupling. Although dc coupling is normally used for germanium spectrometers in laboratory applications, ac coupling appears to be the clear choice for this application. First, ac coupling allows a higher range of detector leakage current than dc coupling, which could have the leakage current increase enough through temperature elevation or contamination to saturate the preamplifier, effectively terminating the experiment. Under these conditions, ac coupling would still provide a useful signal, although somewhat degraded. Second, if dc coupling were used, the outer surface of the detector would have to be held at about -3000 V. With space in the penetrator at a premium, the available volume for the detector would have to be reduced in order to prevent high voltage breakdown (corona and/or arcing). Finally, although ac coupling introduces some additional system noise, its amplitude will probably not be sufficient to measurably affect the performance of the spectrometer.

Another important factor affecting the design and mounting of the gamma-ray detector is the necessity to avoid contamination. The detector must be placed in an enclosure that protects it from potential surface contaminants, particularly moisture, small amounts of which can significantly degrade

detector performance. This enclosure could either be evacuated, or filled with an inert gas such as argon or helium. A substantial voltage will exist between the enclosure wall and the detector. If a low gas pressure developed in the enclosure, arcing could occur. This will be avoided either with an evacuated enclosure that contains gettering material to absorb trapped gases released, or an enclosure sealed reliably to retain an inert gas through the life of the mission. These considerations are discussed further in section 5.7 where it is shown that the inert gas filled enclosure is more amenable to test verification of seal integrity.

3.2 Alpha-Backscatter Spectrometer Design Issues

The basic alpha-backscatter spectrometer design issues are well understood as the instrument to be used on the penetrator has already had considerable development and is evolutionary. The major issue for the penetrator application is associated with the sample to be analyzed.

It is necessary for the alpha particle source and all the detectors to have an unobstructed view of the cometary material. Several factors must be considered in developing a design that allows this geometry. First, because our primary goal is to establish the composition of the most pristine nucleus material available, it is desirable to place the alpha particle instrument as far forward in the penetrator as possible. It would, of course, be valuable to obtain measurements both at depth and at the surface, so that any difference in composition could be determined. However, presently available resources allow only one fixed alpha particle instrument, and the first-order objectives of the mission dictate that it be used to sample as far beneath the surface as possible.

A second consideration is that we must avoid sampling material modified by passage of the penetrator. Tests have shown that a thin (1-2 mm) layer of soil immediately adjacent to a penetrator wall may undergo chemical modification due to heating during penetration. Having the instrument placed as far forward as possible will place it in the region that will have been least altered, but this is not considered totally adequate in itself.

Sampling drills have been considered for alpha particle instruments on Mars penetrators, but are inappropriate for the CRAF mission because of volume, power, and cost restrictions. We have considered several other simpler, yet effective, means of acquiring an unaltered sample. Penetration tests show that even hard crystalline material is finely crushed by passage of a penetrator, to a distance of up to one penetrator diameter from the wall. One approach, then, might be to have an external "scraper" that would mix crushed material and guide it into a chamber where it would be viewed by the detector. A possible drawback to this approach is that there is no simple way to ensure that the opening would not be jammed by large particles, or that it would not be filled with volatile-depleted material as the penetrator passed through the mantle. The simplest method, and the one in our baseline penetrator design, is to have a port in the wall of the penetrator with a small obstacle immediately in front of it that will divert and mix the flow. The port must be covered with a door that protects the sources and detectors during the impact. Experience shows that the pressure produced by passage of

the penetrator is highest on the nose, and is relatively small on the straighter sections. Sandia tests show that material will be pressed firmly against the penetrator body after it comes to rest. In order to minimize these forces and simplify the door mechanism, the door is placed immediately behind the base of the nose.

3.3 Physical Properties Instruments

Complete description of the penetrator's path requires that a record of acceleration be acquired for the entire penetration event from at least two groups of triaxial accelerometers. The penetrator design includes two triaxial accelerometer packages, widely separated. The electronic sampling of these signals must be in the sub-millisecond range.

Another objective of the accelerometer investigation is to determine the density and thickness of the mantle. It is expected that the mantle is fairly thin and has very low strength and is unlikely to be adequately detected by the triaxial accelerometers; which have a range of $+ 5886 \text{ m s}^{-2}$ ($+ 600 \text{ g}$), sufficient to cover the maximum possible decelerations. Consequently, an additional accelerometer is required which is axially-oriented, capable of detecting up to $+ 98.1 \text{ m s}^{-2}$ ($+ 10 \text{ g}$) with a resolution of the order of 0.1 m s^{-2} and with a sampling interval of about 100 microseconds.

The objective of the temperature sensors is to measure the temperature profile of the nucleus with depth and to estimate thermal diffusivity. When a penetrator strikes and enters a material, the major energy dissipation goes into fracturing and disturbing the material, and the disturbance stretches out for several penetrator diameters. However, significant changes in temperature only occur close to the penetrator shaft itself. Since it is not practical to deploy temperature sensors far enough away from the penetrator shaft to be in material unaltered by the penetration event, the requirements placed upon the design of the temperature sensors spaced along the penetrator shaft are:

- 1) The sensors have to be deployed away from the penetrator shaft as soon as possible after penetrator emplacement to measure temperatures before the profile is modified by the altered material properties and the presence of the penetrator.
- 2) The sensors should have a low thermal mass and be thermally isolated from the penetrator structure.
- 3) Relative accuracy between sensors is more important than absolute accuracy.

The altered material around the penetrator precludes the possibility of determining thermal diffusivity of the pristine cometary material by active techniques after emplacement.

4.0 Baseline Design Summary

4.1 Penetrator System Structure and Science Instruments

4.1.1 Nose and Shaft Structure

The design of the penetrator system is shown in Figures 2-1a and 2-1b. A mass summary is given in Table 4-1. The nose, shaft and front portion of the terrabrake are made in two parts from a titanium alloy (Ti-5Al-2.5Sn) that has good yield strength and ductility characteristics at cryogenic temperatures. The nosepiece, which also includes the first 10 cm of the shaft taper, screws onto the main shaft section and is keyed and locked into the correct orientation. The nosepiece has several penetrations: a 2 cm diameter opening through which the alpha particle instrument will view the cometary material, a 0.7 cm diameter opening through which one of the temperature sensors will be deployed, and several small access holes (to be sealed prior to launch) to enable opening and closing of the alpha particle instrument door and shutter mechanisms manually during tests. The alpha particle instrument, one high range triaxial accelerometer package, the single axis low range accelerometer, and a deployable temperature sensor are mounted to a flange on the main shaft section so that the complete instrument assembly is accessible when the nosepiece is removed.

*Table 4-1
Penetrator System Estimated Mass Summary*

Component	Mass, kg
Nosepiece (Threaded)	1.17
Main Shaft Section	1.86
Alpha Particle Instrument Assembly, Mounts, & Pin Puller	0.22
Front Support Assembly	0.20
Gamma Ray Detector Assembly	1.20
Rear Caging Assembly, Mounts & Pin Puller	0.72
Titanium Terrabrake Section (Plus Ring)	0.99
Kevlar I-Beams	0.28
Front Shelf (Honeycomb) (Plus Inserts)	0.25
Kevlar Terrabrake Section (Plus Rings)	0.46
Support Tube	0.09
Electronics Support Shelf (Plus Inserts)	0.64
Support Shelf Mounting Flange	0.31
Electronics Enclosure	0.71
Electronics Boxes, Harness Cabling, & Batteries	6.70
Back Plate	0.65
Rocket Motor & Insulator	1.49
Torque Cylinder	0.55
Clamp Cylinder	0.90
Push Pull Disconnect	0.22
Multilayer Insulation	0.11
Structural Fasteners	0.34
Accelerometers	0.07
Temperature Sensors	0.22
Penetrator Total	20.35
Marmon Clamp, Explosive Bolts, & Bolt Catchers	0.90
Penetrator Support Module Electronics & Cabling	2.50
Receiver Antenna & Cabling	0.30
Spacecraft Tiedown	0.72
Support Column	0.77
Spin/Eject Assembly	1.15
Radiation Shield	0.68
Penetrator Support Module Total	7.02
Penetrator System Total	27.37

The wall thicknesses in the nose section and in most of the shaft section, were determined by the bending loads caused by our design worst-case impact (20° angle of attack, 30° surface slope) into the hardest material ($S = 2$). Under these worst-case conditions and selected wall thicknesses, the calculated stresses are less than the yield stress of the titanium alloy at 80 K. As a further safety margin it should be noted that some yielding and permanent bending can be tolerated in this design.

In order to anchor the penetrator to prevent it from backing out, four spring loaded tabs are attached to the forward part of the nose. The tabs are hinged at the front and are held in place by a slip ring. The slip ring will be forced off the tabs and flattened against the main tapered portion of the nose when the penetrator enters into the nucleus, so releasing the tabs. If the penetrator tends to back out, the tabs will hinge out and dig into the nucleus material and hold the penetrator in place. The hinges are designed with a controlled yield that begins when the tabs are extended by 45° , and finally prevents extension beyond 90° . If the nucleus is too soft to move the slip ring, the penetrator will end up well below the surface, and additional anchoring will not be required.

4.1.2 Temperature Sensors

A fixed temperature sensor is embedded as far into the nose as permitted from a structural strength standpoint. The electrical connections are made via a self-centering fixture attached on a bracket to the structure that supports the alpha-backscatter instrument. The fixture contains sprung wiper contacts that make contact with the concentric contacts at the end of the temperature sensor. This form of interconnect allows for relative rotation during assembly.

Three other temperature sensors are mounted along the length of the penetrator, one just behind the alpha particle instrument, one near the shaft-terrabrake junction, and one near the aft end of the terrabrake. The sensors are mounted on probes that are spring loaded and released with non-explosive initiator devices. They are driven into the crushed comet material surrounding the penetrator immediately following impact. The deployed sensor mechanism is considerably smaller in diameter than the opening in the penetrator wall, and is designed to make good thermal contact with the cometary material while remaining thermally isolated from the penetrator structure. A small deflector is mounted upstream of each of the deployable temperature sensor openings, to prevent a significant amount of material from lodging in the opening. The deployment distance for each sensor will be determined by measuring the residual spring force, with a pressure transducer at the base of the spring, to aid in data interpretation. Since the spring load for emplacing the temperature probes can be accurately calibrated, they can also serve as miniature penetrometers to sense the mechanical properties of the crushed material adjacent to the penetrator.

The temperature sensors use dual-redundant thermocouples as sensing elements, with periodic self-calibration of the high gain signal amplifiers. Type E chromel-constantan thermocouples will be used (27 to $45 \mu\text{V K}^{-1}$, depending on the temperature regime), terminated in contact with a precision platinum

resistor. Thermocouples were selected as temperature sensors because of their simplicity, ruggedness, and stability. The sensing elements have very low thermal capacity, to achieve a rapid response time. By selecting low-power signal amplifiers, the power consumption is about 1 mW for each operational amplifier. The reference junction and bias network also consume 1 mW. The major error source is bias drift of the electronics. Most of this effect can be calibrated out by periodically shorting the amplifier input.

4.1.3 Accelerometers

One low range single axis accelerometer and one full range triaxial accelerometer package are mounted in the nose of the penetrator. Another full range triaxial package is mounted in the terrabrake. We have selected quartz accelerometers manufactured by PCB Piezotronics. These devices are compact, lightweight, and have been extensively tested and used for many applications. Special cryogenic models are available and have been used at liquid nitrogen temperatures. Consequently, the low operating temperature expected does not present a development problem. The triaxial accelerometers used will be the cryogenic version of model 306A06, with a $\pm 5886 \text{ m s}^{-2}$ ($\pm 600 \text{ g}$) range. The low range accelerometer will be the cryogenic version of the high sensitivity model 303A11, with a $\pm 98.1 \text{ m s}^{-2}$ ($\pm 10 \text{ g}$) range. Each accelerometer contains its associated microelectronic amplifier in the same package, and provides a nominal 5 V output at full range, using a constant current excitation source. The co-location of the sensor and amplifier, and the low output impedance of the amplifier, result in a low noise system. Typical peak-to-peak noise output for these accelerometers is $\sim 200 \text{ } \mu\text{V}$; this is the limiting parameter for accelerometer resolution, and is in any case less than the penetrator data system A/D converter 1sb digitization resolution of 1/1000 of full scale. The accuracy of the measurement will be $\sim 6\%$ of the reading or as limited by the digitization error.

4.1.4 Alpha Particle Instrument

A compact alpha particle instrument will be used. The instrument incorporates the alpha particle sources and several detectors in a small package. The arrangement of the sources, detectors, and the sample in the detector head of the instrument is shown in Figure 4-1. The overall dimensions of the sensor head are those of a cylinder about 4.0 cm in diameter and 4.5 cm high. The important components of the instrument are a set of radioactive alpha sources, a mechanical shutter, two detecting assemblies for the alpha and proton modes, and an x-ray detector for the x-ray mode. In addition, a door mechanism is required to prevent cometary nucleus material being forced into the instrument during the penetration event. The door mechanism has been designed to withstand high side loads during penetration, but to open with relatively low moving forces. The guides and link mechanisms are such that the door backs in towards the alpha particle instrument detectors and then translates sideways towards the rear of the penetrator, leaving the alpha particle instrument sources and detectors with a clear view of the cometary material. The door is moved in a single motion by a negator spring that is released by a non-explosive pin-puller. The door can also be moved manually to permit assembly and system testing. The alpha particle instrument geometry is optimized for viewing a sample at the outer surface of the penetrator.

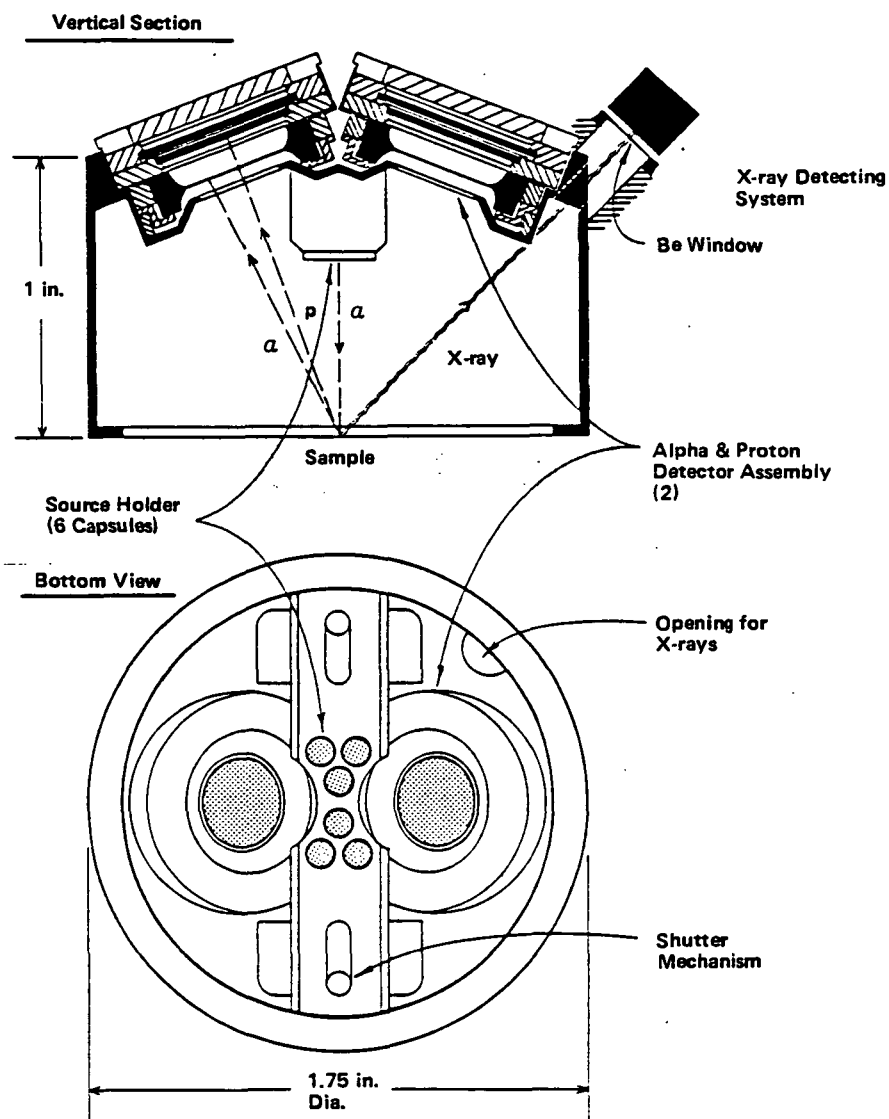


Figure 4-1 Configuration of Alpha Particle Instrument

When the door is in the closed position, a calibration sample mounted on the inside of the door provides a high quality calibration, even though the door thickness sets the calibration sample slightly closer than the optimum position. A small protrusion is mounted on outside of the nosepiece of the penetrator, upstream of the door, to provide mixing of the comet material that has not been in intimate contact with the penetrator wall.

4.1.5 Gamma-Ray Spectrometer

The penetrator shaft is essentially filled by the gamma-ray detector assembly as shown in Figure 4-2. This assembly is caged up to the completion of emplacement, providing good thermal contact for annealing and cooldown while on the spacecraft and providing a firm attachment during the impact. In the caged configuration the detector assembly is firmly clamped between the front support assembly and the rear support assembly. The front support assembly is fixed at the front end of the shaft and comprises a shaped seat for the front end of the detector assembly outer housing and a spring loaded post-emplacment support mechanism. In the caged configuration the spring in the support is compressed by 2.5 mm. The detector assembly is uncaged and supported very loosely for thermal isolation between two spring loaded low thermal conductivity Kevlar pin contacts after emplacement. When the system is uncaged by retracting the rear support seat immediately following the emplacement, the spring pushes the detector assembly away from the front seat centering and supporting the assembly between the point supports at the front and rear support assemblies. In the caged configuration the rear caging seat is held in place against the rear end of the detector assembly by a pin-puller clamped to the support frame. This non-explosive pin-puller is designed to carry a 4500 N axial load, and has a 5 mm travel. When the pin-puller is activated, the spring loaded rear caging seat moves away from the detector assembly housing by about 5 mm and the detector assembly moves about 2.5 mm towards the rear spring-loaded point support mechanism. The stops on the support mechanisms are adjusted during assembly such that the distance between the two points is a little larger than the distance between the point seating locations on the detector assembly outer housing. This assures that, when uncaged, there is a low pressure contact between the points and the detector assembly outer housing, minimizing the thermal conduction path. The inside of the penetrator shaft and the outside of the detector assembly housing have highly reflective vapor deposited gold surfaces to minimize radiative heat transfer. Some care will be needed in the surface treatment of the seating areas to assure separation when uncaged.

The gamma-ray detector assembly has an external thermal isolation can, internal crushable honeycomb to absorb high peaks during deceleration, and a sealed inner contamination protection can. This sealed enclosure will either be evacuated or filled with an inert gas. It may be vented to space after launch. The outer surface of the inner can is coated with a thin layer of material rich in a neutron absorber, such as boron, to provide the neutron detection capability. The emissivity of this surface is of no concern, since the radiative thermal isolation occurs between the polished gold surfaces of the detector assembly outer housing and the penetrator shaft inner wall. The major material used in the gamma-ray detector mounting assembly is the same titanium alloy as used for the penetrator structure. The same material is

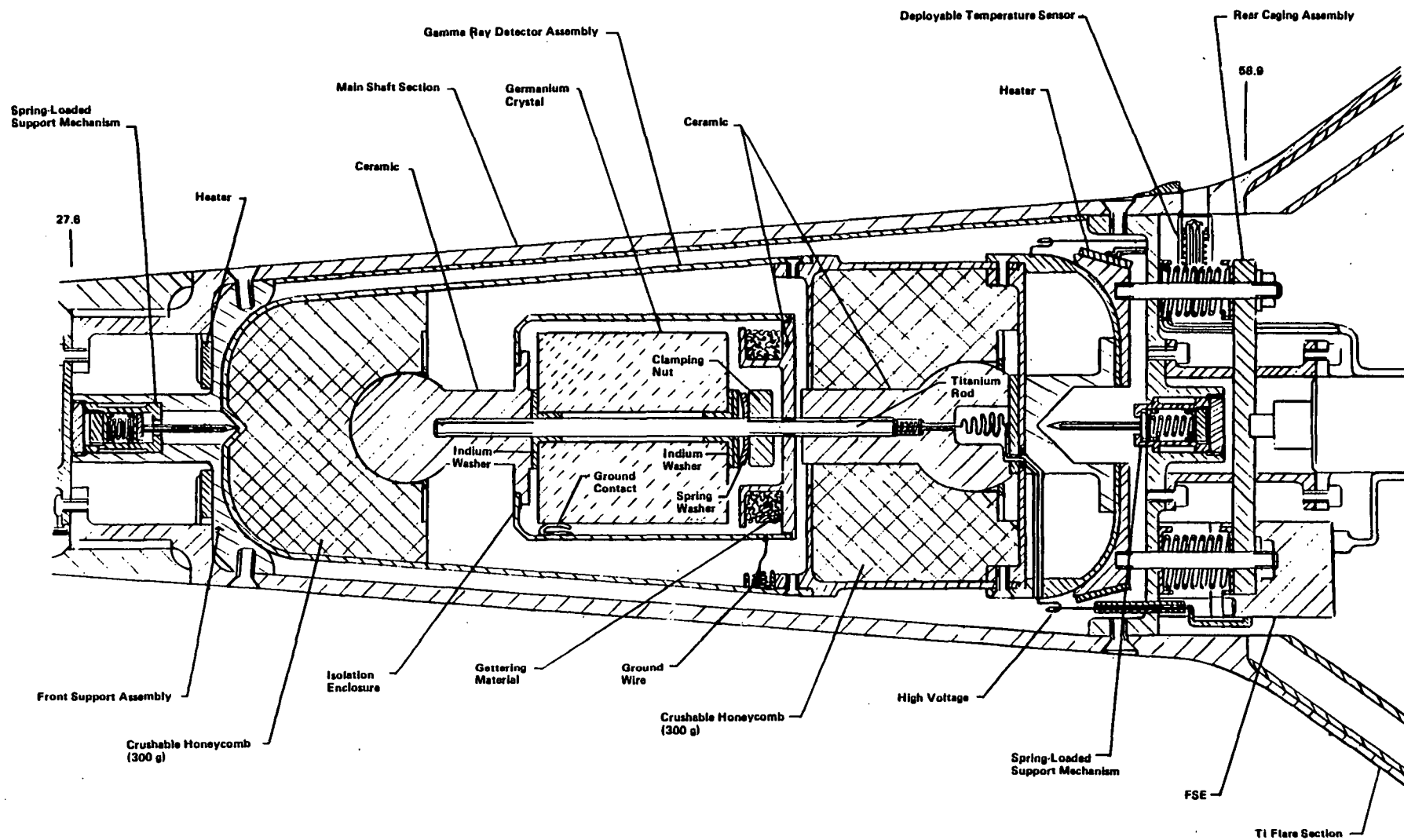


Figure 4-2 Gamma Ray Detector Assembly

used as much as possible in order to avoid the introduction of additional chemical elements that may degrade the experimental results. In addition, the physical properties of this titanium alloy at cryogenic temperatures make it very suitable for both the structure and for the spring washers that are used as part of the assembly, maintaining compression on the contact between the central support rod and the detector crystal.

The gamma-ray detector crystal is a single, true coaxial, high purity germanium crystal. It is a reverse electrode design, with the lithium diffused n^+ surface on the inside and the boron-implanted p^+ surface on the outside, to minimize the effects of radiation damage. Because the lithiated surface is more rugged ($\sim 500 \mu\text{m}$ thick) than the borated surface ($\sim 0.2 \mu\text{m}$ thick), the lithiated surface is extended a short distance out onto each end of the crystal to provide adequate mounting surfaces. In our baseline design, the Ge crystal is mounted inside a can to provide isolation from contamination. The cylindrical part of the can is titanium with the end pieces alumina insulators (alumina is used instead of silica to avoid interference with the gamma-ray signal from Si). The forward alumina piece is shaped to provide a part of the load limitation system, and is brazed to the titanium cylinder. A titanium rod, with an outside diameter less than the inside diameter of the germanium crystal, screws into this endpiece along the axis of the can. A washer/sleeve made from a soft metal, such as indium or annealed gold, is placed over the rod and down against the endpiece to act as the seat for the germanium crystal. The germanium crystal is then mounted on the rod through the central hole and is inserted into the can. A second soft washer/sleeve, load bearing washer, spring washers, and locking nuts are then placed over the end of the rod and screwed down to firmly hold the crystal in place and under compression. The soft seating washer/sleeves are intended to flow during this assembly process to take up any surface roughness so as to evenly distribute the load to the germanium crystal. The spring washers ensure that the crystal will be firmly held when the system is at any temperature and after a significant number of thermal cycles.

The alumina lid to the can, to which is attached a 33 g SAES Zr-Al activated getter (for the evacuated approach), is placed over the titanium rod and laser beam welded in place to the rod and to the can. The getter has enough excess capacity to absorb any outgassing products from the welding. All of this final assembly will be performed in a specially constructed clean high-vacuum assembly chamber which is either evacuated or backfilled with inert gas during detector assembly. The signal and positive high voltage electrical connection is made to the n^+ crystal electrode through the titanium rod at the lithiated surface and the ground electrical contact is made by a spring connection from the titanium can to the borated surface. This spring connection is held away from the borated surface during assembly with a fixture that is removed when the crystal clamping has been completed. The high voltage lead is attached to the free end of the rod and threaded through another shaped alumina endpiece that is also a part of the load limitation system.

The detector mounting technique described here is the present baseline approach. However, there are several areas requiring further study before a final design approach is selected. The question regarding whether to vacuum

seal the crystal can, or backfill with inert gas, or provide a vent to space is also still open. This will be resolved at a later time. Present indications suggest that the backfilled enclosure would be best. New proprietary ultrasensitive leak detection techniques developed at Martin Marietta have provided a substantial breakthrough in capability, and would be able to verify adequate sealing of the backfilled enclosure against inward diffusion of moisture for the duration of the pre-launch period (leak rate $Q < 1.33 \times 10^{-13} \text{ Pa m}^3 \text{ s}^{-1}$ ($1 \times 10^{-12} \text{ torr l s}^{-1}$)) and more than adequate sealing against outward leakage during the 6.5 year time from sealing to end of mission. In the evacuated approach the Zr-Al getter would maintain a $1.33 \times 10^{-10} \text{ Pa}$ ($1 \times 10^{-12} \text{ torr}$) vacuum after gettering 133 Pa m^3 (1000 torr liters) of hydrogen at 250°C (the principal outgassing product from the Ge crystal and contamination protection can). This pressure would rise to only $1.33 \times 10^{-8} \text{ Pa}$ ($1 \times 10^{-10} \text{ torr}$) during the 100°C crystal anneal, and would drop well below $1.33 \times 10^{-10} \text{ Pa}$ ($1 \times 10^{-12} \text{ torr}$) after cooldown. Care has been exercised in the selection of this getter to avoid a material with unwanted low level radioactivity that would increase the gamma-ray background.

The approach taken to load limitation for the crystal is to provide crushable aluminum honeycomb that provides a controlled yield above a selected deceleration threshold, both axially and radially. We have performed a detailed calculation of how much of the total kinetic energy of the detector assembly is dissipated axially above selected deceleration thresholds for penetration into materials of different penetrability. The baseline design uses a material that, at the impact temperature, has a crushing threshold of 2943 m s^{-2} (300 g), consequently the maximum crystal deceleration is limited to 2943 m s^{-2} (300 g). Recent successful tests at 3434 m s^{-2} (350 g) show this to be an acceptable level for the single crystal germanium detector.

In the worst-case penetration condition, about 4% of the detector assembly energy lies above 2943 m s^{-2} (300 g) and needs to be absorbed by crushing the honeycomb. This is shown in section 5.1, figure 5.1-3. The honeycomb maximum crush distance has been selected to provide absorption of 15% of the detector assembly energy, so providing a significant margin for absorbing unexpected energy spikes, should any occur. The honeycomb is laid in to take both axial and radial loads. The supports into the honeycomb are keyed to prevent rotation of the crystal relative to the housing during penetration spindown. The 12 mJ of crystal rotation energy is transmitted to the support rod through the spring washer/soft metal seat described above. The electrical interconnectors have sufficient slack to allow travel of the full crush distance without breaking. The first stage electronics (FSE) package for the gamma-ray spectrometer is required to be mounted close to the detector in order to minimize system noise, and has a minimum operating temperature requirement of 130 K. This FSE package is mounted on standoffs to a part of the rear caging assembly and is tied thermally to the wall of the penetrator shaft. The FSE, which will dissipate about 20 mW during operation, will have a backup heater to keep it warm enough in the case of a cold comet. The wires running between the detector and the FSE include thermal barrier regions to minimize the heat leak into the crystal.

4.1.6 Terrabrake Structure

Wall thickness designs for the terrabrake and the terrabrake-shaft region were determined for a worst-case impact that generates a maximum side load force by putting essentially all of the terrabrake forces on one side of the terrabrake (an intermediate hardness material with a surface slope of 30°). Under these worst-case conditions and the selected wall thicknesses, the calculated stresses are less than the yield stress of the titanium alloy at 80 K.

The rear portion of the terrabrake is fabricated from Kevlar-Epoxy and reinforced with Kevlar-Epoxy I-beams. The front shelf and the electronics support shelf are Kevlar honeycomb. These Kevlar-Epoxy components reduce weight and provide thermal isolation between the cold forward section of the penetrator and the warm electronics in the terrabrake region. The hold-down to the penetrator support module and the separation guide surface are a part of the circular wall on the inside of the electronics annular region. The penetrator support module is discussed in Section 4.1.8.

The penetrator electronics and batteries are mounted in three annular segment magnesium packages. The batteries are contained in two identical packages and the electronics in a third. Packaging techniques are relatively conventional, both the batteries and electronics packaging having Galileo Probe heritage. The thermal isolation requirements are, however, very stringent. The electronics and battery packages are separated from and boxed in Kevlar-Epoxy packages that, in turn, are wrapped in multilayer insulation. Extreme care has been exercised in the design of the package support standoffs. Electrical interconnects between packages are laid in support channels where necessary (in order to minimize destabilizing energy dissipation while in flight between the spacecraft and the comet) and are wrapped in thermal insulation in order to minimize heat loss. The batteries and electronics will be operated at the low end of their acceptable operating temperature range. These extreme measures are necessary to minimize heat leakage into the gamma-ray detector crystal and minimize the electronics package heater power requirements. The actual operating temperature to be selected for the batteries will also take account of battery energy output capabilities as a function of operating temperature.

4.1.7 Rocket Motor

The rocket motor is mounted separately from the electronics support shelf on an isolated assembly in order to minimize heat from the fired motor leaking back into the penetrator. The rocket motor selected is a Morton Thiokol TEM 712. This motor was developed and qualified as a part of the Minuteman program. The motor uses hydrocarbon ammonia perchlorate fuel in a front burner mode. This results in a slow burn with very uniform thrust, which is a necessary characteristic for our application. The initiator will meet the requirements of MIL STD 1562. The temperature of the rocket motor will be controlled to a lower limit of -18°C during the coast from the spacecraft towards the comet in order to retain the burn characteristics within acceptable limits. The rocket motor selection is discussed in section 5.8.

4.1.8 Penetrator Support Module

The penetrator support module provides the major mechanical and electrical interfaces with the spacecraft, and is fabricated from Kevlar-Epoxy, except for the spin-eject mechanism. The penetrator is held to the PSM by a 20 cm diameter Marmon clamp assembly. Release of the clamp is actuated by redundant pyro initiators. These initiators are wired directly into the spacecraft pyro firing circuits and their firing is a spacecraft function. Locking the Marmon clamp pulls the penetrator into a compressive support to the PSM structure around its periphery, providing a very rigid mount for carrying launch vibration loads. Pyro actuated separation of the electrical connector between the penetrator and the PSM is also a direct spacecraft function. As well as providing all the necessary interconnects between the penetrator and the PSM, the separation connector also carries redundant shorting links that provide a short circuit across the rocket motor igniter and assure that the rocket motor cannot be fired until after the penetrator is separated from the PSM.

The spin-eject mechanism spring is held in the compressed state when the penetrator is locked in place by the Marmon clamp. When the clamp is released, the spring pushes the penetrator away and also rotates it as a result of guide pins in a helical groove. The moving part of the PSM spin-eject mechanism is supported and guided throughout the whole of its travel by ball races and the penetrator is also guided by another set of ball races attached to the PSM. This approach is expected to provide separation tip-off rates well within the worst-case bounds assumed in the penetrator flight dynamics analysis.

The electronics package in the PSM is fabricated from magnesium and contains the support electronics, including the receiver for receiving the signal from the penetrator after emplacement and the bus interface unit (BIU) for interfacing with the spacecraft. The receiver antenna will be mounted on the low resolution scan platform and connected to the PSM via a coaxial cable.

4.1.9 Penetrator Thermal Shield

The Penetrator Thermal Shield (PTS) consists of multilayer insulation on a lightweight half cylinder metal or Kevlar-epoxy frame. The PTS is necessary to maintain a small penetrator-spacecraft view factor, thus allowing use of passive cooling of the gamma-ray detector prior to separation. Both outer surfaces of the shield are blackened. This provides adequate shielding provided the shield is also in shadow during the cooldown cycle. Design of the shield will proceed when the spacecraft configuration and the mission scenario have become sufficiently firm.

4.2 Thermal Control

The penetrator's thermal design has four principal drivers. First, before release from the CRAF Spacecraft, the Ge crystal gamma-ray detector must be heated to 100°C for up to 30 hr to anneal it and reduce radiation damage suffered during the long transit to the comet. About 36 W of spacecraft electrical power is necessary to heat the detector.

Second, the gamma-ray detector and the penetrator must be cooled to the low operating temperature of 100 K just prior to release from the spacecraft. This is accomplished by turning the spacecraft so that the penetrator is away from the sun, permitting it to radiate to space. A lightweight thermal shield (the PTS) is used between the penetrator and the spacecraft. A thermal analysis of the penetrator system shows that a temperature of ~102 K is achieved passively in ~50 hr. Analysis also shows that during the ~80 min trajectory to the comet, the penetrator is not measurably warmed by insolation or by waste heat from the rocket motor. There could even be a cooling effect if the penetrator is directed such that the main solar load is on the aft end. During penetration, experience at Sandia suggests that ~5% of the penetrator's kinetic energy is transferred to the nose in the form of heat. The resulting temperature rise of the nose structure is less than 1 K, with negligible effect on the detector temperature. More details of the thermal modelling are discussed in section 5.4.

Third, the gamma-ray detector must be maintained below ~120 K after impact for a minimum of two days and a nominal period of five days to obtain sufficient data integration time. The highest ambient temperature below the surface of the nucleus (i.e., below the diurnal thermal wave) is expected to be less than 160 K. The approach used to maintain the detector temperature is a passive design that thermally isolates it from the penetrator body and the surrounding environment following impact. Under the worst conditions, 3 days of operation below 120 K can be expected. This is a conservative estimate, as the detector design may still function, in a somewhat degraded fashion, at warmer temperatures. The nominal temperature below the surface of the comet nucleus is expected to be near or below 120 K. Under this condition, thermal control for the planned 5 day operation should not be a problem.

Finally, the data handling, communication, and power subsystems must be within appropriate operating temperature ranges. This is accomplished by thermal isolation of these units and use of dissipated power within them, and by electrical heaters within the units using some of the battery power onboard the penetrator.

We have performed an extensive trade study to select the thermal concept for cooling the gamma-ray detector after annealing, and then maintaining it in its operating range while in the nucleus. Active cooling was ruled out due to weight and reliability concerns. A passive radiator concept held the promise of maintaining a steady state cooling for an indefinite period, but due to the uncertainties in thermal view factors due to topography, possible coating of the radiator by dust after impact, and even complete burial, that concept was eliminated. A reliable thermal isolation approach was selected.

The thermal performance of the penetrator system was analyzed using a thorough three dimensional radiative-conductive model using 118 nodes, with 563 radiative conductors and 165 linear conductors. All portions of the penetrator were divided radially into four sections, to take into account the variation in view factors to space and to the spacecraft. Low emissivity surfaces ($\epsilon = 0.1$) were assumed on all interior parts except for the vacuum-deposited gold surfaces of the gamma-ray spectrometer housing where the surfaces at the ends of the housing (which could be marred during impact) were

assumed to have $\epsilon = 0.05$, and the side walls to have $\epsilon = 0.03$. A conservative emissivity of 0.05 was used for all multilayer insulation (MLI) shielded surfaces. For the exterior radiation interface on the spacecraft side, the Penetrator Thermal Shield, consisting of a half-cylinder shield of MLI blanket with a radius slightly larger than the aft end of the penetrator and extending along the full length of the penetrator, was modeled. The spacecraft, at 210°C, was assumed to be covered by a blanket of MLI painted black ($\epsilon = 0.95$), and the PTS outer surfaces were also blackened or degraded ($\epsilon = 0.95$).

For analysis of the penetrator on the spacecraft, the electronics and the batteries were maintained at -40°C and -30°C, respectively. The motor was maintained at -18°C. With these conditions, the germanium crystal can attain a steady-state temperature of 102 K, approximately 50 hours after the start of cooldown from 100°C.

The temperatures attained in cooldown were then used in an analysis of the implanted penetrator. As a worst-case scenario, we assumed the comet nucleus temperature to be 160 K, with the penetrator fully buried. Thermal conductivity of the material external to the penetrator was taken to be the maximum probable for a wide range of possible comet nucleus properties. The electronics and batteries were held at a nominal operating temperature of -30°C. The gamma-ray spectrometer first-stage electronics were held above 130 K, dissipating 20 mW. The wires from the first stage electronics to the detector were taken to be 0.102 mm (4 mil) CRESS (these could be larger without significant effect). Mechanical support of the detector is achieved with hollow pins of Kevlar; these were assumed to be in continuous perfect contact with the detector housing, which over-estimates their heat load. Under these conditions, the detector would reach 120 K after 72 hours. The main heat load to the detector will be radiation from the titanium walls which quickly reach the temperature of the comet. Because these surfaces are vacuum-deposited gold, the emissivity would probably be lower than the values we have used and could be as low as 0.005 to 0.01. Using these emissivities, the detector could remain below 120 K for more than 100 hours in a 160 K nucleus. During the period from launch to rendezvous, the batteries, electronics, and rocket motor will need to be kept above their respective minimum temperatures. If the penetrator is in shadow, it will be necessary to heat the electronics (1.25 W) and batteries (0.5 W).

4.3 Electronics Systems

Figures 4-3 and 4-4 show the system-level electronics block diagrams for the Penetrator and the PSM. Both the penetrator and PSM systems include the following elements: controller and data handling subsystem, power subsystem, communications subsystem, active thermal control subsystem, and various interface elements. The penetrator also includes the subsystems associated with the various sensors and the propulsion control subsystem. Where practical, designs are similar for the penetrator and the PSM for cost effectiveness.

The design goal was to produce a system with minimal weight and cost and maximum reliability. Minimal weight and cost dictated a single string

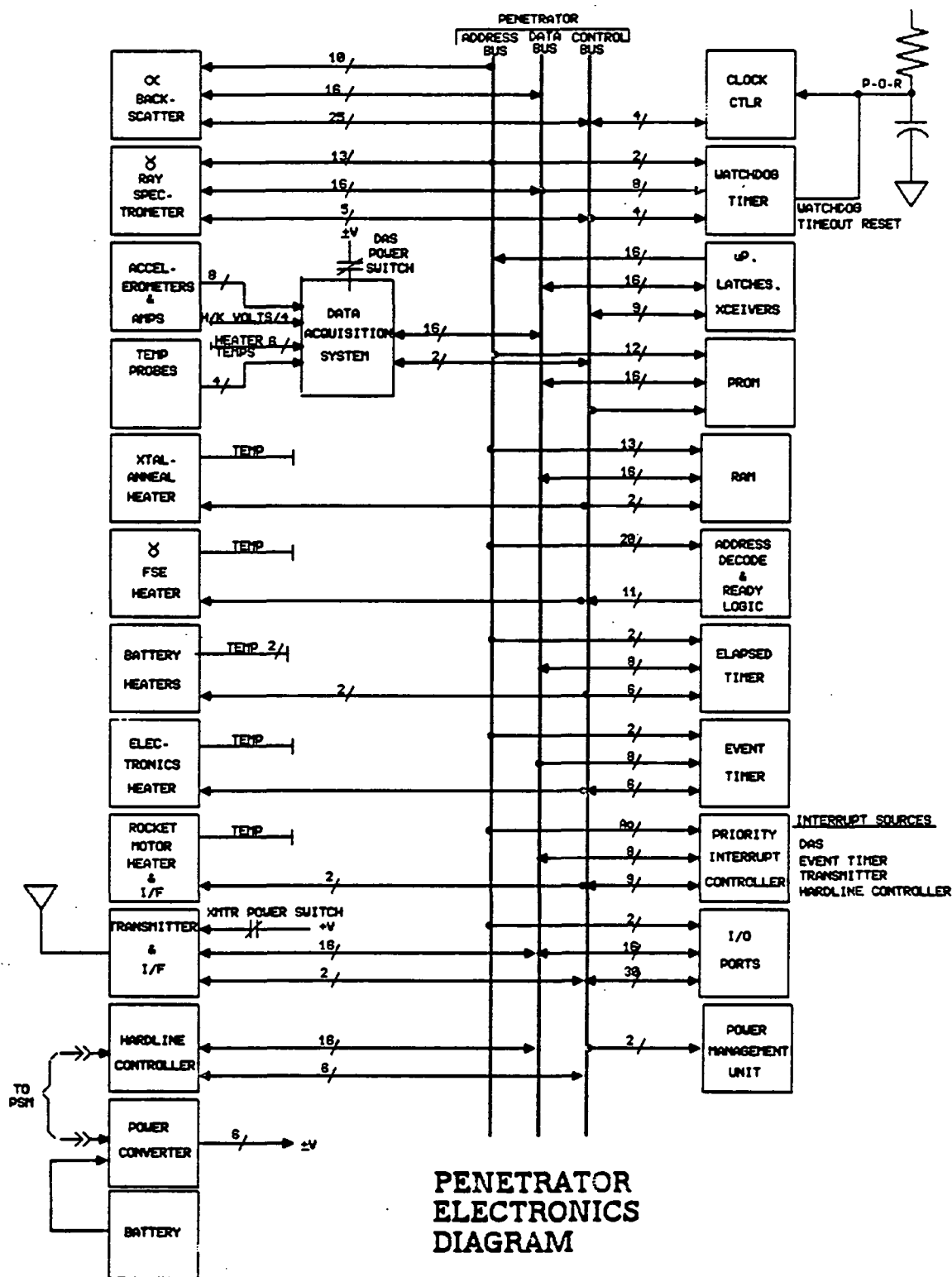


Figure 4-3 Penetrator Electronics, System Block Diagram

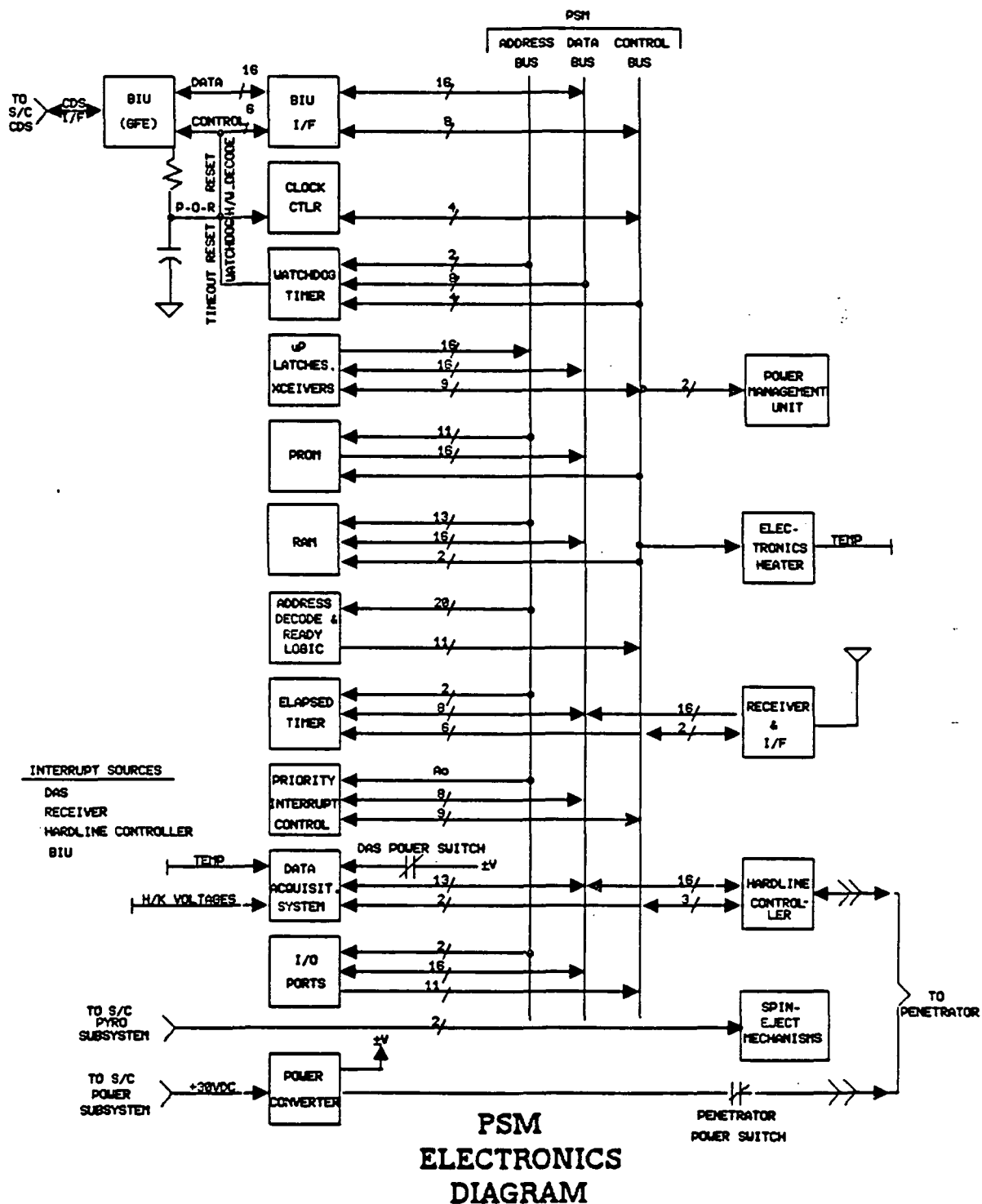


Figure 4-4 Penetrator Support Module Electronics, System Block Diagram

system. To maximize reliability, selected redundancy and some error-recovery features were incorporated. The solid rocket motor firing circuit contains redundant inhibit functions to prevent premature firing. Both the penetrator and PSM microcomputers contain watchdog timers for error-recovery purposes. Penetrator science data is inherently redundant since it continually integrates and is transmitted periodically to the spacecraft. Both the penetrator and PSM programs will have the capability of being modified in flight, by uplinking executable code to RAM.

4.3.1 Controller and Data Handling Subsystems

The controller and data handling subsystems in the penetrator and the PSM are almost identical. They are based on the 16-bit 80C86 microprocessor family, as per the CRAF Proposal Information Package (JPL PD699-10). Address, data, and control busses provide 16-bit wide interconnects between the various components of the system. Data transfer is transacted on the de-multiplexed data bus, addressing on the de-multiplexed address bus, and all of the strobe, select, and clock signals necessary to perform the data transactions are carried on the control bus. Because of concern with the 80C86 single-event upset rate, it is possible that it will be necessary to convert the design to another microprocessor family. This is not expected to be a problem, since the system architecture will be unchanged.

The memory requirements are 6 kbytes of programmable read only memory (PROM) and 16 kbytes of random access memory (RAM) for the penetrator, and 4 kbytes of PROM and 16 kbytes of RAM for the PSM. Operating software is contained in PROM and the estimates for the required PROM sizes were determined by decomposing the software requirements to the module level. An average of 100 instructions per module was assumed, and a scaled Gibson mix was used to calculate the average number of bytes per instruction. A further margin of 50% was added for growth. RAM estimates were based upon data storage needs, assuming a typical compression of 8:1 when using the JPL data compression algorithm for the gamma-ray spectrometer data, and a similar compression ratio for the alpha particle instrument data. The actual compression ratio for the alpha data will probably be better. RAM margin also exists for storing updated parameters and software, scratchpad usage, and to allow for growth. Memory capacity is sufficient to store the total data collected from all instruments for 5 days. The acceleration data require 30 kbits. The alpha particle instrument will require 512 channels of data each for both the alpha and proton mode measurements, and an additional 1024 channels for the x-ray mode. Each channel will be assigned a 14-bit word to record the total integrated signal for the maximum period of operation. The total storage requirement for the alpha particle instrument is 28 kbits. The gamma-ray spectrometer will quantize the gamma-ray spectrum into 8192 bins. A 16-bit word is assigned to each bin to record the total 5-day integration. The total storage requirement for the gamma-ray spectrometer is 131 kbits. Temperatures will be measured in four locations using a 10-bit word for each temperature measurement at 1 minute intervals for the first hour, and subsequently every 60 min. The total memory requirement for the temperature measurements is 7.2 kbits.

The penetrator firmware contains all of the necessary operating and sequencing controls to allow the penetrator to operate autonomously, once separated from the PSM, and to execute its mission to completion. The PSM firmware contains the necessary functions to execute its role as the interface between the Penetrator and the CRAF spacecraft.

4.3.2 Power Subsystem

The low voltage dc-dc converters in the Penetrator and PSM are identical. The penetrator also includes adjustable high voltage power supplies for the gamma-ray spectrometer detector bias (750-3000 V(dc)), and for the alpha particle instrument x-ray mode silicon detector bias (50-200 V(dc)). The control loop reference voltage for each supply is generated by a D/A converter under the control of the penetrator microcomputer. After gamma-ray detector annealing and prior to penetrator release, the voltages will be stepped by 250 V/step for the gamma-ray detector and by 25 V/step for the alpha particle instrument detector in order to measure the voltage vs. current characteristics for each. These measurements will permit selection of the optimal operating voltage levels for both detectors.

Power dissipation within these supplies can be minimized by setting the reference voltage to zero and turning off its complementary clock inputs. The penetrator supplies operate directly from the spacecraft 30 Vdc power bus through a power switch in the PSM when the penetrator is attached to the PSM, and from the 30 Vdc internal battery supply when it has separated from the spacecraft.

In order to conserve power, power switching has been implemented in both the penetrator and the PSM. The power management units are controlled by the microcomputer system and remove power from circuits when not in use. For example, the penetrator transmitter will be turned off between transmissions, reducing its power consumption from 5.6 W peak to ~50 mW average.

In order to minimize weight, our baseline design uses lithium thionyl chloride (Li/SOCl₂) cells, which have the highest energy density of any non-radioactive battery system. Galileo battery modules were also investigated, but their Li/SO₂ chemistry provides 6-7 ampere hours per cell at -40°C, compared to 10 ampere hours per cell for Li/SOCl₂, with a proportional increase in system weight. Two parallel stacks of nine Li/SOCl₂ D-cells are required to support a 5-day penetrator mission. The principal advantage of the Li/SO₂ battery is that it is qualified for use on the Galileo mission. If the additional weight proves to be acceptable, or if penetrator power estimates can be reduced during detail design, then the Galileo modules could be used.

4.3.3 Communication Subsystem

An FM design was selected for the penetrator-to-PSM RF link, primarily because of the abundance of off-the-shelf hardware available. The baseline design uses an Aydin Vector Model RCC 201-1 receiver on the PSM and an Aydin Vector Model TM-502/L transmitter on the penetrator. The antennae are identical 6.35 cm (2.5 inch) square microstrip patches. The penetrator antenna is

mounted on its aft end, and the penetrator relay antenna is mounted on the low precision scan platform. The PSM receiver is located with the PSM electronics module on the spacecraft bus. The link analysis for the communication system is shown in Table 4-2. The RF signal strength margin of 10 dB is somewhat pessimistic because the FM output signal-to-noise performance is nonlinear with respect to input signal-to-noise. In this case, the RF signal strength margin of 10 dB corresponds to ~20 dB of output signal-to-noise ratio margin for a 1 in 10^5 bit error rate. The communication link is discussed in detail in Appendix E.

Table 4-2 Penetrator System Link Analysis

Transmit Power	+23.0
Cable Loss	-0.5
Antenna Gain, Transmit	+6.0
Pointing Loss	-3.0
Comet Material Attenuation	-6.0
Space Loss, 55 km	-131.5
Antenna Gain, Receive	+6.0
Pointing Loss	-0.5
Polarization Loss	-0.5
Cable Loss	-0.5
Received Signal Strength	-107.5 dBm
Receiver Noise Floor Density	-168.0 dBm/Hz
Signal-to-Noise Density	60.5 dB-Hz
Bit Bandwidth 1 kHz	30.0 dB-Hz
E_B/N_0 Input	30.5 dB
Required E_B/N_0 Output, $P(E) = 10^{-5}$	13.5 dB
Modulation Loss, IF Bandwidth = 200 kHz (Frequency Deviation = 20 kHz)	7.0 dB
Required E_B/N_0 Input, $P(E) = 10^{-5}$	20.5 dB
Link Margin	10.0 dB

Because a very wide range of penetrability index must be accommodated, the base of the penetrator where the relay antenna is mounted could be, upon impact with the softest material, as much as 1 m below the surface of the nucleus. Experience with terrestrial penetrators indicates that the hole left by the impact will probably be very clear down to the base of the penetrator. In the low gravity, we expect that very little ejecta will remain in the hole. Nevertheless, our design allows for complete burial of the penetrator. A preliminary analysis shows that the 6 dB loss allowance for attenuation in the cometary material is more than adequate. This includes evaluation of cometary models with conducting particles, such as elemental iron, provided the particles are separated from each other by insulating material. Water ice at the low temperatures expected does not present a problem.

4.3.4 Thermal Control Subsystem

The penetrator contains five different heater subsystems. Each region requiring thermal control will contain temperature sensors that will be periodically interrogated by the microcomputer system. The microcomputer system will control power switching to the heaters to maintain the temperatures at the appropriate values. The thermally controlled regions are: (1) Gamma-ray detector (100°C during anneal), (2) gamma-ray detector first stage electronics (~130 K when operating), (3) main electronics package, (4) battery modules, and (5) rocket motor (~-180°C). Our thermal analysis has

indicated that active heating of the rocket motor will only be required between penetrator release and rocket motor firing.

4.3.5 Interfaces

The PSM provides the direct electrical interfaces between the penetrator and the spacecraft. These comprise the interface with the power bus and the Bus Interface Unit (BIU), which is mounted in the PSM. Three chips are used to interface the BIU with the PSM microcomputer busses. All commands, data, and updates from the spacecraft to the penetrator system and all data from the penetrator system to the spacecraft pass through the BIU. Data packets from the PSM to the spacecraft will contain approximately 40 kbits.

Spacecraft prime power will be routed through a power switch in the PSM to the penetrator.

Command and data transactions between the penetrator and the PSM prior to ejection are handled by the hardline controller interface. For simplicity, this interface was designed to be serial, asynchronous, and half duplex. It will use bi-phase data handled by the same chip planned for the spacecraft data system, the Harris HD15530.

Ejection of the penetrator requires two pyro-activated steps: (1) separation of the connector between the penetrator and the PSM, and (2) separation of the Marmon clamp holding the penetrator to the PSM. Each pyro event requires firing two redundant pyro devices. These pyro devices are cabled directly to the spacecraft, bypassing the PSM electronics. The spacecraft, therefore, is responsible for safety inhibits, control, and firing of these devices. Pyro commands will be coordinated with the penetrator and PSM electronics via the BIU.

4.3.6 Sensor Electronics

Output pulses from the gamma-ray spectrometer first stage electronics are fed to two parallel amplifying stages having a factor of 2 difference in gain. Depending on the amplitude of the pulse, the output of one of these amplifying stages is fed into a 8192 channel pulse height analyzer (PHA) with 16 bit accumulation in each channel. The reason for the two amplifying stages is to be able to obtain better resolution for the lower energy pulses. The data accumulation in the RAM in the PHA can be read by the penetrator microcomputer for subsequent transmission to the spacecraft.

The alpha particle instrument operates in alpha, proton, and x-ray modes. Pulses from the x-ray detector are multiplexed with pulses from the alpha/proton coincidence logic, with the resulting pulse-height analysis performed in the coincidence PHA. This PHA will be configured to perform a 1024 channel by 16-bit analysis on the x-ray pulses or a 512 channel by 8-bit analysis on the alpha/proton pulses. Two other PHA's are 512 channels by 8 bits. RAM in all three PHA's is independently readable by the penetrator microcomputer for subsequent transmission to the spacecraft. Status and control logic is used to control start and stop of data collection, to control the instrument's electromechanical devices, and to provide temperature and

device status housekeeping data. Commands to control a sequence of events during the mission (operation of source and sample shutters, polar calibration, start/stop, analysis of standard and comet samples, etc..) will be stored in memory.

The electronics provide constant current sources for the accelerometers and provide sampling and analogue to digital (A/D) conversion of the accelerometer outputs. In addition to sampling the accelerometers at impact, the low range accelerometer will be sampled at ejection and during the burn of the penetrator's solid rocket motor. Because the time of impact cannot be accurately predicted (within a 100 ms timeframe), accelerometer data are continuously written into a wrap-around memory. Sampling is terminated 75 ms after a threshold of 294 m s^{-2} (30 g) is sensed, and data are preserved from 25 ms before threshold sensing to 75 ms after threshold sensing. This procedure ensures acquisition and preservation of the important data concerning the possible mantle at the surface of the nucleus. The 75 ms period is long enough to sense the entire deceleration profile for all nucleus penetrability indices in the range of possible comet material properties ($S = 2$ to 100).

Immediately after impact, the temperature sensors will be deployed and the four thermocouples will be sampled once per minute for a period of 60 minutes at 10-bit resolution and the data stored for later transmission. Following this, they will be sampled at 60-minute intervals. The electronics provide amplification of the thermocouple outputs, periodically short the amplifiers' inputs to determine amplifier offsets, and determine the temperature of the platinum resistor sensor at the reference junction for the thermocouples.

4.3.7 Propulsion Electronics

The function of the penetrator propulsion electronics is to ignite the solid rocket motor during the post-ejection coast phase, at a time redundantly stored in the penetrator microcomputer memory before ejection. This subsystem must also provide the safety inhibits required by NHB 1700.7A, Safety Policy and Requirements for Payloads Using the Space Transportation System. Paragraph 202.2a of NHB 1700.7A states: "(Payloads) shall be equipped with an S&A (safe and arm) device that provides a mechanical interrupt in the pyrotechnic train immediately downstream of the initiator. A minimum of two additional inhibits shall be provided." In lieu of this, we propose to use a three-inhibit circuit that includes an interlock through the PSM such that the motor cannot be fired until after the penetrator physically separates from the spacecraft. Similar circuits have been approved by JSC safety on previous programs.

4.3.8 Ground Support Equipment

The ground support equipment for the Comet Nucleus Penetrator will consist of Bench Checkout Equipment (BCE) and System Test Support Equipment (STSE). There will be three basic test modes, allowing BCE to test the PSM and the penetrator separately or combined. To do this, the BCE must simulate the spacecraft, the PSM, and the penetrator.

The BCE is microcomputer-based, with custom logic to perform the required simulations. Part of the custom logic will consist of circuits designed for use in flight, on the PSM and the penetrator. For example, the hardline controller, transmitter, and receiver will be identical to their flight counterparts. Other custom logic, such as the command and data subsystem simulator and pyro initiator, will be new designs. Custom logic will be interfaced to the microcomputer through a BCE bus interface unit, which will route command and data information as required. Either a general purpose interface bus or RS232C bus will be used to handle the transactions, depending on further analysis of BCE system throughput requirements. Test connectors on the PSM and penetrator electronics modules will allow STSE access to critical test points while the system is cabled to the spacecraft.

The microcomputer tentatively selected for the ground support equipment is the Hewlett Packard Integral Personal Computer. It was selected primarily because of its portability and its internal features: electroluminescent display, disc drive, and printer. This computer will presently support applications programs written in BASIC and C, and will support other languages in the future. It is anticipated we will require 4000 to 7000 lines of code, based on similar designs for three Galileo Probe instruments.

4.4 Flight Dynamics

The penetrator is separated from the CRAF spacecraft while it is 6 - 10 km from the nucleus. It is spun and ejected from the spacecraft by a spring-driven mechanism on the PSM that provides the penetrator with a linear velocity of 0.7 m s^{-1} and a spin rate of 116 rpm. The velocity is a tradeoff between minimizing transit time to the nucleus and limiting the angular impulse imparted to the spacecraft to no more than 14 N m s. The spin rate is defined by the angle of attack considerations discussed below. The initial pointing of the penetrator when it leaves the spacecraft is 10.3° from the nadir so that by the time it has coasted on its elliptical path to a distance of $\sim 1 \text{ km}$ above the surface of the nucleus, it is pointed at the nadir. A small solid-propellant rocket motor then is fired by a timed command, programmed into the penetrator command system prior to ejection, providing a velocity of 40 m s^{-1} along the spin axis. The penetrator travels the remaining 1 km along a nearly rectilinear path.

An adaptable targeting capability is necessary, because the nucleus size and gravitational field will not be known a priori. Also, the altitude of the spacecraft at penetrator release will depend largely upon the dust hazard observed. Therefore, the aim angle from the nadir and the coast time from penetrator release to rocket motor firing must be commands uplinked from Earth prior to release.

The targeting accuracy depends upon (1) the knowledge of the state vector of the spacecraft at the time of release, (2) the accuracy of the aiming maneuver, (3) the dynamics of the separation from the spacecraft, (4) the spin dynamics during the coast trajectory, and, (5) the accuracy of the rocket burn. The expected accuracy of the spacecraft state vector at the time of release has been stated to be $\sim 100 \text{ m}$ in radius and about $\sim 1 \text{ cm s}^{-1}$ in velocity. The 3σ aiming capability for the body-mounted penetrator is

expected to be about 7 mrad. The spin/eject mechanism described in section 4.1.8 is designed to release the penetrator at 116 rpm and is expected to be capable of a tip-off rate of $< 20 \text{ s}^{-1}$. To this must be added the spacecraft reaction to the penetrator release, which adds an additional 0.40 s^{-1} . The rocket motor will deliver its impulse with a thrust offset of less than 0.3° and a burn time error of less than $\pm 2\%$. A six degree of freedom computation of the entire separation maneuver, coast trajectory, rocket burn, and final impact trajectory using the error parameters stated above indicates that the impact site can be targeted with a 3σ accuracy of $\sim 70 \text{ m}$ for a release distance of 6 km.

The tip-off rate resulting from residual asymmetries in the spin/eject mechanism causes a slight offset of the spin momentum vector with respect to the centerline of the penetrator. This results in a slight nutation of the spin axis about the momentum vector. The nutation motion of the penetrator spin axis contributes to the targeting error of emplacement following the rocket burn, and to the angle of attack (i.e. the angle between the penetrator symmetry axis and the velocity vector) at impact. This angle is one of the factors that determines impact lateral loads and bending moments. The nutation continues without change throughout the trajectory until the rocket firing. Great care is taken in the penetrator design to eliminate energy dissipation, such as flexing, as this would cause the nutation angle to grow. The baseline design has an inertia ratio of 3.5, and for a spin rate of 116 rpm, the nutation angle is about 1.0° .

Internal energy dissipation effects on the growth of the nutation angle during the coast from the spacecraft to the propulsive maneuver was a motivating factor in the selection of a solid rocket motor over a liquid rocket motor. The destabilizing effect of propellant slosh on a prolate spinning body could be disastrous. In addition, care is taken in our design to limit the sources of internal energy dissipation to structural damping and friction from relative motion of internal parts. Internal energy dissipation over the coast period that precedes the rocket firing must be less than 1.3 mJ to prevent an initial nutation angle of 1.0° from growing by no more than 0.1° . Calculations based on Explorer I nutation growth data as a worst case (with flexible whip antennas) indicate that nutation growth in our penetrator design is unlikely to be a problem.

If any debris surrounds the nucleus, collisions with particles could conceivably deflect the penetrator. The largest effect would come if a particle elastically collided with the tapered forward third of the penetrator nose cone, since the relative velocity between the penetrator and the particle would have a maximum component along the surface normal, and since the moment arm of the imparted impulse about the center of mass would be maximum. Impact with a particle having a mass of 1 g would produce a maximum angle of attack increase of 0.25° . However, the probability of a collision with this surface of the nose is low because of its small projected surface area (3.1 cm^2). A more probable collision could occur on the surface of the terrabrake (7630 cm^2). Because of the shorter moment arm for the imparted impulse, collision of a particle with a mass as large as 6 g would be necessary to produce a maximum angle of attack increase of 0.25° .

To minimize the angle of attack following the rocket burn, the burn period must be synchronized with the nutation period of the spinning penetrator. A rocket burn duration of 7.27 s is required with the thrust of our chosen rocket motor to produce the necessary velocity of 40 m s^{-1} . Since the burn duration is constrained by the desire to use a readily available motor, the synchronization is achieved by adjusting the spin rate. The nutation period is exactly one-half of the burn duration. The velocity increment of 40 m s^{-1} is thus averaged over two nutation periods, and is added along the momentum vector. The resulting angle of attack at impact is no more than 1.2° .

5.0 . Design Discussions

5.1 Penetrator Configuration

The development during the last two decades of military penetrators and of their test facilities has been centered at the Sandia National Laboratories. In order to accurately predict depth of penetration and impact acceleration levels, a large data base of tests has been accumulated by Sandia. From these data, techniques have been developed that permit reasonably accurate predictions of axial deceleration loads and penetration depths into homogeneous and layered materials for both simple and complex shapes. These empirical techniques have been applied to a series of penetrator configurations. The unique requirements for a comet nucleus penetrator system have led to the adoption of a configuration somewhat different from the majority of penetrators comprising the Sandia data base. This leaves some room for differences in the application of the penetration and load equations. Different techniques have been examined. However, the differences in results are smaller than the data base results indicate that we can expect as an absolute error. The accuracy of our computational techniques has been supported by the results of full-scale comet penetrator penetration tests.

The Sandia data base expresses soil hardness in terms of a function termed the penetrability index, S . The penetrability index is an empirical measure of impact strength. A value of 2 is characteristic of hard sea ice or weathered igneous rock, and a value of 100 is characteristic of soft snow. A design requirement placed upon the penetrator system, is the ability to operate over a range of penetrability index from 2 to 100.

The peak axial deceleration calculated for the impact for the baseline configuration is shown in Figure 5.1-1 as a function of soil penetrability index. Penetration distance as a function of S is shown in Figure 5.1-2. For the hardest expected comet nucleus material ($S = 2$), the peak deceleration is about 3335 m s^{-2} (340 g) and the penetration is about 35 cm. For slightly softer surfaces, the peak deceleration decreases as the penetration depth increases. At $S = 4$, the penetration is sufficient to bury the entire shaft and the terrabrake flare just encounters the surface. For softer surfaces, the impact of the terrabrake results in an increase in the peak deceleration to a maximum level of 4120 m s^{-2} (420 g) for $S = 8$, the penetrability of hard packed clay. At this penetrability, the tip is buried about 72 cm and the flare is about half buried. For very soft surfaces, peak loads decrease to about 540 m s^{-2} (55 g) for $S = 100$ (characteristic of soft snow). For this extreme condition, the penetrator lies completely beneath the surface, with the aft end at a depth of about 1 m.

The penetrator may also experience significant lateral loads and bending moments caused by impacts not normal to the local surface or at small angles of attack (i.e., where the velocity vector at impact is not coincident with the axis of the penetrator). Experience from terrestrial penetrators indicates that the lateral loads imposed by impact angles of 30° off-normal or by angles of attack of about 2° are typically the same order of magnitude as the axial loads.

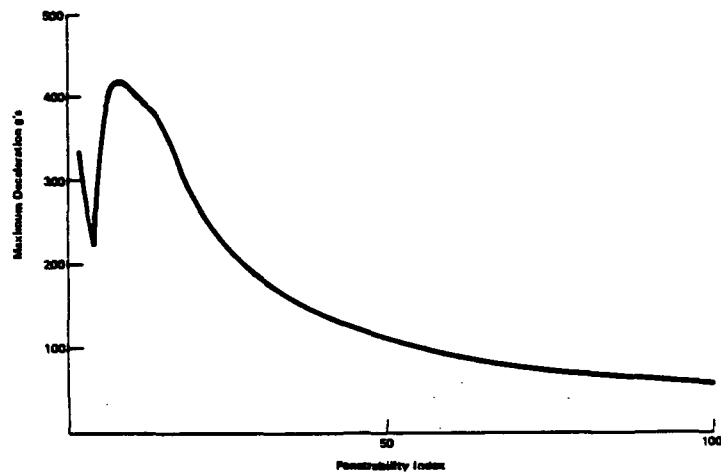


Figure 5.1-1 *Maximum Deceleration as a Function of Penetrability Index*

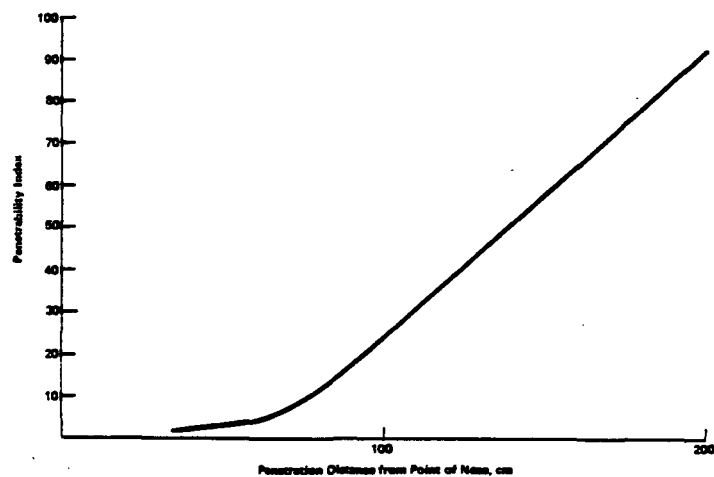


Figure 5.1-2 *Penetration Distance as a Function of Penetrability Index*

The final configuration selected represents a judgmental compromise between the factors involved, following parametric surveys of the interrelationships between the various key parameters.

Significant efforts were made to configure the penetrator so that the rear surface would remain unburied in the softest material. Specially shaped terrabrakes were investigated to provide more controlled deceleration, but the physical limits on size imposed by the spacecraft (an assumed 75 cm diameter envelope) still resulted in the rear of the penetrator being buried in the softest material. A large diameter terrabrake is also advantageous for flight dynamics stability, but a design to make maximum use of the 75 cm envelope was rejected because the increased mass of the larger penetrator structure exceeded the penetrator weight limitation assumed for the CRAF mission. Other configuration approaches were investigated and rejected as previously mentioned in section 1.

A major consideration driving the configuration was concern relating to the brittleness of the germanium crystal. Deceleration loads have been kept to reasonable minimums and a shock isolation system designed to protect the crystal. It is not possible to provide the crystal with impact loads much less than experienced by the penetrator as a whole, without the deceleration distance for the crystal being much longer than the deceleration distance for the penetrator. This is clearly not practical, when all of the other constraints are considered, and consequently the approach taken has been to design a shock isolation system that limits the maximum deceleration loads seen by the crystal to an acceptable level by using a crushable honeycomb that yields only when the deceleration reaches a predefined threshold and holds it constant to the crystal at the threshold value at times when the penetrator deceleration exceeds the limit. Figure 5.1-3 contains a series of plots, calculated by integrating the deceleration with time data, showing energy

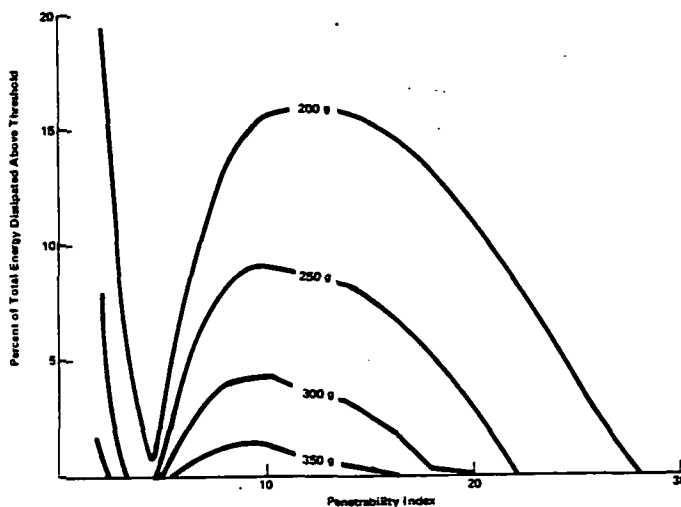


Figure 5.1-3 Energy Dissipation Above Threshold as a Function of Penetrability Index

dissipation above various deceleration thresholds as a function of penetrability index for the baseline penetrator configuration. A threshold level of 2943 m s^{-2} (300 g) was selected for the baseline design.

5.2 Penetrator Structure

The penetrator structure must be strong enough to absorb impact loads, and because it comprises about half of the system weight, it is necessary to choose materials of high strength-to-weight ratio. Experience has shown that ductility is also very important. Further, the material of the penetrator will produce an unwanted gamma-ray signal. Therefore, structural material, particularly in proximity to the gamma-ray detector, must be chosen so as not to seriously affect gamma-ray measurements. Materials interferences are discussed more fully in section 5.3.

Titanium has been selected as the principal structural material for the nose, shaft, and the forward part of the terrabrake. Titanium is very strong at low temperatures. However, it is rather brittle, and some alloys also lack ductility. Therefore, an alloy of titanium (Ti-5Al-2.5Sn) that has an optimum combination of ductility and strength has been chosen. The use of this alloy severely restricts the ability of the gamma-ray spectrometer to detect and measure Ti and Al in the comet nucleus. The alpha particle instrument will provide a measurement of Al, however, and may also detect Ti. Other possible material choices such as high-strength steel alloys are undesirable from both weight and interference points of view. A high strength composite like Kevlar would interfere principally with measurement of nitrogen, which is a very high priority scientific objective, and consequently composites of this type are unacceptable for the forward part of the penetrator.

The terrabrake and the components enclosed at the rear end of the penetrator are further away from the germanium crystal detector, and consequently, there is a wider choice of materials available to us for this part of the structure because the induced interference signal will be much less. This allows the use of higher strength-to-weight ratio materials and materials more suitable for the proper thermal control of the gamma-ray detector to isolate it from heat from the support subsystems in the terrabrake. The terrabrake structure will be constructed of a Kevlar composite that combines low thermal conductivity with a very high strength-to-weight ratio.

A stress analysis of the structure has been performed in order to support the baseline design process. This analysis, included as Appendix A, evaluates the parts of the structure that are expected to see the highest stress loads. It should be noted that the worst-case at different locations in the penetrator occur for different penetrability indices.

5.3 Materials Interference

5.3.1 Penetrator Materials

Materials of construction, as well as all of the materials within the various components in the penetrator, are potential sources of interference with the measurement of cometary composition. First, it is necessary to minimize the

use of material that is even slightly radioactive. Three elements--potassium (K), uranium (U), and thorium (Th)--include isotopes which are naturally radioactive. It is fundamentally of great importance to detect even the low expected abundances of these elements in the nucleus, and thus the penetrator must be free of contamination by these elements. The instrument also has excellent sensitivity for many non-radioactive elements that are expected to be abundant in the comet. These include H, C, O, Mg, Si, S, Fe and Ni. Small amounts of these materials can be tolerated in the penetrator. It is of considerable interest to attempt the detection and measurement of nitrogen (N) and chlorine (Cl). If these measurements are to be successful, every effort must be made to minimize their presence in penetrator materials. Epoxies and many plastics contain amides or imides and, in some cases, are also chlorinated. Kevlar, the aft structural material, is an aromatic polyamide (i.e., it contains approximately 12% nitrogen), but as will be shown below, it is sufficiently remote from the gamma ray detection crystal that it is not a major problem.

Several other elements, e.g. Na, Al, Ca, Ti and Mn, fall into the category where the detection limit for the optimum isotope is only 5 to 15 times the expected abundance level for the optimum isotope. If materials containing these elements are needed in the penetrator, they could compromise sensitivity and accuracy. For example, the titanium (Ti) alloy for the penetrator shell structure will overwhelm the Ti signal from the comet, as does the 5% aluminum component within this alloy. From the scientific standpoint, the loss of information on Ti abundance in the comet is not necessarily serious because the dust analyzer instruments on board the main spacecraft will measure Ti to high accuracy. Aluminum may be deemed more important. Unfortunately, Al-free Ti alloys (such as Ti-11.5Mo-6Zr-4.5Sn) are generally beta phase and have unfavorable low-temperature properties. However, the alpha particle instrument will provide a reasonable aluminum measurement since it directly views the cometary material.

A software model (MTLINF) was developed to calculate the germanium crystal response to elements in the penetrator and in the comet. Each component of the penetrator was modeled using its mass, composition, and position in the penetrator. The accepted percentages of elemental isotopes were used to give the actual amount of all relevant isotopes in that component. Large components were broken into segments to give a more accurate representation of the penetrator mass/distance distribution. Crystal response to these components was calculated using a lumped-node approach; the mass of each element at a given node produces a certain intensity of gamma rays at a specific emission line which is reduced by both the $1/R^2$ factor and the attenuation for that emission energy. Calculation of gamma-ray attenuation includes the effect of the density of the penetrator section traversed, as well as the attenuation by any cometary material traversed.

Calculation of the response from the comet involved summing the responses from concentric spherical shells of cometary material. The response at a certain isotope energy will depend on the amount of that isotope present, the density of the cometary material, and the attenuation at that energy level. Without the attenuation effect, the crystal would in theory detect material to an infinite distance, because as the response from sequential shells decreases

with the $1/R^2$ distance factor, the amount of material within the shell increases by an R^2 factor. The attenuation effect limits this by increasingly masking the response for more distant material. Lower energy gamma rays are attenuated more than higher energy gamma rays, so the mean free path of a certain line increases as the energy of the line increases, (Table 5.3-1). The mean free path decreases with increasing density of the cometary material because attenuation increases linearly with density. However, an increase in comet density has in general little effect on total response because both the generated intensity of gamma rays and the

Table 5.3-1
Gamma Ray Mean Free Paths
(mfp) (sp gr = 1.0)

E, MeV	mfp, in.
0.3	3.5
0.8	5.8
1.0	6.6
1.5	7.9
2.0	9.4
3.0	10.9
4.0	13.0
6.0	15.0
8.0	15.7
10.0	16.4

attenuation increase with density. The density of the comet nucleus is most reasonably assumed to be in the range 0.3 to 1.0 g/cm³. Figure 5.3-1 demonstrates the "spheres of influence" for selected energies in different densities of cometary material. At the lower energies, gamma rays are measured only from material near the crystal. In the important 1-2 MeV range, the surface effect may be seen slightly, depending on local density.

The cometary material can be input to the software as desired; for most runs it was assumed to be a 50% soil, 50% ice mixture. The soil model is a CI class carbonaceous chondrite, and the ice model typically used was 50% water, 25% carbon dioxide, 12.5% ammonia and 12.5% carbon disulfide. Again, the mass of each element was divided into its component isotopes of interest. The density of the comet was a variable, usually assumed to be 1 g/cm³. Shells of cometary material centered on the germanium crystal were modeled, with sections occupied by the penetrator excluded. The shell thickness was a variable that affected the speed and accuracy of the computer calculation. A 1-cm shell thickness resulted in a reasonably fast calculation with less than a 1% degradation in accuracy from a 0.1-cm shell thickness, which is thin enough to be essentially a continuum. These shells were summed to a limiting distance, determined by the desired accuracy. A typical choice was that the sum was considered complete when the next individual shell contributed less than 0.05% of the sum response. The summation was then usually completed before a 100-cm distance was reached. Since the penetrator was here assumed to be buried to its full length, the surface effect rarely came into play in this calculation.

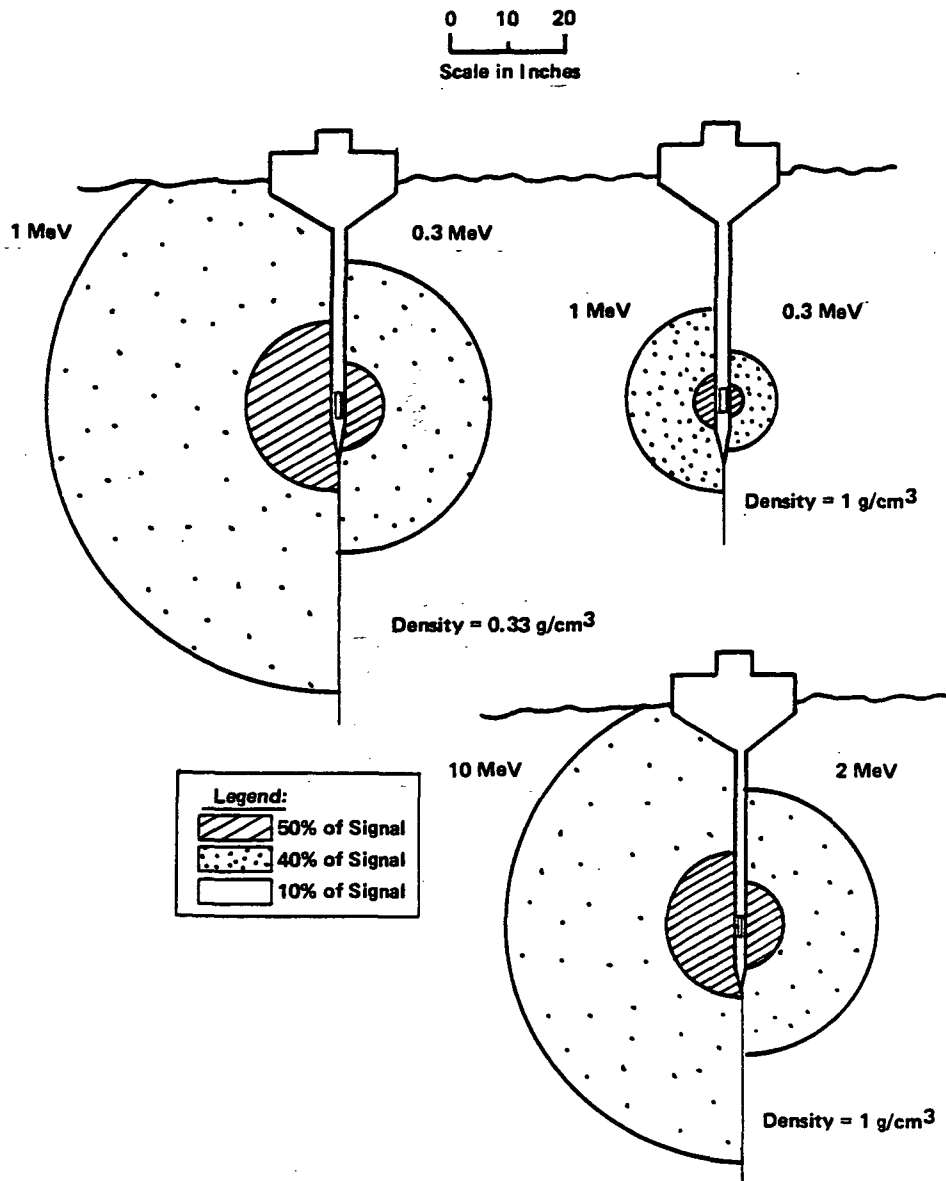


Figure 5.3-1 Gamma Ray Detector Effective Sampling Volumes

The software was arranged so that each component of the penetrator could be shown separately, or the entire penetrator effect could be plotted against the comet response. Single isotopes could be selected and responses for each component displayed, to aid in identification of troublesome components. For each isotope, the fraction of the gamma ray signal that originated from the cometary material is calculated (the comet response divided by the sum of the penetrator and comet responses). This comet fraction is ideally 1.0; in other words, the penetrator should make a negligible contribution. A comet fraction

of 0.5 means that the response from the comet and the penetrator are equal. A comet fraction of 0.9 indicates a comet response nine times higher than the "noise" level from the penetrator, while 0.8 is equivalent to a ratio of 4 in signal-to-noise. Penetrator components were evaluated in terms of this criterium; any comet fraction under 0.8 was considered unacceptable, and 0.9 was a nominal minimum goal. Obviously, the most difficult task is to find a satisfactory material for the main structural components that will not destructively interfere with one or more isotope responses. A Kevlar epoxy composite was considered as the main structural material. This composite contains about 12% nitrogen by weight, which does not present a problem when the specific ice model discussed above is used; even if the entire structure is Kevlar, the nitrogen comet fraction is still above 0.9. Table 5.3-2 shows the interferences resulting from various materials usage for the penetrator component parts for this ice model. However, if an ice model is used that contains no ammonia (NH_3), the nitrogen response from the comet decreases by a factor of 40, and the nitrogen in the forward structure of the penetrator then overwhelms the signal from the comet, Table 5.3-3. The Kevlar in the aft structure does not present such a problem, because of the increased distance from the crystal.

The forward structure then presents a problem in terms of finding a strong material with good low-temperature properties that does not contain restricted elements. The optimum compromise is the chosen Ti-5Al-2.5Sn alloy, with excellent strength, elasticity and low-temperature properties. Titanium and aluminum are both lost to detection by the gamma-ray spectrometer, as shown in Tables 5.3-4 and 5.3-5, but this deficiency can be rectified to some extent by the alpha backscatter experiment and by spacecraft measurements of these elements in collected dust. The same alloy can then be used for the crystal casing and structural components around the crystal. This is a bonus, because the other materials considered for these parts (magnesium alloys, steels, aluminum alloys and beryllium) all caused problems in terms of material interferences, cost or impurities, as can be seen from Tables 5.3-6 and 5.3-7. Maximum potential impurities for the Ti alloy are included in the model.

Table 5.3-8 shows the results of the analysis for the baseline penetrator design. This shows elimination of only two elements--titanium and aluminum. The chlorine comet fraction is at 0.89, which is still acceptable (a factor of 8 signal-to-noise), and could not be altered without changing the choice of battery type. Table 5.3-9 shows the breakdown of the chlorine interference. The response of certain elements in the comet--C, H, O, N--is highly dependent on the ice composition assumed for the comet model. These elements should be controlled by limiting their use in the penetrator. Then if the ice composition is different than estimated, these elements will still be observable. For the current penetrator, this should not be a concern; nitrogen comet fraction only goes down to 0.89 if the comet ice has no nitrogen, and the carbon fraction decreases to 0.95 for carbon-free ice.

Table 5.3-2 Nitrogen Response for Various Materials Usage for Penetrator Components and Comet Composition (50% CI Soil, 25% H₂O, 12.5% CO₂, 6.25% NH₃, and 6.25% CS₂)

28 N- 14 ENERGY= 10.829 MeV

Comet2 DENSITY OF COMET = 1 g/cm3

BLACK BOX	BLACK BOX RESPONSE	COMET RESPONSE	COMET/TOTAL RATIO
Crystal Case Ti	0.0121458	52.2342852	.99977
Honeycomb Al	0.0000000	52.2342852	1.00000
Ti Rod & Housing	0.0150583	52.2342852	.99971
Batteries LiSOCl ₂	0.0000000	52.2342852	1.00000
Ceramic Insulators	0.0000000	52.2342852	1.00000
Insulator Plates Kev	0.0035722	52.2342852	.99993
Nose Cone Ti	0.0008236	52.2342852	.99998
Alpha-Back Plate Ti	0.0001118	52.2342852	1.00000
Fwd Kevlar Ins	0.0377656	52.2342852	.99928
Fwd Accel	0.0000000	52.2342852	1.00000
Forward Shell Ti	0.0131456	52.2342852	.99975
Forward Shell Kev	1.3898425	52.2342852	.97408
Crystal Case Mg .01	0.0000000	52.2342852	1.00000
Outer Xtal Case SS50	0.0000000	52.2342852	1.00000
Case Support Ti	0.0010480	52.2342852	.99998
Aft Accel	0.0000000	52.2342852	1.00000
Kev Flare 1	0.0236327	52.2342852	.99955
Kev Flare 2	0.0169194	52.2342852	.99968
Kev Flare 3	0.0065292	52.2342852	.99988
Outer Elec Housing K	0.0125120	52.2342852	.99976
Aft Kevlar Support	0.0479612	52.2342852	.99908
Back Plate Kev	0.0158713	52.2342852	.99970
Ribs Kevlar	0.0329811	52.2342852	.99937
Motor	0.0000150	52.2342852	1.00000
Torque Assy Ti	0.0001210	52.2342852	1.00000

Table 5.3-3 Nitrogen Response for Various Materials Used for the Penetrator Components and Comet Composition with no NH₃ Ice

28 N- 14 ENERGY= 10.829 MeV

Comet1 DENSITY OF COMET = 1 g/cm3

BLACK BOX	BLACK BOX RESPONSE	COMET RESPONSE	COMET/TOTAL RATIO
Crystal Case Ti	0.0121458	1.2854624	.99064
Honeycomb Al	0.0000000	1.2854624	1.00000
Ti Rod & Housing	0.0150583	1.2854624	.98842
Batteries LiSOC12	0.0000000	1.2854624	1.00000
Ceramic Insulators	0.0000000	1.2854624	1.00000
Insulator Plates Kev	0.0035722	1.2854624	.99723
Nose Cone Ti	0.0008236	1.2854624	.99936
Alpha-Back Plate Ti	0.0001118	1.2854624	.99991
Fwd Kevlar Ins	0.0377656	1.2854624	.97146
Fwd Accel	0.0000000	1.2854624	1.00000
Forward Shell Ti	0.0131456	1.2854624	.98988
Forward Shell Kev	1.3898425	1.2854624	.48049
Crystal Case Mg .01	0.0000000	1.2854624	1.00000
Outer Xtal Case SS50	0.0000000	1.2854624	1.00000
Case Support Ti	0.0010480	1.2854624	.99919
Aft Accel	0.0000000	1.2854624	1.00000
Kev Flare 1	0.0236327	1.2854624	.98195
Kev Flare 2	0.0169194	1.2854624	.98701
Kev Flare 3	0.0065292	1.2854624	.99495
Outer Elec Housing K	0.0125120	1.2854624	.99036
Aft Kevlar Support	0.0479612	1.2854624	.96403
Back Plate Kev	0.0158713	1.2854624	.98780
Ribs Kevlar	0.0329811	1.2854624	.97498
Motor	0.0000150	1.2854624	.99999
Torque Assy Ti	0.0001210	1.2854624	.99991

Table 5.3-4 Response Levels and Comet Fractions for Titanium

7 Ti- 48 ENERGY= 1.381 MeV

Comet2 DENSITY OF COMET = 1 g/cm3

BLACK BOX	BLACK BOX RESPONSE	COMET RESPONSE	COMET/TOTAL RATIO
Crystal Case Ti	15.9521973	0.0900917	.00562
Honeycomb Al	0.0000000	0.0900917	1.00000
Ti Rod & Housing	19.4193823	0.0900917	.00462
Batteries LiSOC12	0.0000000	0.0900917	1.00000
Ceramic Insulators	0.0000000	0.0900917	1.00000
Insulator Plates Kev	0.0000000	0.0900917	1.00000
Nose Cone Ti	0.5210090	0.0900917	.14743
Alpha-Back Plate Ti	0.0955754	0.0900917	.48523
Fwd Kevlar Ins	0.0000000	0.0900917	1.00000
Fwd Accel	0.0087206	0.0900917	.91175
Forward Shell Ti	10.8722919	0.0900917	.00822
Forward Shell Kev	0.0000000	0.0900917	1.00000
Crystal Case Mg .01	0.0000000	0.0900917	1.00000
Outer Xtal Case SS50	0.0000000	0.0900917	1.00000
Case Support Ti	0.9736736	0.0900917	.08469
Aft Accel	0.0053480	0.0900917	.94396
Kev Flare 1	0.0000000	0.0900917	1.00000
Kev Flare 2	0.0000000	0.0900917	1.00000
Kev Flare 3	0.0000000	0.0900917	1.00000
Outer Elec Housing K	0.0000000	0.0900917	1.00000
Aft Kevlar Support	0.0000000	0.0900917	1.00000
Back Plate Kev	0.0000000	0.0900917	1.00000
Ribs Kevlar	0.0000000	0.0900917	1.00000
Motor	0.0088692	0.0900917	.91038
Torque Assy Ti	0.0406251	0.0900917	.68921

Table 5.3-5 Response Levels and Comet Fractions for Aluminum

22 Al- 27 ENERGY= 7.724 MeV

Comet2 DENSITY OF COMET = 1 g/cm3

BLACK BOX	BLACK BOX RESPONSE	COMET RESPONSE	COMET/TOTAL RATIO
Crystal Case Ti	1.2161318	4.0662232	.76977
Honeycomb Al	4.8602193	4.0662232	.45553
Ti Rod & Housing	1.5062579	4.0662232	.72970
Batteries LiSOCl2	0.0019507	4.0662232	.99952
Ceramic Insulators	3.4954497	4.0662232	.53774
Insulator Plates Kev	0.0000000	4.0662232	1.00000
Nose Cone Ti	0.0792325	4.0662232	.98089
Alpha-Back Plate Ti	0.0109313	4.0662232	.99732
Fwd Kevlar Ins	0.0000000	4.0662232	1.00000
Fwd Accel	0.0008980	4.0662232	.99978
Forward Shell Ti	1.2833686	4.0662232	.76010
Forward Shell Kev	0.0000000	4.0662232	1.00000
Crystal Case Mg .01	0.0794866	4.0662232	.98083
Outer Xtal Case SS50	0.0000000	4.0662232	1.00000
Case Support Ti	0.1029643	4.0662232	.97530
Aft Accel	0.0005143	4.0662232	.99987
Kev Flare 1	0.0000000	4.0662232	1.00000
Kev Flare 2	0.0000000	4.0662232	1.00000
Kev Flare 3	0.0000000	4.0662232	1.00000
Outer Elec Housing K	0.0000000	4.0662232	1.00000
Aft Kevlar Support	0.0000000	4.0662232	1.00000
Back Plate Kev	0.0000000	4.0662232	1.00000
Ribs Kevlar	0.0000000	4.0662232	1.00000
Motor	0.0014353	4.0662232	.99965
Torque Assy Ti	0.0112428	4.0662232	.99724

Table 5.3-6 Response Levels and Comet Fractions for Chromium Using Alternative Materials

8 Cr- 52 ENERGY= 1.434 MeV

Comet2 DENSITY OF COMET = 1 g/cm3

BLACK BOX	BLACK BOX RESPONSE	COMET RESPONSE	COMET/TOTAL RATIO
Crystal Case Ti	0.0000000	0.5783168	1.00000
Honeycomb Al	0.0078084	0.5783168	.98668
Ti Rod & Housing	0.0000000	0.5783168	1.00000
Batteries LiSOC12	0.0003208	0.5783168	.99945
Ceramic Insulators	0.0000000	0.5783168	1.00000
Insulator Plates Kev	0.0000000	0.5783168	1.00000
Nose Cone Ti	0.0000000	0.5783168	1.00000
Alpha-Back Plate Ti	0.0000000	0.5783168	1.00000
Fwd Kevlar Ins	0.0000000	0.5783168	1.00000
Fwd Accel	0.0016970	0.5783168	.99707
Forward Shell Ti	0.0000000	0.5783168	1.00000
Forward Shell Kev	0.0000000	0.5783168	1.00000
Crystal Case Mg .01	0.0000000	0.5783168	1.00000
Outer Xtal Case SS50	0.7226768	0.5783168	.44452
Case Support Ti	0.0000000	0.5783168	1.00000
Aft Accel	0.0006056	0.5783168	.99895
Kev Flare 1	0.0000000	0.5783168	1.00000
Kev Flare 2	0.0000000	0.5783168	1.00000
Kev Flare 3	0.0000000	0.5783168	1.00000
Outer Elec Housing K	0.0000000	0.5783168	1.00000
Aft Kevlar Support	0.0000000	0.5783168	1.00000
Back Plate Kev	0.0000000	0.5783168	1.00000
Ribs Kevlar	0.0000000	0.5783168	1.00000
Motor	0.0000000	0.5783168	1.00000
Torque Assy Ti	0.0000000	0.5783168	1.00000

Table 5.3-7 Response Levels and Comet Fractions for Iron Using Alternative Materials

27 Fe- 54 ENERGY= 9.299 MeV

Comet2 DENSITY OF COMET = 1 g/cm3

BLACK BOX	BLACK BOX RESPONSE	COMET RESPONSE	COMET/TOTAL RATIO
Crystal Case Ti	0.0028352	5.2415826	.99946
Honeycomb Al	0.0000000	5.2415826	1.00000
Ti Rod & Housing	0.0035137	5.2415826	.99933
Batteries LiSOCl2	0.0004142	5.2415826	.99992
Ceramic Insulators	0.0000000	5.2415826	1.00000
Insulator Plates Kev	0.0000000	5.2415826	1.00000
Nose Cone Ti	0.0001891	5.2415826	.99996
Alpha-Back Plate Ti	0.0000258	5.2415826	1.00000
Fwd Kevlar Ins	0.0000000	5.2415826	1.00000
Fwd Accel	0.0006639	5.2415826	.99987
Forward Shell Ti	0.0030370	5.2415826	.99942
Forward Shell Kev	0.0000000	5.2415826	1.00000
Crystal Case Mg .01	0.0000000	5.2415826	1.00000
Outer Xtal Case SS50	1.0088937	5.2415826	.83859
Case Support Ti	0.0002427	5.2415826	.99995
Aft Accel	0.0002212	5.2415826	.99996
Kev Flare 1	0.0000000	5.2415826	1.00000
Kev Flare 2	0.0000000	5.2415826	1.00000
Kev Flare 3	0.0000000	5.2415826	1.00000
Outer Elec Housing K	0.0000000	5.2415826	1.00000
Aft Kevlar Support	0.0000000	5.2415826	1.00000
Back Plate Kev	0.0000000	5.2415826	1.00000
Ribs Kevlar	0.0000000	5.2415826	1.00000
Motor	0.0000034	5.2415826	1.00000
Torque Assy Ti	0.0000274	5.2415826	.99999

Table 5.3-8 Material Interferences Analysis for Baseline Penetrator Design

Penetrator3 Comet2
 DENSITY OF COMET = 1 g/cm3
 Slice= 1 Limit= .05 %

ISOTOPE	GAMMA RAY (MeV)	PENETRATOR RESPONSE	COMET RESPONSE	COMET/TOT RATIO
1 Co- 59	.23	0.000000	0.06463	1.00000
2 Na- 23	.44	0.000000	0.89984	1.00000
3 Cd-113	.56	0.000000	0.00002	1.00000
4 U -238	.61	0.000000	0.00000	1.00000
5 K - 39	.77	0.000000	0.08868	1.00000
6 Mg- 24	1.37	0.041143	21.32458	.99807
7 Ti- 48	1.38	47.897692	0.09009	.00188
8 Cr- 52	1.43	0.010432	0.57832	.98228
9 K - 40	1.46	0.000000	0.00000	1.00000
10 Mg- 25	1.61	0.005506	2.92843	.99812
11 Si- 28	1.78	0.026285	30.24248	.99913
12 Mg- 26	1.81	0.006238	3.36857	.99815
13 Ca- 40	1.94	0.000000	3.43442	1.00000
14 Cl- 35	1.95	0.012649	0.10715	.89441
15 H - 1	2.22	0.043476	26.22944	.99835
16 Th-232	2.61	0.000000	0.00000	1.00000
17 C - 12	4.44	0.889082	51.15520	.98292
18 S - 32	5.42	0.020133	70.61680	.99971
19 O - 16	6.13	3.756425	500.67093	.99255
20 Mn- 55	7.24	0.000631	0.90091	.99930
21 Fe- 56	7.63	0.174254	80.55062	.99784
22 Al- 27	7.72	12.570597	4.06622	.24441
23 Ni- 60	7.82	0.000928	1.38254	.99933
24 Zn- 64	7.86	0.000160	0.09143	.99825
25 Cr- 53	8.88	0.001497	0.11159	.98676
26 Ni- 58	9.00	0.002443	3.64097	.99933
27 Fe- 54	9.30	0.011174	5.24158	.99787
28 N - 14	10.83	0.216581	52.23429	.99587

Crystal Case Ti
 Honeycomb Al
 Ti Rod & Housing
 Batteries LiSOCl2
 Ceramic Insulators
 Insulator Plates Kev
 Nose Cone Ti
 Alpha-Back Plate Ti
 Fwd Kevlar Ins
 Fwd Accel
 Forward Shell Ti
 Case Support Ti
 Aft Accel
 Kev Flare 2
 Kev Flare 3
 Outer Elec Housing Kev
 Aft Kevlar Support
 Back Plate Kev
 Ribs Kevlar
 Motor
 Torque Assy Ti

Table 5.3-9 Response Levels and Comet Fractions for Chlorine

14 C1- 35 ENERGY= 1.951 MeV

Comet2 DENSITY OF COMET = 1 g/cm3

BLACK BOX	BLACK BOX RESPONSE	COMET RESPONSE	COMET/TOTAL RATIO
Crystal Case Ti	0.0000000	0.1071454	1.00000
Honeycomb Al	0.0000000	0.1071454	1.00000
Ti Rod & Housing	0.0000000	0.1071454	1.00000
Batteries LiSOCl2	0.0126486	0.1071454	.89441
Ceramic Insulators	0.0000000	0.1071454	1.00000
Insulator Plates Kev	0.0000000	0.1071454	1.00000
Nose Cone Ti	0.0000000	0.1071454	1.00000
Alpha-Back Plate Ti	0.0000000	0.1071454	1.00000
Fwd Kevlar Ins	0.0000000	0.1071454	1.00000
Fwd Accel	0.0000000	0.1071454	1.00000
Forward Shell Ti	0.0000000	0.1071454	1.00000
Forward Shell Kev	0.0000000	0.1071454	1.00000
Crystal Case Mg .01	0.0000000	0.1071454	1.00000
Outer Xtal Case SS50	0.0000000	0.1071454	1.00000
Case Support Ti	0.0000000	0.1071454	1.00000
Aft Accel	0.0000000	0.1071454	1.00000
Kev Flare 1	0.0000000	0.1071454	1.00000
Kev Flare 2	0.0000000	0.1071454	1.00000
Kev Flare 3	0.0000000	0.1071454	1.00000
Outer Elec Housing K	0.0000000	0.1071454	1.00000
Aft Kevlar Support	0.0000000	0.1071454	1.00000
Back Plate Kev	0.0000000	0.1071454	1.00000
Ribs Kevlar	0.0000000	0.1071454	1.00000
Motor	0.0000000	0.1071454	1.00000
Torque Assy Ti	0.0000000	0.1071454	1.00000

Oxygen is high in the soil composition itself, and will not be a problem to observe. Hydrogen may not be present in the comet soil, but even with only small amounts of water in the nucleus, the hydrogen is still easily detectable over the penetrator response level: a comet that is only 5% ice will still show a hydrogen fraction of 0.98.

Uranium and thorium are two critical elements that can be present only in extremely low levels in the penetrator to still allow detection of their signals from the comet. To bring the comet fraction for these elements above 0.9, the amount of uranium contamination in the penetrator forward structure must be less than 10 ppb; in the aft-end battery and electronics sections, uranium must be less than 0.4 mg and the total thorium must be less than 0.2 mg. It was assumed that ceramics and alloys in the electronics section would be the main candidates for this type of contamination. All forward components would need to be carefully screened for these elements; Kevlar and titanium alloys are both, fortunately, considered "clean" where radioactive contamination is concerned. The use of beryllium for some forward components, considered at one time, becomes a problem because of the relatively high level of uranium contamination in all U.S. sources of beryllium.

5.3.2 Mantle Interference

The second function of the MTLINF software was to preliminarily evaluate the effect of less than full penetration and/or the presence of an ice-free mantle of dust at the cometary surface. As the crystal "sees" more of an ice-free mantle, the resultant values for the icy elements--C, H, O, N--become more and more inaccurate.

There is an error induced by insufficient depth of the crystal under the surface, even in a comet with no mantle. When the crystal is only a short distance below the surface, a greater proportion of cometary mantle material is closer to the crystal than when there is full penetration. The isotopes with low energy gamma rays then undergo less attenuation, and appear with more intensity. Likewise, the higher-energy isotopes appear proportionately dampened.

These errors are calculated by determining the ratio of the response of a given element to the response of silicon, and this ratio is compared to a reference (ideal) ratio calculated at maximum depth with no mantle. Interestingly, if the crystal rests on the surface of a mantle-free comet, all values are correct since the crystal sees exactly one-half of a sphere. In these calculations, the maximum error produced by insufficient penetration depth alone occurs at a depth (of the crystal under the surface) of 5 cm. At this point the error of the lowest energy isotope is +16% and the error of the highest energy isotope is -7.5%. The errors then decrease with increasing depth until at a depth of 30 cm all errors are less than 5%. It should be pointed out that changes in neutron flux levels and spectral distribution have been ignored in these simplified calculations.

Addition of an ice-free mantle (CI type soil only) increases the low-penetration error significantly for the ice elements. Taking carbon as a typical element included in the ice portion of the nucleus,

Figure 5.3-2 shows how the C/Si ratio varies for different mantle thicknesses and depth of penetration. A mantle thickness of 1 cm causes a maximum negative deviation of 10% at a depth of 5 cm. A 1 cm mantle is the most likely thickness, and penetration below 5 cm is almost certain, so it seems that in this case the error is not likely to be a problem. Exploring worst cases: a 4 cm mantle causes a negative error of 30% at the surface; this decreases to 10% at 20 cm depth and 5% at 40 cm depth. A 16 cm mantle causes a 60% error at the surface, and penetration depth must be more than 35 cm to decrease this to 10%, below 55 cm for 5% error. If a 100 cm mantle exists (the extreme maximum that has been suggested), the true values of the ice elements are unrecoverable unless the crystal penetrates below 100 cm and knowledge of the mantle thickness and density is obtainable from other data (e.g., the accelerometer readouts).

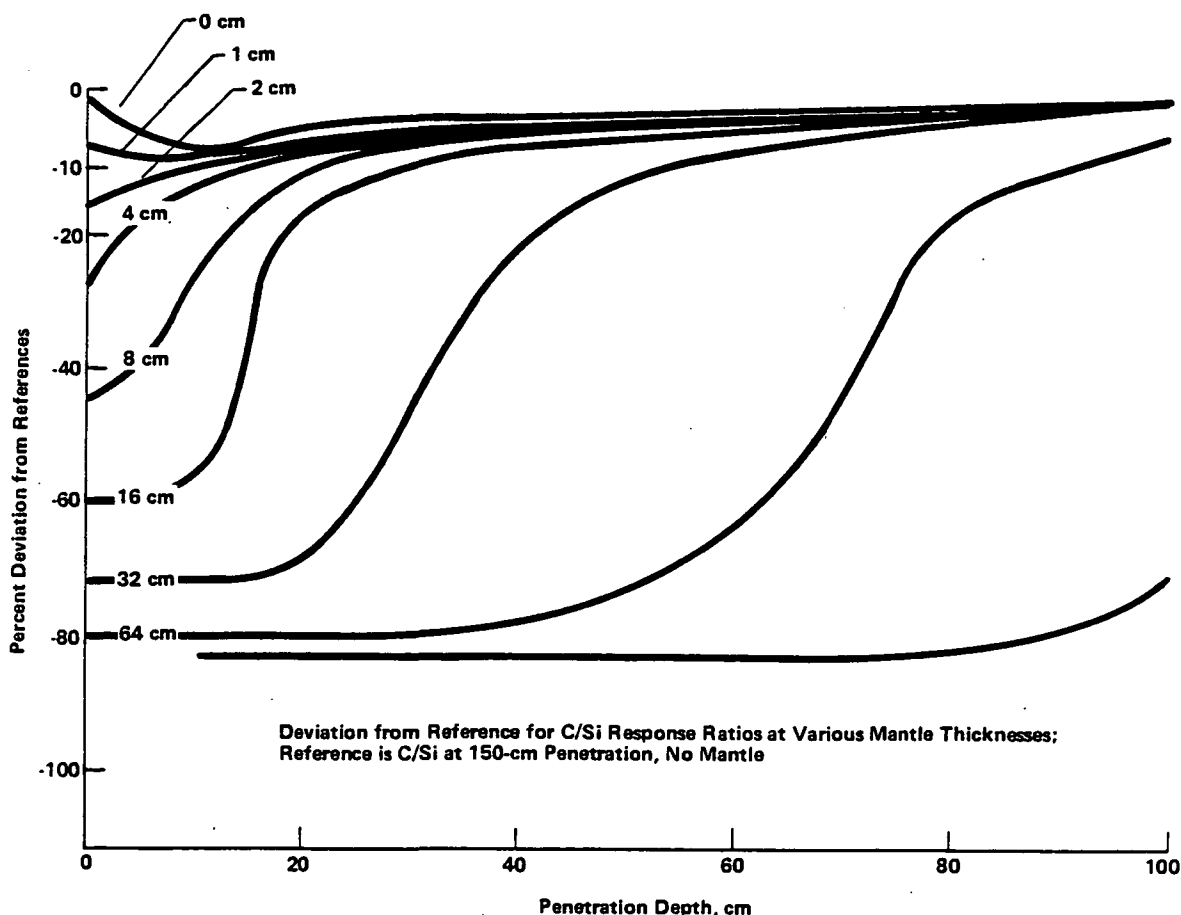


Figure 5.3-2 Deviation of C/Si Ratio for Various Mantle Thicknesses

In general, the deviation from the reference response for the isotopes included in the ice can be maintained below 10% if the crystal penetrates more than 25 cm below the mantle depth, and error will be less than 5% if the crystal reaches a depth at least 40 cm below the mantle. This is demonstrated for oxygen in Figure 5.3-3 and shown explicitly for hydrogen, the element with highest mantle-related errors, in Figure 5.3-4. Since the mantle material is expected to be loose or very poorly consolidated dust, the penetrator will lose very little velocity during mantle penetration, and therefore be able to penetrate well below the boundary surface.

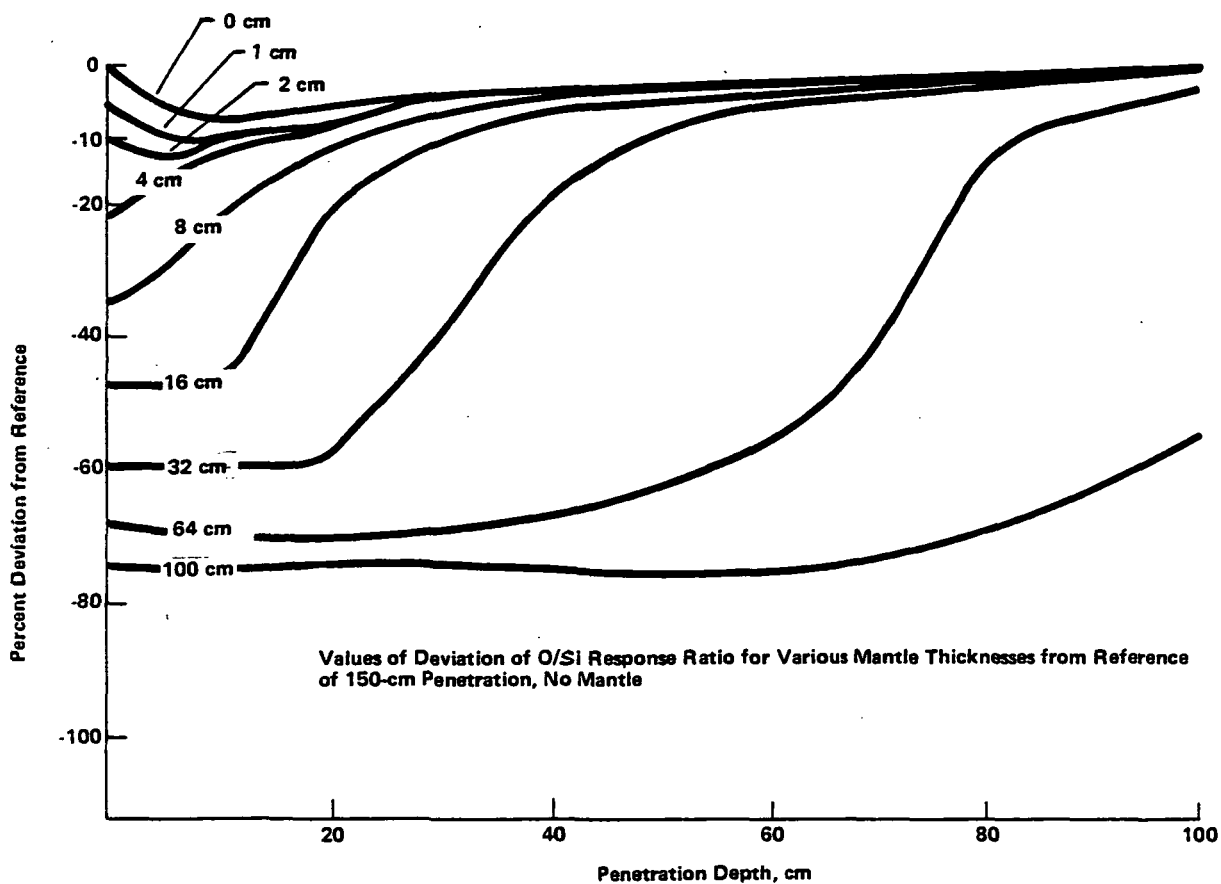


Figure 5.3-3 Deviation of O/Si Ratio for Various Mantle Thicknesses

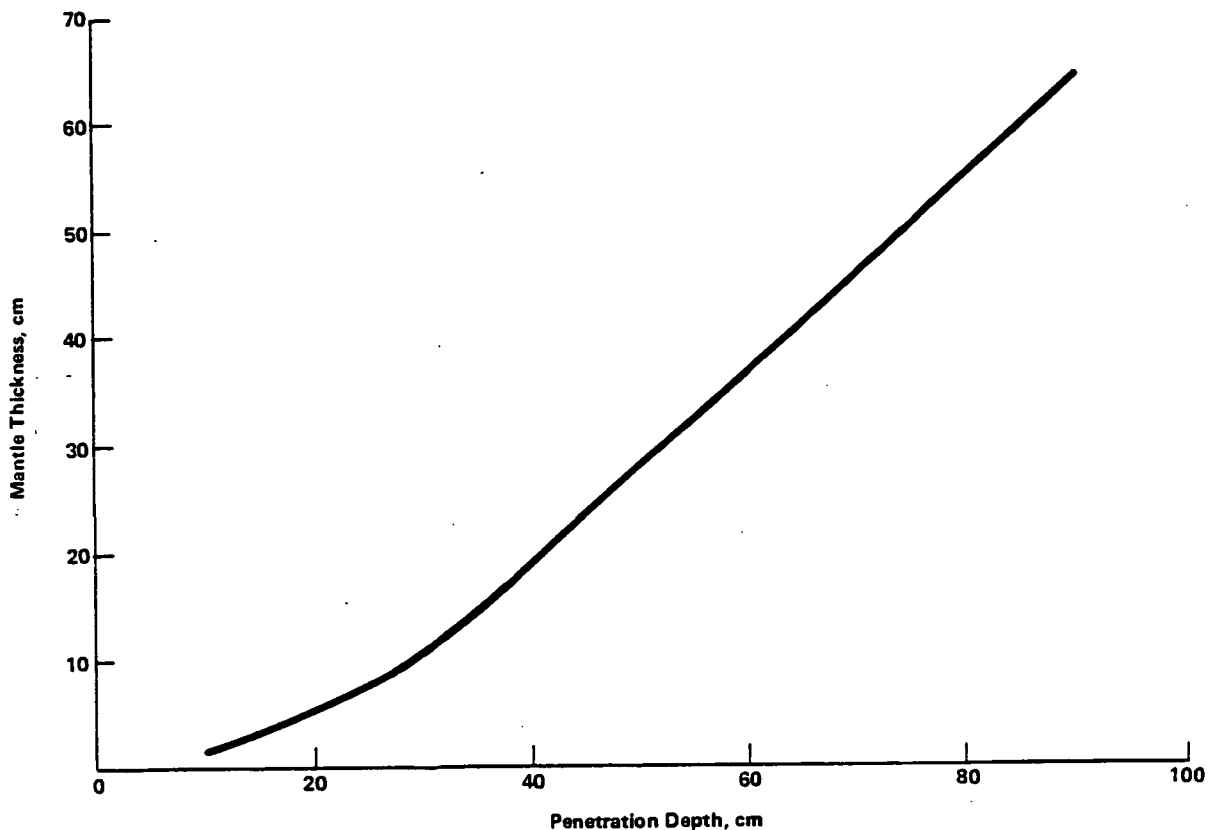


Figure 5.3-4 Minimum Penetration Depth for 10% Error in Hydrogen

5.4 Thermal Approach

Analytical thermal models for both the radiation network and temperature calculation have been constructed to describe the penetrator system thermal behavior, verify the thermal control design, and aid in optimization of performance, mass and power. The analyses include both steady-state and transient predictions for behavior during the annealing cycle, cooldown on the spacecraft, ejection from the spacecraft and delta-V phase, and implantation in the comet.

The radiation model was developed to determine radiation interchange between all elements of the system, including the penetrator thermal shield (PTS) and S/C where applicable. The Thermal Radiation Analysis System (TRASYS) computer program was implemented on our CDC main-frame system for this analysis. TRASYS was developed by Martin Marietta and is in general use throughout the industry. TRASYS was used to determine the radiative flux on all surfaces, considering the effects of reflections and shadowing. Surface properties such as emissivity were varied to evaluate worst-case conditions.

The Martin Marietta Interactive Thermal Analyzer System (MITAS) was used to perform temperature calculations. This program was developed by Martin Marietta as an improved version of the commercial thermal program SINDA. Lumped parameter thermal math models for each penetrator design and configuration were developed, with each node tied to other nodes or boundaries

by appropriate radiation and/or linear conductors. The radiation conductor array is input directly from the TRASYS program. The thermal math model was used to size various heaters, and determine whether designed penetrator component properties (i.e., emissivity, thermal conductivity) would assure adequate thermal performance.

Any successful design for the penetrator system must conform to four principal thermal requirements. The structure around the germanium crystal must be such that the crystal may be heated to 100°C during flight without excessive use of power. The thermal control system must be capable of cooling the detector crystal to below its maximum operating temperature of 120 K while onboard the spacecraft. The cooldown must be reasonably rapid and, ideally, continue after ejection from the spacecraft. After implantation in the comet, the thermal control system must maintain the crystal at operational temperatures for at least 3-5 days, even with a worst-case comet configuration. Finally, the data handling, communication and power subsystems must be kept within appropriate operating temperature ranges, without releasing a damaging amount of heat to the crystal.

The initial thermal models were developed for the radiator version of the penetrator. This system used a passive cooler radiator at the aft end of the penetrator to provide thermal control of the crystal. Active cooler system designs were discarded early in the study for reasons of mass, power and reliability. This passive radiator design used a flat plate radiator on the aft end of the penetrator, open in the center for motor clearance. This radiator had a total area of 2787 cm² (432 in²) for radiation to space. The thermal path between the germanium crystal and the radiator was an aluminum tube with 3.175 mm (0.125 in) walls. The waste heat from the electronics was dissipated from a flat ring radiator at the outer diameter of the electronics housing. Figure 5.4-1 shows the thermal math model for this configuration.

This design was evaluated in the implanted configuration using the range of comet properties shown in Table 5.4-1. The ideal result would be that the

Table 5.4-1 Comet Nucleus Parameter Set

	Minimum	Expected	Maximum
Surface Temperature	100 K	130 K	170 K
Sampling Depth Temperature		130 K	160 K
Albedo	0.01	0.05	0.5
Solar Flux	3 AU	4 AU	5 AU
Rotation Period	3 Hours	10-15 Hours	
Nucleus Thermal			
Conductivity ($\frac{\text{mW}}{\text{cm} \cdot \text{K}}$)	0.02	1-2*	100
Specific Heat ($\frac{\text{cal}}{\text{gr} \cdot \text{K}}$)	0.3	0.5-0.8	1.0
FSE Operating Temperature	130 K		
Crystal Operating Temperature	90 K		120 K
Electronics Operating Temperature	253 K	293 K	
Radiator Form Factor to Comet	0.0		1.0
Radiator Surface Area Total	400 in. ²		720 in. ²

*KICE = 22 $\frac{\text{mW}}{\text{cm} \cdot \text{K}}$

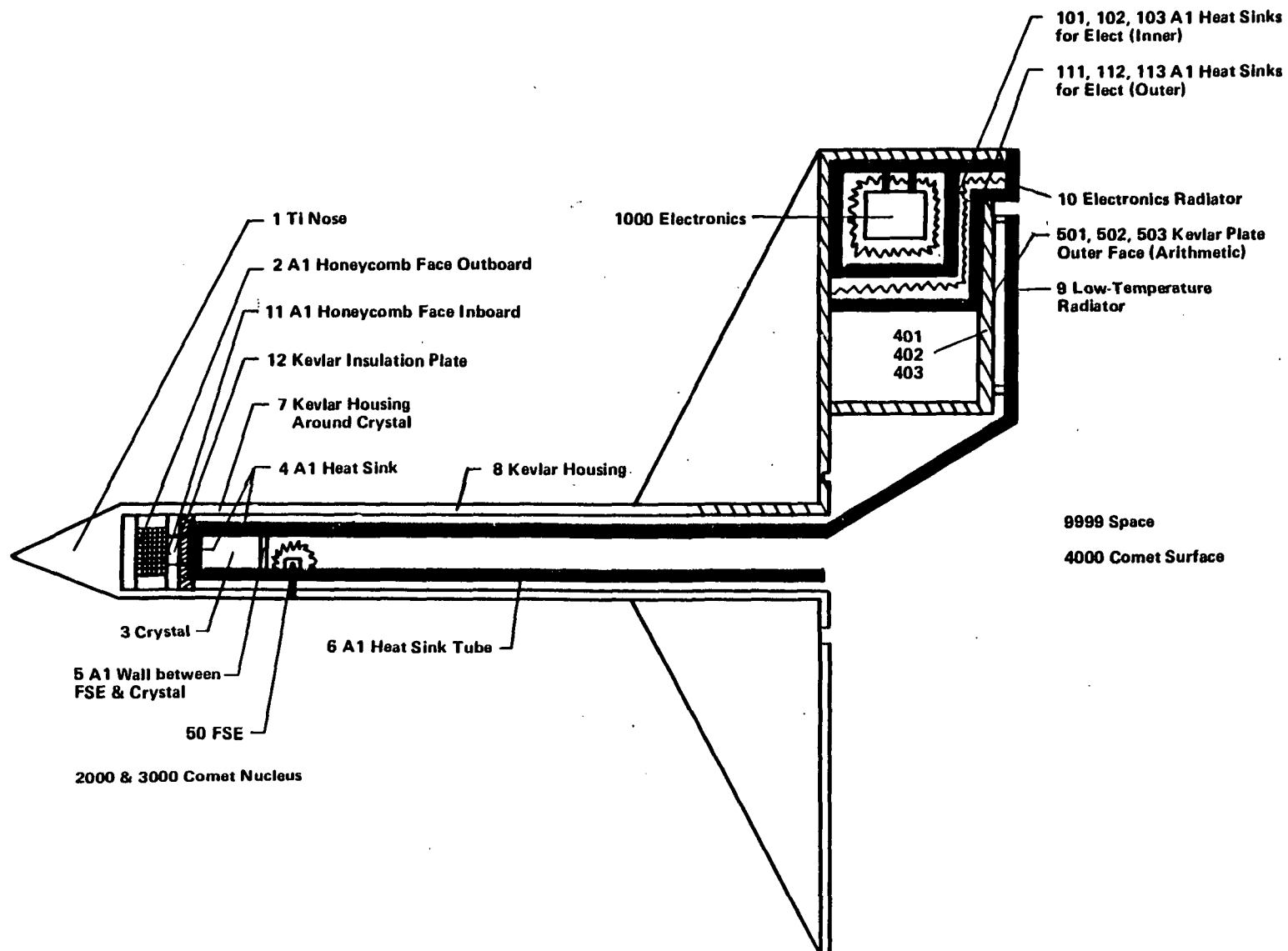


Figure 5.4-1 Penetrator Thermal Matb Model Nodalization, Radiator Concept

radiator dissipates enough heat to maintain the crystal below 120 K indefinitely in any potential configuration. The problem with this design is that it cannot meet all worst-case design parameters. The principal factors that will determine the steady-state crystal temperature are: the view factor of the radiator to the comet surface, the solar flux level on the radiator, the potential damage to the radiator by dust, the temperature of the comet surface and interior, and the surface area possible for the radiator. Figure 5.4-2 shows the results of the temperature calculation with a reasonable assumption of parameters. The worst-case comet temperatures are assumed: 170 K for the surface and 160 K for the nucleus. The view factor of the radiator to the comet is 0.05. The electronics are assumed to operate at -20°C , however this parameter affects the detector temperature very little. The emissivity of the comet surface is 0.8; the α/ϵ factor for the silver coated teflon radiator is 0.1/0.8. The solar flux on the radiator is assumed to be 70% of the solar flux at 4 Astronomical Units (AU). The first-stage electronics (FSE) is thermally shorted to the penetrator wall, which will keep it above its minimum operating temperature of 130 K. A heater is provided to accommodate the possibility of comet temperatures below 130 K. The steady-state crystal temperature under these conditions is 119.6 K, which allows no margin for parameter variation or model error. The central factor that cannot be guaranteed is the form factor of the radiator to the comet. Any increase in the radiative load from the comet or from the sun will push this design past operable limits. If it were possible to guarantee a 0.05 form factor to the comet and no solar load, the steady-state crystal temperature would be 93 K. Even with a 25% solar load at 4 AU, the crystal temperature would be only 105 K. This increases to 111 K if the form factor to the comet is 0.25. The radiator design is attractive because it allows indefinite operation of the detector, but it could not be used without a better knowledge of the penetrator-comet configuration. Also, cooldown would have to be done after implantation--there is no provision for cooling and testing the detector on the spacecraft. Additional problems include heating effects from the motor, degradation of the radiator, potentially complex structure of the electronics isolation, little flexibility to adapt this design to a different comet, and the probability that the penetrator may become buried during emplacement.

The final penetrator system design uses thermal isolation to maintain the low operating temperature of the crystal. While onboard the spacecraft, the crystal is clamped tightly in an titanium structure, presenting a good thermal path from the detector to the penetrator skin. The entire outer surface of the penetrator, covered with silverized Teflon tape, functions as a radiator, with a shield to cut off its view of the spacecraft. This passive radiative cooling is used to cool the crystal to its initial implantation temperature. The thermal performance of this design was evaluated with 5 separate TRASYS programs for different sections of the penetrator, and a three-dimensional radiative-conductive MITAS program using 118 nodes, 563 radiative conductors and 165 linear conductors. Four different phases of penetrator operation were analyzed: the annealing cycle, the spacecraft cooldown, the inflight post-ejection phase (including motor burn), and the implanted phase. Each phase included many different variables and worst-case parameters.

Analysis Parameters:

Electronics
 Operating Temp. = -20°C
 Temp. Comet Surface = 170 K
 Temp. Comet Nucleus = 160 K
 Radiator Areas 432 in.²
 91.1 in.²
 Solar Flux = 70% @ 4 AU
 Form Factor to Comet = 0.05
 Form Factor to Space = 0.95

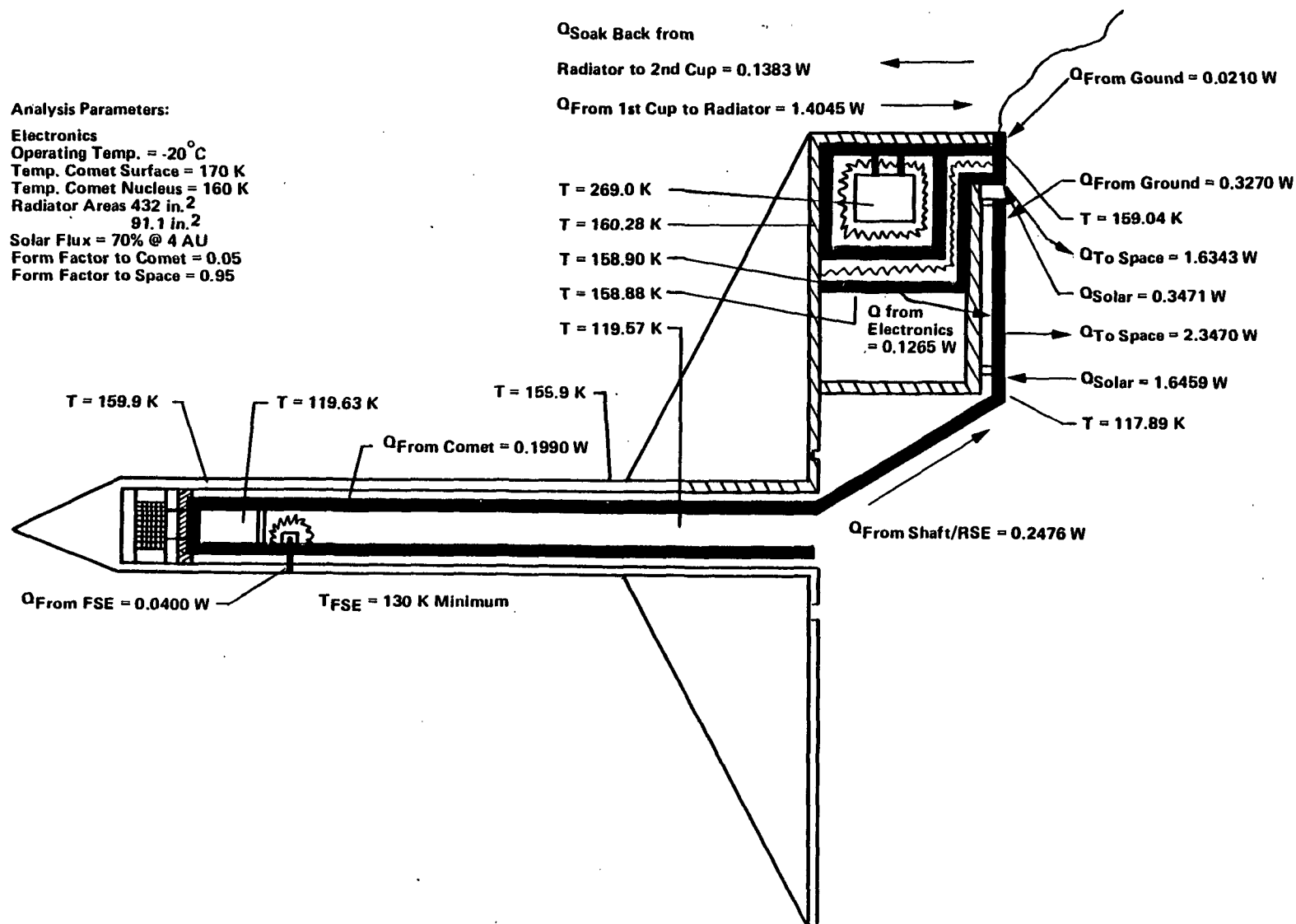


Figure 5.4-2 Typical Energy Balance and Temperatures for Steady State Penetrator Operation (Implanted), Radiator Concept

The three-dimensional radiation network TRASYS runs, shown in Figures 5.4-3 to 5.4-7, use about 20 nodes for each section shown to calculate the radiative conductors. The emissivity of all internal metal surfaces except the detector casing was assumed to be 0.1, and MLI surfaces were taken to have an emissivity of 0.05. The radiative interaction between the penetrator and its shield was also treated in a TRASYS run. The shield consisted of a half-cylinder of MLI blanket with a radius slightly larger than the aft end of the penetrator, extending along the full length of the penetrator. The emissivity of these surfaces was a parameter that could vary to incorporate clean or dust-covered MLI. The radiative network found using TRASYS was input to the MITAS program.

Figure 5.4-8 shows the penetrator divided into the nodes used by MITAS. The penetrator is divided along its length into 6 main sections: the nose, the cylinder housing the detector, the forward section of the flare, the aft section of the flare, the electronics section and the aft section for attachment to the spacecraft. Each section is divided radially into 4 parts to handle the asymmetries of electronics, view factors to space, etc.. For most of the analyses, the crystal and its housing were assumed to be a single node. MLI was assumed on the forward side of the two Kevlar disks. One way to further optimize the thermal performance would be to assume MLI blanketing on both sides of all Kevlar structural disks. The electronics and battery boxes were each enclosed in a 0.508 mm (0.020 in) thick Kevlar shell, with MLI on the outside. The batteries were fastened with titanium bolts on Kevlar standoffs: four bolts to the forward plate and three bolts to the cylinder side. The electronics used six bolts to the forward plate and four bolts to the side. This thermal isolation of the electronics and batteries is not a

COMET NUCLEUS PENETRATOR MODEL

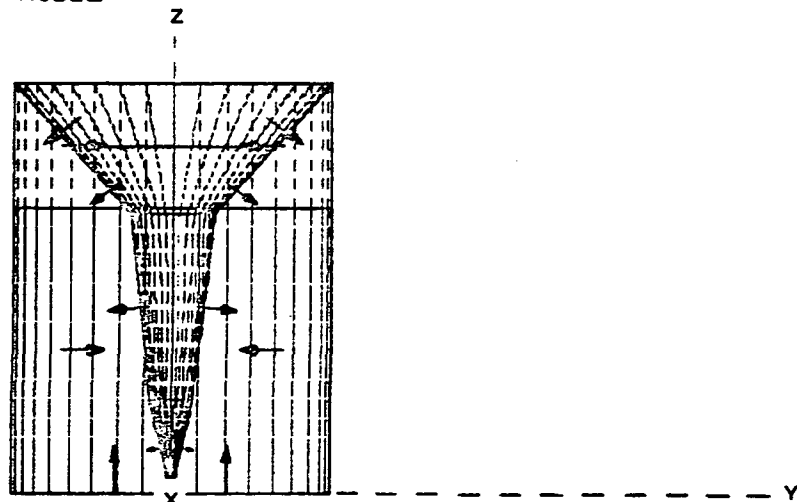


Figure 5.4-3 TRASYS: Exterior Penetrator Nodes

COMET NUCLEUS PENETRATOR MODEL

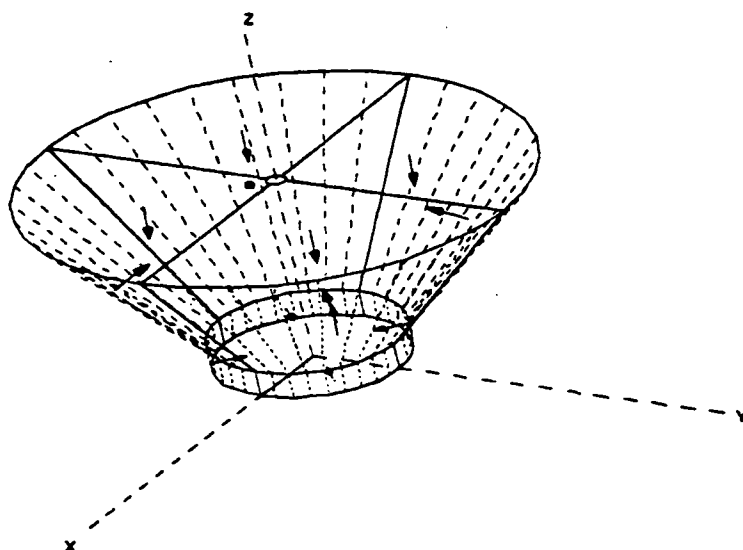


Figure 5.4-4 TRASYS: Forward Section of Flare

COMET NUCLEUS PENETRATOR MODEL

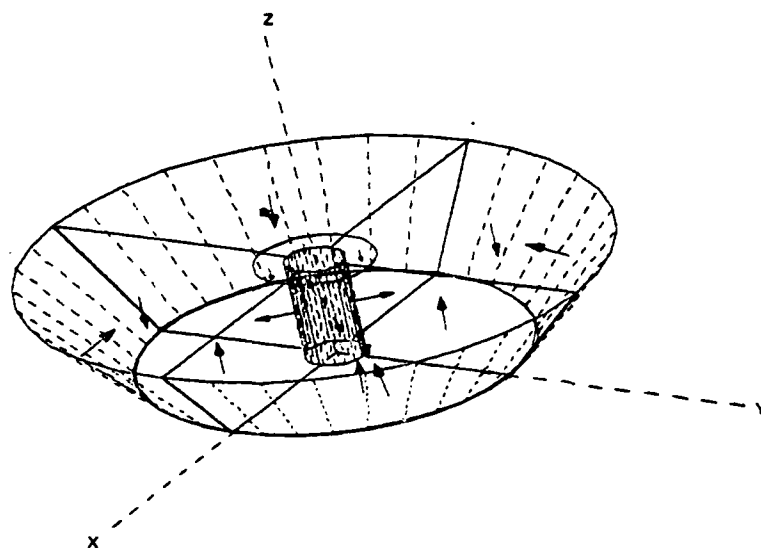


Figure 5.4-5 TRASYS: Aft Section of Flare

COMET NUCLEUS PENETRATOR MODEL

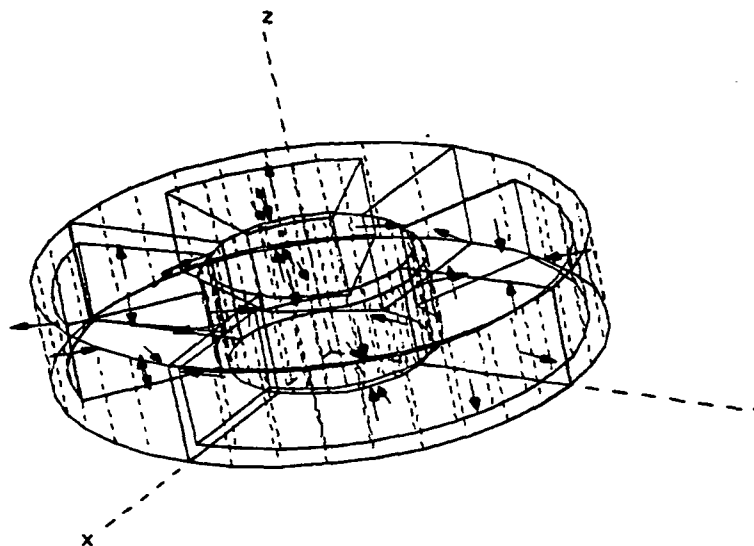


Figure 5.4-6 TRASYS: Electronics Section

COMET NUCLEUS PENETRATOR MODEL

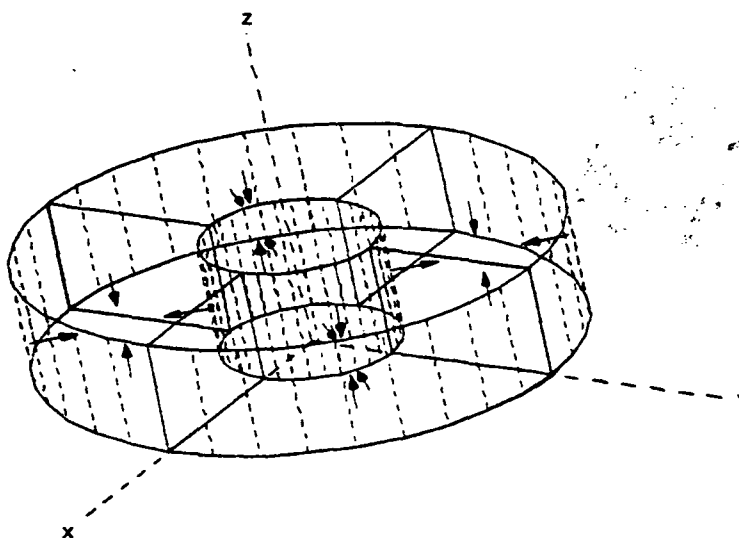


Figure 5.4-7 TRASYS: Aft Section

ORIGINAL PAGE IS
OF POOR QUALITY

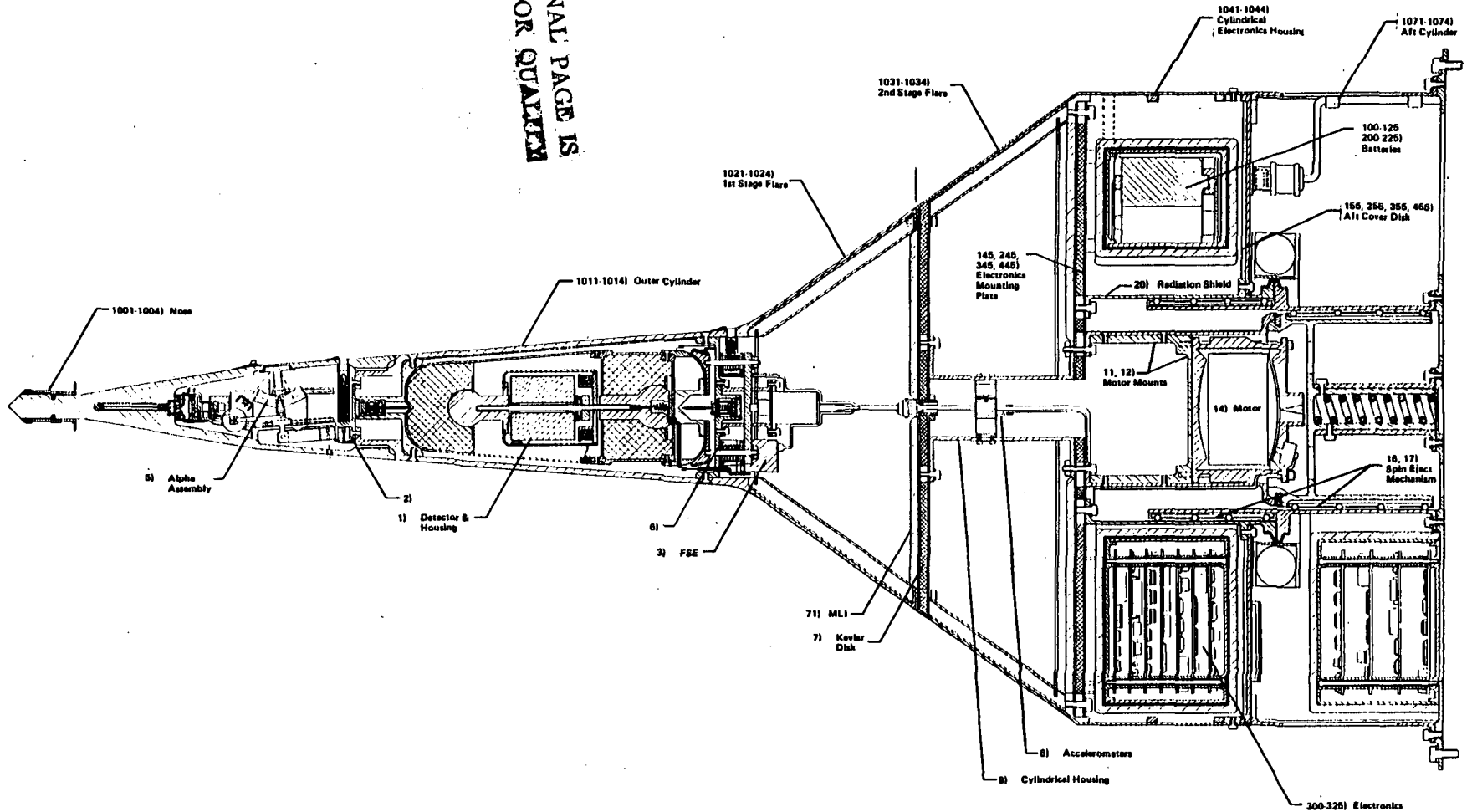


Figure 5.4-8 MITAS Nodes for Final Penetrator Design

complex structure to fabricate, and it adequately insulates these warm components. This performs the double function of minimizing heat leakage to the crystal, and conserving the power necessary to heat the batteries and electronics. The wires from the electronics to the forward portion (detector, alpha, etc..) were assumed to be ribbon cables, except for the pin-puller actuators. These carry more current, and were thus assumed to be 2.124 mm (0.060 in) wires. For all phases before motor burn, the motor was held at or above -18°C . For the implanted mode, the FSE was held above its operational temperature of 130 K. The electronics were maintained at -40°C , and the batteries at -30°C .

The first phase of concern is annealing of the crystal. While on the spacecraft, the crystal must be brought to 100°C for annealing of cosmic ray induced damage. To minimize the power needed for this, the thermal path between the cold nose and the detector must be limited. To implement this analysis, the crystal and its housing were broken up into component nodes. The most power-efficient way to heat the crystal is to heat the titanium casing on the aft honeycomb, because the highest power loss is down the nose. Teflon rings were assumed in the titanium clamping structure, which degrades the thermal path enough to make heating the crystal possible at low power, without sacrificing the necessary cooldown characteristics. This analysis shows a power consumption of 17.5 W necessary to maintain the crystal at 100°C . Figure 5.4-9 shows the range of temperatures of the surrounding components. Although this design is the most power-efficient, it allows too large a temperature gradient for accurate determination and control of crystal temperature, as well as producing potentially severe thermal stresses. An approach more thermally stable is to heat both the fore and aft honeycomb, which requires substantially more power. The required power then depends on the type of insulating ring used in the clamp design. With a 2.54 mm (0.1 in) thick teflon ring insulator, the crystal requires 36 W to maintain 100°C : 32 W on the forward heater and 4 W on the aft. Figure 5.4-10 shows the node temperatures in the detector region for this design which is much better for accurate determination of crystal temperature. To provide a reasonably rapid heating cycle, 40-45 W should be allowed for the time to raise the crystal temperature to 100°C , and 36 W can be used to maintain that temperature.

The second and possibly most critical phase is the detector cooldown on the spacecraft. Variable parameters for this phase include the optical characteristics of the penetrator skin and shield, the view factor of the shield to the spacecraft, and the non-operating temperature used for the electronics and batteries. Two types of analyses were used for these cases: steady-state, to determine final temperatures as a function of several variables, and transient, to determine the cooldown time for the final set of parameters. Initially, the spacecraft blankets were assumed to be black, the penetrator skin was silverized Teflon tape ($\alpha/\epsilon = 0.1/0.8$) and the penetrator thermal shield (PTS) was clean MLI blanket ($\epsilon = 0.05$). The configuration of the PTS and the spacecraft has not been fully defined; the first estimate of the view factor of the outside of the shield to the spacecraft was 60 %. The electronics storage temperature was -40°C , and the batteries were at -30°C . Using these parameters, the final temperature was 102.5 K. Figure 5.4-11 shows the steady-state temperatures at each node of the penetrator system. Dropping the maintenance temperatures of the batteries and

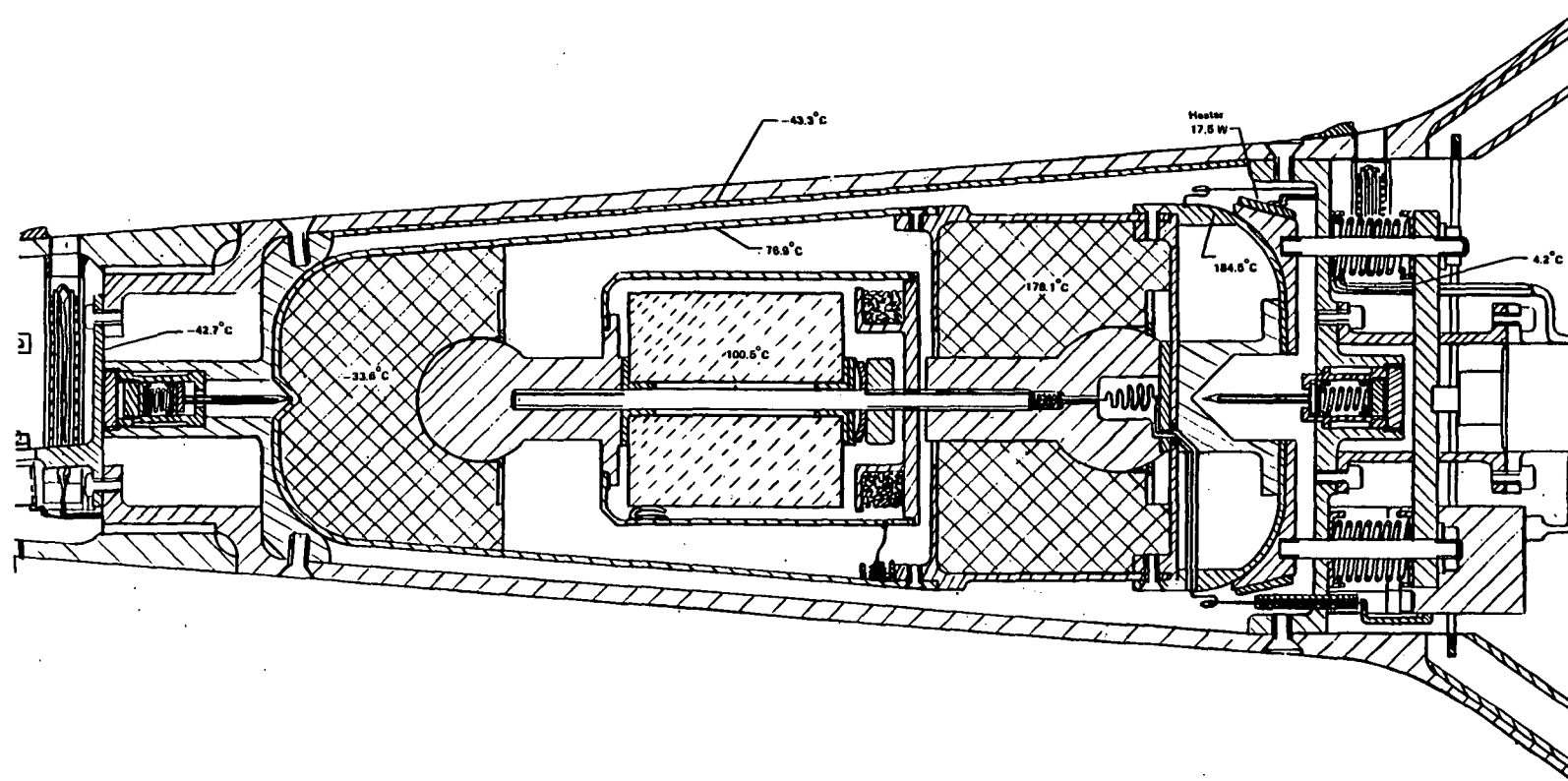


Figure 5.4-9. Temperatures in Crystal Region during Annealing Cycle (17.5 W Heater on Aft Section)

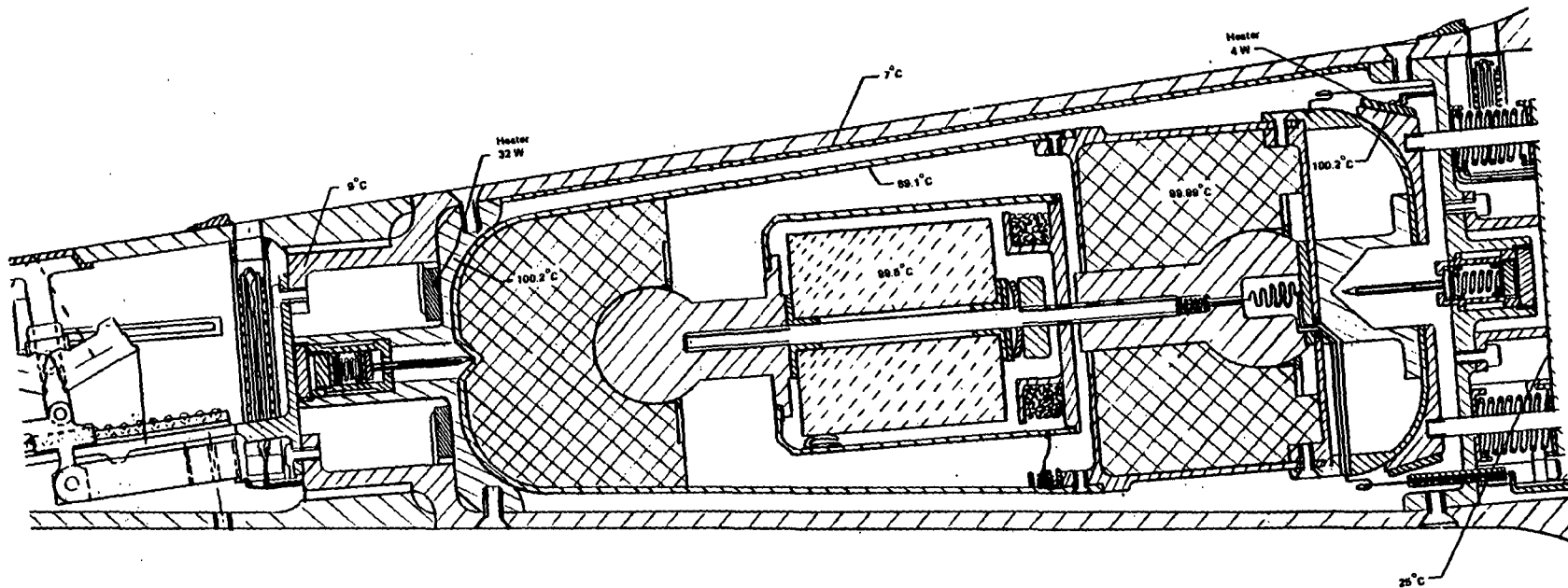


Figure 5.4-10 Temperatures in Crystal Region for Final Design of Anneal Heater (36 W)

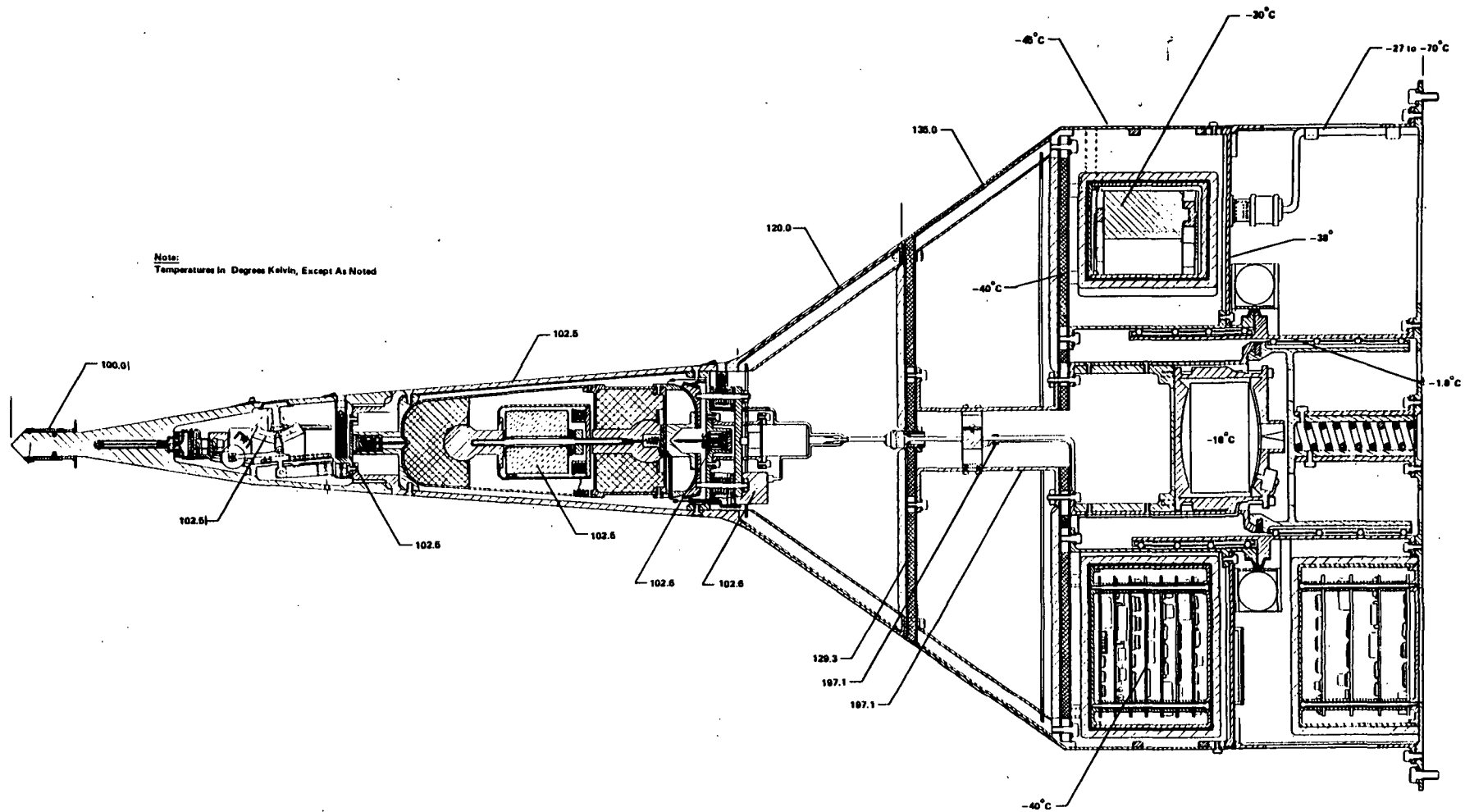


Figure 5.4-11 Steady-State Node Temperatures during Onboard Cooldown

electronics to -40°C and -55°C , respectively (still within the specifications for both), brings the final temperature down to 99.8 K. Increasing the PTS view factor to the S/C to 70% only raises this by half a degree (100.3 K). The supposed worst-case of shield degradation by comet dust was examined. Since a good portion of the shield interior is seeing deep space, an increase in emissivity is not disastrous. For a completely degraded shield ($\epsilon = 1.0$), electronics at -40°C and batteries at -30°C , the steady-state temperature is 101.6 K, actually better than the "clean" case. The optimum case is actually when the interior surface of the shield (toward the penetrator) is black, and the spacecraft-facing side remains clean. When the penetrator is in shadow for cooldown, it will be necessary to heat the electronics (1.25 W) and batteries (0.5 W). To maintain the motor above its minimum temperature of -18°C will require about 1 W.

The cooldown transient for the original parameters is shown in Figure 5.4-12. Many runs were performed with slight variations in parameters, and steady-state was always achieved within 50 hrs.

The next phase is approximately 80 minutes long, between ejection from the spacecraft and implantation in the comet. The main variable parameters are the level of solar load and the state of the penetrator exterior. Ideally, the solar load would be mainly on the aft disk of the penetrator, which will be a relatively clean surface since it is protected from dust contamination until ejection. This minimizes the heat load and allows more insulation length between the solar load and the crystal. More realistically, there will be some solar load on the sides of the penetrator; this is highly dependent on the ejection configuration. A nominal choice is full solar load on the aft disk and 10% load on the sides. The worst-case solar load used, so pessimistic as to not be realistic, is that there is full solar load on the entire penetrator. Three cases were also used for the potential state of degradation of the penetrator surface. First, the penetrator could remain unaffected by dust so that the optical characteristics of its silverized Teflon surface remain the same: $\alpha/\epsilon = 0.1/0.8$. The worst case is that the entire surface, except for the protected aft disk, is completely degraded by comet dust so that the surface becomes a perfect blackbody: $\alpha = 1.0$, $\epsilon = 1.0$. A more reasonable assumption is that the outboard half of the penetrator is degraded, while the shield-facing side remains clean. The worst-case heat impact of the motor firing was also included in this calculation, but had negligible effect on the crystal temperature. The results of these calculations are shown in Table 5.4-2.

Table 5.4-2
Final Crystal Temperatures after Ejection/Cruise Phase

State of Degradation			
Solar Load	α/ϵ		
	1.0/1.0	0.5/0.5	0.1/0.8
Full	119.8 K	119.9 K	103.4 K
Full Aft & 10% Sides	102.6 K	102.1 K	101.6 K
Full Aft Only	100.5 K	101.0 K	101.4 K

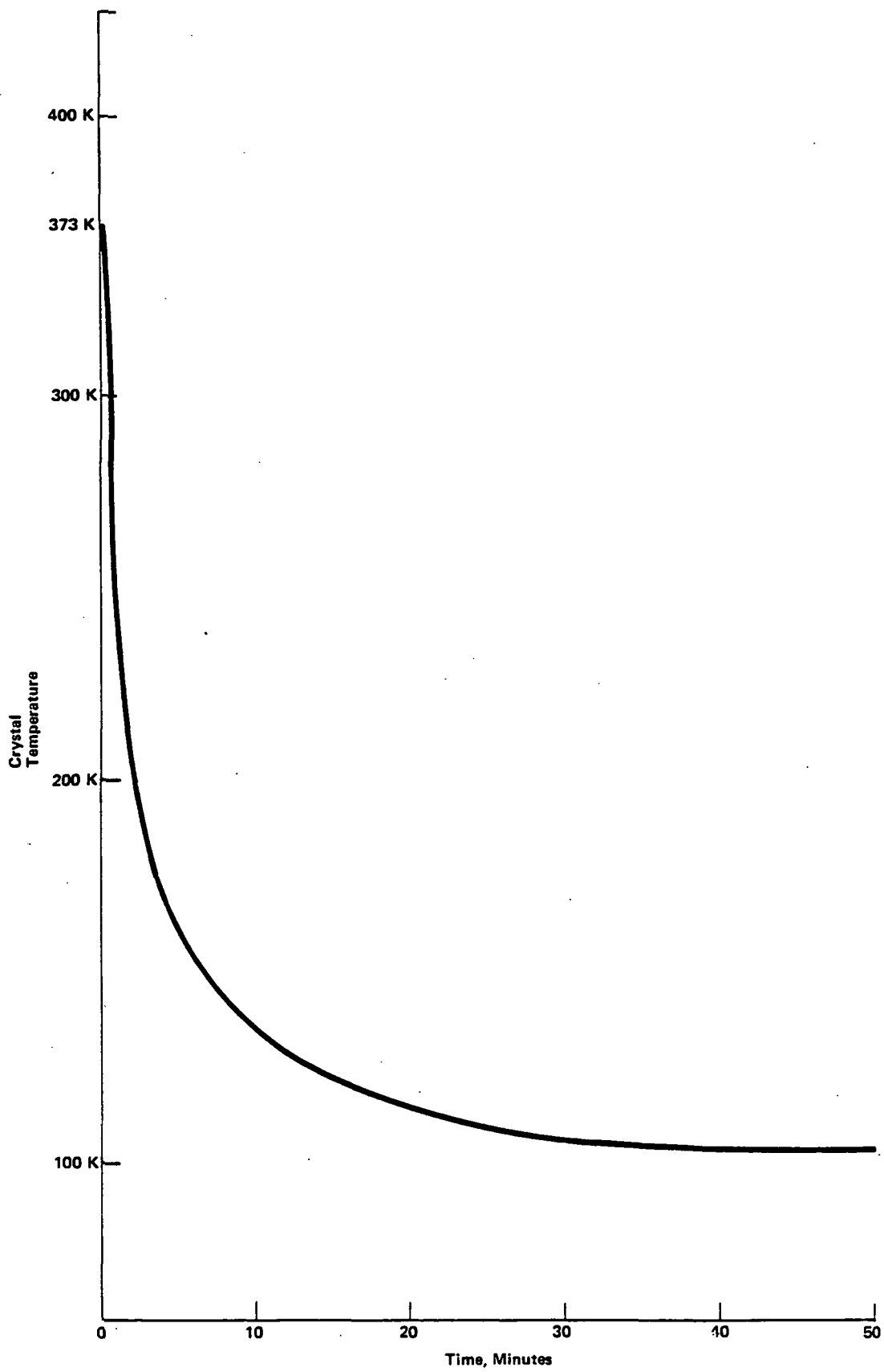


Figure 5.4-12 Onboard Cooldown after Anneal Cycle

Any of these potential configurations, except for a combination of the two worst cases, produces acceptable thermal performance. A clean penetrator, even under full solar load, produces only a 1° rise in temperature. Lesser solar load allows a 1- or 2-degree drop in crystal temperature before implantation. For a semi-degraded penetrator, the range in thermal effect is from a 9.5° rise for full solar load to a 1.5° drop with solar load on the aft section only. A fully degraded penetrator surface, almost impossible to achieve, will produce a 17-degree rise in detector temperature under full solar load: final temperature 119.8 K. Any solar load less than 10% on the sides will produce a temperature drop; full solar load aft and 30% load on the sides will only raise the crystal temperature 4° . If, after further analysis of the ejection configuration, full solar load is determined to be a possibility, some method for maintaining at least partial cleanliness of the penetrator surface should be devised.

The behavior in the fourth phase, implanted, will determine the amount of time that is available to take gamma-ray spectrometer data. The detector region is designed for minimum heat leakage from a warm comet to the detector crystal. After impact, the large pin-puller is activated to pull the titanium clamps away from the detector housing. The housing is then supported between two pins: hollow, Kevlar, 1.27 mm (0.050 in) diameter and 0.102 mm (0.004 in) wall thickness. The conservative assumption was made that the housing is in continuous perfect contact with the pins. Actually, the housing will rest lightly and intermittently against the support pins, producing a high contact resistance which lessens their heat load. The outer walls of the housing and the inner surface of the penetrator shaft are finished with vacuum-deposited gold to provide a high-reflectivity surface. The wires from the first-stage electronics to the crystal are 0.102 mm (0.004 in) stainless steel. The initial temperature at impact was assumed to be 102.4 K. The comet was modeled using typical figures from the range of properties estimated: thermal conductivity $1.5 \text{ mW cm}^{-1} \text{ K}^{-1}$, specific heat $2.72 \text{ J g}^{-1} \text{ K}^{-1}$, density 1.0 g cm^{-3} , and temperature at depth 160 K. Heat of impact was calculated and found to have negligible impact on crystal temperature. The aft end of the penetrator was assumed, worst-case, to be buried in the comet.

The fore and aft ends of the detector housing will probably be treated to avoid vacuum-welding of the gold surfaces during the mission. Thus, a conservative emissivity of 0.05 was assigned to these surfaces. The cylindrical sides were assumed at an emissivity of 0.03. Figure 5.4-13 shows the variation of crystal temperature with time for different comet nucleus temperatures using these parameters. Successful operation is possible but not expected once the crystal temperature has exceeded 120 K. Figure 5.4-14 shows the heat flow to the crystal for this configuration. Obviously, the main thermal load on the crystal is the radiative transfer from the penetrator walls. If care is taken to ensure that the gold surface on these walls is unmarred, an emissivity of 0.02 is not an unreasonable figure. Using this number for the side walls, the crystal remains below 120 K for 105 hours ($\sim 4 \frac{1}{2}$ days in a 160 K comet). The implanted operation of the penetrator will depend highly on care used in fabrication of the components near the detector, particularly the surfaces of the side walls.

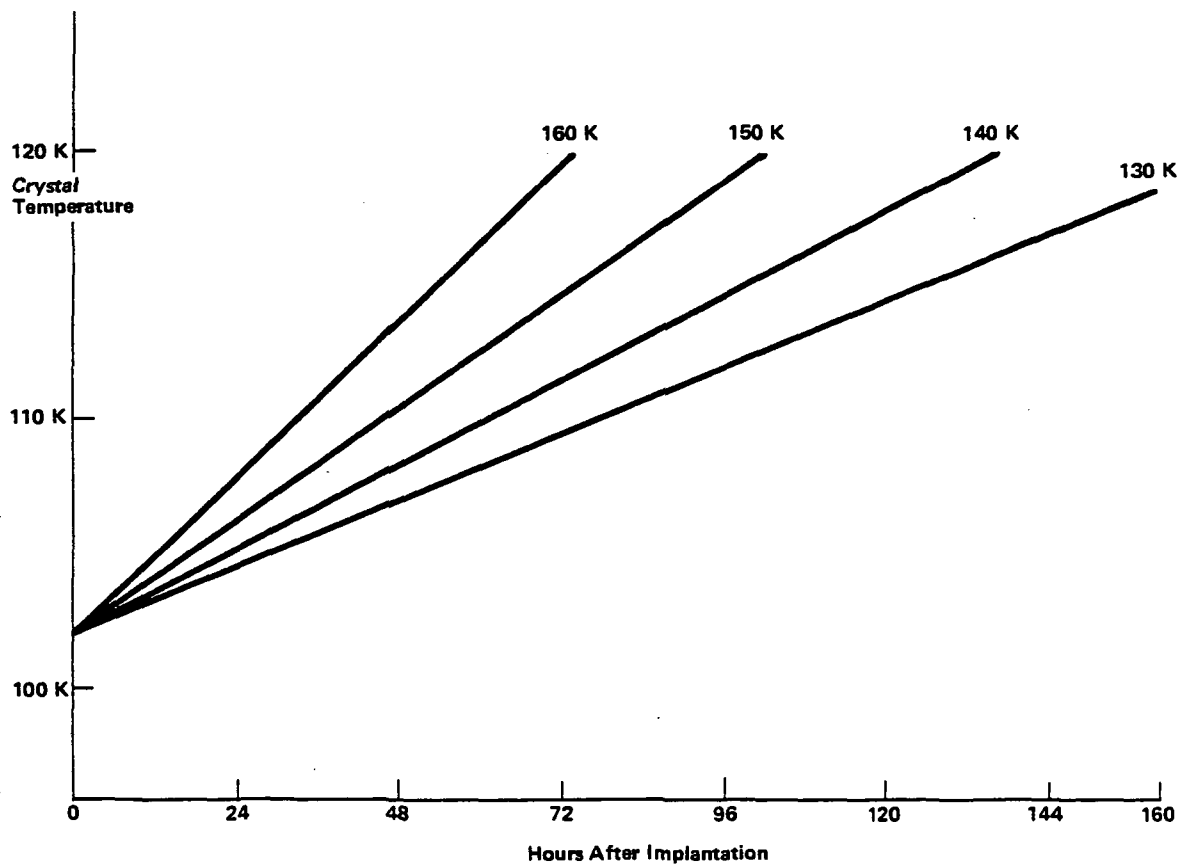


Figure 5.4-13
Thermal Performance of Implanted Penetrator for Various Comet Temperatures

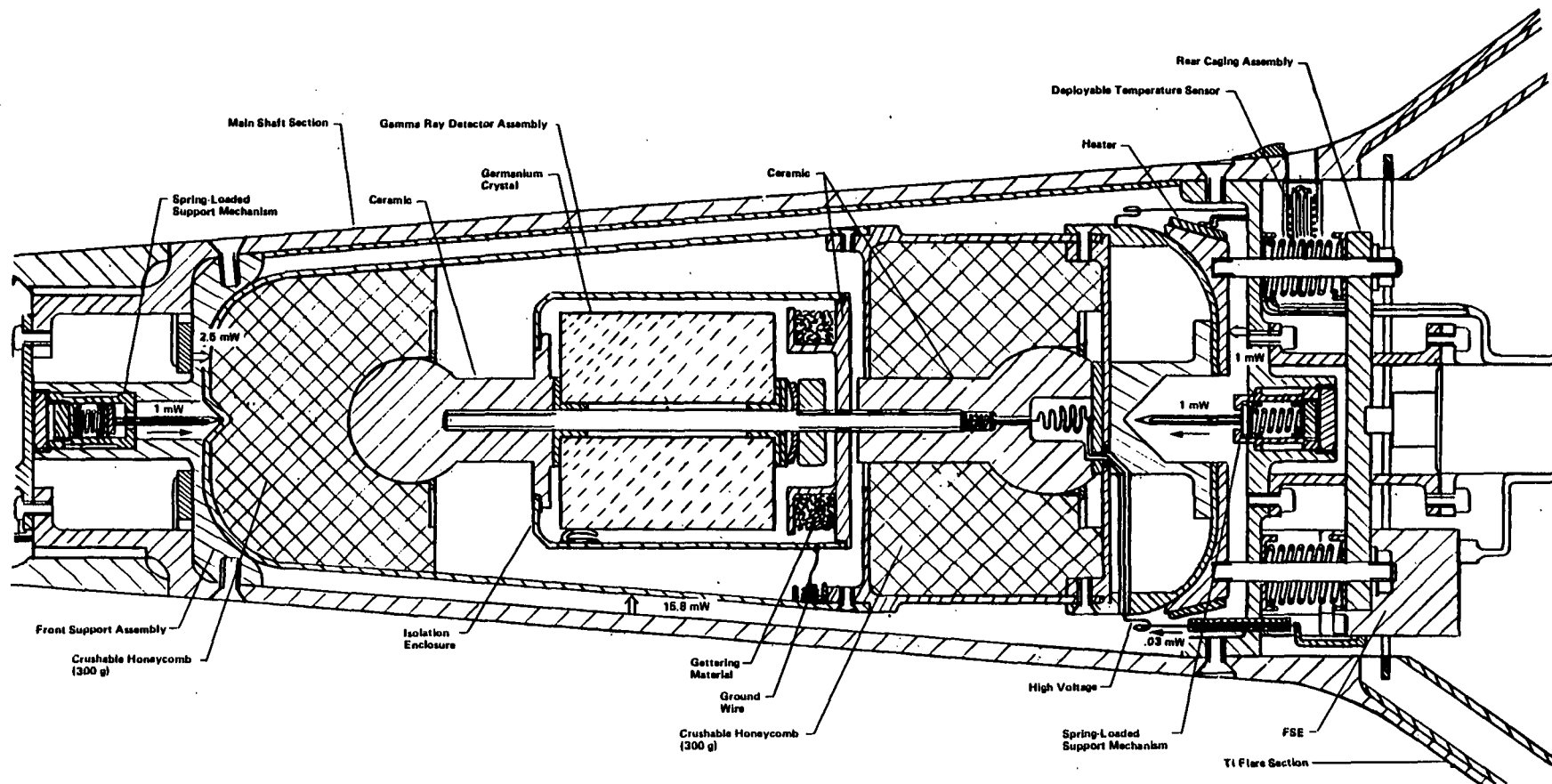


Figure 5.4-14 Thermal Impacts on Detector While Implanted

5.5 Flight Dynamics Analyses

This section treats the predicted attitude performance of the comet nucleus penetrator. Mathematical models are derived that form the basis of a computer program that was used to predict attitude performance for the currently proposed penetrator configuration. The mathematical models represent closed-form solutions, under reasonable assumptions, for the attitude motion over all phases of the penetrator descent trajectory. These solutions have permitted insights into the attitude motion of the penetrator that would have been more difficult to achieve with a numerically integrated solution of the equations of motion.

The primary objective of the attitude performance analysis was to determine the influence of descent implementation errors, such as spin/eject tipoff rates and rocket motor thrust misalignments, on penetrator angle of attack errors at comet nucleus impact. A small impact angle of attack is critical to the success of the comet nucleus penetration experiment. An angle of attack that is too large may cause the penetrator to buckle upon impact or to penetrate the nucleus to a depth that is not sufficient for proper operation of the penetrator's gamma-ray spectrometer.

The analysis is a worst case analysis, not a statistical one, in that expressions are obtained for the maximum possible angle of attack error at all important events along the descent trajectory. Since trajectory effects were not considered to be significant for predicting penetrator attitude performance, the coast phases of the descent trajectory were assumed to be described by uniform motion along a straight line. Hence, any subsequent reference to angle of attack or flight path angle should be interpreted as angle of attack error or flight path angle error, respectively, relative to the targeted values of these parameters. Subsequent attitude performance predictions assume that the targeted angle of attack at impact is zero. If this is not the case, then the non-zero targeted impact angle of attack must be added to the predicted impact angle of attack error to obtain the total impact angle of attack. Finally, environmental torques were assumed to be negligibly small and appropriate small angle assumptions were made in obtaining solutions of the equations of motion.

Penetrator attitude performance is determined at all important events as the penetrator descends along its trajectory from spin/eject to comet nucleus impact. Superscript notation is used to define penetrator state parameters at each event:

- ()⁽⁰⁾ : spin/eject
- ()⁽¹⁾ : end of long coast phase = start of delta-v phase
- ()⁽²⁾ : end of delta-v phase = start of final coast phase
- ()⁽³⁾ : comet nucleus impact

Important penetrator state parameters are shown in Figure 5.5-1 at each event in the trajectory sequence. These parameters are defined as follows:

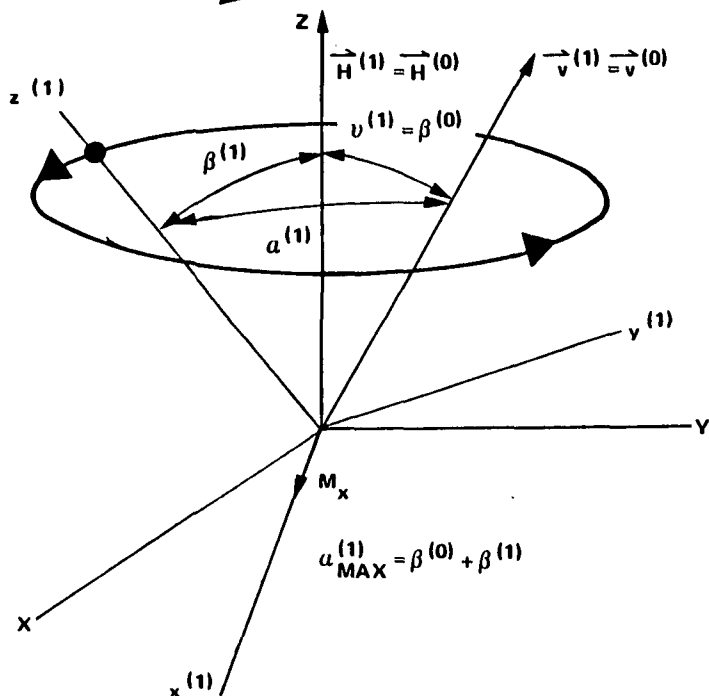
- z : axis of symmetry
- v : inertial velocity
- γ : flight path angle

1. Spin/Eject

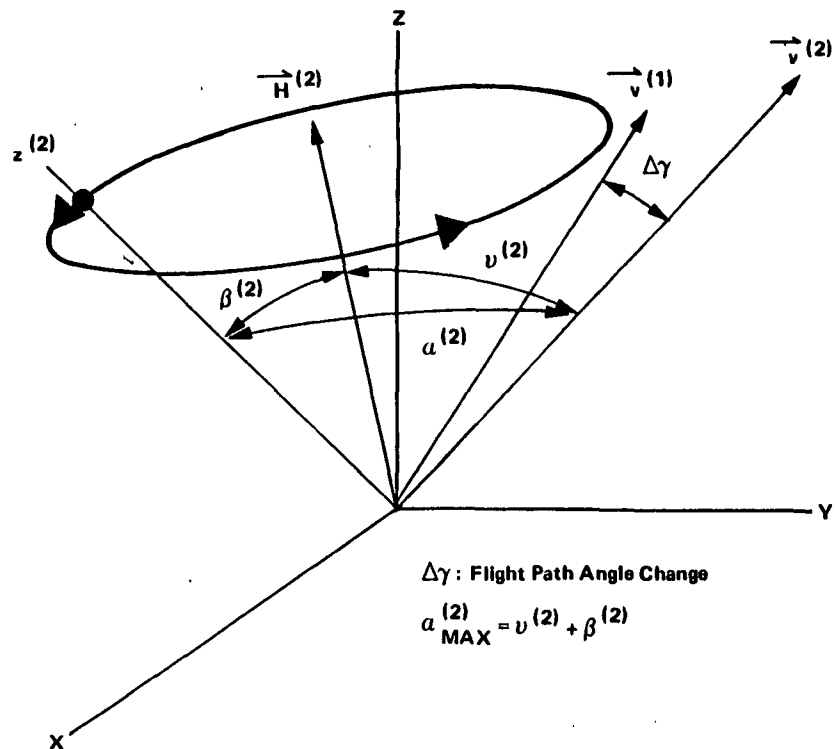
$\beta^{(0)}$: Initial Nutation Angle
 $a_{MAX}^{(0)} = 2\beta^{(0)}$: Max Angle of Attack

2. ΔV Start (End of Pre- ΔV Coast)

$\beta^{(0)} \xrightarrow{\dot{T}} \beta^{(1)}$



3. ΔV End (Start of Post- ΔV Coast)



4. Impact

$\beta^{(2)} \xrightarrow{\dot{T}} \beta^{(3)}$
 $a_{MAX}^{(3)} = v^{(2)} + \beta^{(3)}$

Figure 5.5-1 Penetrator State vs Trajectory Sequence of Events

H : angular momentum
 β : nutation angle; angle between axis of symmetry and angular momentum
 ν : angle between velocity and angular momentum
 α : angle of attack
 α_{max} : maximum angle of attack

Coordinate frame XYZ denotes an inertial frame, while xyz denotes the penetrator body frame.

A brief overview of the penetrator attitude behavior during the descent will be provided next. The descent is initiated with the spin/eject of the penetrator. The initial nutation angle β^0 is induced by the inertial tipoff rate produced by the spin/eject mechanism and the reaction of the Mariner Mark II spacecraft. Internal energy dissipation rate T will cause the initial nutation angle to increase to β^0 across the long pre-delta-v coast since the penetrator is a passive prolate spinner. Proper structural design of the penetrator will ensure that this increase is small. Just prior to the start of the delta-v phase, the penetrator axis of symmetry is precessing about the angular momentum vector \vec{H}^0 , and the inertial velocity \vec{v}^0 has a fixed orientation relative to \vec{H}^0 . The rocket motor is ignited at delta-v start and accelerates the penetrator to the desired impact velocity. A small misalignment of the rocket motor thrust, however, will produce a disturbance torque M_x which not only deflects the final velocity by an angle $\Delta\gamma$ relative to the initial velocity, but also deflects the angular momentum vector and the axis of symmetry. Thus, at the end of the delta-v phase the angle between the velocity and the angular momentum has changed to ν^2 ; the nutation angle, to β^2 ; and the angle of attack, to α^2 . Since the axis of symmetry z^2 resumes its torque-free precession about the angular momentum vector, the angle of attack α^2 will vary with time. However, its maximum value is attained when z^2 , \vec{H}^2 , and \vec{v}^2 are all coplanar. During the final brief coast to impact, internal energy dissipation can again cause the nutation angle to increase. But this increase will be negligibly small because of the brevity of the final coast (less than 1 minute).

5.5.1 Spin/Eject Phase

The spin/eject phase imparts both translational and angular velocities to the penetrator relative to the Mariner Mark II spacecraft (s/c) to initiate the spin-stabilized descent to the comet nucleus. Initial penetrator attitude and trajectory errors are induced by spin/eject phase errors that include spin/eject mechanism misalignment and tipoff rate errors. A simplified model was developed to determine the effect of such errors on penetrator attitude accuracy. Transverse and axial dynamics are assumed to be independent planar problems.

Figure 5.5-2 depicts the geometrical relationships for the transverse problem. The displacement of the penetrator center of mass (CM) relative to the spacecraft CM is denoted by ρ . The displacement of the system CM relative to the spacecraft CM is denoted by ρ_s . All 3 centers of mass are

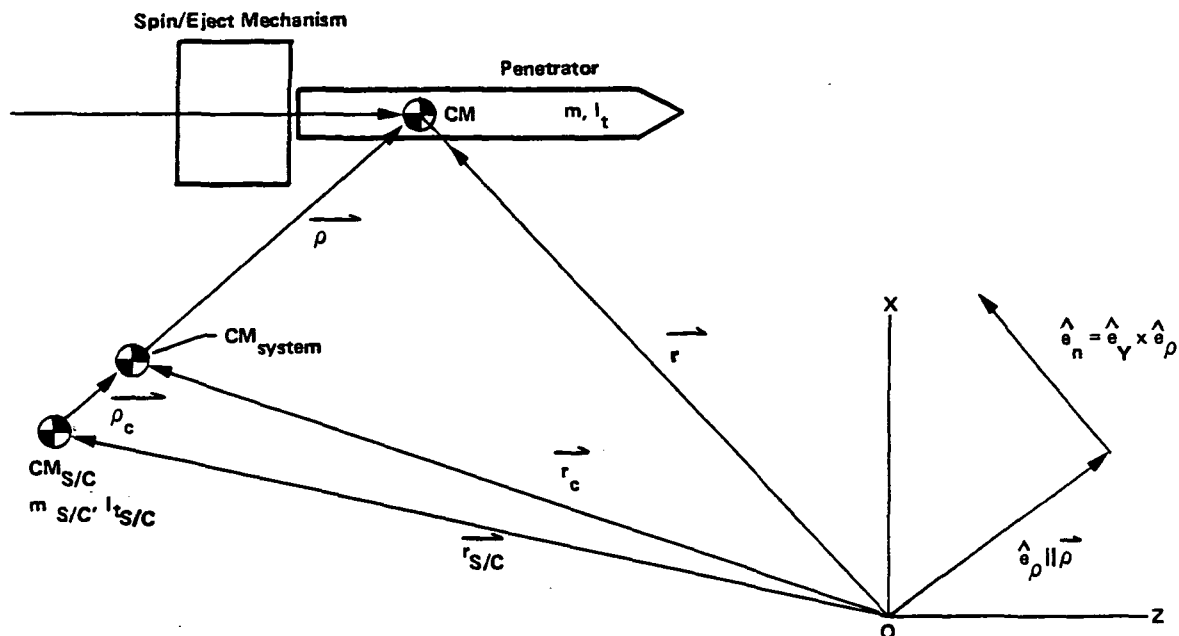


Figure 5.5-2 Spin/Eject Phase Geometry

displaced relative to an inertial frame centered at O by vectors \vec{r} , \vec{r}_c , and $\vec{r}_{s/c}$. It is convenient to select the inertial Z axis to be collinear with the ideal penetrator ejection direction. Inertial axis Y is perpendicular to the plane of the paper. Unit vector \hat{e}_ρ is parallel to $\vec{\rho}$, while unit vector \hat{e}_n is perpendicular to $\vec{\rho}$.

The basic momentum equations for a system of bodies were based on Reference 1. The total angular momentum of the penetrator and s/c relative to a uniformly moving system center of mass is given by:

$$\vec{H}_c = \vec{H}_{s/c} + \vec{H} + \vec{\rho}_c \times m_{s/c} \dot{\vec{\rho}}_c + (\vec{\rho} - \vec{\rho}_c) \times m (\dot{\vec{\rho}} - \dot{\vec{\rho}}_c) \quad (5.5-1)$$

where $\vec{H}_{s/c}$ and \vec{H} are the angular momenta of the s/c and penetrator, respectively, about their own centers of mass, $m_{s/c}$ and m are their masses, and $\dot{\vec{\rho}}_c$ and $\dot{\vec{\rho}}$ are inertial rates of change of previously defined displacement vectors.

-
1. Greenwood, D.T., "Principles of Dynamics", Prentice-Hall, Inc., Englewood Cliffs, New Jersey, 1965.

The total linear momentum is given by:

$$\vec{P}_c = (\dot{\vec{\rho}} - \dot{\vec{\rho}}_0) m + (-\dot{\vec{\rho}}_0) m_{s/c} \quad (5.5-2)$$

The spin/eject event is assumed to be impulsive with a relative ejection velocity of v_r (positive along Z) and a relative tipoff rate ω_r (positive along Y). The s/c may have an initial inertial rate ω_{s/c_0} . Both linear and angular momenta are conserved across the spin/eject event, so that the post-spin/eject states of penetrator and s/c can be determined by evaluating both equations (5.5-1) and (5.5-2) across the impulsive spin/eject event.

Pre-spin/eject conditions are denoted by ρ_0 , ρ_{c_0} , ω_{s/c_0} , etc., whereas, post-spin/eject conditions are denoted by ρ , ρ_c , $\omega_{s/c}$, etc.

Evaluation of equations (5.5-1) and (5.5-2) immediately before the impulse yields the following:

$$H_c = I_{s/c} \omega_{s/c_0} + I_r \omega_{s/c_0} + m_{s/c} \omega_{s/c_0} \rho_{c_0}^2 + m \omega_{s/c_0} (\rho_0 - \rho_{c_0})^2 \quad (5.5-3)$$

$$P_{c_x} = m \omega_{s/c_0} (\rho_0 - \rho_{c_0}) \hat{e}_n \cdot \hat{e}_x - m_{s/c} \omega_{s/c_0} \rho_{c_0} \hat{e}_n \cdot \hat{e}_x \quad (5.5-4)$$

$$P_{c_z} = m \omega_{s/c_0} (\rho_0 - \rho_{c_0}) \hat{e}_n \cdot \hat{e}_z - m_{s/c} \omega_{s/c_0} \rho_{c_0} \hat{e}_n \cdot \hat{e}_z \quad (5.5-5)$$

where $I_{s/c}$ and I_r are the transverse moments of inertia of the s/c and penetrator, respectively. The following equations are required for the evaluation of equations (5.5-1) and (5.5-2):

$$\dot{\vec{\rho}}_c = \omega_{s/c_0} \rho_{c_0} \hat{e}_n \quad (5.5-6)$$

$$\dot{\vec{\rho}} = \omega_{s/c_0} \rho_0 \hat{e}_n \quad (5.5-7)$$

Evaluation of equations (5.5-1) and (5.5-2) immediately after the impulse yields the following:

$$H_c = I_{s/c} \omega_{s/c} + I_r (\omega_{s/c} + \omega_r) + m_{s/c} \left[-\rho_{c_0} v_{s/c_x} (\hat{e}_n \cdot \hat{e}_z) + \rho_{c_0} v_{s/c_z} (\hat{e}_n \cdot \hat{e}_x) + \omega_{s/c} \rho_{c_0}^2 \right] + m \left[-(\rho_0 - \rho_{c_0}) (v_r + v_{s/c_z}) (\hat{e}_n \cdot \hat{e}_x) + (\rho_0 - \rho_{c_0}) v_{s/c_x} (\hat{e}_n \cdot \hat{e}_z) + \omega_{s/c} (\rho_0 - \rho_{c_0})^2 \right] \quad (5.5-8)$$

$$P_{c_x} = m \omega_{s/c} (\rho_0 - \rho_{c_0}) \hat{e}_n \cdot \hat{e}_x + m v_{s/c_x} + m_{s/c} v_{s/c_x} - m_{s/c} \omega_{s/c} \rho_{c_0} \hat{e}_n \cdot \hat{e}_x \quad (5.5-9)$$

$$P_{c_z} = m (v_r + v_{s/c_z}) + m \omega_{s/c} (\rho_0 - \rho_{c_0}) \hat{e}_n \cdot \hat{e}_z + m_{s/c} v_{s/c_z} - m_{s/c} \omega_{s/c} \rho_{c_0} \hat{e}_n \cdot \hat{e}_z \quad (5.5-10)$$

where it has been assumed that the spin/eject mechanism adds the initial s/c rate to the penetrator at the moment of ejection, i.e., the inertial tipoff rate of the penetrator is given by

$$\omega_T = \omega_{s/c} + \omega_{T_r} \quad (5.5-11)$$

The following equations are required for the evaluation of equations (5.5-1) and (5.5-2):

$$\dot{\rho}_c = - (v_{s/c_x} \hat{e}_x + v_{s/c_z} \hat{e}_z) + \omega_{s/c} \rho_0 \hat{e}_n \quad (5.5-12)$$

$$\dot{\rho} = v_r \hat{e}_z + \omega_{s/c} \rho_0 \hat{e}_n \quad (5.5-13)$$

where v_{s/c_x} and v_{s/c_z} are the inertial translational velocity components of the s/c after spin/eject.

Conservation of momentum across the impulse permits equations (5.5-3), (5.5-4), and (5.5-5) to be equated to equations (5.5-8), (5.5-9), and (5.5-10), respectively. Since the resulting equations are relatively intractable, the following reasonable simplifying assumptions were made:

1. $m \ll m_{s/c}$ ($m \sim 20\text{kg}$, $m_{s/c} \sim 1000\text{ kg}$)
2. $\rho_0 \dot{=} 0$, because of the preceding assumption
3. $\vec{\rho}$ perpendicular to ideal ejection direction

The simplified conservation of momentum equations are then used to define the states of both s/c and penetrator immediately after the impulse.

The transverse state of the s/c is defined by the following equations:

$$\omega_{s/c} = \omega_{s/c_0} + \frac{mv_r \rho - I_i \omega_{T_r}}{I_{s/c} + I_i + m\rho^2} \quad (5.5-14)$$

$$v_{s/c_x} = 0 \quad (5.5-15)$$

$$v_{s/c_z} = \frac{m}{m_{s/c}} \left[-v_r + \rho \left(\frac{mv_r \rho - I_i \omega_{T_r}}{I_{s/c} + I_i + m\rho^2} \right) \right] \quad (5.5-16)$$

$$\Delta H_{t_{s/c}} = I_{t_{s/c}} \left(\frac{mv_t \rho - I_t \omega_{t_r}}{I_{t_{s/c}} + I_t + m\rho^2} \right) \quad (5.5-17)$$

$$\Delta P_{s/c_z} = -mv_t + m\rho \left(\frac{mv_t \rho - I_t \omega_{t_r}}{I_{t_{s/c}} + I_t + m\rho^2} \right) \quad (5.5-18)$$

where subscript t has been appended to $\omega_{s/c}$ to indicate that it refers to the transverse, rather than axial, angular velocity of the s/c. Equations (5.5-17) and (5.5-18) define the transverse angular momentum and linear momentum that is imparted to the s/c as a result of the spin/eject event.

The transverse state of the penetrator is defined by the following equations:

$$\begin{aligned} v^{\theta} &= v_z \\ &= v_r - \rho \left(\omega_{s/c_0} + \frac{mv_t \rho - I_t \omega_{t_r}}{I_{t_{s/c}} + I_t + m\rho^2} \right) + v_{s/c_z} \end{aligned} \quad (5.5-19)$$

$$\omega_T = \omega_{t_r} + \omega_{s/c_0} + \frac{mv_t \rho - I_t \omega_{t_r}}{I_{t_{s/c}} + I_t + m\rho^2} \quad (5.5-20)$$

where v^{θ} is the inertial ejection velocity and ω_r is the inertial tipoff rate. Because of assumption number 3, v^{θ} is collinear with the ideal ejection direction and penetrator axis of symmetry.

The axial dynamics of the impulsive spin/eject are much simpler than the transverse dynamics. Only the final results will be summarized below:

$$\omega_{s/c} = \omega_{s/c_0} - \omega_{s_r} \left(\frac{I_a}{I_{s/c} + I_a} \right) \quad (5.5-21)$$

$$\Delta H_{s/c} = - \left(\frac{I_{s/c} \cdot I_a}{I_{s/c} + I_a} \right) \omega_{s_r} \quad (5.5-22)$$

$$\omega_s = \omega_{s/c_0} + \omega_{s_r} \left(\frac{I_{s/c}}{I_{s/c} + I_a} \right) \quad (5.5-23)$$

where subscript a indicates axial parameters, and ω_s and ω_{s_r} are the inertial and relative spin angular velocities of the penetrator, respectively.

It remains to determine precession rate, nutation angle, angle of attack, and related parameters for the penetrator immediately after spin/eject. The inertial angular velocity and momentum are given by

$$\vec{\omega} = \omega_s \hat{e}_s + \omega_T \hat{e}_T \quad (5.5-24)$$

$$\vec{H} = I_s \omega_s \hat{e}_s + I_T \omega_T \hat{e}_T \quad (5.5-25)$$

where \hat{e}_s and \hat{e}_T are orthogonal axial and transverse unit vectors. Then angular momentum magnitude and kinetic energy are given by:

$$H^{(0)} = \left[I_s^2 \omega_s^2 + I_T^2 \omega_T^2 \right]^{1/2} \quad (5.5-26)$$

$$T^{(0)} = 1/2 \left[I_s \omega_s^2 + I_T \omega_T^2 \right] \quad (5.5-27)$$

Nutation angle is defined by equation (5.5-44) in the coast phase analysis section:

$$\cos \beta^{(0)} = \frac{I_s \Omega^{(0)}}{H^{(0)}} \quad (5.5-28)$$

where relative spin rate $\Omega^{(0)}$ is given by

$$\Omega^{(0)} = \omega_s \quad (5.5-29)$$

Then

$$\tan \beta^{(0)} = \frac{[H^{(0)2} - I_s^2 \omega_s^2]^{1/2}}{I_s \omega_s} = \frac{I_T \omega_T}{I_s \omega_s} \quad (5.5-30)$$

or,

$$\beta^{(0)} = \tan^{-1} \left[\left(\frac{I_T}{I_s} \right) \left(\frac{\omega_T}{\omega_s} \right) \right] \quad (5.5-31)$$

Thus, the initial nutation angle only depends on the ratio of transverse and axial moments of inertia and the ratio of tipoff and spin rates. Precession rate is given by

$$\dot{\psi}^{(0)} = - \frac{H^{(0)}}{I_T} \quad (5.5-32)$$

Since $v^{(0)}$ is collinear with penetrator axis of symmetry, angle $\nu^{(0)}$ between inertial velocity and angular momentum vectors is given by

$$\nu^{(0)} = \beta^{(0)} \quad (5.5-33)$$

The maximum angle of attack occurs when the axis of symmetry and the inertial velocity and angular momentum vectors are all coplanar. Thus,

$$\alpha_{max}^{(0)} = 2\beta^{(0)} \quad (5.5-34)$$

Finally, the initial flight path angle (error) is given by

$$\gamma^{(0)} = \theta_{s/c_0} + \theta_s \quad (5.5-35)$$

where θ_{s/c_0} is the initial s/c attitude and θ_s is the spin/eject mechanism misalignment error.

5.5.2 Coast Phases

During the coast phases no external torques are acting on the penetrator, so that the classical torque-free solutions for an axisymmetric body can be used directly. However, internal energy dissipation will cause nutation angle β to increase since the penetrator is a prolate spinner ($I_z > I_x$). Internal energy dissipation results from structural damping and friction due to relative motion of internal parts. Reference 2 describes the difficulties in analytically predicting such effects, and summarizes some of the techniques that may be used. The equations presented below do not include predictions of internal energy dissipation. Rather, they define the nutation angle growth across a coast phase for a given decrease in penetrator kinetic energy. Thus, they can only be used to determine the amount of energy that may be dissipated so that the nutation angle does not exceed a specified tolerance.

The remainder of this section will be divided into 3 parts. First, the equations that define the state of the penetrator at the end of the pre-delta-v coast will be derived. Second, the interface equations that relate the penetrator state at the end of the pre-delta-v coast to the state at the start of the delta-v phase (Section 5.5.3) will be presented. Finally, the equations that define the penetrator state at the end of the post-delta-v coast, i.e., at impact, will be derived.

Internal energy dissipation is likely to be a concern only over the pre-delta-v phase since its duration is much greater than the post-delta-v

-
2. Likins, P.W., "Effects of Energy Dissipation on the Free Body Motions of Spacecraft", Technical Report No. 32-860, Jet Propulsion Laboratory, Pasadena, California, July 1, 1966.

duration. The duration of the pre-delta-v phase is given by

$$t^{(1)} = D^{(1)} / v^{(0)} \quad (5.5-36)$$

where $D^{(1)}$ is the penetrator distance from the s/c at the start of the delta-v phase. If an average internal energy dissipation rate $\dot{T}_{pre-\Delta v}$ is known, then the kinetic energy at the end of the coast is given by

$$T^{(1)} = T^{(0)} - \dot{T}_{pre-\Delta v} \cdot t^{(1)} \quad (5.5-37)$$

where $\dot{T}_{pre-\Delta v}$ is assumed to be positive.

Because trajectory effects have been neglected, we can write

$$v^{(1)} = v^{(0)} \quad (5.5-38)$$

$$\gamma^{(1)} = \gamma^{(0)} \quad (5.5-39)$$

$$v^{(1)} = v^{(0)} = \beta^{(0)} \quad (5.5-40)$$

The classical torque-free solutions for an axisymmetric body given in Reference 1 can be used to obtain the following equations for angular momentum, total spin rate, precession rate, and nutation angle, respectively:

$$H^{(1)} = H^{(0)} \quad (5.5-41)$$

$$\Omega^{(1)} = \left[\frac{2 I_t T^{(1)} - H^{(1)2}}{I_a (I_t - I_a)} \right]^{1/2} \quad (5.5-42)$$

$$\dot{\psi}^{(1)} = \dot{\psi}^{(0)} \quad (5.5-43)$$

$$\beta^{(1)} = \cos^{-1} \left(\frac{I_a \Omega^{(1)}}{H^{(1)}} \right) \quad (5.5-44)$$

The maximum angle of attack occurs when the spin axis lies in the plane defined by the angular momentum and velocity vectors. Thus,

$$\alpha_{max}^{(1)} = \beta^{(0)} + \beta^{(1)} \quad (5.5-45)$$

We next turn to the derivation of the interface equations that define the relationships between the penetrator states at the end of the pre-delta-v phase and the start of the delta-v phase. Figure 5.5-3 depicts the relevant geometry at the start of the delta-v phase. The inertial XYZ frame is defined so that Z is collinear with the penetrator angular momentum $\vec{H}^{(1)}$ at the

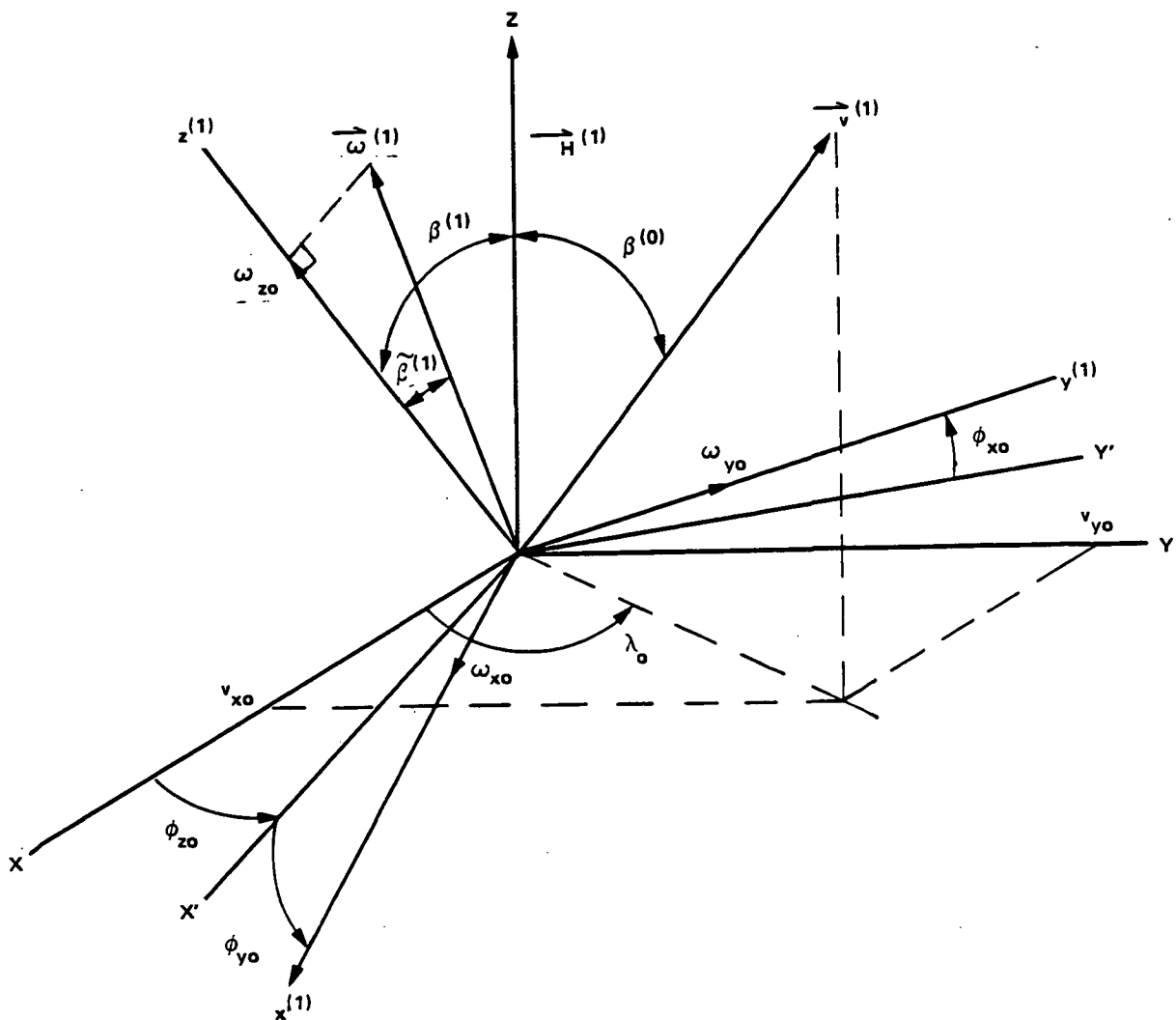


Figure 5.5-3 Interface Geometry between End of Coast Phase and Start of ΔV Phase

start of the delta-v phase, and X lies in the plane defined by Z and z'' . Penetrator body axes x'' , y'' , and z'' are oriented relative to the inertial frame by Euler angles ϕ_{x_0} , ϕ_{y_0} , and ϕ_{z_0} (see Section 5.5.3). Since the spin/eject phase solutions (Section 5.5.1) were based on planar assumptions, these Euler angles cannot be completely defined. A full-dimensional solution of the spin/eject phase equations would permit these Euler angles to be predicted, in theory, but coast duration and internal energy dissipation uncertainties would make such predictions highly unreliable. It was therefore decided to evaluate the delta-v phase solutions (Section 5.5.3) over the entire range of possible penetrator states at the start of the delta-v phase. These states are not completely arbitrary. The assumption that angle of attack dispersions are insensitive to trajectory effects (Section 5.5.1) entails that the angle between the angular momentum and velocity vectors is still β^0 at the start of delta-v. The torque-free

solutions for an axisymmetric body entail that the axis of symmetry $z^{(n)}$ is constrained to move on a cone centered about the angular momentum vector with a semi-vertex angle $\beta^{(n)}$. Penetrator angular velocity $\omega^{(n)}$ is constrained to lie in the plane defined by $z^{(n)}$ and $H^{(n)}$, and oriented relative to $z^{(n)}$ with a fixed angle $\tilde{\beta}^{(n)}$. This angular velocity has body frame components ω_{x_o} , ω_{y_o} , and ω_{z_o} . Velocity $v^{(n)}$ has inertial frame components of v_{x_o} , v_{y_o} , and v_{z_o} , and is oriented relative to the inertial frame by angles λ_o and $\beta^{(n)}$, where λ_o is undefined for the same reasons that Euler angles ϕ_{x_o} , ϕ_{y_o} , and ϕ_{z_o} were not completely defined.

Reference to Figure 5.5-3 shows that axis of symmetry $z^{(n)}$ can be expressed in both body and inertial frames as follows:

$$z^{(n)} = \begin{bmatrix} \sin \beta^{(n)} \\ 0 \\ \cos \beta^{(n)} \end{bmatrix}_{x,y,z} = \begin{bmatrix} 0 \\ 0 \\ 1 \end{bmatrix}_{x,y,z} \quad (5.5-46)$$

Body and inertial frame components are related via coordinate transformation T_{IB} given by equation (5.5-89). This entails the following dependency of ϕ_{x_o} and ϕ_{y_o} on the undefined ϕ_{z_o} :

$$\phi_{x_o} = \sin \phi_{z_o} \tan \beta^{(n)} \quad (5.5-47)$$

$$\phi_{y_o} = \cos \phi_{z_o} \tan \beta^{(n)} \quad (5.5-48)$$

From the same figure it can be seen that

$$v_{x_o} = v^{(n)} \sin \beta^{(n)} \cos \lambda_o \quad (5.5-49)$$

$$v_{y_o} = v^{(n)} \sin \beta^{(n)} \sin \lambda_o \quad (5.5-50)$$

$$v_{z_o} = v^{(n)} \cos \beta^{(n)} \quad (5.5-51)$$

The classical torque-free solutions in Reference 1 permit angle $\tilde{\beta}^{(n)}$ and angular velocity magnitude $\omega^{(n)}$ to be expressed as follows:

$$\tilde{\beta}^{(n)} = \tan^{-1} \left(\frac{I_a}{I_t} \tan \beta^{(n)} \right) \quad (5.5-52)$$

$$\omega^{(n)} = \frac{\Omega^{(n)}}{\cos \tilde{\beta}^{(n)}} \quad (5.5-53)$$

Then, based on Figure 5.5-3, we can write:

$$\vec{\omega}^{(n)} = \begin{bmatrix} \omega^{(n)} \sin (\beta^{(n)} - \tilde{\beta}^{(n)}) \\ 0 \\ \omega^{(n)} \cos (\beta^{(n)} - \tilde{\beta}^{(n)}) \end{bmatrix}_{x,y,z} \quad (5.5-54)$$

These inertial frame components can be related to the body frame components using equation (5.5-89):

$$\omega_{x_0} = \omega^{(1)} \cos \phi_{x_0} \sin (\beta^{(1)} - \tilde{\beta}^{(1)}) - \omega^{(1)} \phi_{y_0} \cos (\beta^{(1)} - \tilde{\beta}^{(1)}) \quad (5.5-55)$$

$$\omega_{y_0} = -\omega^{(1)} \sin \phi_{x_0} \sin (\beta^{(1)} - \tilde{\beta}^{(1)}) + \omega^{(1)} \phi_{x_0} \cos (\beta^{(1)} - \tilde{\beta}^{(1)}) \quad (5.5-56)$$

$$\omega_{z_0} = \Omega^{(1)} \quad (5.5-57)$$

The subsequent delta-v phase solutions also require an initial value for Euler rate $\dot{\phi}_0$. This is readily obtained by evaluating equation (5.5-74) at the start of the delta-v phase:

$$\dot{\phi}_0 = \omega_{y_0} - \omega_{x_0} \phi_{x_0} \quad (5.5-58)$$

Thus, the interface between the penetrator state at the end of the pre-delta-v phase and the start of the delta-v phase has been defined. These interface equations, along with the delta-v phase equations presented in Section 5.5.3, must be evaluated over all possible initial values of angles ϕ_{x_0} and λ_0 .

It remains to present the equations that define the penetrator state at the end of the post-delta-v coast, i.e., at impact. These are completely analogous to the pre-delta-v coast equations. Time at the start of the post-delta-v coast is given by

$$t^{(2)} = t^{(1)} + \Delta t \quad (5.5-59)$$

where Δt is the duration of the delta-v phase. Time of penetrator impact is given by

$$t^{(3)} = t^{(2)} + \frac{D^{(3)} - D^{(2)}}{v^{(2)}} \quad (5.5-60)$$

where $D^{(2)}$ and $D^{(3)}$ are the penetrator distances at the end of the delta-v phase and at impact, respectively.

The remaining equations require no further description:

$$T^{(3)} = T^{(2)} - \dot{T}_{\text{post-}\Delta v} \cdot (t^{(3)} - t^{(2)}) \quad (5.5-61)$$

$$v^{(3)} = v^{(2)} \quad (5.5-62)$$

$$\gamma^{(3)} = \gamma^{(2)} \quad (5.5-63)$$

$$v^{(3)} = v^{(2)} \quad (5.5-64)$$

$$H^{(3)} = H^{(2)} \quad (5.5-65)$$

$$\Omega^{(3)} = \left[\frac{2 I_t T^{(3)} - H^{(3)2}}{I_t (I_t - I_d)} \right]^{1/2} \quad (5.5-66)$$

$$\dot{\psi}^{(3)} = \dot{\psi}^{(2)} \quad (5.5-67)$$

$$\beta^{(3)} = \cos^{-1} \left(\frac{I_d \Omega^{(3)}}{H^{(3)}} \right) \quad (5.5-68)$$

$$\alpha_{max}^{(3)} = v^{(3)} + \beta^{(3)} \quad (5.5-69)$$

5.5.3 Delta-v Phase

The purpose of the delta-v phase is to accelerate the penetrator so that comet nucleus impact occurs with the proper velocity and with sufficiently small angle of attack. Because the preceding spin/eject and coast phases may induce non-zero nutation angle and transverse angular rates, it is important to develop delta-v phase solutions that acknowledge non-zero transverse conditions at delta-v start. The analysis presented below was guided by related analyses that appear in References 3, 4, and 5.

The penetrator is assumed to be axisymmetric with constant mass properties across the delta-v phase. The thrust force F is assumed constant, but has a misalignment ϵ and a lateral offset l relative to the penetrator z axis of symmetry. Because we have assumed the penetrator to be axisymmetric, we can define ϵ and l as shown in Figure 5.5-4 to produce an external torque only about the x body axis without any loss of generality.

-
3. Armstrong, R.S., "Errors Associated With Spinning-Up and Thrusting Symmetric Rigid Bodies", Technical Report No. 32-644, Jet Propulsion Laboratory, Pasadena, California, February 15, 1965.
 4. Longuski, J.M., "Solution of Euler's Equations of Motion and Eulerian Angles for Near Symmetric Rigid Bodies Subject to Constant Moments", AIAA Paper 80-1642, August 1980.
 5. Hintz, G.R. and Longuski, J.M., "Error Analyses for the Delivery of a Spinning Probe to Jupiter", Journal of Guidance, Control, and Dynamics, Vol. 8, May-June 1985, pp. 384-390.

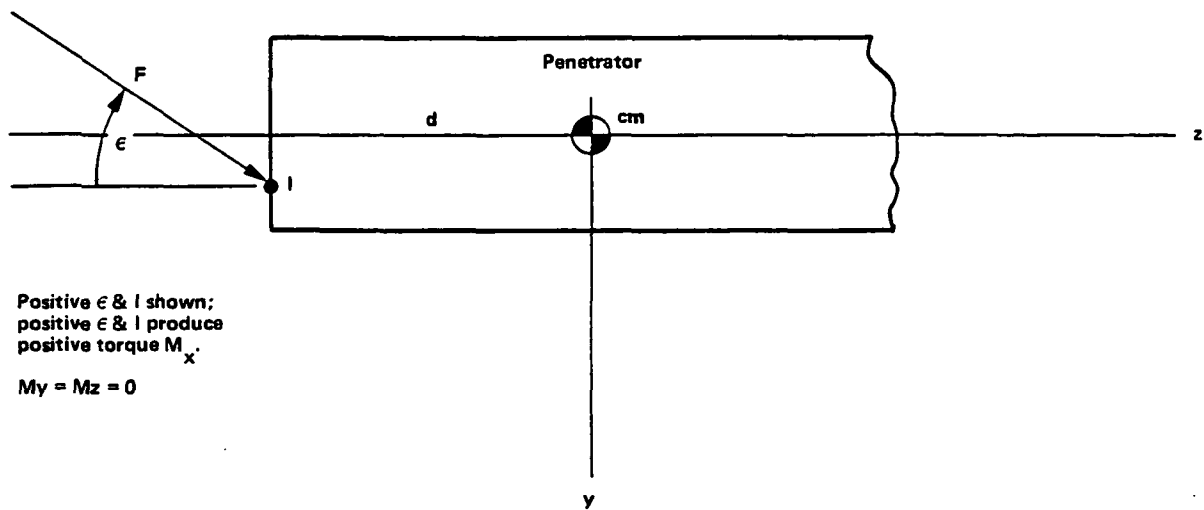


Figure 5.5-4 Thrust Misalignment and Offset

The xyz body frame is oriented relative to the XYZ inertial frame via Euler angles ϕ_x , ϕ_y , and ϕ_z with a 3-1-2 Euler sequence as shown in Figure 5.5-5. It is convenient to select the inertial Z axis to be collinear with the penetrator angular momentum \vec{H}^m at the start of the delta-v. With the assumptions stated previously, Euler's equations of motion can be written as follows:

$$I_t \dot{\omega}_x + (I_z - I_t) \omega_y \omega_z = M_x \quad (5.5-70)$$

$$I_t \dot{\omega}_y + (I_t - I_z) \omega_x \omega_z = 0 \quad (5.5-71)$$

$$\dot{\omega}_z = 0 \quad (5.5-72)$$

where ω_x , ω_y , and ω_z are inertial body angular rates, I_t is the axial moment of inertia, I_z is the transverse moment of inertia, and M_x is the torque due to the misaligned and offset thrust vector. Note that equations (5.5-70) and (5.5-71) are linear since equation (5.5-72) implies that ω_z is constant.

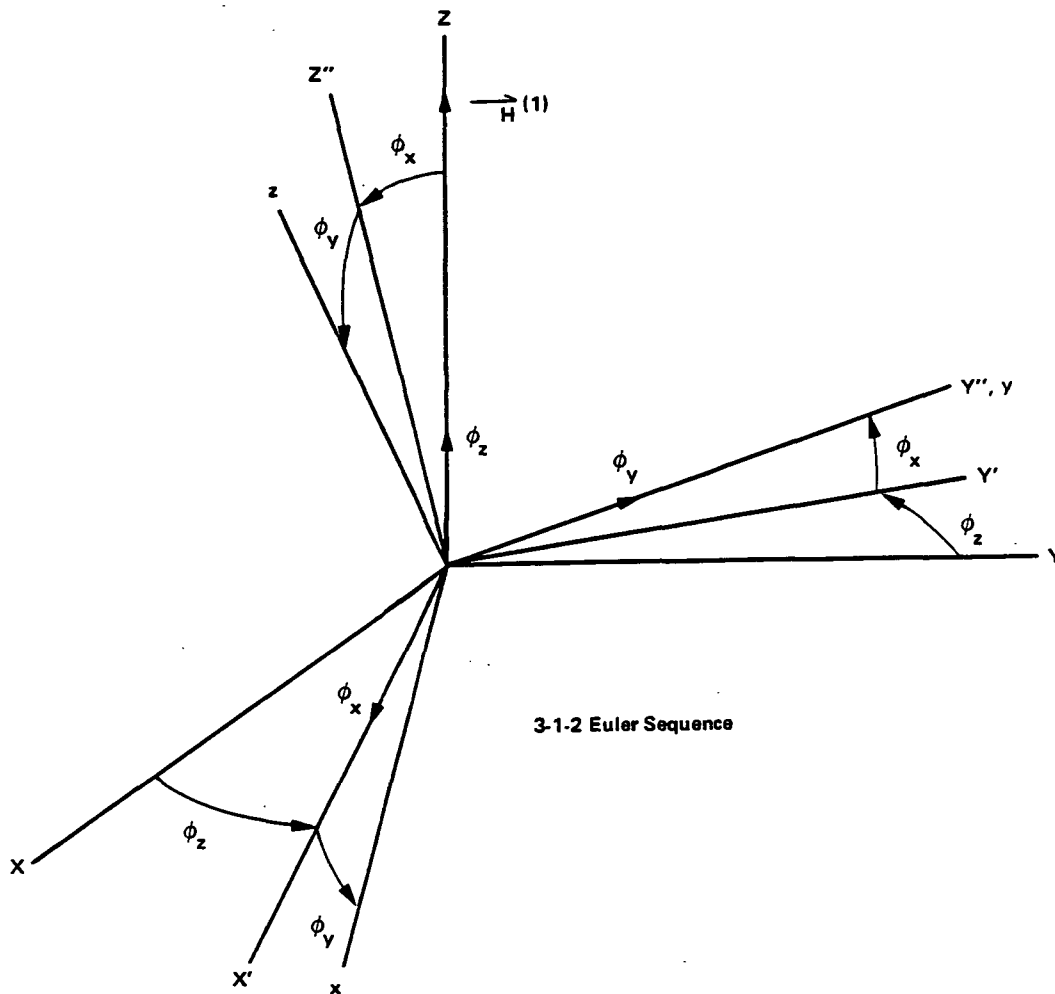


Figure 5.5-5 ΔV Phase Euler Angles

Referring to Figure 5.5-5, it is reasonable to assume Euler angles ϕ_x and ϕ_y are small angles. Following Longuski in Reference 4, we will also assume that the product $\phi_x \omega_x$ is negligibly small relative to ω_x , so that the linearized kinematic equations of motion are given by:

$$\dot{\phi}_x = \omega_x + \phi_y \omega_z \quad (5.5-73)$$

$$\dot{\phi}_y = \omega_y - \phi_x \omega_z \quad (5.5-74)$$

$$\dot{\phi}_z = \omega_z \quad (5.5-75)$$

The translational equations of motion are written in inertial frame components:

$$\dot{v}_x = F_x/m \quad (5.5-76)$$

$$\dot{v}_y = F_y/m \quad (5.5-77)$$

$$\dot{v}_z = F_z/m \quad (5.5-78)$$

where v_x , v_y and v_z are inertial velocity components; F_x , F_y and F_z are inertial thrust components; and m is mass.

The solution of the previous 9 equations of motion for arbitrary initial conditions ω_{x_0} , ω_{y_0} , ω_{z_0} , ϕ_{x_0} , ϕ_{y_0} , ϕ_{z_0} , v_{x_0} , v_{y_0} and v_{z_0} will be outlined below.

Differentiating equation (5.5-71), using equation (5.5-70) to eliminate $\dot{\omega}_x$, and substituting the solution of equation (5.5-72) yields the following equation:

$$\ddot{\omega}_x + \omega_n^2 \omega_x = - \frac{\omega_n M_x}{I_t} \quad (5.5-79)$$

where

$$\omega_n = \left(\frac{I_t - I_o}{I_t} \right) \omega_{z_0} \quad (5.5-80)$$

Equation (5.5-79) can be readily solved for ω_x , and can then be used in equation (5.5-71) to obtain the solution for ω_x .

The complete solution of Euler's equations of motion can then be written as follows:

$$\omega_x = \omega_{x_0} \cos \omega_n t + \omega_{y_0} \sin \omega_n t + \frac{M_x}{\omega_n I_t} \sin \omega_n t \quad (5.5-81)$$

$$\omega_y = - \omega_{x_0} \sin \omega_n t + \omega_{y_0} \cos \omega_n t + \frac{M_x}{\omega_n I_t} (\cos \omega_n t - 1) \quad (5.5-82)$$

$$\omega_z = \omega_{z_0} \quad (5.5-83)$$

We now turn our attention to the solution of the kinematical equations of motion. Differentiate equation (5.5-74) and eliminate $\dot{\phi}_x$ with equation (5.5-73) to obtain:

$$\ddot{\phi}_y + \omega_{z_0}^2 \phi_y = \dot{\omega}_y - \omega_{z_0} \omega_x \quad (5.5-84)$$

Since Euler's equations have already been solved, the right-hand side of this equation is a known function of time. Its solution for $\dot{\phi}_x$ can be obtained using Laplace transform number 72 in Reference 6, and then used in Equation (5.5-74) to obtain the solution for ϕ_x :

$$\phi_x = \frac{\omega_z - \dot{\phi}_x}{\omega_z} \quad (5.5-85)$$

The complete solution of the kinematical equations of motion can then be written as follows:

$$\phi_x = \bar{A} + \bar{B} \sin \omega_x t + \bar{C} \cos \omega_x t + \bar{D} \sin \omega_z t + \bar{E} \cos \omega_z t \quad (5.5-86)$$

$$\phi_y = \bar{F} \cos \omega_x t + \bar{G} \sin \omega_x t + \bar{D} \cos \omega_z t - \bar{E} \sin \omega_z t \quad (5.5-87)$$

$$\phi_z = \omega_z t + \phi_{z_0} \quad (5.5-88)$$

where expressions for constants \bar{A} , \bar{B} , ..., \bar{G} are given in Appendix B.

It remains to solve the translational equations of motion. Since these are most conveniently solved in inertial components, the coordinate transformation from the body frame to the inertial frame will be required. It will be denoted by T_{ib} , and is given by:

$$T_{ib} = \begin{bmatrix} \cos \phi_z & -\sin \phi_z & \phi_y \cos \phi_z + \phi_x \sin \phi_z \\ \sin \phi_z & \cos \phi_z & \phi_y \sin \phi_z - \phi_x \cos \phi_z \\ -\phi_y & \phi_x & 1 \end{bmatrix} \quad (5.5-89)$$

where the assumption of small ϕ_x and ϕ_y has been used.

The inertial thrust components F_x , F_y , and F_z can be related to the constant body frame thrust components F_x , F_y , and F_z using equation (5.5-89):

$$F_x = -F_y \sin \phi_z + F_z (\phi_y \cos \phi_z + \phi_x \sin \phi_z) \quad (5.5-90)$$

$$F_y = F_y \cos \phi_z + F_z (\phi_y \sin \phi_z - \phi_x \cos \phi_z) \quad (5.5-91)$$

$$F_z = F_z \quad (5.5-92)$$

6. Levy, E.C., "Table of Laplace Transforms", Report No. SM-14745, Douglas Aircraft Co., July 1951.

where body frame component F_z is zero by definition (see Figure 5.5-4), and where product $F\phi_x$ has been assumed negligibly small relative to F_z . Reference to Figure 5.5-4 also shows that

$$F_y = F \sin \epsilon \quad (5.5-93)$$

$$F_z = F \cos \epsilon \quad (5.5-94)$$

$$M_x = F_y d + F_z l \quad (5.5-95)$$

Translational accelerations a_y and a_z are defined by

$$a_y = F_y/m \quad (5.5-96)$$

$$a_z = F_z/m \quad (5.5-97)$$

Substitution of equations (5.5-90), (5.5-91), and (5.5-92) into equations (5.5-76), (5.5-77), and (5.5-78), respectively, and replacing body frame thrust components with acceleration components, yields:

$$\dot{v}_x = -a_y \sin \phi_z + a_z (\phi_y \cos \phi_z + \phi_x \sin \phi_z) \quad (5.5-98)$$

$$\dot{v}_y = a_y \cos \phi_z + a_z (\phi_x \sin \phi_z - \phi_y \cos \phi_z) \quad (5.5-99)$$

$$\dot{v}_z = a_z \quad (5.5-100)$$

Since the kinematical equations of motion have already been solved, the right-hand side of the previous equations are known functions of time. Thus, these equations can be directly integrated to yield the following solutions:

$$v_x = v_{x_0} - a_y (bI_1 + aI_2) + a_z \left[(\bar{E}a + \bar{D}b)t + (\bar{F}b + \bar{C}a)I_3 + (\bar{B}b - \bar{G}a)I_4 + (\bar{G}b + \bar{B}a)I_5 + (\bar{C}b - \bar{F}a)I_6 + \bar{A}bI_1 + \bar{A}aI_2 \right] \quad (5.5-101)$$

$$v_y = v_{y_0} + a_y (bI_2 - aI_1) + a_z \left[(\bar{D}a - \bar{E}b)t + (\bar{F}a - \bar{C}b)I_3 + (\bar{G}b + \bar{B}a)I_4 + (\bar{G}a - \bar{B}b)I_5 + (\bar{F}b + \bar{C}a)I_6 + \bar{A}aI_1 - \bar{A}bI_2 \right] \quad (5.5-102)$$

$$v_z = v_{z_0} + a_z t \quad (5.5-103)$$

where

$$a = \sin \phi_{z_0} \quad (5.5-104)$$

$$b = \cos \phi_{z_0} \quad (5.5-105)$$

Expressions for constants \bar{A} , \bar{B} , ..., \bar{G} and integrals I_1 , I_2 , ..., I_6 are given in Appendix B.

All of the above equations must be evaluated at $t = \Delta t$, where Δt is the delta-v burn duration, to define the state of the penetrator at the end of the delta-v. Note that variable t in the previous equations (in this Section 5.5.3) is measured relative to the start of the delta-v phase.

The inertial velocity and angular momentum of the penetrator at the end of the delta-v burn can be expressed in inertial components as follows:

$$\vec{v}^{(i)} = (v_x, v_y, v_z)^T \quad (5.5-106)$$

$$v^{(i)} = [v_x^2 + v_y^2 + v_z^2]^{1/2} \quad (5.5-107)$$

$$\vec{H}^{(i)} = T_B (I_x \omega_x, I_y \omega_y, I_z \omega_z)^T \quad (5.5-108)$$

$$H^{(i)} = [I_x^2 (\omega_x^2 + \omega_y^2) + I_z^2 \omega_z^2]^{1/2} \quad (5.5-109)$$

Its kinetic energy, relative spin, and precession rate are given by:

$$T^{(i)} = 1/2 [I_x (\omega_x^2 + \omega_y^2) + I_z \omega_z^2] \quad (5.5-110)$$

$$\Omega^{(i)} = \omega_z \quad (5.5-111)$$

$$\dot{\psi}^{(i)} = -H^{(i)} / I_x \quad (5.5-112)$$

The orientation of the penetrator spin axis at the end of the delta-v burn is required so that the nutation angle and angle of attack can be determined. The unit vector \hat{z} aligned with the spin axis is given by

$$\hat{z}^{(i)} = \begin{bmatrix} \phi_x \cos \phi_z + \phi_y \sin \phi_z \\ \phi_x \sin \phi_z - \phi_y \cos \phi_z \\ 1 \end{bmatrix} \quad (5.5-113)$$

This vector must be normalized to preserve numerical accuracy. The nutation angle can then be determined from

$$\beta^{(2)} = \cos^{-1} \left[\frac{\hat{z}^{(2)} \cdot \vec{H}^{(2)}}{H^{(2)}} \right] \quad (5.5-114)$$

while the angle ν between the velocity and angular momentum vectors is given by

$$\nu^{(2)} = \cos^{-1} \left[\frac{\vec{v}^{(2)} \cdot \vec{H}^{(2)}}{\nu^{(2)} H^{(2)}} \right] \quad (5.5-115)$$

Since the maximum angle of attack results when vectors $\hat{z}^{(2)}$, $\vec{H}^{(2)}$ and $\vec{v}^{(2)}$ are coplanar, we can write

$$\alpha_{max}^{(2)} = \nu^{(2)} + \beta^{(2)} \quad (5.5-116)$$

The flight path angle change across the delta-v is given by

$$\Delta\gamma = \cos^{-1} \left[\frac{\vec{v}^{(1)} \cdot \vec{v}^{(2)}}{\nu^{(1)} \nu^{(2)}} \right] \quad (5.5-117)$$

so that

$$\gamma^{(2)} = \gamma^{(1)} + \Delta\gamma \quad (5.5-118)$$

Finally, the distance of the penetrator at the end of the delta-v burn has increased to

$$D^{(2)} = D^{(1)} + \frac{1}{2} a t^2 + v_{z_0} t \quad (5.5-119)$$

5.5.4 Results and Recommendations

Penetrator attitude performance predictions based on the solutions derived in earlier sections will be presented in this section for the current penetrator configuration. Numerical values of all relevant penetrator and Mariner Mark II parameters are shown in Table 5.5-1. The Mariner Mark II transverse angular momentum constraint of 14 N m s dictates that the relative ejection velocity of the penetrator not exceed 0.7 m/s. An ejection velocity of this magnitude easily satisfies the linear momentum constraint of 40 N s. Penetrator spin rate was selected as 116 rpm to synchronize the delta-v phase periodic attitude motions with the delta-v phase duration, and easily satisfies the Mariner Mark II angular momentum constraint of 14 N m s.

Table 5.5-1
Penetrator and Spacecraft Parameter Values

Penetrator Mass	$m = 20.26 \text{ kg}$
Penetrator Axial Moment of Inertia	$I_a = 0.38 \text{ kg-m}^2$
Penetrator Transverse Moment of Inertia	$I_t = 1.34 \text{ kg-m}^2$
Rocket Motor Thrust (Thiokol)	$F = 111.25 \text{ N}$
Rocket Motor Thrust Misalignment	$\epsilon = 0.3^\circ$
Distance from CM to Rocket Motor	$d = 0.276 \text{ m}$
Lateral CM Offset	$l = 0.0 \text{ m}$
Moment Arm of Spin/Eject Mechanism Relative to S/C CM	$\rho = 1.0 \text{ m}$
Relative Ejection Velocity	$v_r = 0.7 \text{ m/s}$
Relative Spin Rate	$\omega_{Sr} = 694^\circ/\text{s} \text{ (116 RPM)}$
Relative Tipoff Rate	$\omega_{Tr} = 3.0^\circ/\text{s}$
S/C Mass (Mariner Mark II)	$m_{S/C} = 1056.0 \text{ kg}$
S/C Axial Moment of Inertia	$I_{a \text{ S/C}} = 4446.0 \text{ kg-m}^2$
S/C Transverse Moment of Inertia	$I_{t \text{ S/C}} = 2036.0 \text{ kg-m}^2$
S/C Attitude Error	$\theta_{S/C}(0) = 0.0^\circ$
S/C Rate Error	$\dot{\omega}_{S/C}(0) = 0.0^\circ/\text{s}$
Spin/Eject Mechanism Misalignment	$\theta_e = 0.0^\circ$
Penetrator Rocket Motor Delta-V	$\Delta V = 40.0 \text{ m/s}$

The spin/eject phase attitude performance is completely described by Figure 5.5-6, which shows loci of constant nutation angle β^m as a function of penetrator transverse/axial moment of inertia ratio and inertial tipoff/spin rate ratio. Since the spin/eject reaction on the Mariner Mark II can increase penetrator tipoff rate by up to $0.40^\circ/\text{s}$, this effect needs to be acknowledged in the tipoff/spin rate ratio. Penetrator moments of inertia in Table 5.5-1 yield an inertia ratio of 3.5. The reaction tipoff rate of $0.40^\circ/\text{s}$ is added to the maximum relative tipoff rate of $3.00^\circ/\text{s}$ to yield an inertial tipoff rate of $3.40^\circ/\text{s}$, which, when divided by the penetrator spin rate of 116 rpm ($694^\circ/\text{s}$), produces a tipoff/spin rate ratio of 0.0049. As shown in Figure 5.5-6, these ratios will limit the maximum nutation angle β^m to about 1.00° .

Internal energy dissipation effects were assumed to be negligible over the long pre-delta-v coast, so that the nutation angle β^m at delta-v start is still essentially equal to β^m , while maximum penetrator angle of attack at delta-v start is twice the nutation angle, or 2.00° . Such non-zero attitude errors at delta-v start certainly influence penetrator attitude performance at the end of the delta-v. However, it will be helpful to digress in order to first describe penetrator attitude behavior for perfect initial conditions.

If we assume that the penetrator axis of symmetry is aligned with the angular momentum vector at the start of the delta-v, so that $\beta^m = 0$, then the general delta-v phase solutions in Section 5.5.3 can be greatly simplified and become amenable to a useful geometrical interpretation. In particular, the

solutions of the kinematical equations of motion given by equations (5.5-86) and (5.5-87) reduce to the following:

$$\phi_x = -\frac{M_x}{I_t \omega_n \omega_{z_0}} + \frac{M_x}{I_t \omega_n (\omega_{z_0} - \omega_n)} \cos \omega_n t - \frac{M_x}{I_t \omega_{z_0} (\omega_{z_0} - \omega_n)} \cos \omega_{z_0} t \quad (5.5-120)$$

$$\phi_y = -\frac{M_x}{I_t \omega_n (\omega_{z_0} - \omega_n)} \sin \omega_n t + \frac{M_x}{I_t \omega_{z_0} (\omega_{z_0} - \omega_n)} \sin \omega_{z_0} t \quad (5.5-121)$$

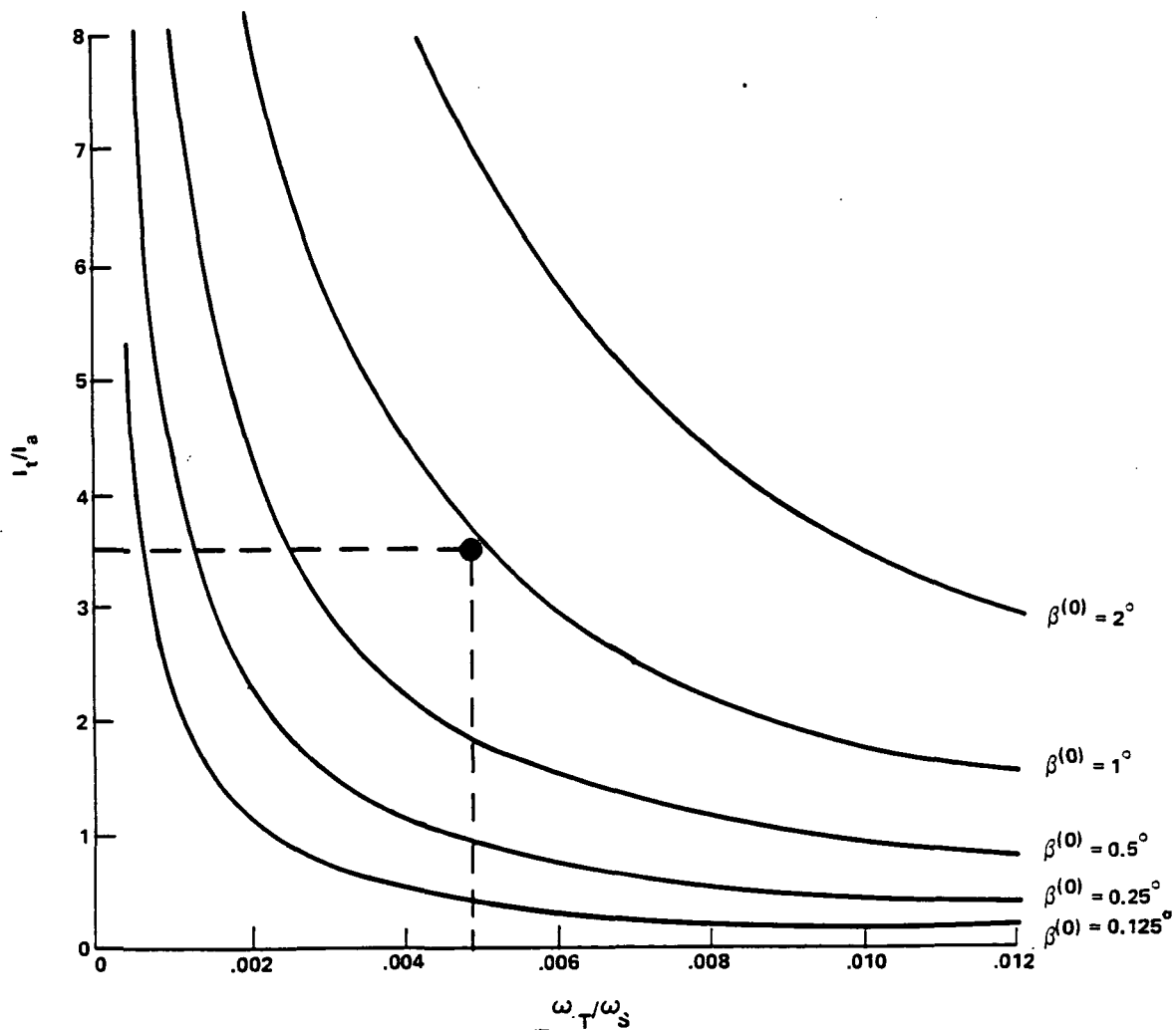


Figure 5.5-6 Spin/Eject Phase Nutation Angle

The components (X, Y) in the inertial XY plane (see Figure 5.5-5) of a unit vector aligned with the penetrator axis of symmetry are related to Euler angles ϕ_x and ϕ_y as follows:

$$X = \phi_y \cos \omega_{z_0} t + \phi_x \sin \omega_{z_0} t \quad (5.5-122)$$

$$Y = \phi_y \sin \omega_{z_0} t - \phi_x \cos \omega_{z_0} t \quad (5.5-123)$$

where X and Y have angular units.

Substitution of equations (5.5-120) and (5.5-121) into equations (5.5-122) and (5.5-123) yields the following:

$$X = R_1 \sin \omega_1 t - R_2 \sin \omega_2 t \quad (5.5-124)$$

$$Y = R_0 - R_1 \cos \omega_1 t + R_2 \cos \omega_2 t \quad (5.5-125)$$

where

$$R_0 = \frac{M_x}{I_s \omega_{z_0}^2} \quad (5.5-126)$$

$$R_1 = \frac{M_x I_t}{I_s (I_t - I_s) \omega_{z_0}^2} \quad (5.5-127)$$

$$R_2 = \frac{M_x}{(I_t - I_s) \omega_{z_0}^2} \quad (5.5-128)$$

and

$$\omega_1 = \omega_{z_0} - \omega_s = \frac{I_s}{I_t} \omega_{z_0} \quad (5.5-129)$$

$$\omega_2 = \omega_{z_0} \quad (5.5-130)$$

A geometrical interpretation of equations (5.5-124) through (5.5-130) is presented in Figure 5.5-7, where the motion of the unit vector aligned with the axis of symmetry is shown to have an epicycloidal character.

Its motion consists of a fixed angular deflection R_0 relative to the inertial Z axis, plus a low frequency (for $I_t > I_s$) circular motion along a circle having angular radius R_1 , plus, finally, a higher frequency circular motion along a circle having radius R_2 . Thus, the motion of the axis of symmetry relative to the inertial Z axis has two fundamental periodic components having frequencies ω_1 and ω_2 . Now the angle between the axis

of symmetry and the inertial Z axis is neither the nutation angle (since the angular momentum vector wobbles during the Δt), nor the angle of attack (since the velocity vector also wobbles during the Δt). However, the periodic motion depicted in Figure 5.5-7 suggests that the angle of attack might also display a periodic nature across the Δt , and that, in fact, it might be possible to select the Δt burn duration to be synchronous with a periodic angle of attack, and so reduce the angle of attack at the end of the Δt . A numerical solution of the angle of attack as a function of burn duration Δt is shown in Figure 5.5-8. Although it corresponds to a penetrator with a different moment of inertia ratio, it shows that penetrator angle of attack is indeed a periodic function.

Based on such observations, a criterion for minimizing angle of attack at the end of the Δt was postulated. Although this criterion has not been rigorously proven, it has, nonetheless, served as a useful guide in the design of certain penetrator parameters. If we let τ_1 and τ_2 denote the periods of the two periodic components, i.e.,

$$\tau_1 = 2\pi / \omega_1 \quad (5.5-131)$$

$$\tau_2 = 2\pi / \omega_2 \quad (5.5-132)$$

and if we let Δt denote the duration of the Δt , then the postulated criterion states that the angle of attack will be minimized if τ_1 , τ_2 and Δt are selected so that integers N_1 and N_2 can be found such that

$$N_1 \tau_1 = \Delta t \quad (5.5-133)$$

$$N_2 \tau_2 = \Delta t \quad (5.5-134)$$

This criterion implies that the moments of inertia must have a ratio given by

$$\frac{I_1}{I_2} = \frac{N_2}{N_1} \quad (5.5-135)$$

Applying this criterion to the current penetrator configuration with a required $\Delta t = 7.27$ s to ensure proper comet nucleus impact velocity, it was found that if spin rate is selected to be 116 rpm, then integers N_1 and N_2 selected as 4 and 14, respectively, would satisfy equations (5.5-133), (5.5-134), and (5.5-135).

Ending this digression, we return to the predicted conditions at the start of the Δt phase, namely, a nutation angle of 1.00° , and a maximum angle of attack of 2.00° . Since initial conditions at Δt start are no longer perfect, the angle of attack for a given Δt duration is now dependent on initial conditions, i.e., on the relative orientations of the axis of symmetry, angular momentum vector, and velocity vector (see Figure 5.5-3). Thus, numerical solutions involve a sweep through the entire range of possible

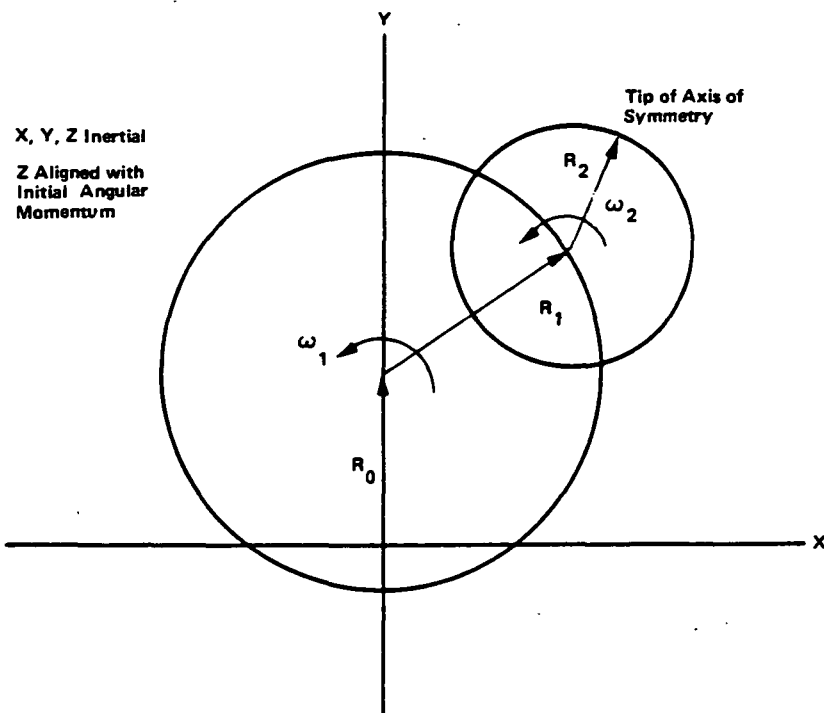


Figure 5.5-7 Geometrical Interpretation of ΔV Phase Wobble

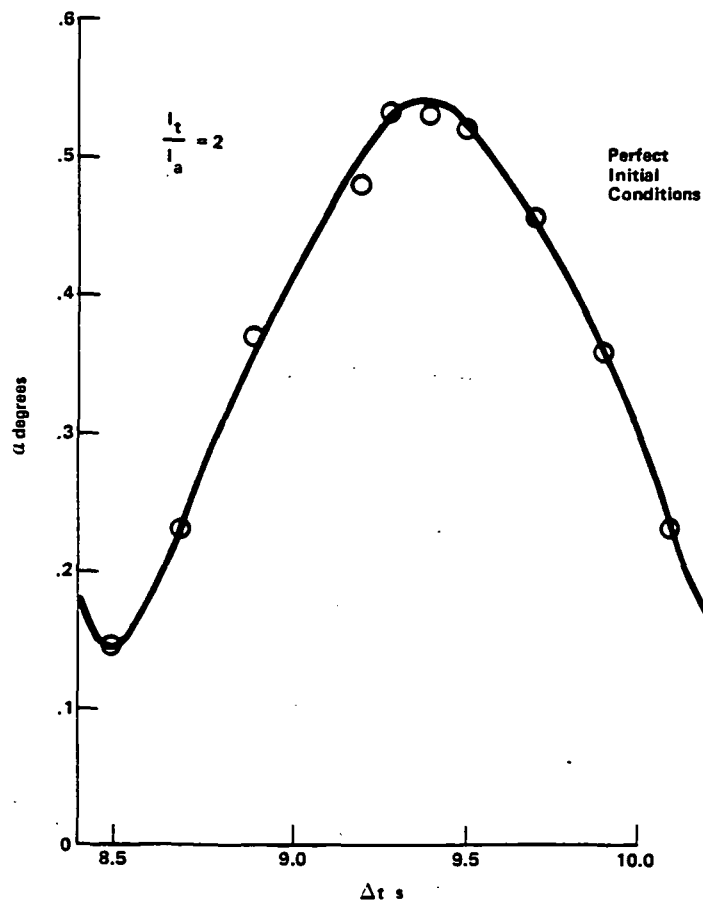


Figure 5.5-8 Periodic Angle of Attack during ΔV Phase

initial conditions to search for the maximum angle of attack for each delta-v duration. Numerical solutions of the maximum angle of attack as a function of delta-v duration for both a non-synchronous spin rate of 100 rpm and the proposed synchronous spin rate of 116 rpm are shown in Figure 5.5-9. It is apparent in this figure that the postulated criterion predicted a minimum in the maximum angle of attack curve for the synchronous spin rate. Note also that for thrust misalignments less than or equal to 0.3° , the angle of attack at the end of the delta-v is less than its value at the start of the delta-v, regardless of the delta-v duration. This is not true for misalignments of 0.4° and larger. Recall also that these results assume an axially symmetric penetrator and a constant thrust level. Since the post-delta-v coast is extremely short, the angle of attack at comet nucleus impact is essentially equal to the angle of attack at the end of the delta-v.

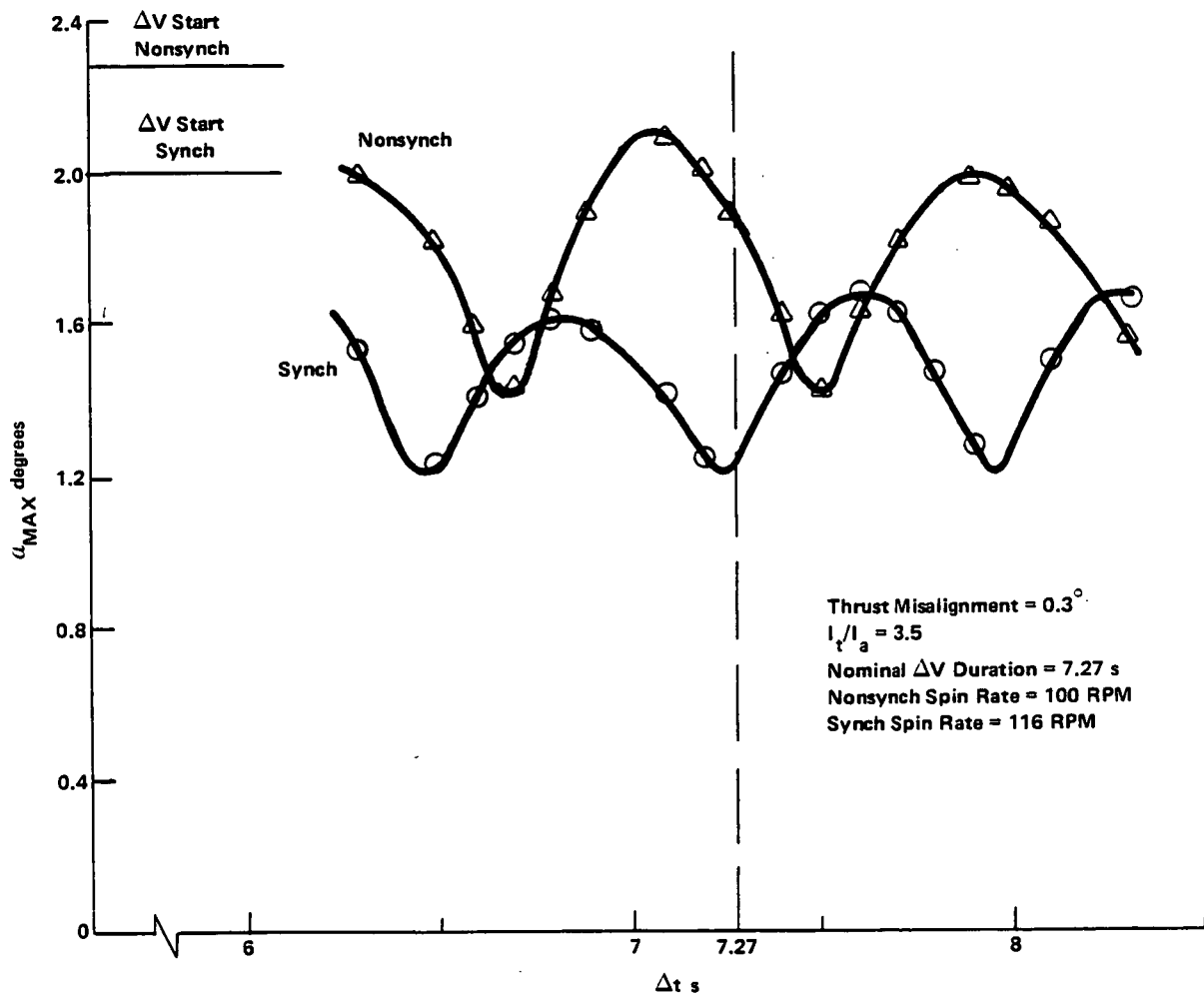


Figure 5.5-9 Maximum Angle of Attack vs ΔV Duration

Recommendations for improving penetrator attitude performance include a reduction of the relative tipoff rate, since Figure 5.5-6 shows that a smaller tipoff/spin rate ratio will reduce the nutation angle at spin/eject. This ratio can also be reduced by increasing spin rate. However, unnecessarily high spin rates must be avoided since internal energy dissipation rate over the long coast can be proportional to the cube of the spin rate. It should be noted that a smaller tipoff rate will also reduce internal energy dissipation since the dissipation rate is also proportional to the initial nutation angle. Other measures that are recommended for reducing internal energy dissipation include maintaining axial symmetry of the structure, minimizing center of mass displacement from the spin axis, embedding wires and other relatively loose elements in epoxy or conduits, and ensuring that the spin and precession frequencies do not induce resonance in structural vibration modes. Performance across the delta-v can also be improved by reducing thrust misalignment.

Future studies should include determining the sensitivity of attitude performance to factors not treated in the current study, i.e., to non-axial symmetry, non-uniform thrust, variable mass dynamics, and jet damping. Sensitivity of attitude performance to trajectory effects and initial Mariner Mark II attitude and rate errors should also be determined.

5.6 Electronics System

The purpose of the electronics part of the CNPS study was to size the black boxes required to implement the CNPS electronics. To achieve this goal, the approach was to identify the requirements and to perform a preliminary design to those requirements in sufficient detail to generate an electronics parts list from which printed circuit board areas and box sizes could be derived.

CNPS electronics comprises two distinct subsystems. The electronics, being a part of the penetrator ejected from the spacecraft and implanted on the comet, is referred to as the Penetrator Electronics. The electronics left on the spacecraft after ejection is referred to as the Penetrator Support Module (PSM) Electronics.

The hardware and software requirements for the design are detailed in Appendix C and Appendix D, respectively.

Figures 5.6-1 and 5.6-2 show system-level diagrams of the PSM and the penetrator electronics. The design goal was to produce a system with minimal weight and cost and maximum reliability. Minimal weight and cost dictated a single-string system instead of a triple-redundant majority-voted system for example. To maximize reliability, selected redundancy and some error-recovery features were incorporated. On the penetrator, for example, the solid rocket motor firing circuit contains redundant inhibit functions to prevent premature firing. Both the penetrator and PSM microcomputers contain watchdog timers, to allow error-recovery.

Penetrator science data is inherently redundant since it continually integrates without reset and is transmitted periodically to the spacecraft. Both the penetrator and PSM programs will have the capability of being modified in flight by uplinking executable code to RAM or, preferably, to electrically-erasable CMOS PROM if the erasable PROM is qualified for use on the CRAF mission.

Both the PSM and the penetrator subsystems comprise the following elements: data handling, thermal, RF, power, and interfaces. The penetrator also has science and propulsion elements. For cost-effectiveness in design and test, there are many similarities between the corresponding elements of the PSM and the penetrator. The data handling systems, for example, use almost identical microcomputer designs. The two systems are microcomputer-based, instead of using discrete logic or a state machine, to allow them to operate autonomously for the short duration of the experiment when closed-loop operation through Earth is not practical.

Not shown in the block diagrams are the pyro subsystems for releasing the PSM/penetrator interface electrical connector and for activating the spin-eject mechanism. These pyro devices are cabled directly to the spacecraft, bypassing the PSM electronics. The spacecraft, therefore, is responsible for the control and safety inhibits associated with these devices.

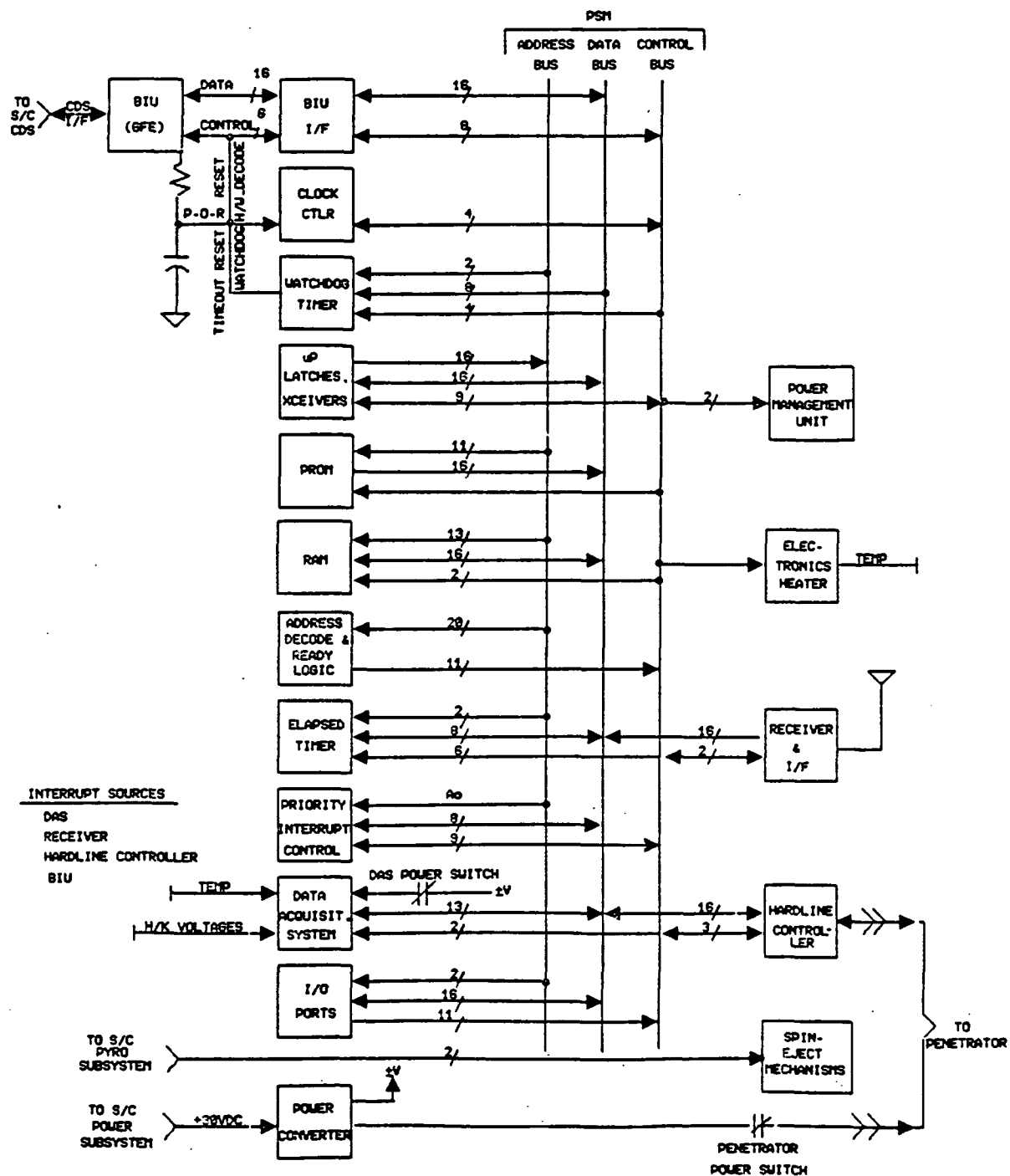


Figure 5.6-1 Penetrator Support Module Electronics
System Block Diagram

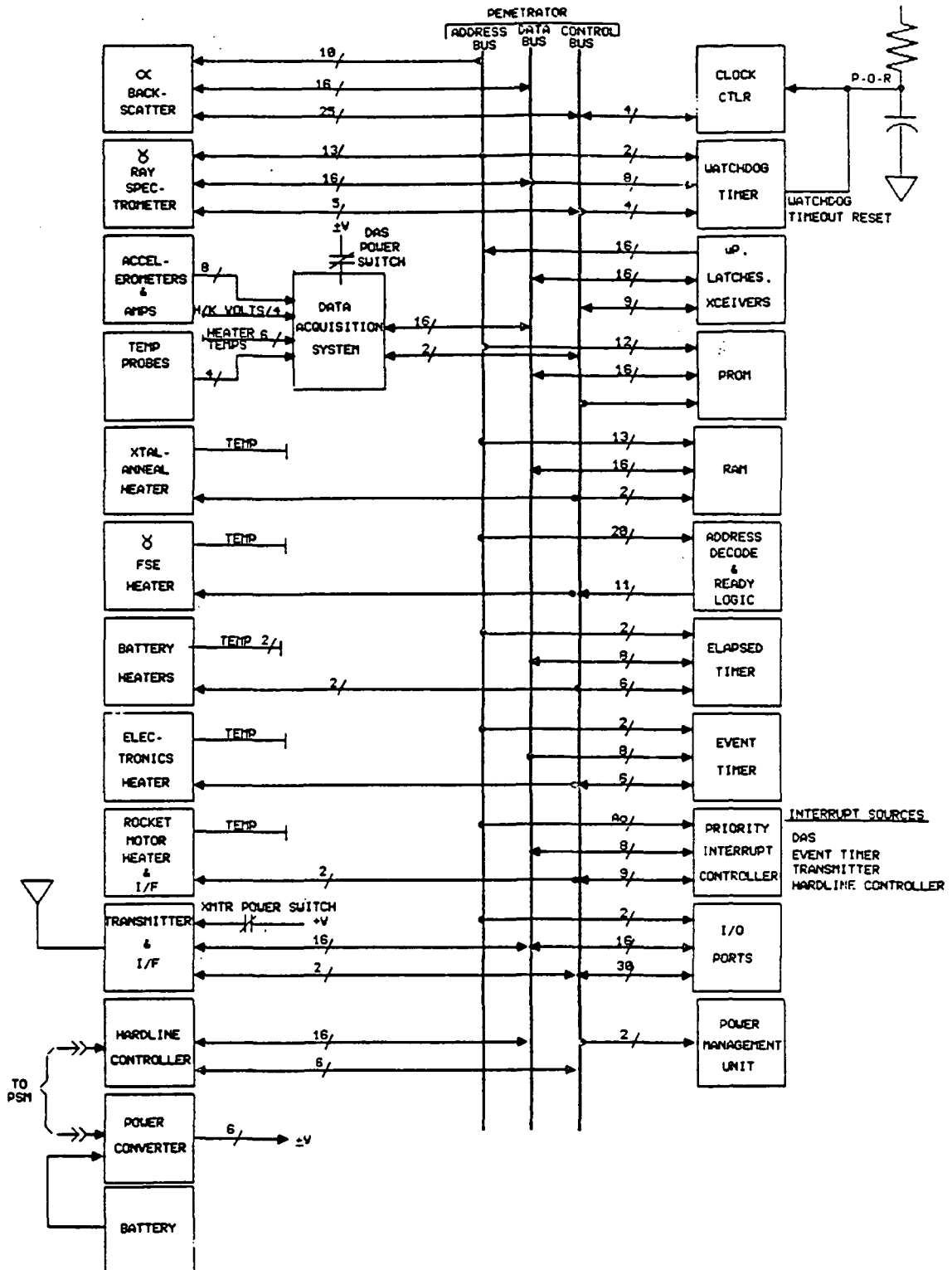


Figure 5.6-2 Penetrator Electronics System Block Diagram

5.6.1 PSM Description

The relationships between PSM subsystem elements is shown in Table 5.6-1.

Table 5.6-1
Penetrator Support Module Subsystem Elements

Data Handling	Clock Controller Watchdog Timer μP, Latches, Transceivers PROM RAM Address Decode & Ready Logic Elapsed Timer Priority Interrupt Control Data Acquisition System I/O Ports
Thermal	Electronics Heater
RF	Receiver & I/F
Power	Power Converter Power Management Unit
Interfaces	BIU BIU I/F Spin-Eject Table Hardline Controller Power

The function of each block is described in the following paragraphs.

5.6.1.1 PSM Data Handling

The PSM data handling subsystem is based on the 16-bit 80C86 microprocessor family recommended by JPL for the CRAF mission. The classical Address, Data, and Control busses are used to interconnect most of the PSM system blocks, with data being transacted on the 16-bit parallel, de-multiplexed data bus. The de-multiplexed address bus is also 16-bits wide, and the control bus contains all of the strobe, select, and clock signals required to perform the data transactions.

(Note: There is some concern with the 80C86 single-event upset rate. If it is necessary to convert the CNPS design to another microprocessor family, this will not be a major problem, since the system architecture will be unchanged.)

Figure 5.6-3 shows the PSM Data Handling Clock, microcomputer, Bus, & Demux subsystem. The microcomputer operates at its maximum 5 MHz clock rate which is generated by the Clock Ctlr. This function is implemented with an 82C85 chip which also provides the capability of either stopping the system clock or running it at a slower frequency, under microcomputer control. This feature allows system power dissipation to be minimized, since most of the system is implemented in CMOS with power dissipation directly proportional to frequency. The microcomputer, Latches, transceiver functions consist of the 80C86 microcomputer, 82C82 latches, and 82C86 transceiver chips. The latches are

used to de-multiplex the 80C86's address/data bus, and the transceivers are used to decouple the 80C86's bi-directional data bus from the rest of the system.

Figure 5.6-4 shows the PSM Data Handling Timers subsystem. The timer functions are implemented with another member of the 80C86 family, the 82C54. The Watchdog Timer will be periodically reset by the PSM program at an approximately 16 msec rate. If a problem, such as a single-event-upset, causes the program to get lost, the timer will time out and send a reset signal to the Clock Ctrl block, restarting the program. The PSM Elapsed Timer will be synchronized with its counterpart in the penetrator and used to help establish the periodic RF link; i.e., to predict when transmissions from the rotating comet nucleus are to be expected. Elapsed timer resolution is approximately one second.

Figure 5.6-5 shows the PSM Data Handling Memory subsystem. Microcomputer program memory and data storage is contained in the PROM and RAM blocks. Since the CNPS memory requirements are small compared to those of the spacecraft's Command and Data Handling (C&DS) system, CNPS memory was implemented with chips organized as 2 k x 8 instead of the 16 k x 1 chips recommended by JPL. However, if qualification of the 2 k x 8 chips is a problem, the microcomputer can use the 16 k x 1 chips with some increase in printed circuit board area requirements.

Figure 5.6-6 shows the PSM Data Handling Address Decode subsystem. The Address Decode & Ready Logic decodes the 16-bit address bus to generate the strobe and select signals required for I/O operation. These signals are logically or'ed to generate a Ready signal which feeds back to the Clock Ctrl to tell the microcomputer that the bus device has acknowledged.

Figure 5.6-7 shows the PSM Data Handling Interrupts subsystem. The Priority Interrupt Controller, an 82C59 chip, is used to handle the six interrupts required for PSM operation:

- (1) Data Acquisition System (DAS) Interrupt- generated by the DAS's A/D converter when conversion is complete.
- (2) Receiver Interrupt- generated by the RF receiver's interface logic when 16 bits of data have been received from the implanted penetrator.
- (3) Hardline Controller Interrupt- generated when 16 bits of data have been received from the penetrator prior to ejection.
- (4) Bus Interface Unit (BIU) Interrupt- 3 interrupts used to synchronize transactions with the spacecraft's Command and Data Subsystem (CDS).

Figure 5.6-8 shows the PSM Data Handling and Data Acquisition System which is used to collect engineering housekeeping data, such as internal temperatures and voltages. It is also used in the feedback path of the electronics heater's bang-bang control loop. The analog multiplexer, HC4051, is addressed from the microcomputer's I/O ports via the control bus. The selected analog signal is buffered and applied to the AD574, one of the monolithic ADC's recommended by JPL. The AD574 is a 12-bit converter which will be short-cycled to 10-bits for the PSM application. The HC241's are used to tristate the ADC output onto the data bus under control of select signals from the control bus. DASCONVERT is an I/O port output used to initiate the conversion, and DASRUPT is an interrupt generated when conversion is complete.

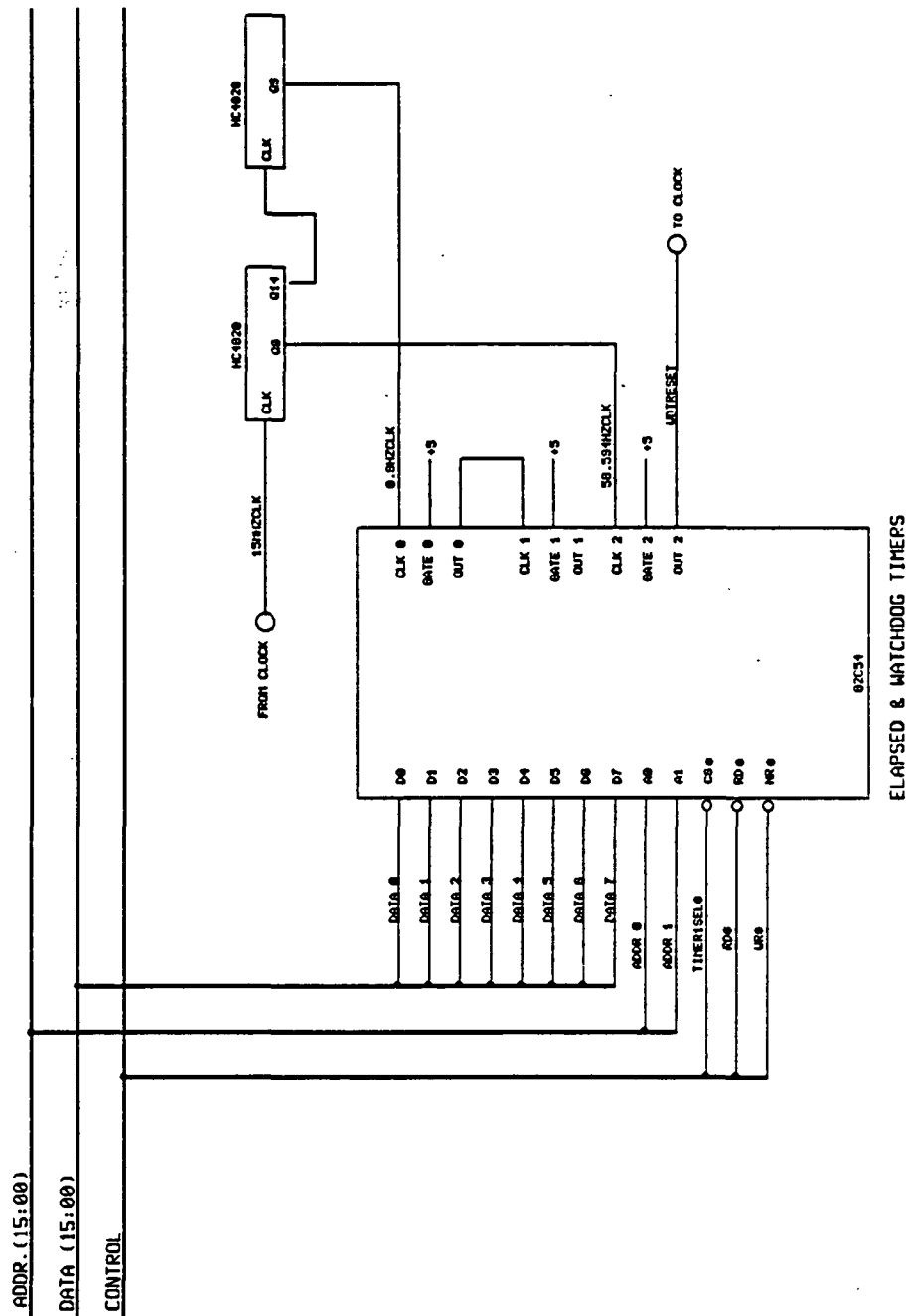


Figure 5.6-4 PSM Data Handling Timers

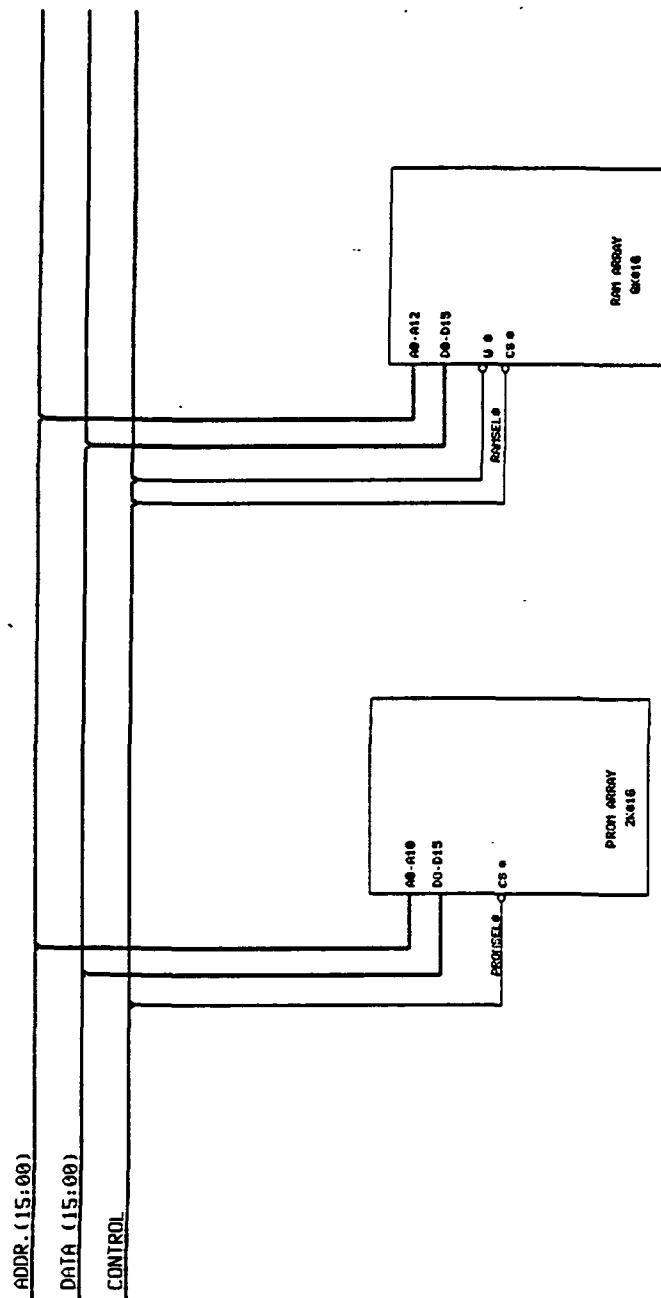


Figure 5.6-5 PSM Data Handling Memory

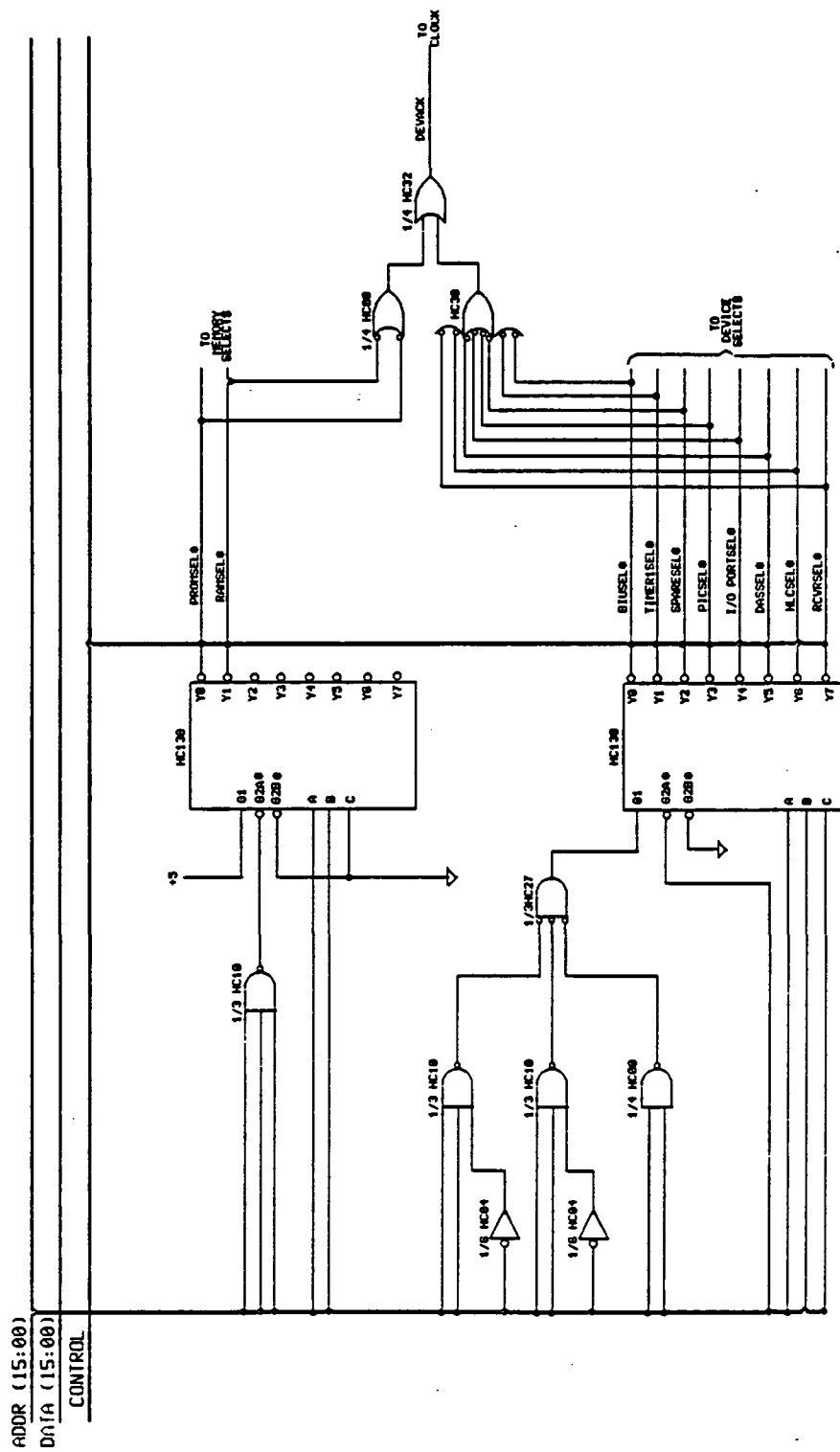


Figure 5.6-6 PSM Data Handling Address Decode

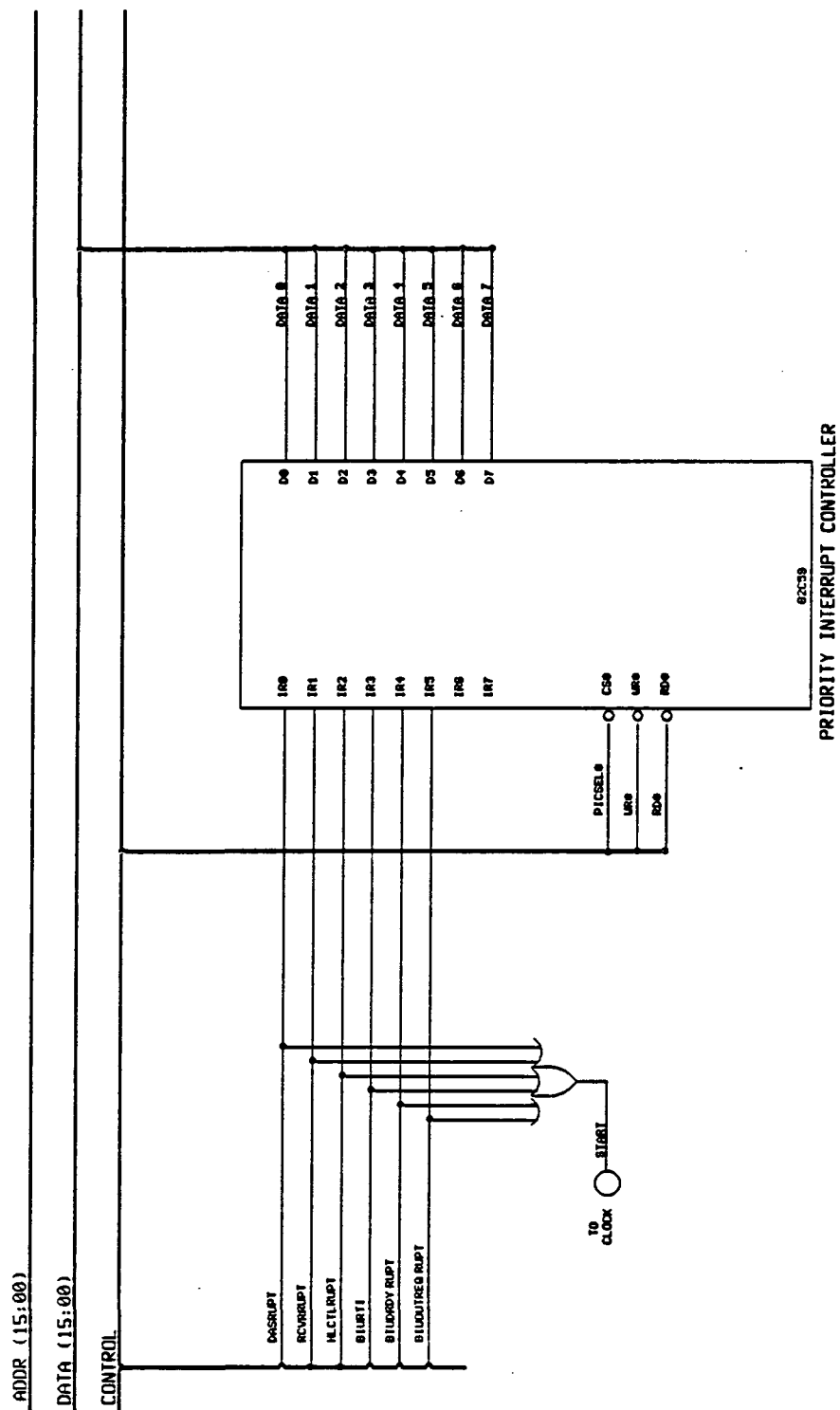


Figure 5.6-7 PSM Data Handling Interrupts

Figure 5.6-9 shows the PSM Data Handling I/O Ports subsystem. An 82C55 chip is used to handle the microcomputer's output signals. No input signals have been identified at this time. Eight bits of data from the low byte of the data bus are written to the output port selected by the ADDR0 and ADDR1 signals from the address bus. The output signals are used to control the various PSM I/O devices: BIU, Hardline Controller, Heater, and DAS. The lines not presently allocated may be configured as outputs and/or inputs.

5.6.1.2 PSM Thermal

As previously described, the control loop for the electronics heater subsystem is closed through the microcomputer. It will read the electronics temperature, compare it to the set-point and deadband values and turn the heater power off or on accordingly.

Since it appears at this time that the spacecraft will maintain the PSM electronics' baseplate temperature at -10 degrees C minimum, it will probably be possible to eliminate the PSM heater subsystem. This decision will be made early in the next phase of the CNPS project.

5.6.1.3 PSM RF

Figure 5.6-10 shows the PSM Receiver subsystem. This includes the off-the-shelf FM receiver selected for the PSM. The specifications for the receiver selected, an Aydin Vector Model RCC201-1, are shown in Table 5.6-2.

**Table 5.6-2 Aydin Vector Model RCC201-1
Receiver Specifications**

Frequency Range: 1435-1540 MHz
Frequency Stability: $\pm 003\%$ Over Temperature
Antenna Impedance: 50 ohms Nominal
VSWR: Less Than 2:1
Noise Figure: 12 db Maximum (6 db Optional)
Spurious Noise Rejection: 60 db Minimum
Image Rejection: 60 db Minimum
Maximum Signal Level: 2 Vrms
Predetect IF Bandwidth: 200 KHz Nominal (-3 db)
Audio Output Sensitivity: .01 v-p/KHz Deviation
Audio Output Distortion: 2% Maximum for p-p Deviation of 50 KHz
Signal Strength Analog: 1-4 Vdc Nominal into 10 K Load
Audio Output Load: 600 ohms Nominal
Audio Frequency Response (± 1 db) : 100 Hz to 50 KHz Minimum
Input Voltage: 24-36 Vdc with Integral Reverse Polarity Protection
Input Current: 100 ma Maximum
Size: 6.0 x 3.25 x 1.315 in. Excluding Connectors
Weight: 26 oz Maximum
Baseplate Temperature: -40° to +70°C
Vibration: Sinusoidal at 20 g from 20 to 2000 Hz in Each Axis
Shock: 1/2 sine at 50 g for 11 msec in Each Axis
Acceleration: 100 g, Each Axis
Altitude: Unlimited
Relative Humidity: 95%

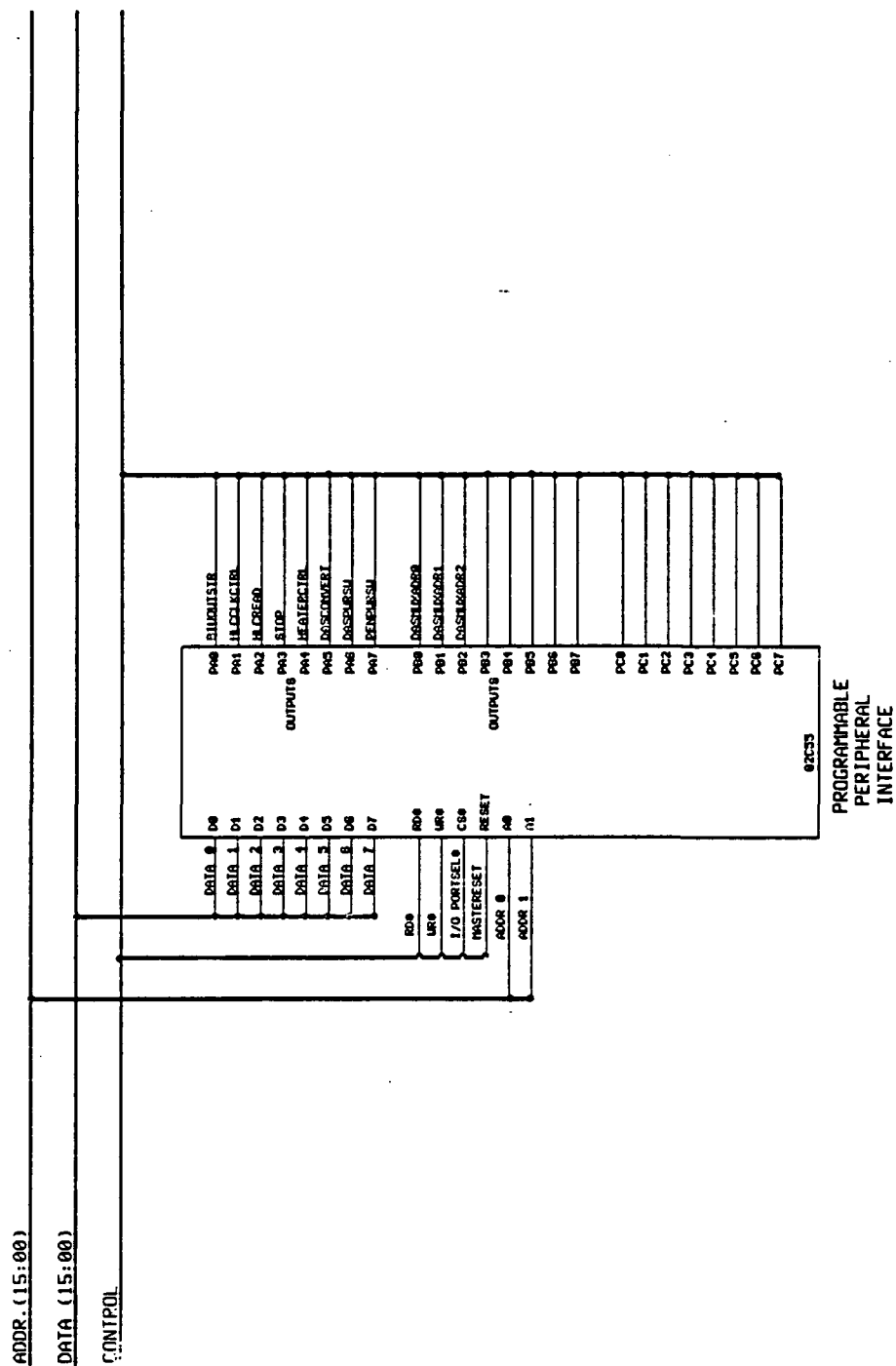


Figure 5.6-9 PSM Data Handling I/O Ports

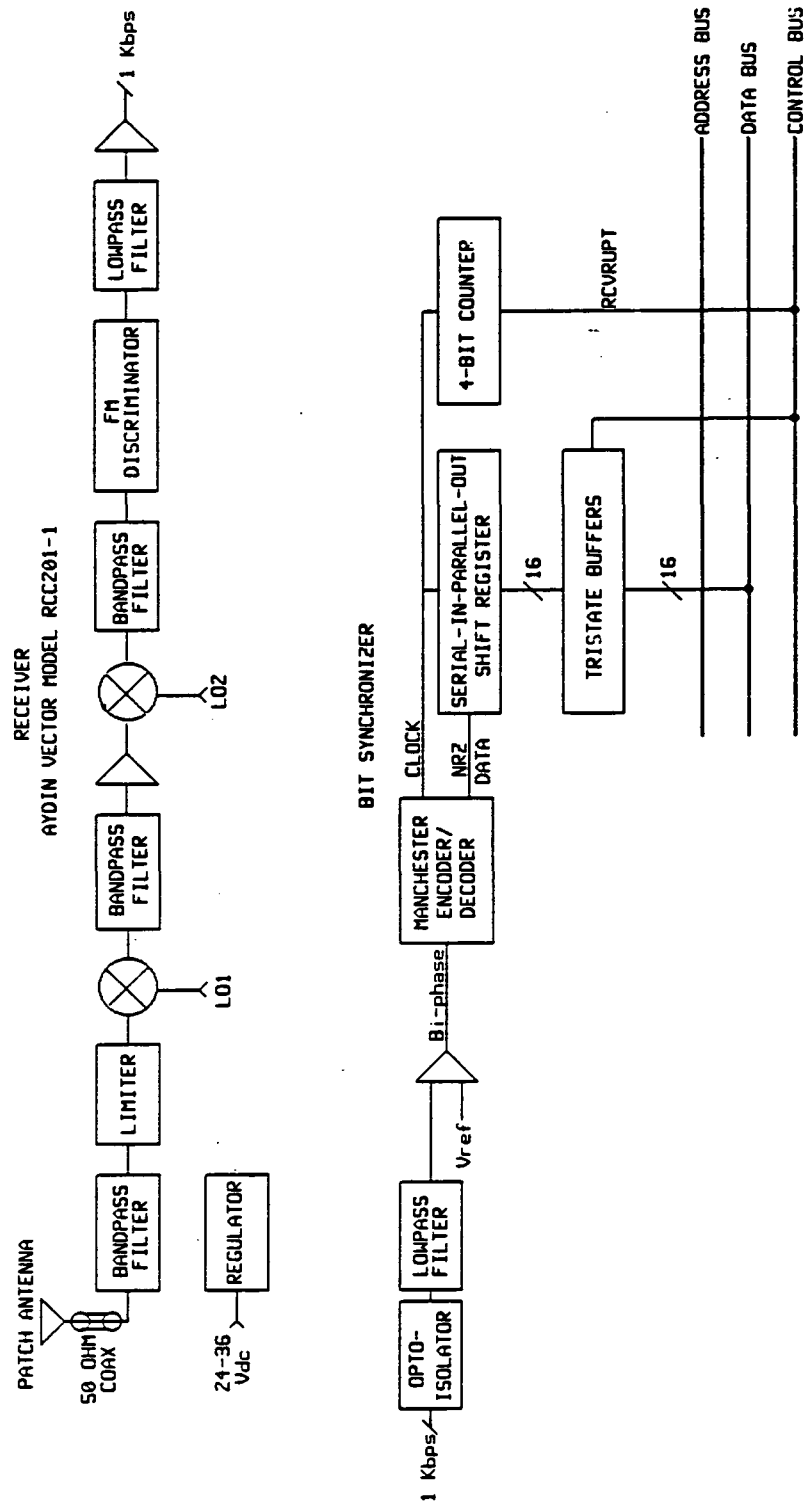


Figure 5.6-10 PSM Receiver Diagram

The receiver will be mounted inside the PSM electronics box on the spacecraft bus. Its antenna, a single microstrip patch, will be mounted on the spacecraft's Low Precision Scan Platform. The link analysis for the FM system showed that a single patch provided adequate gain. (Refer to the RF report in Appendix E.)

Figure 5.6-10 also shows the bit synchronizer logic used to recover NRZ data from the received 1 kbps bi-phase data stream. The data will be packed into a 16-bit serial-to-parallel register for readout by the PSM microcomputer. An interrupt will be generated after each 16-bits. Sync-pattern recognition will be performed by the PSM program, after which all data will be buffered for subsequent transmission to the spacecraft. (Refer to Appendix G for Microcomputer Memory and Telemetry Estimates.)

5.6.1.4 PSM Power

Figure 5.6-11 shows the CNPS Power and Grounding Diagram. This figure shows the routing and conditioning of the spacecraft prime power. Note that the +30 V(dc) from the spacecraft will be used directly by the converter, heater, and RF receiver.

Logic and low-level analog loads will be isolated from the prime-power bus by the PSM and penetrator power converters. Logic interfaces between the RF subsystems and the data handling subsystems will be optically-isolated to maintain separation of primary and secondary returns. Single-point grounds will be established at the secondary returns of both the PSM and the penetrator converters, and these points will be connected prior to ejection to allow proper operation of the hardline control interface. The hardline control interface is also shown in the figure.

5.6.1.5 PSM Converter

Figure 5.6-12 shows the PSM Power Converter subsystem. The PSM Power Converter is a switching power supply that (1) isolates PSM loads from the 30 V(dc) spacecraft power input, and (2) generates the regulated voltages required by the PSM electronics: +5 and +12 V(dc). The design is based on an SG1526 pulse-width modulation control IC. Conversion efficiency is 70% minimum over the load range.

5.6.1.6 PSM Power Management Unit

This unit, under microcomputer control, operates the power switches shown in Figure 5.6-1 (PSM Electronics Diagram). Use of power switches for the higher-power loads is part of the CNPS power minimization strategy. The effect of using these switches on PSM average power consumption can be seen in Appendix J (Power Consumption), which tabulates PSM and penetrator peak and average power consumption as a function of mission phase.

The penetrator Power Switch shown in Figure 5.6-1 also serves the purpose of interrupting power to the penetrator just prior to ejection.

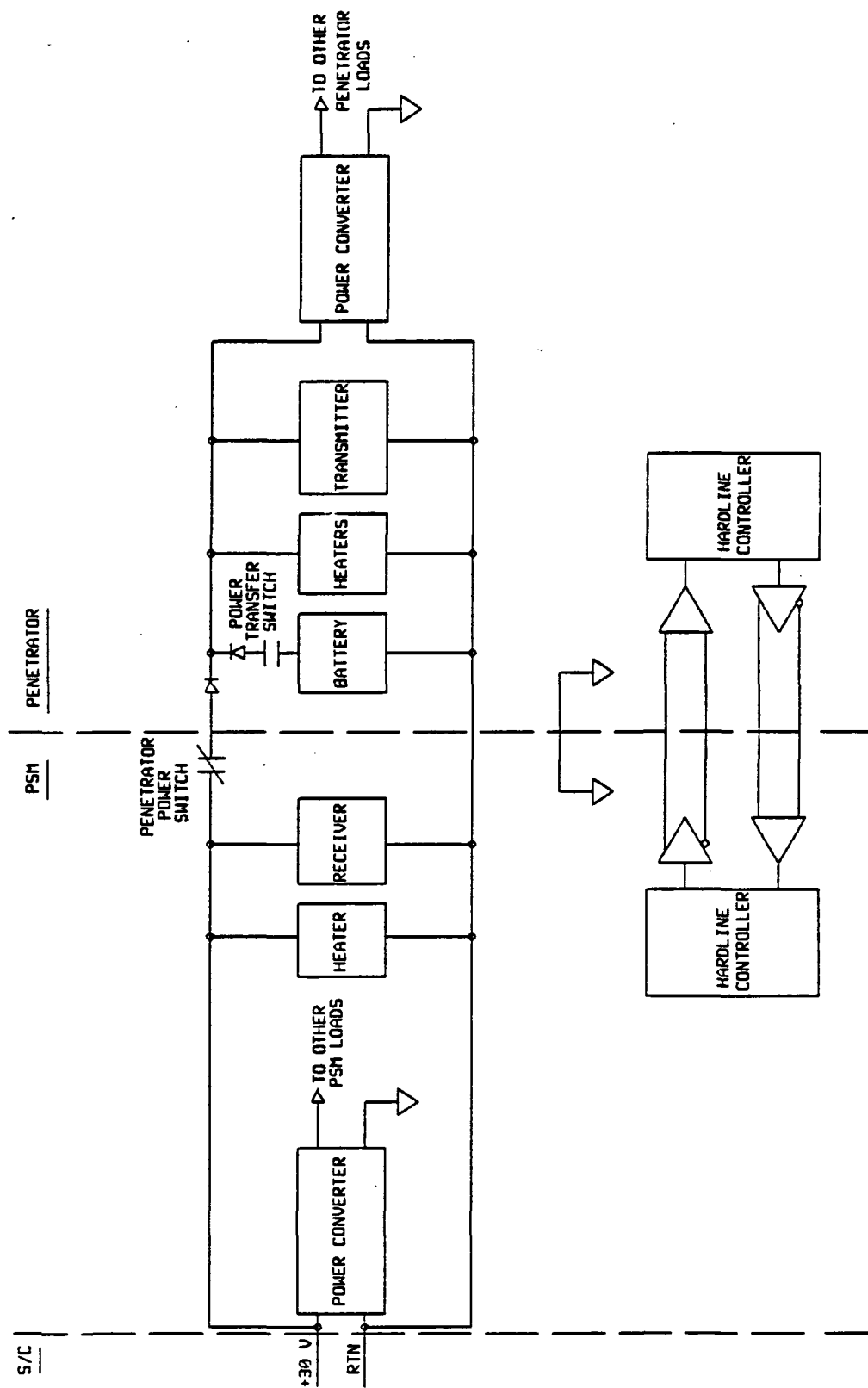


Figure 5.6-11 CNPS Power and Grounding Diagram

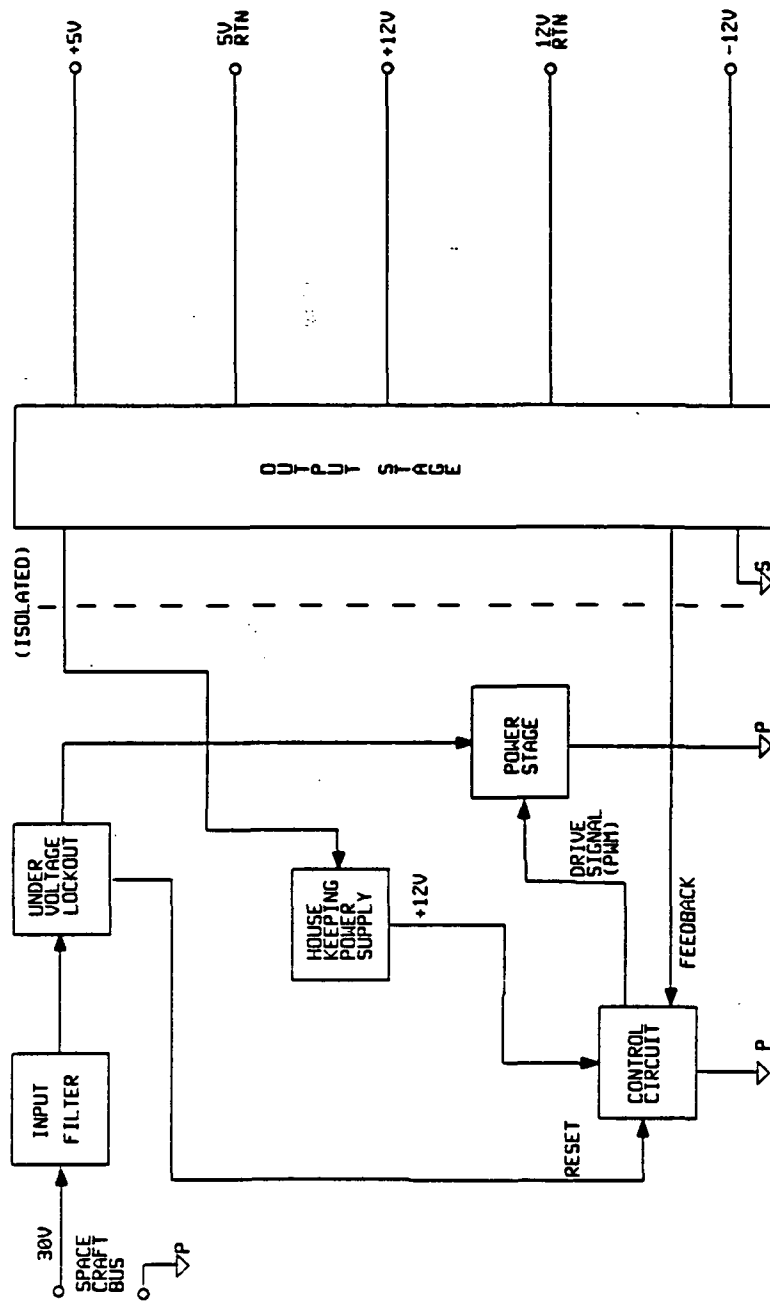


Figure 5.6-12 PSM Power Converter

5.6.1.7 PSM Interfaces

PSM electrical interfaces with the spacecraft and with the penetrator are described in the following paragraphs.

5.6.1.7.1 PSM/Spacecraft Interfaces

5.6.1.7.1.1 PSM/Spacecraft BIU Interface

Figure 5.6-13 shows the PSM Data Handling BIU I/F subsystem. The PSM electronics will interface with the spacecraft Command and Data Subsystem through the Bus Interface Unit (BIU) supplied by JPL. Basically, the BIU converts serial data on the spacecraft bus to 16-bit parallel data for use by the PSM's microcomputer, and vice-versa.

The BIU I/F figure shows that only three chips are used to interface the BIU to the PSM microcomputer busses. Handshaking is performed by the three BIU--RUPT signals and the BIUOUTSTR signal. BIUHWRESET is a signal that is hardware-decoded by the BIU and used to reset the PSM system by a command from the spacecraft CDS. This reset signal is wire-or'ed with the RC-generated Power-On-Reset (P-O-R) signal shown in Figure 5.6-1 (PSM Electronics Diagram).

Data sent to the spacecraft will be packetized to CCSDS standards. Appendix G shows that the source data field will typically be 40,000 bits, or 5 kbytes. The total length will be an integer number of octets.

5.6.1.7.1.2 PSM/Spacecraft Power Interface

As specified in the CRAF document, the spacecraft will provide $+30 \pm 0.75$ V(dc) to the PSM. This voltage will be conditioned by the PSM power converter as previously described.

5.6.1.7.2 PSM/penetrator Interfaces

5.6.1.7.2.1 PSM/penetrator Power Interface

Figure 5.6-11 shows the CNPS Power and Grounding subsystem. The figure shows that spacecraft prime power will be routed through a power switch in the PSM to the penetrator. This switch will be opened just before ejection to avoid interruption of a high-current path by the breaking of the spin-eject electrical connection.

5.6.1.7.2.2 PSM/penetrator Hardline Controller Interface

Figure 5.6-14 shows the PSM Data Handling Hardline Controller interface. The purpose of this interface is to allow command and data transactions between the PSM and the penetrator prior to ejection and use of RF telemetry. For simplicity, this interface was designed to be serial, asynchronous, and half duplex. It will use bi-phase data handled by the same chip planned for the spacecraft data system: the Harris HD15530. It can operate at up to 1.25 Mbps. After ejection, the clock to this all-CMOS circuit will be gated off so

that its power dissipation will be insignificant. The figure shows the other logic associated with connecting the 15530 to the microcomputer busses. Data handshaking is performed by the HLCREAD, HLCWRITE, and HLCTLRUPT signals.

Figure 5.6-11 (CNPS Power and Grounding Diagram) shows the circuit preferred to handle the hardline control interface signals between the PSM and the penetrator. It has the advantage of being balanced for maximum noise rejection. It requires five interface wires in addition to the two power wires shown in the figure.

Other configurations considered for the hardline control interface required fewer interface wires but had the disadvantages of being half-duplex, unbalanced, or, in the case of an optically-coupled interface, more mechanically complex than the chosen configuration.

5.6.2 Penetrator Description

Figure 5.6-2 shows the Penetrator Electronics system block diagram.

The relationship between penetrator subsystem elements is shown in Table 5.6-3.

Table 5.6-3 Penetrator Subsystem Elements

Subsystem	Blocks
Data Handling	Clock Controller Watchdog Timer μ P, Latches, Transceivers PROM RAM Address Decode & Ready Logic Elapsed Timer Priority Interrupt Control Data Acquisition System I/O Ports
Science	Alpha Backscatter Gamma Ray Spectrometer Accelerometers & Amps Temp Probes
Thermal	Crystal-Anneal Heater Gamma FSE Heater Battery Heaters Electronics Heater Rocket Motor Heater
RF	Transmitter & I/F
Power	Power Converter Battery Power Management Unit
Interfaces	Hardline Controller Power

Since one of the design goals for the CNPS electronics was to use as many common designs as possible in the penetrator and the PSM, the following paragraphs will describe in detail only the differences between the two subsystems.

5.6.2.1 Penetrator Data Handling

Figures 5.6-15 through 5.6-22 show that the penetrator data handling subsystem design is almost identical to that of the PSM. PROM requirements are slightly different, as described in Appendix G. And the penetrator requires two 82C54 timer chips instead of one and two 82C55 I/O chips instead of one.

The major difference between the two data handling subsystems is that the penetrator's data acquisition system is more complex than the PSM's. The reason for the difference is that the penetrator electronics is required to sample seven accelerometers at a high rate during comet nucleus impact. Because the rate is too fast to be handled by the microcomputer, additional logic was added to the basic data acquisition system design to perform the sampling and attendant impact-detection in hardware, as shown in Figure 5.6-22.

Appendix I describes the accelerometer sampling analysis.

5.6.2.2 Penetrator Science

5.6.2.2.1 Penetrator Alpha-Backscatter Instrument

Figure 5.6-23 shows the basic elements of the alpha-backscatter instrument and its interface with the penetrator microcomputer busses. The alpha-backscatter instrument operates in alpha, proton, and x-ray modes. Pulses from the x-ray detector are multiplexed with pulses from the alpha/proton coincidence logic, with the resulting pulse-height analysis performed in the Coincidence Pulse Height Analyzer (PHA). This PHA will be configured to perform a 1024 channel by 16-bit analysis on the x-ray pulses or a 512 channel by 8-bit analysis on the alpha/proton pulses. The other two PHA's are both 512 channels by 8 bits. RAM in all three PHA's is independently readable by the penetrator microcomputer for subsequent transmission to the spacecraft.

The Status & Control Logic is used to control start and stop of data collection, to control the instrument's electromechanical devices, and to provide temperature and device status housekeeping data.

The electromechanical devices are located in the sensor head and consist of fuse-link/spring mechanisms to control the shutters and a pin-puller to control the door. The fuse-links are one-shot devices activated by a short-duration, high-current pulse initiated by the microcomputer via its I/O ports. The pin-puller is similarly controlled by an I/O port pulse.

The 50-200 volts shown for the x-ray sensor is derived from the same supply used to generate the 750-3000 volts required by the gamma-ray spectrometer's sensor.

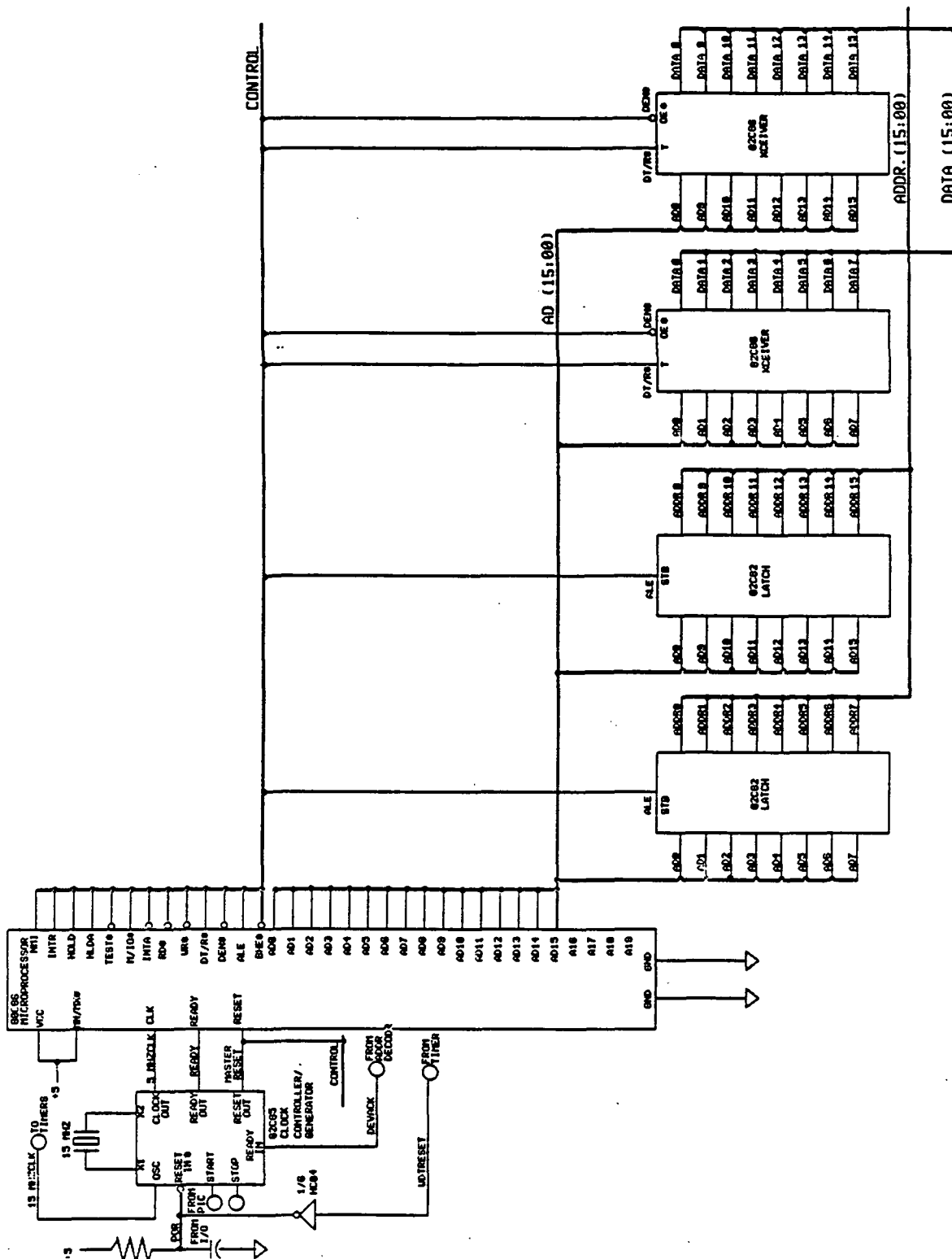
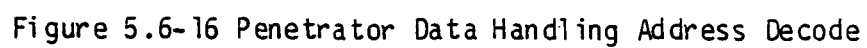


Figure 5.6-15 Penetrator Data Handling Clock, microcomputer, Bus Demux



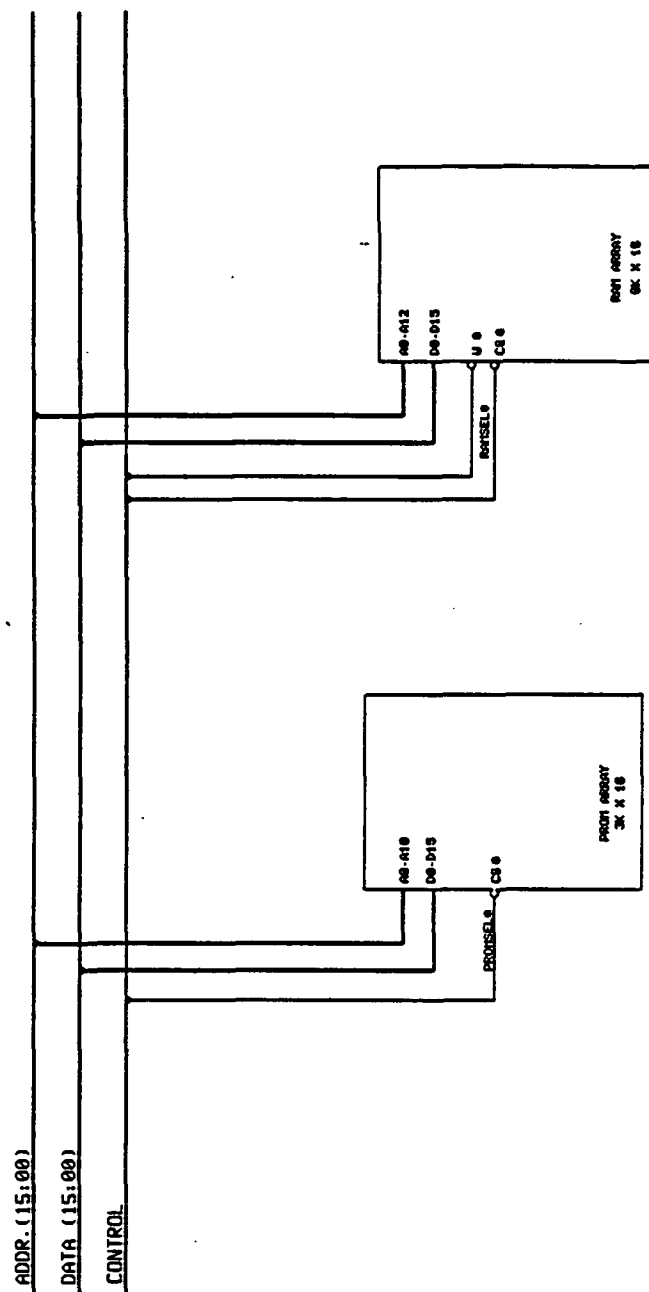


Figure 5.6-17 Penetrator Data Handling Memory

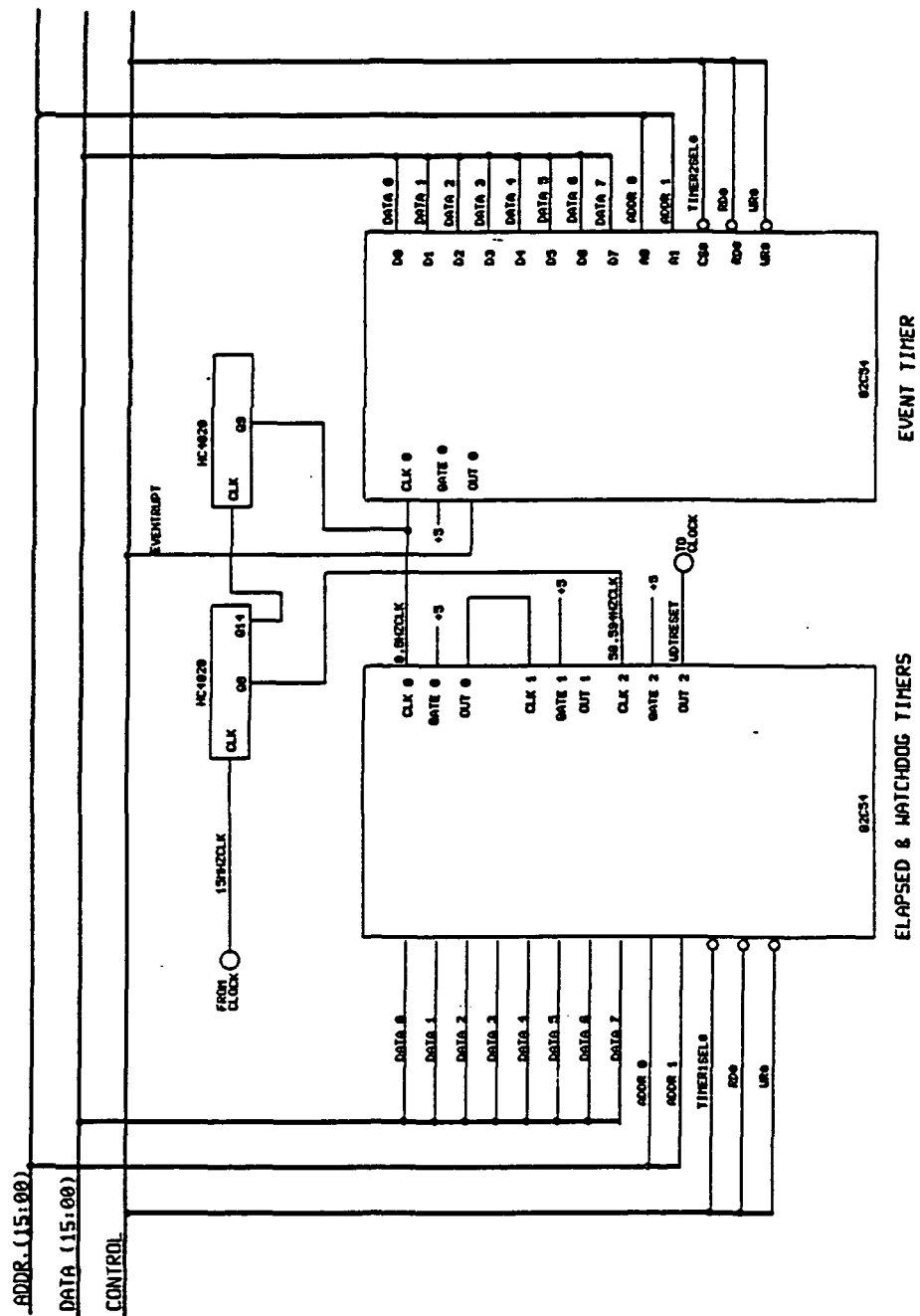


Figure 5.6-18 Penetrator Data Handling Timers

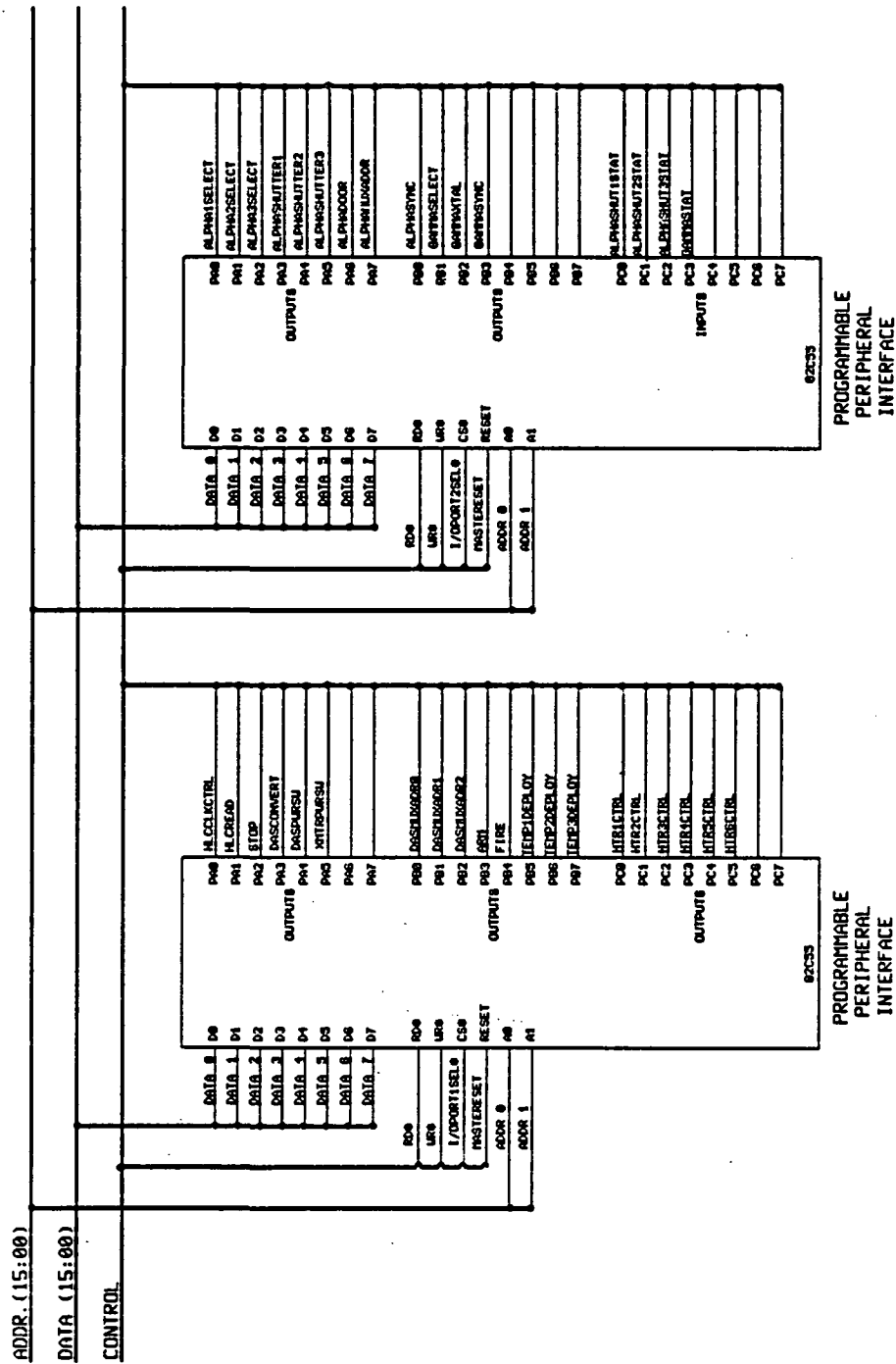


Figure 5.6-19 Penetrator Data Handling I/O Ports

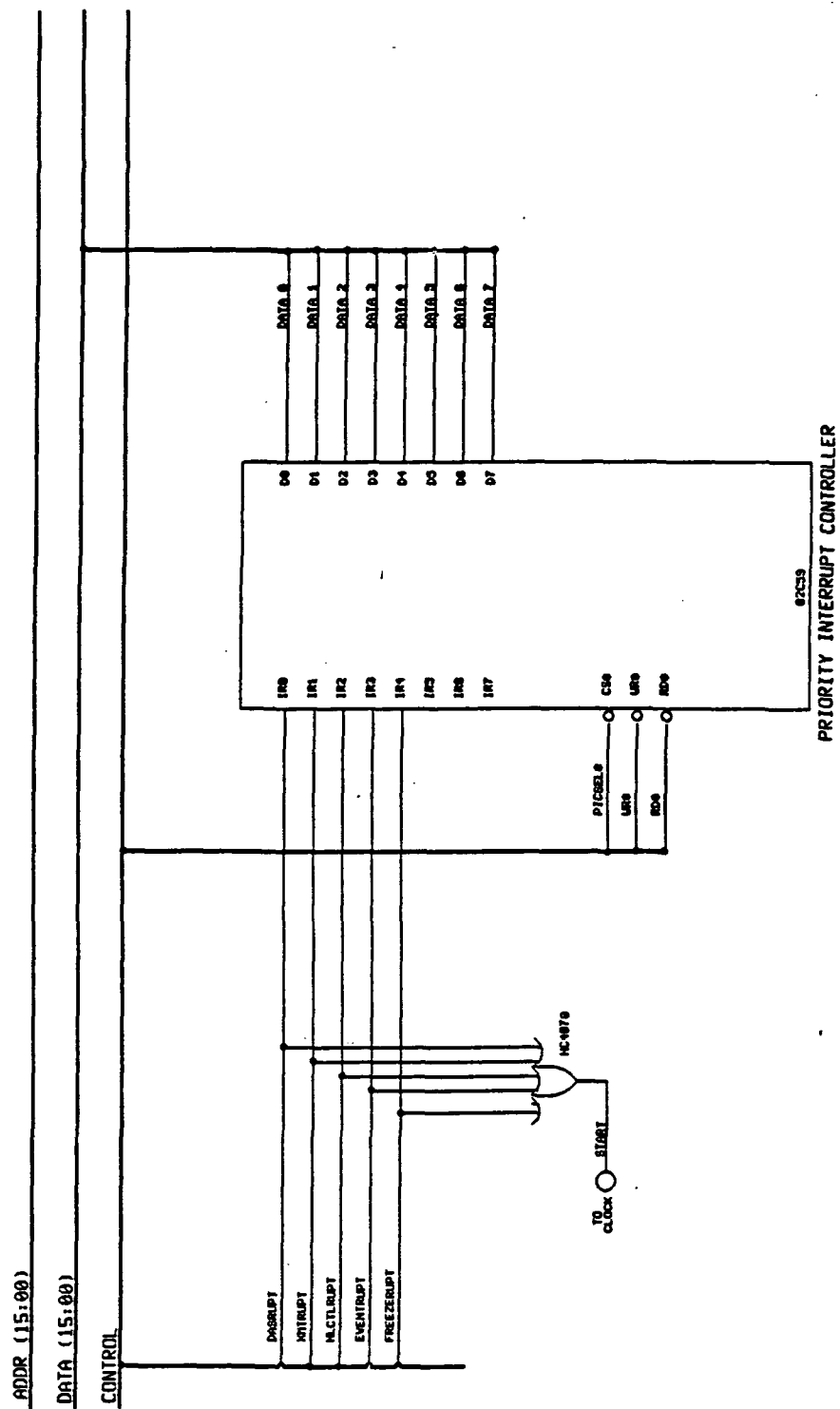


Figure 5.6-20 Penetrator Data Handling Interrupts

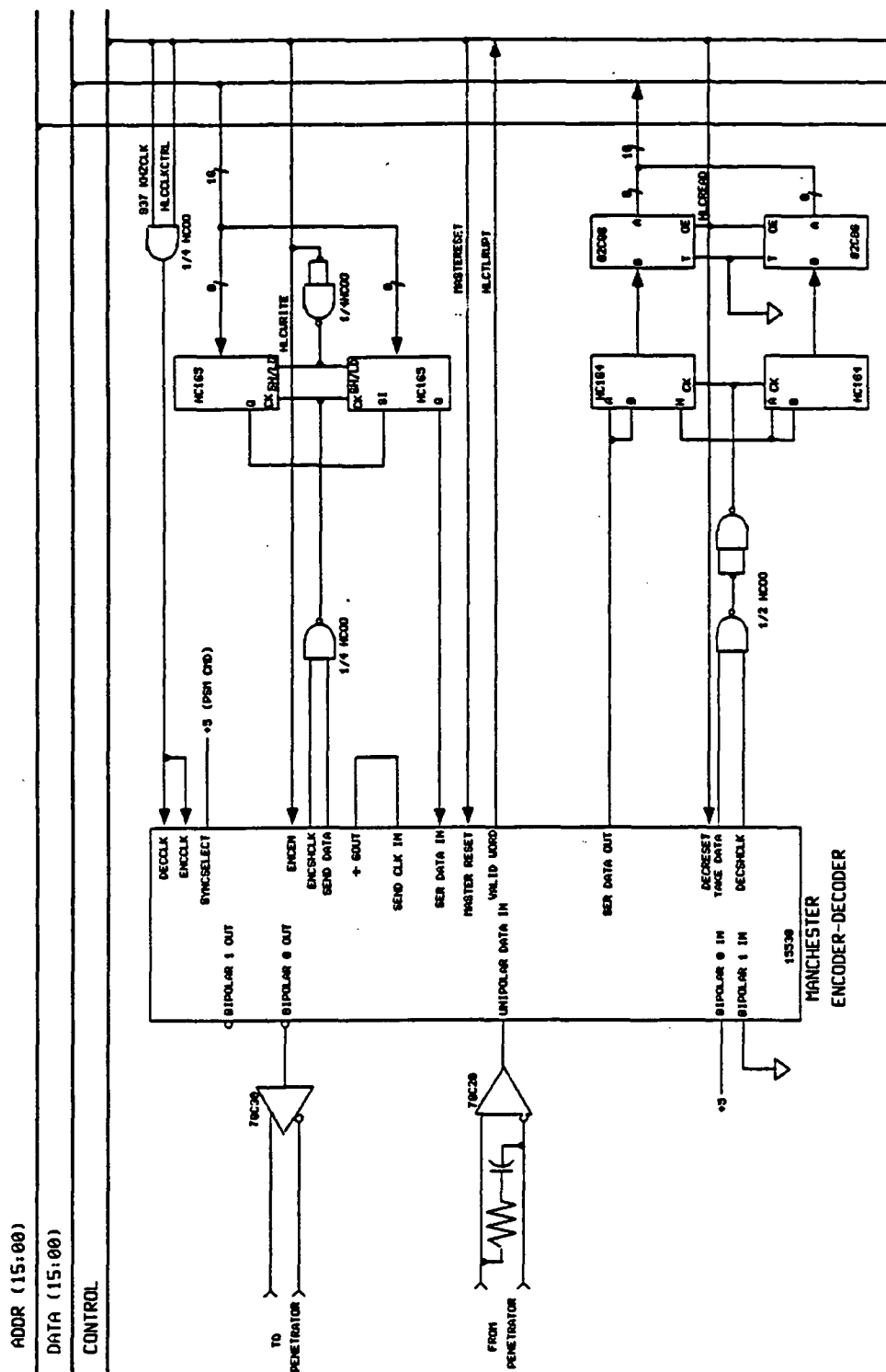


Figure 5.6-21 Penetrator Data Handling Hardline Controller



Figure 5.6-23 Alpha-backscatter Electronics Diagram

Figure 5.6-24 shows an implementation of the "plus-one" or "read-increment-write" logic required in each of the PHA's used in the penetrator. The design shown is for the alpha and proton modes only, at 512 channels by 8 bits; but the design for the 1024 channel by 16-bit x-ray mode is very similar. This type of logic is a good candidate for implementation by either a gate-array chip (without the RAM) or a custom chip (with the RAM). The next phase of the design will address this issue. For now, the cost tradeoff favors a discrete CMOS logic implementation of the PHA logic.

Data requirements for the alpha-backscatter instrument are given in Appendix G.

5.6.2.2.2 Penetrator Gamma-Ray Spectrometer Instrument

Figure 5.6-25 shows the basic elements of the gamma-ray spectrometer and its interface to the penetrator microcomputer busses.

Pulses from the First Stage Electronics (physically near the crystal) are applied to two different channels, one with a gain of twice the other. The reason for this split is to get more resolution at the lower energies. If the pulse is less than approximately 2.5 volts, the output from the X2 channel will be multiplexed to the PHA. Otherwise the output from the X1 channel will be multiplexed to the PHA.

The analysis will be 8192 channels by 16 bits. The PHA RAM will be readable by the penetrator microcomputer for subsequent transmission to the spacecraft. Before transmission, the data will be compressed typically 8:1 using the JPL-provided algorithm. The resultant savings in memory and telemetry requirements are shown in Appendix G.

The high voltage power supply required for the gamma-ray spectrometer is described in the penetrator converter section.

5.6.2.2.3 Penetrator Accelerometers

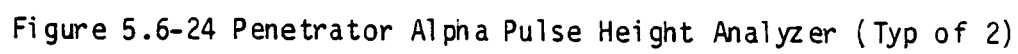
The penetrator will contain two triaxial high-range accelerometers and one low-range accelerometer. The sampling of these devices was discussed in section 5.6.2.1. Refer to Appendix I for details.

In addition to sampling the accelerometers at impact, the low-range accelerometer will be sampled at ejection and during the burn of the penetrator's solid rocket motor.

Since the selected accelerometers have built-in amplifiers, the interface electronics need only supply a constant excitation current of 2-20 mA. The output is typically ± 5 V.

5.6.2.2.4 Penetrator Temperature Probes

The penetrator will contain four thermocouples for science measurements: 3 deployable and 1 fixed. They will be sampled at 10-bit resolution and the data stored for later transmission. They will be sampled every minute for the first hour after impact and every hour subsequently.



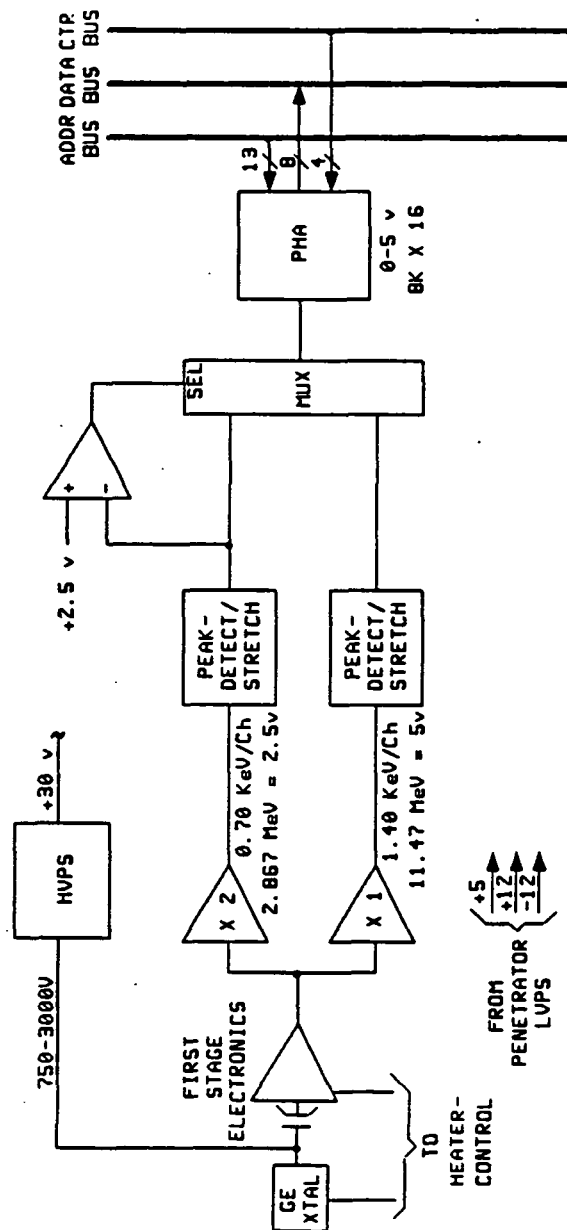


Figure 5.6-25 Gamma Ray Spectrometer Electronics Diagram

5.6.2.3 Penetrator Thermal

The baseline penetrator design contains five different heater subsystems. They are: crystal-anneal heater, gamma first-stage electronics heater, battery heaters (2 each), electronics heater, and rocket motor heater. Two battery heaters are required because the 18 battery cells are packaged in two separate modules as described in section 5.6.4

As described above for the PSM, the heater control loops are closed through the microcomputer, and the control is bang-bang. The crystal-anneal heater will only be used while the penetrator is on the spacecraft. The rocket motor heater will only be used during the approximately one hour coast phase from ejection to ignition.

Peak power allocations for the heaters are shown in Appendix J.

5.6.2.4 Penetrator RF

Figure 5.6-26 shows the subsystem diagram for the off-the-shelf FM transmitter selected for the penetrator. The transmitter, a cylindrical unit, will be mounted on the side of the penetrator electronics module in the aft end of the penetrator. Its antenna is a square microstrip patch antenna identical to that used for the receiver. The antenna will be mounted on the penetrator's rear face, adjacent to the solid rocket motor nozzle. Refer to the RF Report in Appendix E.

The specifications for the transmitter, an Aydin Vector Model TM-502/L are shown in Table 5.6-4

Table 5.6-4 Aydin Vector Model TM-502/L Transmitter Specifications

Total Harmonic Distortion: 1% Maximum for ± 300 KHz Deviation
Input Voltage: 24-32 Vdc with Reverse Polarity Protection
Input Current: 0.2 Amp Maximum
Size: 2.45-in. Diameter x 1.25-in. Excluding Cables
Weight: 6 ± 1 oz
Baseplate Temperature: -20° to $+71^{\circ}$ C
Relative Humidity: 95%
Vibration: Sinusoidal at 20 g from 20 to 2000 Hz in Each Axis
Shock: 15,000 g for 3 ms in Primary Axes (High-g Option)
Acceleration: 1000 g, Each Axis
Altitude: Unlimited
RF Power Output: 200 mw into 50 ohms
RF Load: Stable Operation Into 50 ohms with VSWR = 1.5:1
Output Frequency: Crystal-Controlled, 1435-1540 MHz (1500 for Penetrator)
Output Frequency Stability: $\pm .003\%$ of Specified, Including Setting Tolerance and Drift Due to Environment
Harmonic and Spurious Outputs: In Accordance with IRIG Standards
Modulation Type: FM
Input Impedance: 20 K Minimum
Deviation Sensitivity: ± 300 KHz/V rms
Frequency Response: DC to 500 KHz ± 1.5 db
Deviation Capability: ± 600 KHz Max
Linearity: 1% Maximum Best Straight Line for ± 300 KHz Deviation

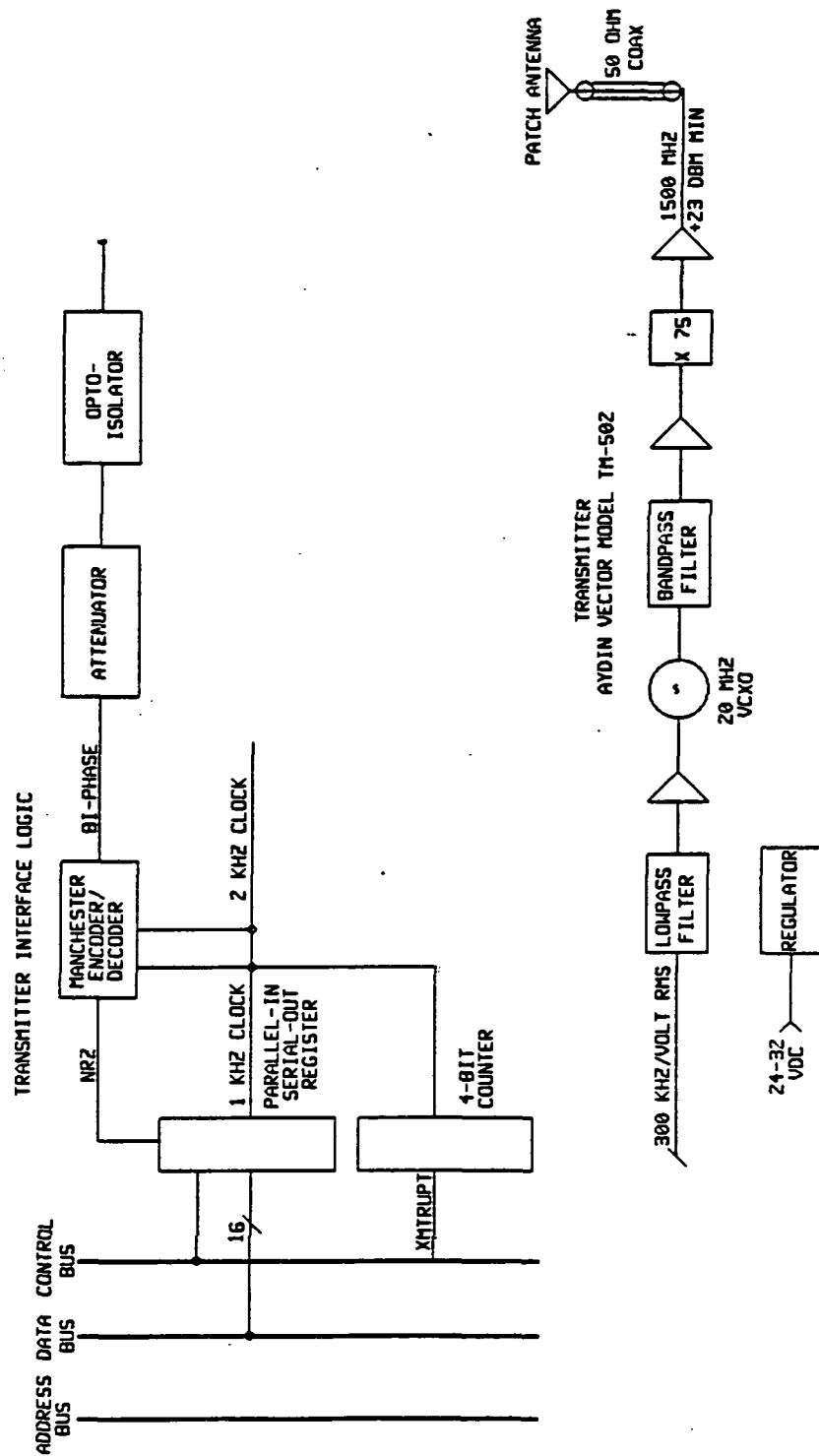


Figure 5.6-26 Penetrator Transmitter Diagram

Figure 5.6-26 also shows the logic used to interface the transmitter to the penetrator microcomputer busses. NRZ data will be strobed into the 16-bit parallel-to-serial register and shifted serially at 1 kbps through the Manchester Encoder chip and into the transmitter. The 4-bit counter will interrupt the microcomputer after each 16 bits have been shifted out of the register so that the next word can be strobed in.

5.6.2.5 Penetrator Power

Figure 5.6-11 shows that, before ejection, spacecraft power will be applied directly to penetrator heaters, RF transmitter, and power converter. Optical isolation and single-point-grounding discussions are the same as in section 5.6.1.4.

5.6.2.5.1 Penetrator Converter

Figures 5.6-27 and 5.6-28 show the Penetrator LVPS and HVPS Power Converter block diagrams. The penetrator LVPS converter design is identical to that of the PSM power converter previously described. The next project phase will include a cost-effectiveness comparison of using an in-house versus a JPL-supplied design for this converter and for the PSM converter.

The penetrator converter block also includes a high-voltage power supply. It is a programmable supply which converts a +30 V(dc) input to a 750 to 3000 V(dc) output for the gamma spectrometer crystal bias and 50 to 200 V(dc) for the alpha backscatter silicon detector. The HVPS figure shows that the control loop reference voltage is generated by a digital-to-analog converter, which is controlled by the penetrator microcomputer. This control will allow the output voltages to be stepped, typically at 250 volts per step up to 3000 V, in order to measure the gamma-ray detector's I/V characteristics, and at about 20 volts per step for the alpha instrument. An optimal fixed level will then be selected for normal operation of the alpha and gamma instruments. The supply's power dissipation can be minimized by setting the reference voltage to zero and turning off the complementary clock inputs.

5.6.2.5.2 Penetrator Battery

In order to minimize weight, the baseline design uses lithium thionyl chloride (Li/SOCl_2) cells, which have the highest energy density of any non-radioactive battery system. Galileo modules were also investigated, and Table 5.6-5 shows a comparison of their Li/SO_2 chemistry with lithium thionyl chloride. Appendix J shows that two parallel stacks of nine Li/SOCl_2 cells are required to support the mission. In comparison, three parallel stacks of thirteen Li/SO_2 cells are required. Based on the above module weights, the total weights for the two systems would be 3.54 kg (7.80 lb) for Li/SOCl_2 and 7.48 kg (16.5 lb) for Li/SO_2 .

The principal advantage of the Li/SO_2 battery is that it is qualified for use on the Galileo mission. If additional weight is acceptable or if penetrator power dissipation can be reduced during detail design, then the Galileo modules may be used.

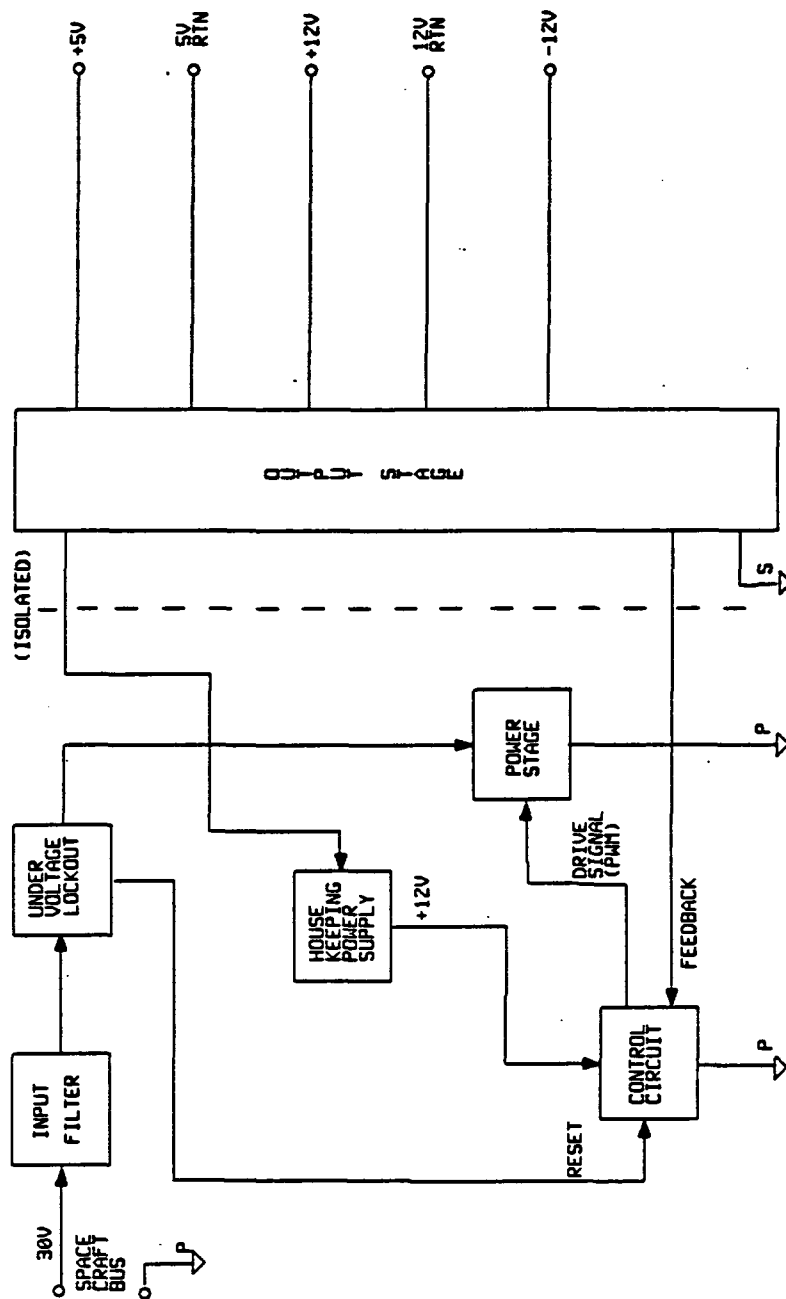


Figure 5.6-27 Penetrator LVPS Power Converter Block Diagram



-137-

Table 5.6-5 Lithium Sulphur Dioxide and Lithium Thionyl Chloride Battery Comparison

	Galileo Li/SO ₂ Module	CN PS Li/SOCl ₂ Module
Open-Circuit Voltage*	40 V	33 V
Operating Voltage*	26-36 V	24-31 V
Capacity @ -40°C	6-7 A hr	10 A hr
Energy Density	42.5 W hr/lb	67.7 W hr/lb
Size	3.2 x 3 x 14 in.	3.2 x 3 x 8 in.
Weight	5.5 lb	3.9 lb

*13 Cells for Li/SO₂; 9 Cells for Li/SOCl₂

Source: Honeywell, Defense Systems Division, Power Sources Center

For the four-year storage period, a temperature range below -10°C is recommended to minimize cell passivation and heating requirements. The coldest recommended temperature is approximately -55°C. For active operation, a range of +20 to +50°C is recommended, although operation to -40°C is possible with some loss of capacity. The battery will be brought on-line several minutes before ejection to allow its voltage to rise as the cell passivation layer decreases with load.

A power transfer switch is required to keep the battery open-circuited during the four-year transit period, except during any testing that may be required by mission operations. Blocking diodes are required in series with each stack of cells to prevent reverse charging from either the stronger stack or from the spacecraft power bus prior to ejection. Cell bypass diodes will be used to maintain the battery circuit in the event of an open-cell failure.

Cell safety features will include an internal pressure vent to prevent cell rupture and an internal fuse to prevent overheating caused by internal shorting. The action of a fuse in a single cell can either make the cell an open circuit or create a bypass short circuit, depending upon construction. The external bypass diodes are recommended in addition to the fuses. Lithium thionyl chloride cell safety is certainly a design issue but not a critical issue, since these cells are presently used in shuttle astronaut space-suits to power communications, temperature-control, and other subsystems.

5.6.2.5.3 Penetrator Power Management Unit

This unit has the same function as the PSM power management unit, described above. In the penetrator it controls the DAS and transmitter power switches shown in Figure 5.6-2 (Penetrator Electronics Diagram). Again, refer to Appendix J to see the effect of these switches on penetrator average power dissipation.

5.6.2.6 Penetrator Propulsion

The function of the penetrator propulsion electronics is to ignite the solid rocket motor during the post-ejection coast phase, at a time redundantly

stored in the penetrator microcomputer memory before ejection. This subsystem must also provide the safety inhibits required by NHB 1700.7A (Safety Policy and Requirements for Payloads Using the Space Transportation System). Quoting from paragraph 202.2.a of NHB 1700.7A: "[Payloads] shall be equipped with an S&A (safe and arm) device that provides a mechanical interrupt in the pyrotechnic train immediately downstream of the initiator. A minimum of two additional inhibits shall be provided." Use of a safe and arm device is not practical with the present front burner motor design. In lieu of this, we propose the three-inhibit circuit shown in Figure 5.6-29. We understand that similar circuits have been approved by JSC safety on previous programs.

Normal circuit operation is as follows:

- (1) Q1 and Q2 are off, and the Interlock Switch is closed prior to ejection.
- (2) The penetrator stores the elapsed time-to-ignition in RAM via the hardline control interface.
- (3) At ejection the Interlock opens, removing one inhibit from the circuit.
- (4) The penetrator program loads the rocket motor ignition time into the Event Timer.
- (5) When the Event Timer times out, the microcomputer sends the ARM signal to turn on Q1 and to charge the capacitor to 30 volts, removing the second inhibit.
- (6) The microcomputer then removes the ARM signal, turning off Q1, and reads the ARMMON voltage to verify the capacitor is charged.
- (7) Before R2 can bleed the capacitor's energy, the microcomputer sends the FIRE signal, turning on Q2 and dumping the energy into the initiator to ignite the motor.
- (8) The program monitors the axial accelerometer to verify that ignition has occurred.

Even if Q1 and Q2 are turned on inadvertently, and the interlock is open, the initiator will not ignite the motor because R1 limits the current to less than the one ampere-one watt no-fire spec of a NASA standard (or equivalent) initiator.

Note that the interlock is in parallel with the initiator. The interlock will be a short, low-impedance loop terminating at the separation connector.

5.6.2.7 Penetrator Interfaces

5.6.2.7.1 Penetrator/PSM Power Interface

Refer to Figure 5.6-11 (CNPS Power and Grounding Diagram).

This figure shows that spacecraft prime power is routed through the PSM, through a power switch to the penetrator where it is diode-or'ed with penetrator battery power. The penetrator battery power transfer switch will be closed just before ejection and just before the PSM's power switch is opened, bringing the battery online.

5.6.2.7.2 Penetrator/PSM Hardline Controller Interface

This circuit is identical to that described for the PSM in section 5.6.1.7.2.2.

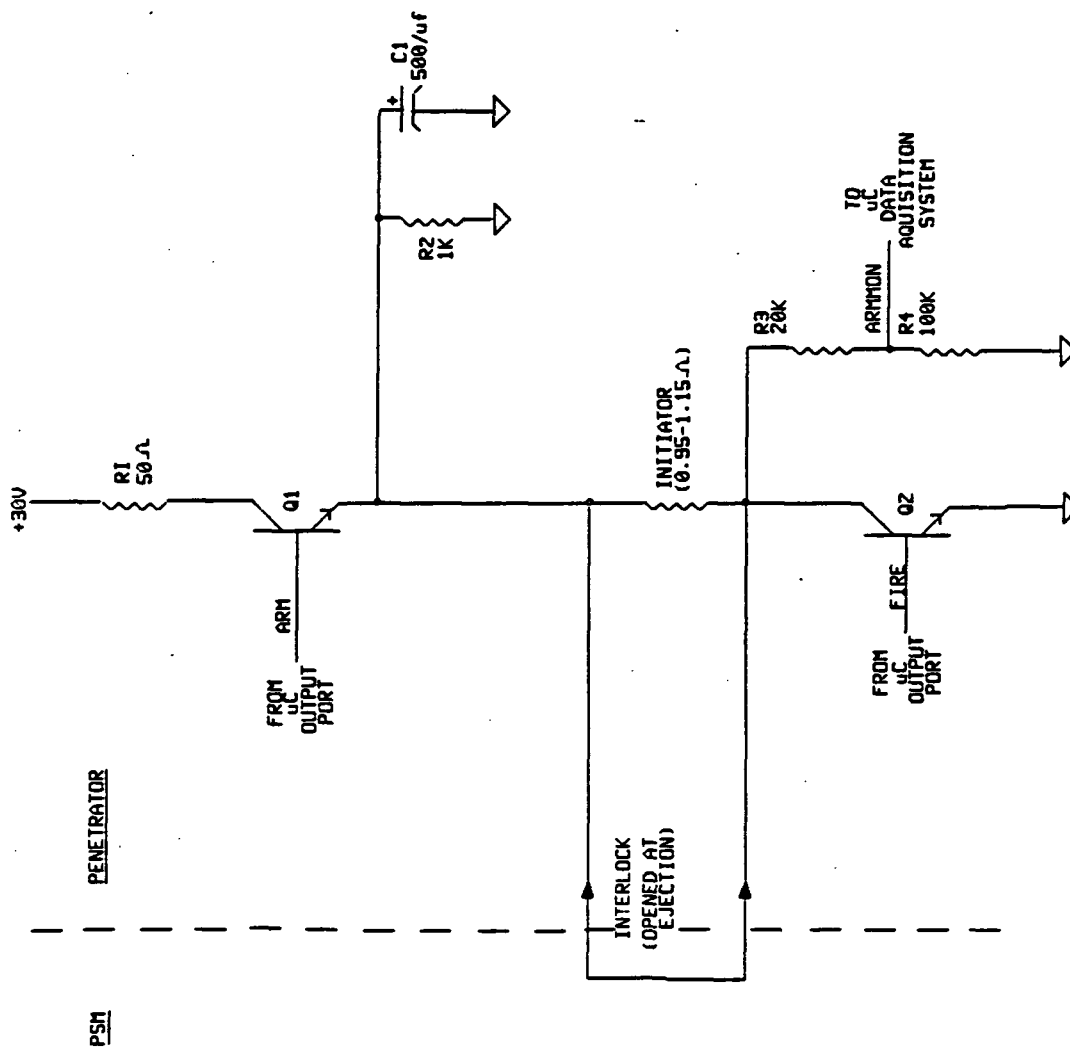


Figure 5.6-29 Penetrator Rocket Motor Electrical Interface

5.6.3 Parts List

The CNPS electronics parts list, which was generated from the design of the various subsystems discussed above, is detailed in Appendix K. Wherever possible, the parts are based on schematic-level detail. Some circuits are based on block-diagram level detail using parts from similar designs. The goal was to provide sufficient detail to allow scoping the electronics packaging effort to a reasonable degree of accuracy.

5.6.4 Packaging

Refer to Figures 5.6-30 through 5.6-32.

The box designs shown in these figures are based on the parts list developed during the study. This list, in turn, is based on a relatively conservative packaging approach; i.e., the use of DIP and flatpack IC's instead of chip carriers, for example. Alternate approaches, such as use of more surface-mount technology parts and use of gate arrays and standard cell devices need to be considered as the CNPS and CRAF designs proceed. In the CNPS the alternate approaches offer a weight reduction versus cost tradeoff. The availability of the IC's in chip carrier packages for the CRAF mission will be a JPL decision, but the use of gate arrays and standard cell chips should be considered separately. A good candidate for use of these chips is the PHA control logic used in the alpha and gamma instruments. Usage would allow a weight reduction and an increase in system reliability.

Table 5.6-6 shows the printed circuit board area requirements as derived from the CNPS Electronics Parts List. Standard values were used for parts per square inch based on the part type and layout on a 4-8 layer board. "I/O" circuits include all of the interface, driver, etc. circuits shown on the parts list.

Table 5.6-6 Printed Circuit Board Area Requirements

Subsystem	Circuit	Required Area (In. ²)	Board
PSM	Microcomputer	23.3	A1
	Hardline Controller	5.6	A1
	DAS	7.6	A2
	BIU	9.0	A2
	I/O	24.1	A3
	LVPS	20.0	A4
Penetrator	Microcomputer	27.5	A1
	Hardline Controller	5.6	A1
	DAS	20.8	A2
	ALPHA	63.9	A3 & A4
	GAMMA	32.8	A5
	I/O	32.7	A6
	LVPS	20.0	A7
	HVPS	20.0	A8

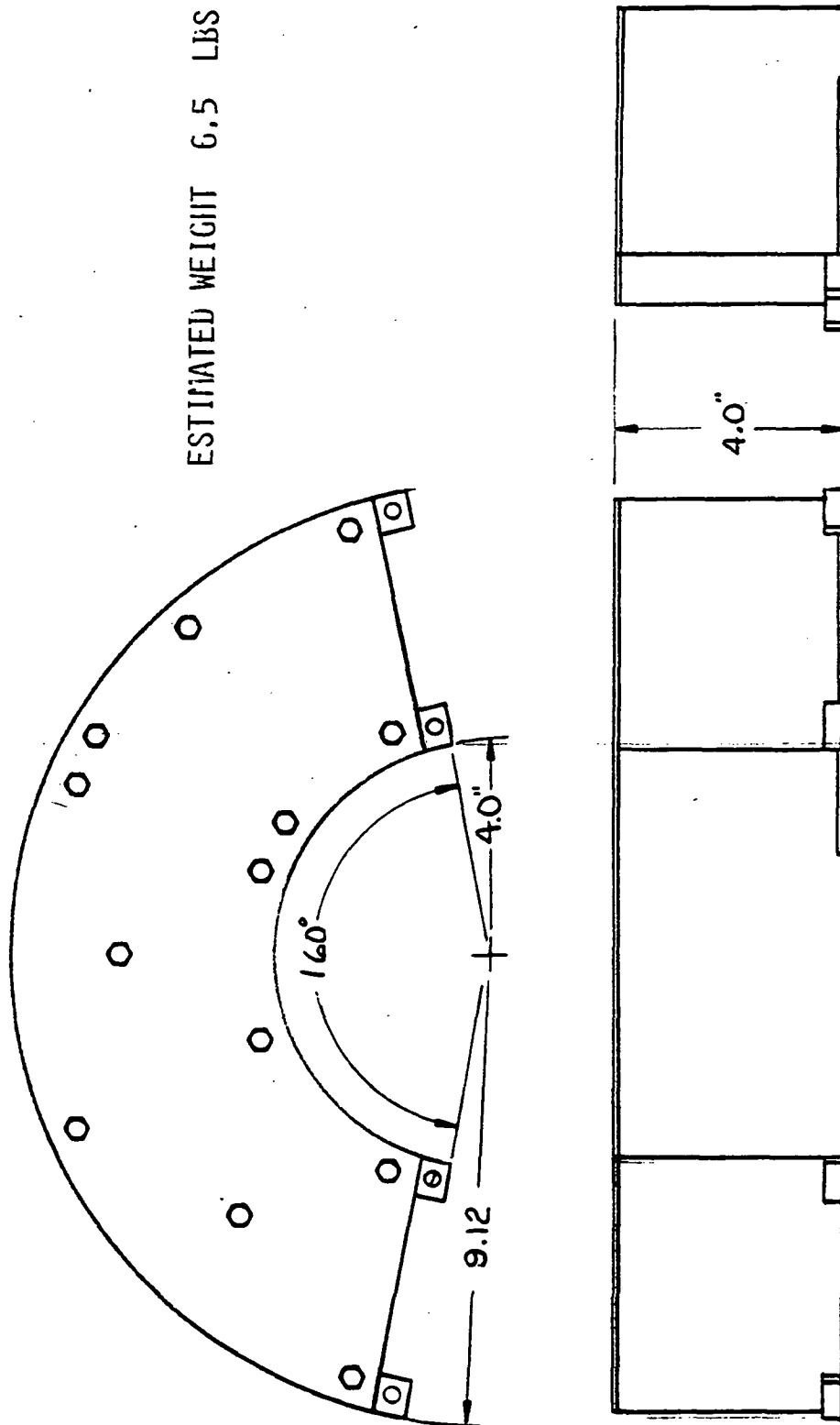
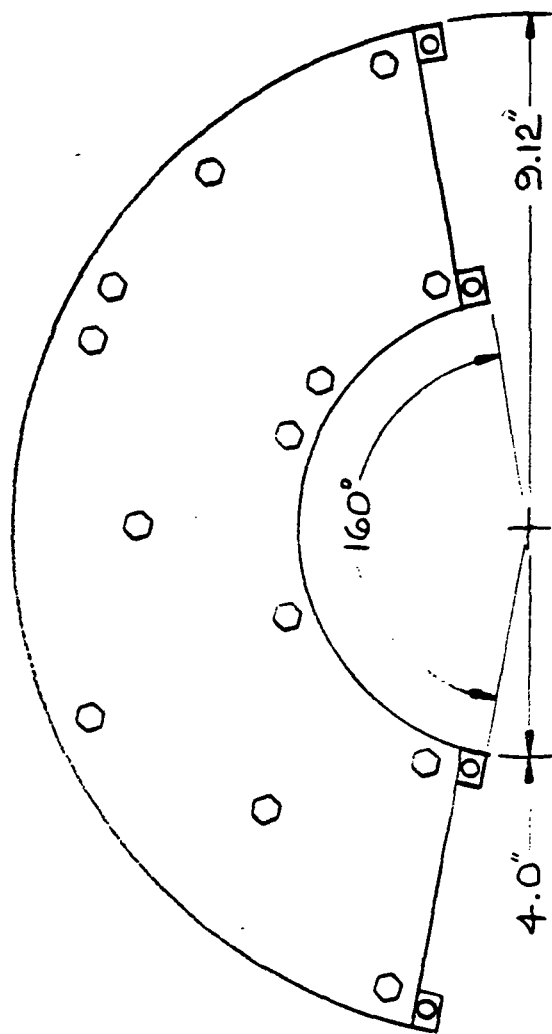


Figure 5.6-30 Penetrator Electronics Module



ESTIMATED WEIGHT 5.8 LBS

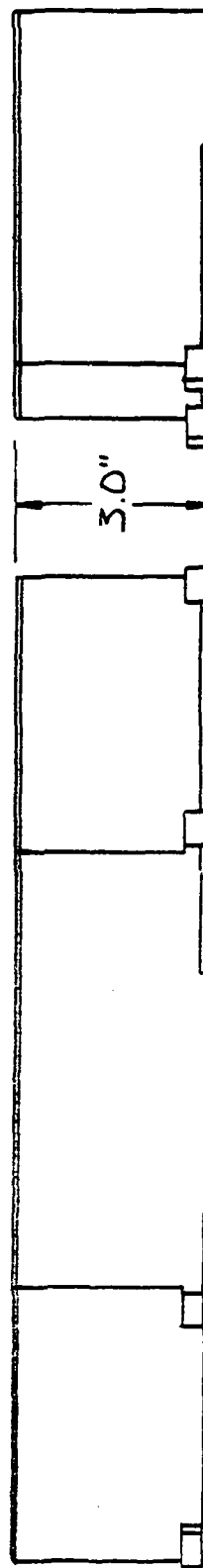


Figure 5.6-31 Penetrator Support Module

ESTIMATED WEIGHT 3.5 LBS

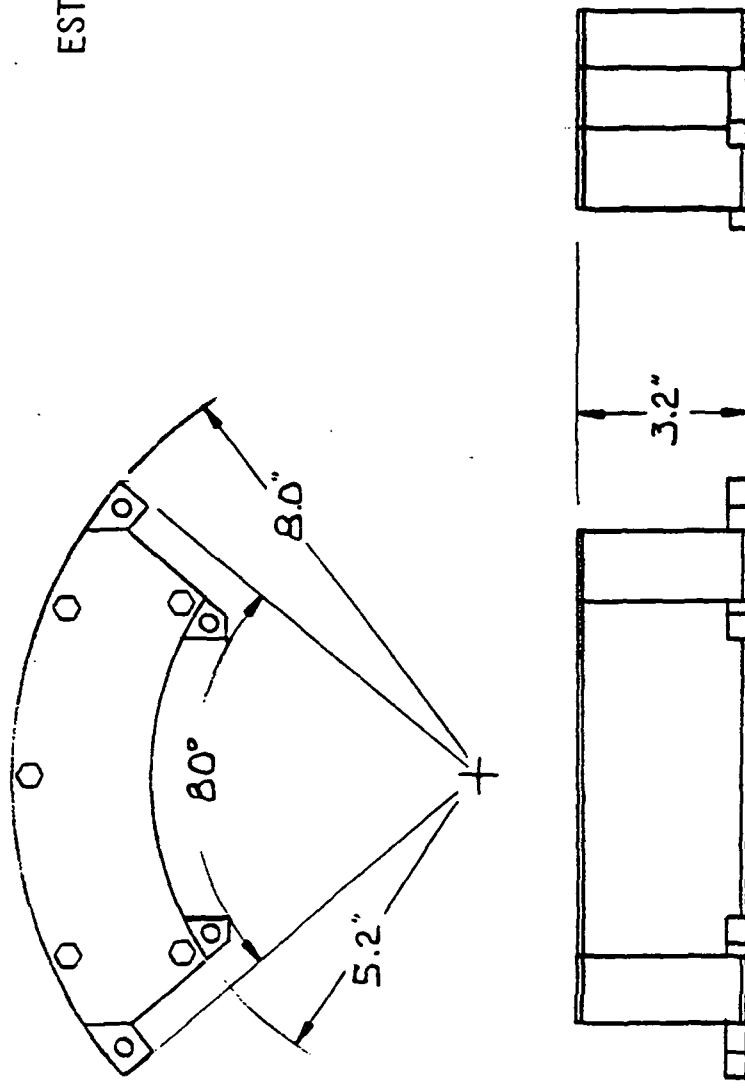


Figure 5.6-32 Penetrator Battery Module

5.6.5 Cabling

Figures 5.6-33 and 5.6-34 show the Cabling Diagrams. The following tables show the interface signals associated with each of the cables shown in the referenced figures is attached as Appendix L.

5.6.6 Ground Support Equipment

CNPS Ground Support Equipment (GSE) consists of a combination of Bench Checkout Equipment (BCE) and System Test Support Equipment (STSE).

Figures 5.6-35 and 5.6-36 show the CNPS Electronics BCE. Figure 5.6-35 shows the top level BCE requirements. There are three basic test modes, allowing the BCE to test the PSM and the penetrator separately or combined. To do this, the BCE must simulate the spacecraft, the PSM, and the penetrator.

Figure 5.6-36 shows that the BCE concept is microcomputer-based, with custom logic to perform the required simulations. Part of the custom logic will consist of circuits designed for use in flight, on the PSM and the penetrator. For example, the Hardline Controller, Transmitter, and Receiver will be identical to their flight counterparts. Other custom logic, such as the CDS Simulator and Pyro Initiator, will be new designs. Custom logic will be interfaced to the microcomputer through the BCE Bus Interface Unit (BIU), which will route command and data information as required. Either a General Purpose Interface Bus (GPIB) or RS232C Bus will be used to handle the transactions, depending on further analysis of BCE system throughput requirements.

Test connectors on the PSM and penetrator Electronics Modules will allow STSE access to critical test points while the system is cabled to the spacecraft.

The microcomputer selected for the initial design concept is the HP Integral Personal Computer. It was selected primarily because of its portability and its internal features: electroluminescent display, disc drive, and printer. Its relevant features are shown in Table 5.6-7.

Table 5.6-7 HP Personal Computer Features

<p>Motorola 68000 Microprocessor Running at 8 MHz Graphics Processor with 32 K bytes of Dedicated RAM 256 K Bytes of ROM 512 K Bytes of RAM, Expandable to 1.5 M Bytes Internal Disc Drive; 3.5-in. Double-Sided, Double-Density Display: Electroluminescent, 9-in. 255 x 512 Pixel Bit-Mapped, 24-Line x 80-Character 90 key Keyboard Internal Printer: Inkjet, 150 cps, 8.5 x 11 in. Paper Size: 7 x 13 x 16 in. Weight: 25 lb Input/Output: GPIB, 2 Expansion Ports, 2 Human Interface Loops System Clock: 1 msec Resolution, Lithium Battery ROM Software: HP-UX/RO, Personal Applications Manager, HP Windows Optional Peripherals: Disc Drives, Printers, Graphics Plotters, Interfaces (Including RS232C), Memory Expansion Cards, Modem Accessories: HP Mouse, Bus Expander, Cover, Carrying Case, Cables</p>

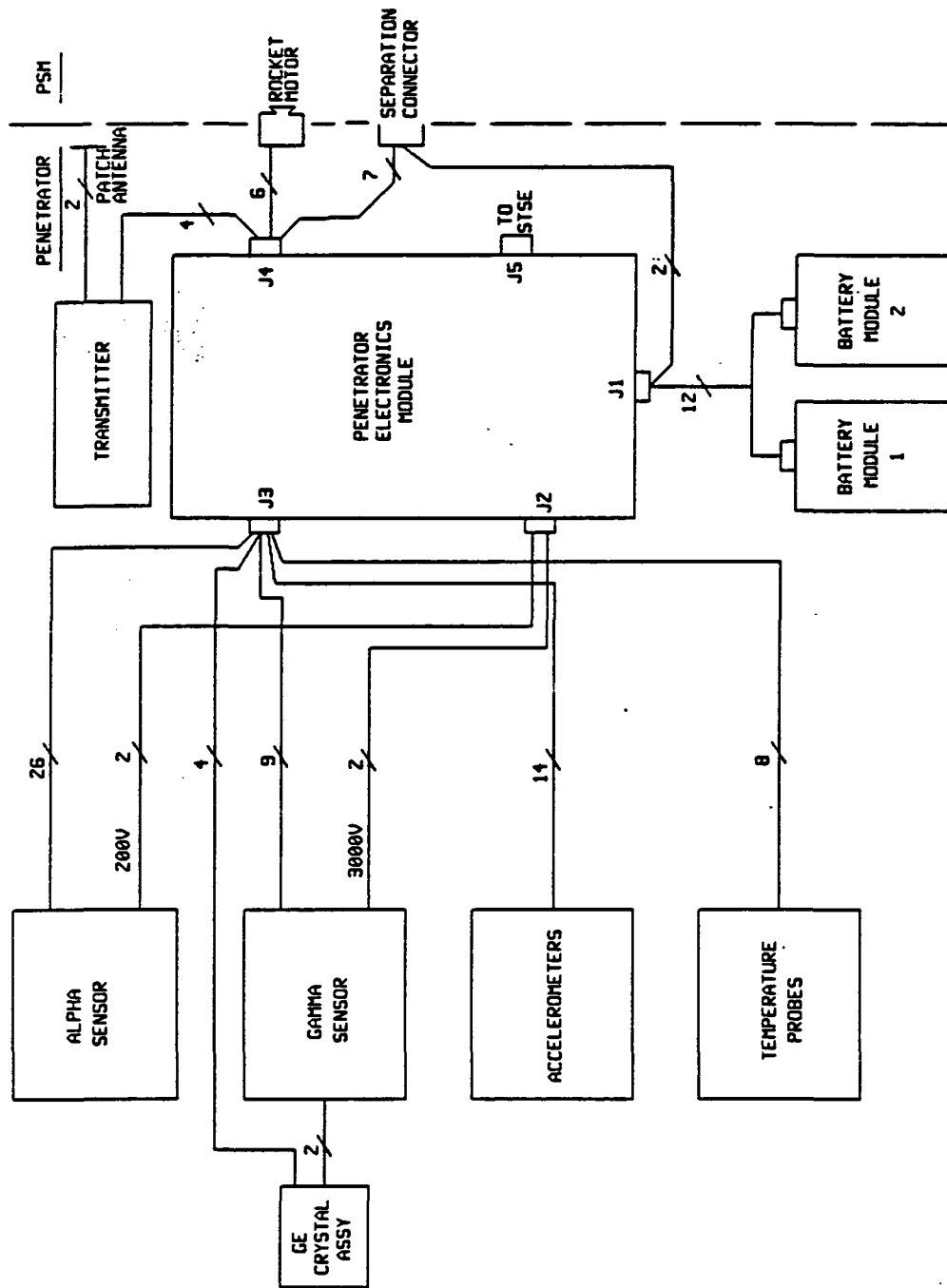


Figure 5.6-33 Penetrator Cabling Diagram

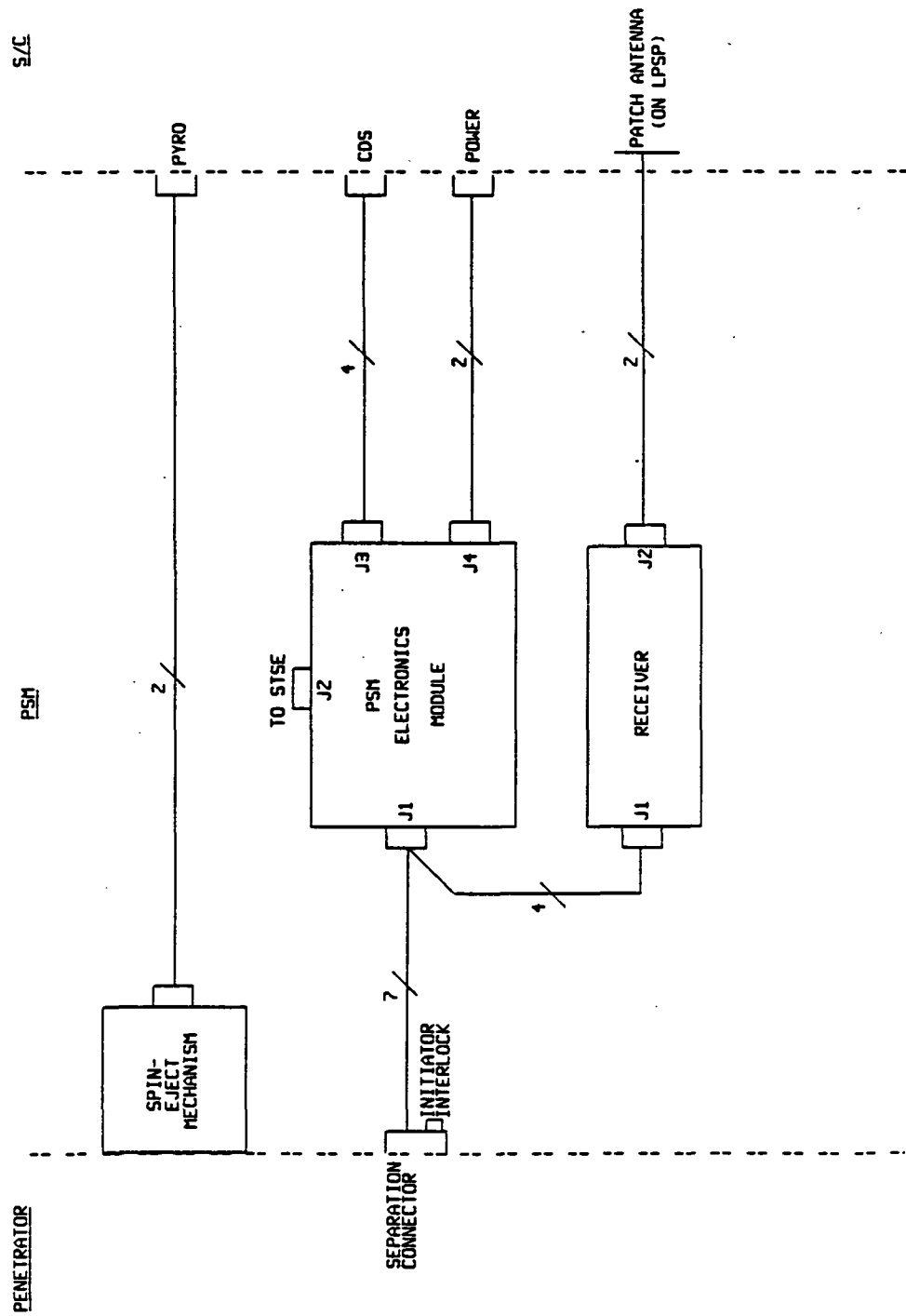
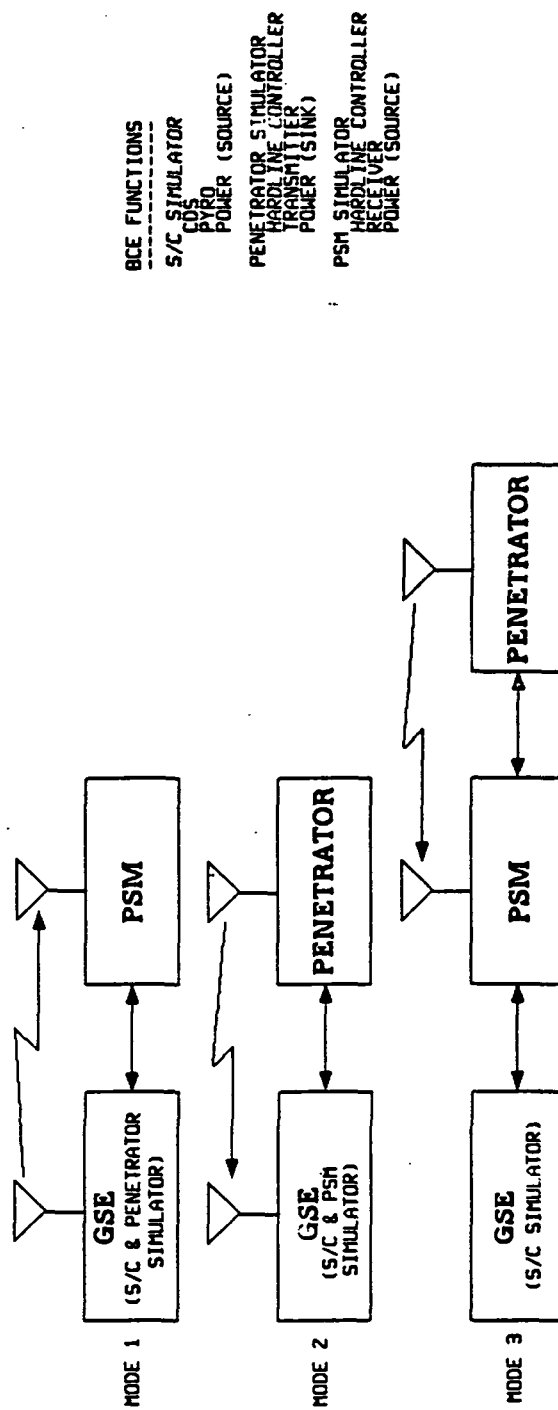


Figure 5.6-34 PSM Cabling Diagram



BCE FUNCTIONS
S/C SIMULATOR
 CDS
 PYRO
 POWER (SOURCE)
PENETRATOR SIMULATOR
 HARDLINE CONTROLLER
 TRANSMITTER
 POWER (SINK)
PSM SIMULATOR
 HARDLINE CONTROLLER
 RECEIVER
 POWER (SOURCE)

Figure 5.6-35 CNPS Electronics BCE

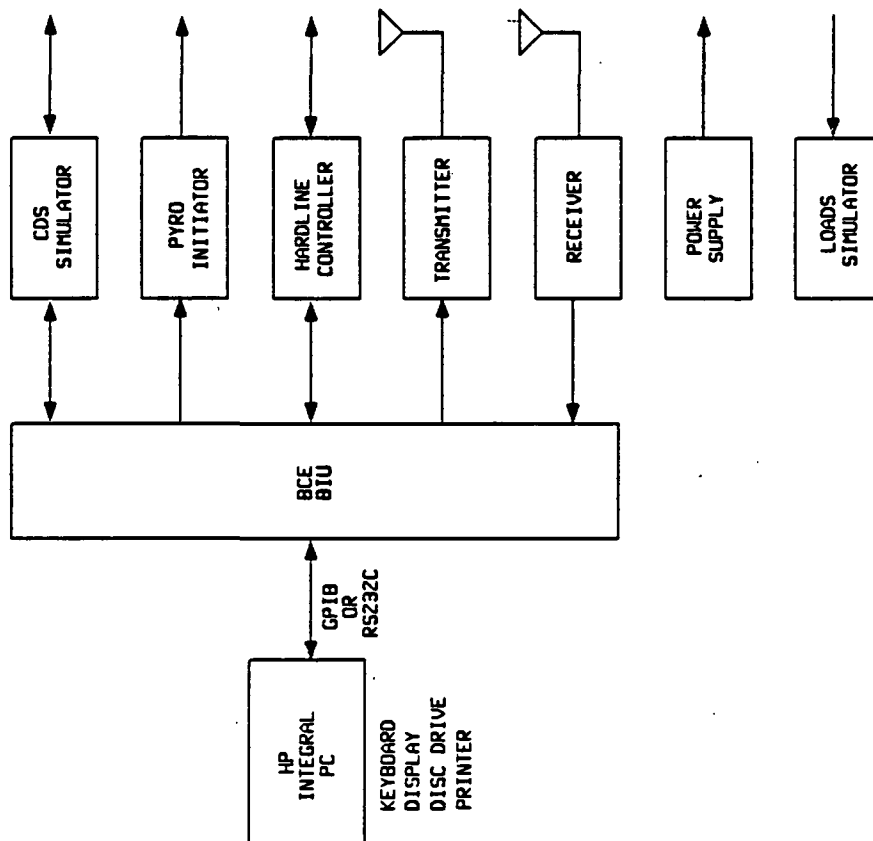


Figure 5.6-36 CNPS Electronics BCE

This computer will presently support applications programs written in BASIC and C, and other languages in the future. It is anticipated that the CNPS application will require 4000 to 7000 lines of code, based on similar designs for the Galileo instruments (ASI, NFR, and Nephelometer).

The computer can be transported in its own case, with the custom logic housed in a separate metal suitcase. The system will operate from 120 V(ac) facility power.

5.7 Ge Detector Enclosure and Contamination Issues

The germanium crystal must be hermetically sealed to protect it from electrical leakage caused by contaminants present in normal atmospheric air. Besides particulates, such contaminants include water vapor, organic vapors, carbon dioxide and other condensable gases. Since the detector is operated at very low temperatures, these gases can form solid or quasi-liquid layers on the surface of the crystal. Such layers provide an electrical leakage path for the high voltage bias across the high impedance of the detector. This becomes a dominating noise source to the Field Effect Transistor (FET) input stage of the electronic preamplifier. Particulate contamination can have a similar effect.

5.7.1 Conventional Laboratory Ge Detector Enclosures

In conventional commercial and laboratory practice, the detector is sealed into its enclosure using "O" rings and sometimes epoxy seals. The sealed volume is pumped externally with a very clean pump, such as a cryopump, tubomolecular pump, or well-trapped diffusion pump, through a special valve which can be sealed with the vacuum pump in operation. The closed-off system is then continuously pumped via the action of the molecular sieve or charcoal trapping material incorporated near the liquid nitrogen (LN₂) cooled detector. The system is designed thermally to allow the detector to be somewhat warmer (from 10 to 50 K) than the sieve itself, guaranteeing differential pumping which favors transfer of condensables from the crystal into the trapping material. Once such a system is allowed to reach room temperature, the condensable phases which leaked in slowly through the "O" ring seals, will vaporize and be redistributed in the enclosure. Proper re-activation of such a system depends on the proper procedure and proper detector design, since simple addition of LN₂ may cool the detector sufficiently rapidly that some vapor will condense onto the crystal before being trapped in the molecular sieve absorbent, thereby degrading the performance of the detector. "Recycling" the system can remove the contamination, especially if an external pumping system is employed to remove the accumulated condensables while the system is warm.

This common approach is not totally practical for the Comet Nucleus Penetrator System because the pumping and valving system is too bulky and incompatible with the mission constraints and the cooling method is dictated by an entirely different set of constraints. Due to the long leadtime delivery of the experiment to the CRAF Project, up to 18 months may elapse from the time of final evacuation until going into the vacuum of space. The sealed detector enclosure is susceptible to in-leakage during this entire time. Furthermore it is susceptible to outgassing of materials in the enclosure during the entire 6.5 years from final evacuation to end of mission.

5.7.2 Inert Gas Backfill Approach

Because of the in-leakage and the outgassing problems, we have considered back-filling the detector enclosure with an inert gas, such as neon or helium to maintain a positive outward pressure, thus minimizing in-leakage of condensable contaminants. However, since small leaks are dominated by processes of diffusion, it is not the pressure differential that controls

in-leakage, but rather the concentration gradient of the contaminant gases across the leak. Such tortuous leak paths will still allow some pervasive inward migration of undesirable gases.

Another problem with a sealed filler gas is that it can leak outward once the experiment is in space. From a contamination standpoint, this is not a problem. But if the gas loss is enough to allow the pressure to decrease to a value in the Paschen pressure range of 0.1333 Pa to 1333 Pa (1×10^{-3} to 10 torr), breakdown (arcing, or high intensity corona) of the high voltage bias across the detector would occur, destroying the detector, and/or the FET preamplifier input or at best creating very high noise on the signal. Even with DC blocking, provided by an AC coupling capacitor, the induced voltage can cause irreversible damage to the sensitive FET. This condition is to be avoided at all cost, since it cannot be remedied by spacecraft command. One approach would be to strongly limit the AC current-supplying capacity of the High Voltage Power Supply (HVPS) using a combination of resistive and inductive series impedance. In addition, a small series resistor and back-to-back clamping diodes could be placed at the input of the FET (these techniques add noise to the system). Finally, one could monitor the current-voltage (I-V) curve of the detector bias supply with an automatic shut-off when a maximum allowable current limit is exceeded. This not only diagnoses the "health" of the detector, but could also detect micro-discharges due to current-limited corona and arcing.

However, if the detector enclosure is sealed with one atmosphere of helium, any significant out-leakage of the fill gas can easily be detected. The sensitivity of the leak measurement is high enough to assure that the seal will prevent any significant in-leakage of condensible vapors. The outleakage, M, during 5 years time in space would be,

$$M = \Delta PV = QT$$

where:

ΔP = Pressure decrease due to out leakage in 5 years
 V = Empty volume in detector enclosure = 0.07 liters
 Q = Leak rate
 T = Time in space vacuum (5 years) = 1.58×10^8 sec

The minimum He leak rate detectable with the Martin Marietta ultra-sensitive leak detector is $Q = 1.333 \times 10^{-13} \text{ Pa m}^3 \text{ s}^{-1}$ (1×10^{-12} torr liter/s). Thus the smallest end-of-mission pressure drop that could be detected would be:

$$\Delta P = QT/V = 0.3066 \text{ Pa } (2.3 \times 10^{-3} \text{ torr})$$

This would be an insignificant pressure drop relative to the original pressure. Therefore any significant out-leakage could very easily be detected.

Furthermore when one calculates the total quantity of water vapor which would leak in under the worst case condition of exposure to 100% humidity for 18 months, one gets $7.693 \times 10^{-8} \text{ Pa m}^3$ (5.77×10^{-7} torr liters). This amounts to less than 10^{-4} monolayer of water molecules distributed over the inner areas of the detector enclosure--not enough to cause any voltage leakage across the detector surface.

5.7.3 Permanent Vacuum Seal

If the enclosure is instead permanently sealed under a vacuum, then a separate problem is that of outgassing. Over very long periods of time, especially when the materials are mechanically stressed (such as at launch), additional outgassing of the materials inside the enclosure can occur. These outgassing products could be deleterious and migrate onto the detector. Another potential problem results from the commercial practice in growing ultra-high purity germanium crystals of employing a reducing atmosphere of pure hydrogen during the process. This traps hydrogen in the crystal. The raw crystal can be outgassed of this trapped hydrogen to some extent by pumping while the crystal is at high temperature, but there is a practical temperature limit, above which the natural contamination of trace copper atoms at the outside surface will diffuse inside and ruin the mobility properties of the crystal. Once the crystal is converted into a gamma detector, by application of the lithium and ion implantation of the boron, it can no longer be raised above a temperature of about 125°C because of the excessive migration of the lithium ions. This renders further outgassing very difficult. Even if the crystal enclosure is thoroughly evacuated and perfectly sealed, the four to six years that must elapse before powering up the detector at the comet could allow significant build-up of hydrogen gas due to diffusion through the crystal and release from the surface. The pressure build-up could be sufficient to reach the Paschen pressure range, resulting in dangerous high voltage breakdown.

A method of solving this outgassing problem is to provide a suitable active getter to continuously remove the hydrogen by chemical action. An excellent material for this purpose is the zirconium-aluminum getter manufactured by SAES. This getter pumps hydrogen and other active gases even at room and lower temperatures. We have generated a configuration concept for the detector containing 3.3 grams of this getter. It will absorb 133.3 Pa m³ (1000 torr liters) of H₂ and still maintain a hydrogen pressure in the enclosure below 1.333×10^{-10} Pa (10^{-12} torr) at 25°C. The pressure would rise to only 1.333×10^{-8} Pa (1×10^{-10} torr) during the 1000°C crystal anneal cycle and would drop to well below 1.333×10^{-10} Pa (1×10^{-12} torr) after cooldown to 100 K. Noble gases and perhaps certain relatively non-reactive gases are not pumped, allowing some build-up of pressure beyond the original ultra-high vacuum. Thus care must be taken to see that such gases are not significantly high in the outgassing products inside the enclosure. The gettering material must be activated by heating in a continuously pumped vacuum. This means both the getter and detector/enclosure must be assembled in an ultra-high vacuum system, without allowing exposure to air or other contaminated atmosphere. In addition, the getter must not contain elements in quantities which could cause interference with the measurements of the cometary composition and must not be a source of contamination itself (e.g., particulates). It also must not contain any trace radioactive elements which would contribute directly to the gamma ray spectrum. All these conditions are met by the Zr-Al getter.

The principal drawback of the permanent vacuum seal approach is the inability to verify that the seal integrity is adequate to protect the detector enclosure from pressure buildup to levels where high voltage discharge would occur. A leak has to be smaller than 2×10^{-18} m³ s⁻¹ (2×10^{-15} liters/second)

in order to avoid reaching the Paschen pressure range during the 18 month pre-launch exposure to the atmosphere.

The maximum allowable leak rate is calculated from

$$F = \frac{P_m V}{P_a T}$$

where: P_m = Maximum allowable internal pressure = 0.1333 Pa
 (1 x 10⁻³ torr)
 P_a = External atmospheric pressure = 1.014 kPa (760 torr)
 V = Empty volume in the crystal enclosure = 7 x 10⁻⁵ m³
 (0.07 liters)
 T = Time in seconds between evacuation and launch (18 months)
 = 4.7 x 10⁷ s

Thus $F = 2.0 \times 10^{-18} \text{ m}^3 \text{ s}^{-1}$ (2.0 x 10⁻¹⁵ liters/second)

If we assume that the getter could absorb all the N₂ and O₂ which leaks in, then the pressure will be dominated by the 1% atmospheric argon which leaks in. This could relax the leak tightness requirement to $F = 2.0 \times 10^{-16} \text{ m}^3 \text{ s}^{-1}$ (2.0 x 10⁻¹³ liters/second). If one were to preload the detector enclosure with He at 1.333 x 10⁻² Pa (1.0 x 10⁻⁴ torr) as a leak tracer then the leak detector sensitivity, Q_L , required to detect it would be $Q_L = P_i F_{He}$

where: P_i = Internal Helium Pressure = 1.333 x 10⁻² Pa
 (1.0 x 10⁻⁴ torr)
 F_{He} = Leak conductance of the detector enclosure leak for He
 = 2.72 F = 5.44 x 10⁻¹⁶ m³ (5.44 x 10⁻¹³ liters/second)

Thus the required leak detector sensitivity would be

$$Q_L = 7.252 \times 10^{-18} \text{ Pa m}^3 \text{ s}^{-1}$$

(5.44 x 10⁻¹⁷ torr liters/second)

The current limit of the Martin Marietta ultra-sensitive leak detector is $Q_L = 1.333 \times 10^{-12} \text{ Pa m}^3 \text{ s}^{-1}$ (1.0 x 10⁻¹² torr liters/second). This is significantly less sensitive than needed. The internal pressure would have to be 227 Pa (1.7 torr) before we could measure the leak rate with sufficient precision. This pressure is certainly right in the Paschen pressure range and makes the vacuum sealing approach questionable.

The only way of ascertaining that the detector enclosure pressure had not built up to a discharge level would be to test the detector for high voltage discharge periodically during the 18 month pre-launch period.

5.7.4 Continuously Pumped Configuration

Based upon established laboratory experience, a good method for assuring detector cleanliness would be to incorporate a very small ion pump directly into the detector enclosure. This approach has been used for an infrared

sensor for a space application, which also involves cryogenic cooling. However, there is the drawback that the ion pump contains titanium, samarium, some iron and possibly other elements which could cause interferences with the gamma spectrum. In addition, the pump would have to be powered almost continuously because if it were allowed to be off, and the pressure rose too high, it might not restart properly and/or could draw very high power which would heat the detector and enclosure.

5.7.5. Enclosure Vented to Space

Another way to solve the problem of long-term effects would be to take advantage of the clean and very hard vacuum of space. The detector enclosure could be hermetically sealed, but contain a very small valve. If this valve were normally closed, but could be opened electromechanically, then the opportunity to outgas the detector enclosure could be used prior to operation at the comet. After impact of the penetrator into the nucleus, it would be preferable for this valve to be closed. This is to prevent migration into the detector housing of water vapor and other gases which are created from the dissipation of kinetic energy during the impact and by subsequent heat dissipation in the electronics section during normal operation.

One method of preventing such migration is to provide an adsorbent trap inside the vent line from the detector enclosure. Even though the vent and the detector crystal would be at the same temperature, the trap material would preferentially take up such vapors because of its higher surface area and adsorption energy and because it would be placed in the path of the incoming vapors. The valve could then be a one-shot type. This allows a highly miniature device, since no solenoid is required, and the seal could be of a much lower leak rate than that of a reversible valve. At Martin Marietta, we are currently developing such a valve, under IR&D task D-91D. The valve and trap could also be mechanically decoupled from the remainder of the penetrator structure, thereby maintaining the high thermal impedance desired between the detector and structure. Only the wires required to electrothermally open the seal (an indium alloy) would provide heat conductance. It may be possible to transformer couple this circuit, or to open the path by impulse fusing one or both of the wires after the vent is opened. In this design approach, it would be possible to assemble the detector into its enclosure under clean-room, but not vacuum conditions. Final evacuation and decontamination of the detector and enclosure could be through a pinch-off tube, made of copper or other suitable, non-interfering material. Such an approach would complicate the detector enclosure configuration.

Selection of a final method for detector encapsulation will require detailed planning and experimental study to optimize reliability and minimize cost. For design purposes, we have shown the permanently evacuated/gettered enclosure approach since this provides the simplest configuration and thereby reduces reliability concerns in implementing simultaneously the requirements for contamination control, high voltage isolation, thermal isolation, and shock protection. However, the helium filled approach appears to be the most promising and therefore needs to be tested carefully.

5.8 Propulsion System for Penetrator Implant Velocity

The principal objective for the penetrator propulsion motor is to provide a velocity impulse of $\Delta v = 40$ m/sec when the penetrator is about 1 km from the comet nucleus surface. This velocity was determined by iterative tradeoffs among desired penetration depths, anticipated range of penetrabilities, and weight and size limitations for the penetrator structure.

An estimate of the total impulse, I_t , requirement can be obtained from the rocket equation:

$$I_v = m_p \Delta v / \ln (1 - m_p/M_T)$$

where: m_p = mass of propellant
 Δv = velocity change required = 40 m/sec
 M_T = total mass of the penetrator = 20 kg

The logarithm can be expanded:

$$\ln(1 - m_p/M_T) = -m_p/M_T - (m_p/M_T)^2 - (m_p/M_T)^3$$

Thus, for propellant mass much smaller than the total penetrator mass, the total impulse requirement is:

$$I_t \sim \Delta v M_T = (40 \text{ m/s}) (20 \text{ kg}) = 800 \text{ N s}$$

5.8.1 Rocket Motor Tradeoff

A search of potential suppliers of small rocket motors surfaced three suppliers with motors in the size range needed for this total impulse. These three motors are compared in Table 5.8-1.

Table 5.8-1 Candidate Rocket Motors for Penetrator

	Atlantic Research	Rocket Research	Morton-Thiokol
Model No.	Mark 6A	H-46 HEFS	TEM-712
M = Mass of Motor (kg)	1.53	—	1.36
l = Length, cm	25.9	18.3	9.9
d = Diameter, cm	7.8	8.4	11.4
Propellant Type		HTPB/Stabilized AN	Hydrocarbon Ammonium Perchlorate
Propellant Designation	Arcite 377	4101	TP-H-3289
m_p = Propellant Mass, kg	0.46	0.49	0.45
I_t = Total Impulse, N s	987	890	993
t_b = Burn Time, s	1.08	5.0	9.0
T = Avg Thrust, N	916	451	110
ϵ = Thrust Accuracy, °	± 0.4	—	± 0.25
I_{sp} = Specific Impulse, m/s	2146	1816	2207
Type of Burn	Internal, Star Ported	Ends and Bore	Front
Prior Use	ARPAT, Pioneer Venus Astrobee Thor-Able II Aerobee	Gas Generator Helicopter Flotation	Minuteman (DANT)
Quantity Built	350	5000	—
Temp Range, °C	-40 +93	-54 +71	-40 +60
Thrust Profile:			
t_{rise}/t_b	0.037	—	0.056
Flatness	$\pm 10\%$	—	$\pm 3\%$
t_{fall}/t_b	0.56	—	0.133

The exact total impulse can be adjusted to 800 N s for any of these motors simply by trimming the size of the propellant grain, resulting in a proportional reduction in burn time and propellant mass. Several considerations led to a selection of the Morton-Thiokol TEM-712 motor. These were: 1) longer burn time, 2) smaller mass, 3) flatter aspect ratio, 4) better thrust alignment accuracy, and 5) flatter thrust profile.

The longer burn time and flatter thrust profile are both very useful in reducing the harmful effects of thrust misalignment in minimizing the angle of attack of the penetrator, as discussed in the "Attitude Performance Analysis" section of this report. Similarly the better inherent thrust alignment accuracy improves the angle-of-attack performance. The attitude performance analysis showed that the angle of attack at the end of the burn could be made smaller than the angle of attack at the start of the burn by synchronizing spin nutation frequency to an integral number of nutations during the burn. However, this was true only for thrust misalignments equal to or less than $\epsilon = 0.30^\circ$, whereas, for $\epsilon \geq 0.40^\circ$, the angle of attack would be larger after the burn. Therefore, the selection of the Morton-Thiokol motor was very significant for meeting this criterium.

The flatter aspect ratio of the Morton-Thiokol motor improves the overall ratio of transverse to axial moments of inertia, I_t/I_a . The smaller the ratio becomes for the penetrator, the more stable the flight will be (to a minimum at $I_t/I_a=2$) and the less susceptible it will be to a nutation growth caused by viscous damping. The current ratio is 3.53:1.

Data from Morton-Thiokol, in the form of two memos concerning the motor, are included as Appendix M. The June 27, 1985 memo shows pressure (proportional to thrust) versus time curves for four static tests performed on front burner motors similar (but not the same) as the TEM-712. The second memo partially addresses the issue of safety requirements.

5.8.2 Shuttle Safety Requirements

In dealing with the NHB 1700.7A NASA document for Safety Policy and Requirements for STS payloads, the Morton-Thiokol fully compliant safe-and-arm device would be difficult to implement for the penetrator. Paragraph 202.2.a of the Safety document states that, "solid propellant rocket motors shall be equipped with a safe and arm (S&A) device that provides a mechanical interrupt in the pyrotechnic train immediately downstream of the initiator". The control system in the penetrator provides a triple redundant inhibit system with three separate fully independent inhibits. The first is a double pole interlock switch which is closed mechanically by the ejection of the penetrator from the penetrator support module (PSM). The second inhibit is an arming transistor which is armed by a signal from the penetrator event timer which is started at ejection by the mechanical interlock. The third inhibit is an initiate transistor which receives a fire signal from the penetrator event timer after the arming transistor has charged the fire capacitor to 30 volts.

The mechanical interlock switch does not mechanically interrupt the pyrotechnic train and therefore, does not technically satisfy the S&A requirement. However, it provides an alternative which should be pursued on the basis of a waiver request in accordance with JSC 13830.

If the waiver request is not successful, a mechanical S&A device will be designed using a concept of initiator insertion into the rocket motor through a guide tube extending from the penetrator to the PSM. The initiator would be inserted on command shortly before penetrator ejection. The three inhibits described above would still be in place.

APPENDICES

Appendix A: STRESS ANALYSIS CNPS STRUCTURE

A 1.0 MATERIAL PROPERTIES

TI-5Al-2.5Sn (ELI) Extra Low Interstitial Grade at 100 K⁽¹⁾

σ_{us} (Ultimate Tensile Strength)	= 1,275 MPa	(185,000 psi)
σ_{ys} (Yield Strength)	= 1,207 MPa	(175,000 psi)
(Shear Strength)	= 1,034 MPa	(150,000 psi)
E (Modulus of Elasticity)	= 127,553 MPa	(18.5x10 ⁶ psi)
ν (Poisson's Ratio)	= 0.313	(0.313)
Density	= 4,482 kg/m ³	(0.162 lb/in ³)

KEVLAR 49/EPOXY (Composite) at 100 K⁽²⁾⁽³⁾

σ_{ys} (Yield Strength)	= 1,103 MPa	(160,000 psi)
Inter Laminar Shear Strength	= 22.7 MPa	(3300 psi)
E (Mod. of Elasticity)	= 117,211 MPa	(17x10 ⁶ psi)
ν (Poisson's Ratio)	= .37	(.37)
Density	= 1,439 kg/m ³	(.052 lb/in ³)

A 2.0 BASELINE ASSUMPTIONS:

Mass: 20 kg (44 lb) Penetrator
Impact velocity: 40.0 m/s (131.05 ft/s)
Rotational speed at impact: 116 RPM

Worse case loading conditions:

- 1) Impacting S = 2 (hard ice) material
20° angle of attack
60° impact angle
(This results in a whipping motion of the penetrator and high stresses in the nose and threaded sections of structure).
- 2) Impacting S = 6-7 material which results in worst case axial loading conditions on the penetrator conical afterbody with the penetrator impacting at 60° impact angle.

-
- 1) Alloys for structural applications at subzero temperatures, by J.E. Campbell: METALS HANDBOOK, 9th Edition, Vol 2, 1979.
 - 2) Mechanical and thermal properties of filamentary-reinforced structural composites at cryogenic temperatures 2: Advanced composites, by M.B. Kasen: CRYOGENICS, Dec 75.
 - 3) The effect of cryogenic temperature on the mechanical properties of cylinders wound with Kevlar 49 ARAMID, reprinted from high performance filament wound composites for pressure vessel applications, by J.T. Hoggatt. The Boeing Company, Boeing Scientific Research Lab, Seattle, WA.

A 3.0 RESULTS

Worse Case 1

The penetrator structure configuration was modeled into a tensile stress analysis program developed by W. Young of Sandia National Laboratory. The program's (SIMPLIFIED ANALYTICAL MODEL FOR PENETRATION WITH LATERAL LOADING) results give the tensile stresses developed by the whipping motion of the penetrator (bending and axial compression stresses).

The worse case stresses calculated by this program were converted to a maximum bending moment, and, thus, a maximum lateral force acting at the center of gravity of the penetrator. The maximum lateral force was then used for stress calculations on the final design geometry (for Case 1 loading).

$$\sigma_{\max} \text{ (Bending \& Compression)} = \frac{Mc}{I} + \frac{P}{A}$$

M = bending moment developed from maximum lateral force applied at the center of gravity

P = maximum axial compression load (worst case assumed to be total mass times 350 g's. The expected maximum for S = 2 is 340 g's.)

$$\tau_{\max} \text{ (Shear \& Torsion)} = \frac{4}{3} \frac{V}{A} + \frac{Tc}{J}$$

V = maximum lateral shear force (worst case assumed to be total mass times 500 g's. The maximum expected lateral g load is 500 g's for impacting an embedded boulder.)

T = torque applied to structure when decelerating from 116 RPM to 0 RPM in 6 msec.

All loading configurations are worst case approaches and no factor of safety was introduced into these calculations.

NOTE: See Figure 2-1a for station locations.

Station cm (in)	σ_{\max} (B&C) MPa (psi)	τ_{\max} (S&T) MPa (psi)
13.1 (5.18)	1,145 (166,125)	202 (29,262)
19.5 (7.67)	1,073 (155,564)	800 (116,002)
27.6 (10.85)*	1,169 (169,505)	116 (16,907)
51.3 (20.20)	144 (20,819)	117 (17,028)
58.9 (23.20)	33 (4,809)	34 (4,979)
58.9 (23.20 ⁺)**	91 (13,195)	54 (7,765)
Maximum Allowable Stress to Yield	1,206 (175,000)	1,034 (150,000)

*NOTE: Station 27.6 is at nosepiece to main shaft mating thread section. Calculated stresses include a stress concentration factor of 3.85 applicable to threaded sections.

**NOTE: Station 58.9 is at main shaft to Ti Flare joint where thickness is approximately 1.09 cm and Station 58.9⁺ is where thickness is approximately .36 cm.

Axial Compression Alone on main shaft – nose section modeled as a column:

Critical buckling of columns.

$$P_{cr} \text{ Buckling} = \frac{\pi^2 EI}{(2L)^2} = 294,628 \text{ N (66,235 lb)}$$

$$P_{\text{actual case 1}} = 195.7 \times 350 = 68,495 \text{ N (15,400 lb)}$$

$$P_{\text{worst case possible}} = 195.7 \times 500 = 97,850 \text{ N (22,000 lb)}$$

Axial Compression Alone on I-Beam stiffeners modeled as columns.

$$P_{cr} \text{ Buckling} = \frac{\pi^2 EI}{(2L)^2} = 22,188 \text{ N/Beam (4,988 lb/Beam)}$$

$$P_{\text{actual}} = \frac{195.7 \text{ N} \times 350 \text{ g}}{8 \text{ Beams}} = 8,562 \text{ N/Beam (1925 lb/Beam)}$$

$$P_{\text{worst case}} = \frac{195.7 \text{ N} \times 500 \text{ g}}{8 \text{ Beams}} = 12,231 \text{ N/Beam (2,750 lb/Beam)}$$

Axial Compression Alone on Ti & Kevlar conical flare sections (4).

$$P_{Cr} \text{ Buckling} = 2 \pi \rho_{avg} t \cos^2 \alpha F_{C_{cr}}$$

For: Ti Flare $P_{Cr} = 263,566 \text{ N (59,252 lb)}$

Kevlar Flare $P_{Cr} = 299,401 \text{ N (67,308 lb)}$

Case 1 Actual load = $195.7 \times 350 = 68,495 \text{ N (15,400 lb)}$

Worst case possible = $195.7 \times 500 = 97,850 \text{ N (22,000 lb)}$

Worst Case 2 S = 6-7

A worst case loading is obtained by assuming a load equal to penetrator total mass times 400 g's (345 g's are expected). This equals 78,285 N (17,600 lb) to be applied perpendicular to the conical surface; 2/3 of the slant height distance up from the joint of the main shaft and the conical Ti Flare. This assumes the Ti-Kevlar Flare sections themselves are a solid piece structurally and tests the stability of the main shaft joint.

<u>Station cm (in)</u>	<u>σ_{max} (B&C) MPa (psi)</u>	<u>τ_{max} (Shear) MPa (psi)</u>
59.7 (23.5)	406 (58,829)	55 (8,029)
58.9 ⁺ (23.2 ⁺)	466 (67,577)	59 (8,522)
58.9 (23.2)	178 (25,835)	20 (2,941)
51.3 (20.2)	785 (113,900)	69 (9,997)
46.2 (18.2)	1,028 (149,047)	74 (10,796)
Maximum Allowable	1,206 (175,000)	1,034 (150,000)

The stresses calculated here assume that the penetrator is cantilevered at the station positions shown in the table. This becomes less probable as we proceed down toward the nose since the Case 2 analyzed here is with the penetrator buried deeper than 60 cm. Thus, the stresses calculated are more unrealistically severe as stations approach the nose.

-
- 4) Critical compressive buckling loads for thin-walled conical shells, in Analysis and Design of Flight Vehicle Structures by E.F. Bruhn.

Case 2: Buckling of Ti and Kevlar conical Flare sections due to hydrostatic pressure developed when impacting S = 6-7 material.

- a) Critical buckling pressures for Ti and Kevlar Flare sections without I-Beam stiffners (skin alone)(5).

$$q_{cr} = \frac{K_y \pi^2 E t^3}{\rho_{avg} L^2 12(1-\nu^2)}$$

FOR: Ti Flare .203 cm (.08 thick): q_{cr} Buckle = 3,013 kPa
(437 psi)

Kevlar Flare .191 cm (.075) thick: q_{cr} Buckle = 1,034 kPa
(150 psi)

- b) Expected Hydrostatic pressure levels for varying penetration distances.

Pressure levels determined by the equation:

$$P = \frac{F_{axial}}{A_{projected}}$$

F_{axial} = total mass times the maximum axial g level at the particular penetration distance

$A_{projected}$ = projected conical area over which the axial force is applied

<u>Station cm(in)</u>	<u>Hydrostatic Pressure kPa (psi)</u>	<u>Allowable Pressure kPa (psi)</u>
60.0 (23.62)	2,399 (348)	Ti Flare $P_{allow} = 3,013$ (437 psi)
61.5 (24.21)	2,275 (330)	
63.0 (24.80)	2,165 (314)	
64.5 (25.39)	1,862 (270)	
66.0 (25.98)	1,482 (215)	
67.5 (26.57)	1,331 (193)	
69.0 (27.16)	1,144 (166)	
70.5 (27.76)	1,007 (146)	
72.0 (28.35)	876 (127)	Kevlar Flare $P_{allow} = 1,034$ (150 psi)
73.5 (28.94)	786 (114)	
75.0 (29.53)	696 (101)	
76.5 (30.12)	621 (90)	
78.0 (30.71)	558 (81)	
79.5 (31.30)	476 (69)	
82.5 (32.48)	386 (56)	
85.0 (33.46)	324 (47)	

- 5) Design buckling curves for thin-walled conical shells, by Bruhn, C8.19 (Boeing Buckling design curves for conical shells under hydrostatic external pressure).

Appendix B: Additional Delta-V Phase Equations

$$A = -\omega_{\gamma_0} \omega_{\tau_0} \left(\frac{\omega_{\tau_1}}{\omega_{\tau_0}} + 1 \right) - \frac{M_x}{I_t} \left(\frac{\omega_{\tau_0}}{\omega_{\tau_1}} + 1 \right) \quad (\text{BI-1})$$

$$B = -\omega_{\tau_0} \omega_{\tau_0} \left(\frac{\omega_{\tau_1}}{\omega_{\tau_0}} + 1 \right) \quad (\text{BI-2})$$

$$C = \phi_{\gamma_0} (\omega_n^2 - \omega_{\tau_0}^2) + B \quad (\text{BI-3})$$

$$D = \frac{\phi_{\tau_0} (\omega_{\tau_0}^2 - \omega_n^2) - A \omega_{\tau_1}}{\omega_{\tau_0}} \quad (\text{BI-4})$$

$$\tilde{A} = \frac{\sqrt{A^2 + B^2}}{\omega_{\tau_0}^2 - \omega_n^2} \quad (\text{BI-5})$$

$$\tilde{B} = \frac{\sqrt{C^2 + D^2}}{\omega_{\tau_0}^2 - \omega_n^2} \quad (\text{BI-6})$$

$$\psi_1 = \text{ATAN2}(-A, B) \quad (\text{BI-7})$$

$$\psi_2 = \text{ATAN2}(D, C) \quad (\text{BI-8})$$

$$\bar{A} = -\frac{M_x}{\omega_{\tau_0} \omega_{\tau_1} I_t} \quad (\text{BI-9})$$

$$\bar{B} = -\frac{\omega_{\tau_0}}{\omega_{\tau_0}} + \frac{\tilde{A} \omega_{\tau_1} \cos \psi_1}{\omega_{\tau_0}} \quad (\text{BI-10})$$

$$\bar{C} = \frac{\omega_{\gamma_0}}{\omega_{\tau_0}} - \bar{A} + \frac{\tilde{A} \omega_{\tau_1} \sin \psi_1}{\omega_{\tau_0}} \quad (\text{BI-11})$$

$$\bar{D} = -\tilde{B} \cos \psi_2 \quad (\text{BI-12})$$

$$\bar{E} = -\tilde{B} \sin \psi_2 \quad (\text{BI-13})$$

$$\bar{F} = \tilde{A} \cos \psi_1 \quad (\text{BI-14})$$

$$\bar{G} = -\tilde{A} \sin \psi_1 \quad (\text{BI-15})$$

$$a = \sin \phi_{\tau_0} \quad (\text{BI-16})$$

$$b = \cos \phi_{\tau_0} \quad (\text{BI-17})$$

$$I_1 = \frac{1}{\omega_{\tau_0}} (1 - \cos \omega_{\tau_0} t) \quad (\text{BI-18})$$

$$I_2 = \frac{1}{\omega_{\tau_0}} \sin \omega_{\tau_0} t \quad (\text{BI-19})$$

$$I_3 = \frac{\sin (\omega_{\tau_0} + \omega_n) t}{2 (\omega_{\tau_0} + \omega_n)} + \frac{\sin (\omega_{\tau_0} - \omega_n) t}{2 (\omega_{\tau_0} - \omega_n)} \quad (\text{BI-20})$$

$$I_4 = \frac{\sin (\omega_{\tau_0} - \omega_n) t}{2 (\omega_{\tau_0} - \omega_n)} - \frac{\sin (\omega_{\tau_0} + \omega_n) t}{2 (\omega_{\tau_0} + \omega_n)} \quad (\text{BI-21})$$

$$I_5 = \left[\frac{1 - \cos (\omega_{\tau_0} + \omega_n) t}{2 (\omega_{\tau_0} + \omega_n)} \right] - \left[\frac{1 - \cos (\omega_{\tau_0} - \omega_n) t}{2 (\omega_{\tau_0} - \omega_n)} \right] \quad (\text{BI-22})$$

$$I_6 = \left[\frac{1 - \cos (\omega_{\tau_0} + \omega_n) t}{2 (\omega_{\tau_0} + \omega_n)} \right] + \left[\frac{1 - \cos (\omega_{\tau_0} - \omega_n) t}{2 (\omega_{\tau_0} - \omega_n)} \right] \quad (\text{BI-23})$$

Appendix C: ELECTRONICS SYSTEMS REQUIREMENTS

Sources of CNPS electronics system requirements include the following:

- (1) RFP No. 2-31766, "A Study of a Comet Nucleus Gamma-Ray Spectrometer penetrator System (GSPS);" Statement of Work; September 27, 1984.
- (2) Technical Proposal- "Comet Nucleus Gamma-Ray Spectrometer penetrator System;" Martin Marietta; November 1984.
- (3) "Baseline Spacecraft Description;" JPL; March 1985.
- (4) "Comet Rendevous Asteroid Flyby (CRAF) Proposal Information Package"; July 1985.

Other design inputs were handled through inhouse project meetings, memos, and design reviews. The following hardware and software sections summarize the explicit and derived requirements from all sources.

HARDWARE REQUIREMENTS

C 1.0 Penetrator Support Module (PSM)

C 1.1 Interfaces

C 1.1.1 Carrier Spacecraft

a. Command & Data

(1) Bus Interface Unit (GFE/JPL)

- (a) +5 V(dc), 1 watt
- (b) 5 MHz Clock from user
- (c) RTI; 15 to 20 Hz; to user
- (d) BIUBUS; 16-bit bidirectional data bus
- (e) CMDSTAR; hardware command strobe; to user
- (f) DRDY; software-decoded data ready; to user
- (g) INENA; input enable; to user
- (h) OUTREQ; input request; to user
- (i) OUTSTR; output strobe; from user
- (j) CDSIF; CDS/BIU serial bus

b. Voltage: 30 V(dc) + 2.5%

c. Spin/Eject Pyros (Driven by spacecraft)

C 1.1.2 Penetrator (Hardline)

a. Command & Data

(1) Protocol: asynchronous, serial, half-duplex

(2) Interface Characteristics

- (a) Bi-phase
- (b) = 1.25 Mbps max

b. Voltage: 24-32 V(dc)

C 1.2 Thermal

C 1.2.1 Electronics Heater

- a. Power: 1 watt peak
- b. Setpoint: 0°C

C 1.3 Data Handling

C 1.3.1 Hardware

a. Microcomputer

- (1) Clock Oscillator/Divider
 - (a) Frequency: 5 MHz
- (2) Microprocessor
 - (a) 16-bit
 - (b) 80C86
- (3) Memory
 - (a) PROM
 - (i) 4 kbytes
 - (ii) 200 nsec access time
 - (b) RAM
 - (i) 16 kbytes
 - (ii) 200 nsec access time
- (4) Address Decode
 - (a) Memory-mapped I/O
- (5) I/O
 - (a) Parallel ports
- (6) Timers
 - (a) Watchdog
 - (i) Resolution: 20 msec
 - (ii) 16 bits
 - (b) Elapsed
 - (i) Resolution: 1 sec
 - (ii) 20 bits

b. Data-Acquisition System

- (1) Analog Multiplexer
 - (a) Input Voltage Range: ± 5 V(dc)
 - (b) Inputs
 - (i) 3 Internal Voltages
 - (ii) 1 Heater Temperature
- (2) Amplifier
- (3) ADC
 - (a) Resolution: 10-bits
 - (b) Conversion Time: 25 usec.

C 1.3.2 Throughput

Worst-Case Timing: 80 usec/BIU word

C 1.4 Communications

C 1.4.1 RF

a. Receiver

- (1) Center Frequency: 1500 MHz
- (2) IF Bandwidth: 200 kHz ± 0 , -5 % @ -3 db
- (3) Noise Figure: 6 dB maximum
- (4) Sensitivity: TBD dBm

b. Antenna

- (1) Beamwidth: 100-120 degrees
- (2) Gain: 5-7 dBi
- (3) Polarization: circular

c. Link Margin: 10 dB

d. Bit-Error Rate: $1E-5$

C 1.4.2 Bit Sync

- a. Input Voltage: 0-4 V(dc)
- b. Encoding: Bi-phase
- c. Bit Rate: 1000 bps

C 1.5 Power Converter

- a. Input: 30 V(dc) \pm 2.5%
- b. Output Voltages: \pm 5 V(dc) @ 1 A; \pm 12 V(dc) @ 100 mA
- c. Regulation: \pm 5 V(dc) \pm 10%; \pm 12 V(dc) \pm 5%
- d. Ripple: 250 mV p-p @ \pm 5 V(dc); 100 mV p-p @ \pm 12 V(dc)

C 1.6 Cabling

C 1.6.1 Coax

- a. Antenna
 - (1) Length: 20 ft
 - (2) Impedance: 50 ohms
- b. Other- not required

C 1.6.2 Harnesses

- a. Signal
- b. Power

C 1.7 Temperatures

- a. Design: -30 to +85°C
- b. Qual: -20 to +75°C
- c. Flight -10 to +65°C
- d. Storage -65 to +150°C

C 2.0 Penetrator

C 2.1 Interfaces

C 2.1.1 PSM (Hardline)

- a. Command & Data
 - (1) Same as PSM
- b. Power
 - (1) Same as PSM

C 2.2 Science

C 2.2.1 Gamma-Ray Spectrometer

- a. GFE Items
 - (1) Ge Crystal Assembly
 - (2) First Stage Electronics
 - (3) Amps
 - (4) Peak-Detect/Stretch
 - (5) Discriminators
 - (a) Upper-Level
 - (b) Lower-Level

- (6) Pulse-Height Analyzer (PHA)
 - (a) 13-bit ADC
 - (b) 8000 X 16 RAM
 - (c) Control Logic
 - (i) PHA sequencing
 - (ii) Plus-one
 - (d) Higher resolution at lower energies
 - b. Data-Handling Interface
 - (1) 16-bit parallel data
 - (2) Microcomputer access to gamma PHA RAM
 - (3) Control and status interface
 - c. HVPS
 - (1) Input: 24-32 V(dc)
 - (2) Output: 750-3000 V(dc)
 - (3) Resolution: 250 V(dc) Steps
 - (4) Regulation: 10%
 - (5) Ripple: .01%
 - (6) Monitors: Voltage and Current
- C 2.2.2 Alpha-Backscatter Detector
 - a. GFE Items
 - (1) Sensor Head
 - (2) Electronics
 - b. Data-Handling Interface
 - (1) 16-bit parallel data
 - (2) Microcomputer access to alpha PHA RAM's
 - (3) Control and status interface
 - c. Modes
 - (1) Alpha
 - (2) Proton
 - (3) X-Ray
 - d. HVPS (X-Ray)
 - (1) Input: 24-32 V(dc)
 - (2) Output: 50-200 V(dc)
 - (3) Regulation: 10%
 - (4) Ripple: .01%
 - (5) Monitors: Voltage and Current
- C 2.2.3 Accelerometers
 - a. Ranges: 6 @ 500 g; 1 @ 10 g
 - b. V/I Characteristics: 2-20 mA input; \pm 5 V(dc) output
- C 2.2.4 Temperature Probes
 - a. Thermocouples: 27-45 μ V K⁻¹
 - b. Quantity: 4, (3 deployable, 1 fixed)
- C 2.3 Thermal
 - C 2.3.1 Crystal-Anneal Heater
 - a. Power: 37 watts
 - b. Setpoint: 110°C
 - C 2.3.2 Electronics Heater
 - a. Power: 1 watt
 - b. Setpoint: -30°C

- C 2.3.3 Rocket Motor Heater
 - a. Power: 0.6 watts
 - b. Setpoint: -180C
- C 2.3.4 First Stage Electronics Heater
 - a. Power: 0.5 watt
 - b. Setpoint: -1330C
- C 2.3.5 Battery Heaters
 - a. Power: 1 watt each (quantity: 2)
 - b. Setpoint: -300C
- C 2.4 Electromechanical
 - C 2.4.1 Temperature Probe Deployment Mechanisms
 - a. Fuse-Links
 - b. V/I Characteristics: TBD
 - C 2.4.2 Alpha backscatter mechanisms
 - a. Shutters:
 - (1) Fuse-Links
 - (2) V/I Characteristics: TBD
 - b. Door
 - (1) Pin-Puller
 - (2) 4.5 A for 30 msec
 - C 2.4.3 Gamma Spectrometer Mechanisms
 - a. Pin-Puller
 - b. 4.5 A for 30 msec
- C 2.5 Data Handling
 - C 2.5.1 Hardware
 - a. Microcomputer
 - (1) Same as PSM
 - b. Data-Acquisition System
 - (1) Analog Multiplexer
 - (a) Input Voltage Range: ± 5 V(dc)
 - (b) Inputs
 - (i) 7 Accelerometers
 - (ii) 10 Temperature Transducers
 - (iii) 4 Internal Voltages
 - (iv) 4 Alpha/Gamma V/I Monitors
 - (2) Amplifier
 - Unity-gain buffer
 - (3) Sample/Hold
 - (a) Acquisition time : 2 usec
 - (b) Settling time : 2 usec
 - (4) ADC
 - (a) Resolution: 10-bits
 - (b) Conversion Time: 25 usec.
 - (5) Throughput: 20,000 samples per second maximum
 - C 2.5.2 Throughput
 - Worst Case Timing: : 16 usec/ hardline controller word

C 2.6 RF Communications

- a. Transmitter
 - (1) Center Frequency: 1500 MHz
 - (2) Frequency Stability: + .003%
 - (3) Frequency Response: 500 kHz
 - (4) Output Power: +23-26 dBm
 - (5) Power Consumption: 5.6 watts
 - (6) Load: 50 ohms
 - (7) VSWR: 1.5:1
 - (8) Modulation: FM
 - (9) Data Format: Bi-phase
- b. Antenna
 - Same as PSM
- c. Link Margin
 - Same as PSM

C 2.7 Propulsion

Rocket Motor

- a. Initiator Characteristics: 5 amps, 10 msec (all-fire)
- b. Separate, multiple, fully-independent inhibits (NHB 1700.7A)

C 2.8 Power

C 2.8.1 Battery

- a. 24-32 V(dc)
- b. Sufficient energy for a 5-day mission
- c. Temperature: -40 to +40°C

C 2.8.2 Converter

- a. Input: 30 V(dc) from PSM, or battery voltage
- b. Output Voltages: +5 V(dc) @ 1 amp; + 12 V(dc) @ 200 mA
- c. Regulation: +5 + 10%; + 12 + 1%; +24 \pm 10%
- d. Ripple: 250 mV p-p @ +5; 100 mV p-p @ \pm 12 & +24

C 2.9 Power Management Unit

Switch +30 V(dc) at 1 amp

C 2.10 Cabling

C 2.10.1 Coax

- a. Gamma-Spectrometer FSE
 - (1) Length: TBD
 - (2) Impedance: TBD
- b. Antenna
 - (1) Length: TBD
 - (2) Impedance: 50 ohms

C 2.10.2 Harnesses

- a. Fore electronics to aft electronics
- b. Intra-aft electronics

C 2.11 Temperatures

- a. Design: -60 to + 105°C
- b. Qual: -50 to + 95°C
- c. Flight: -40 to +85°C
- d. Storage: -65 to +150°C

Appendix D: SOFTWARE REQUIREMENTS

The following software requirements are defined as a function of three mission phases: "Prerelease" is approximately one hour before ejection; "Flight" is from ejection until impact; "Post-impact" is implanted operation.

D 1.0 Penetrator Support Module (PSM)

D 1.1 Prerelease phase

D 1.1.1 Initialize subsystems

- a. Data handling
- b. Thermal
- c. Power
- d. RF
- e. BIU interface
- f. Hardline controller interface

D 1.1.2 Perform self-test

- a. Microcomputer
 - (1) Checksum ROM
 - (2) Read/write test RAM

D 1.1.3 Handle hardline controller interface

- a. Send commands to penetrator
- b. Accept data from penetrator
- c. Protocol: Asynchronous, serial, half-duplex
- d. Word Format
 - (1) 3 sync bits
 - (2) 16 data bits
 - (3) 1 odd parity bit

D 1.1.4 Handle spacecraft computer interface (BIU)

- a. Accept commands from spacecraft
 - (1) penetrator updates
 - (2) PSM updates
- b. Send packetized data to spacecraft
 - (1) penetrator data
 - (2) PSM data
 - (3) Format: CCSDS Standard
- c. Protocol: See Volume IV, Appendix E of CRAF document

D 1.1.5 Control temperature

- a. Read temperature transducer
- b. Compare with set-point
- c. Control heater

D 1.1.6 Handle power management unit

Control power switches

D 1.1.7 Periodically reset watchdog timer

- D 1.2 Flight and post-impact phases
 - D 1.2.1 Handle elapsed timer
 - a. Reset at release
 - b. Read periodically
 - c. Maintain elapsed time
 - D 1.2.2 Handle receiver operation
 - a. Read receiver buffer
 - b. Error-correct data (optional)
 - D 1.2.3 Handle spacecraft computer interface (BIU)
 - a. Accept commands from spacecraft
 - (1) PSM updates
 - b. Send data to spacecraft
 - (1) Packetize data
 - (a) penetrator data
 - (b) PSM data
 - (c) Format: CCSDS Standard
 - c. Protocol: See Volume IV, Appendix E of CRAF document
 - D 1.2.4 Handle power management unit
 - Control power switches
 - D 1.2.5 Periodically reset watchdog timer

D 2.0 Penetrator

- D 2.1 Prerelease phase
 - D 2.1.1 Initialize subsystems
 - a. Data handling
 - b. Science
 - c. Thermal
 - d. Power
 - e. RF
 - f. Hardline controller interface
 - D 2.1.2 Perform self-test
 - a. Microcomputer
 - (1) Checksum ROM
 - (2) Read/write test RAM
 - b. Gamma-ray spectrometer
 - Read status data
 - c. Alpha backscatter
 - Read status data
 - D 2.1.3 Handle hardline controller interface
 - a. Accept commands from PSM
 - b. Send data to PSM
 - c. Protocol: Same as for PSM
 - D 2.1.4 Control heaters
 - a. Crystal-anneal
 - b. Electronics
 - c. Rocket motor
 - d. Spectrometer FSE
 - e. Battery
 - D 2.1.5 Handle power management unit
 - Control power switches
 - D 2.1.6 Periodically reset watchdog timer

- D 2.2 Flight phase
 - D 2.2.1 Handle elapsed timer
 - a. Reset at release
 - b. Read periodically
 - c. Maintain elapsed time
 - D 2.2.2 Handle event timer
 - D 2.2.3 Handle power management unit
 - Control power switches
 - D 2.2.4 Handle gamma-ray spectrometer data
 - D 2.2.5 Handle alpha-backscatter data
 - D 2.2.6 Handle accelerometer data
 - D 2.2.7 Ignite rocket motor
 - D 2.2.8 Confirm impact
 - a. Handle impact interrupt
 - b. Read event timer
 - D 2.2.9 Periodically reset watchdog timer
- D 2.3 Post-impact phase
 - D 2.3.1 Freeze accelerometer data
 - D 2.3.2 Deploy temperature probes
 - D 2.3.3 Collect temperature probe data
 - D 2.3.4 Compress data (optional)
 - D 2.2.5 Encode data (optional)
 - D 2.3.6 Transmit data
 - a. Accelerometers
 - (1) Ejection Data
 - (2) Rocket motor burn data
 - (3) Impact data
 - b. Temperature probes
 - c. Gamma-ray spectrometer
 - d. Alpha-backscatter instrument
 - e. Housekeeping
 - D 2.3.7 Handle power management unit
 - Control power switches
 - D 2.3.8 Switch to low-power mode after 5 days
 - Periodically transmit data
 - a. Temperature probes
 - b. Gamma-ray spectrometer
 - c. Alpha-backscatter
 - d. Housekeeping
 - D 2.3.9 Periodically reset watchdog timer

Note: The sequencing and control associated with crystal annealing and operating points optimization have not yet been fully identified. These items will be addressed when the crystal requirements are better defined.

Appendix E: CNPS RF SUBSYSTEM DESIGN

E 1.0 Scope

The CNPS study effort has been conducted at the conceptual design level, including RF Subsystem performance requirements analysis, hardware identification, and interface definitions. Detailed design and analysis is to follow in a later phase. Typical follow-on activities are RF link simulation tests for selection of optimum modulation parameters and verification of link margin, and antenna prototype evaluation, including soil and ice comet nucleus material attenuation and beam aberration effects. The CNPS RF Subsystem conceptual design baseline consists of RF operating frequency selection, link analysis, antenna design selection, and receiver and transmitter design selections.

E 2.0 Subsystem Description

The CNPS RF Subsystem consists of a transmitter subsystem, located on the penetrator outboard structure, and a receiver subsystem, located on the host Spacecraft as part of the penetrator support electronics. As illustrated in Figure E-1(a), antennas are connected to a transmitter and receiver at either end of the comet-to-Spacecraft data link.

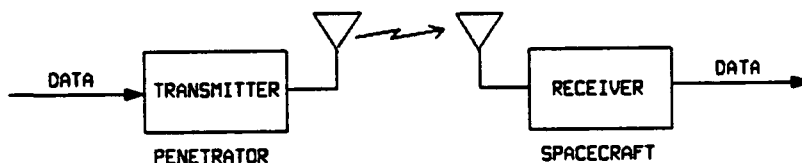


Figure E-1(a) One Way Link

Prior to the data transmission interval, the transmitter is powered up by the penetrator power management circuitry for a 1 minute warmup period, during which satisfactory transmitter status is verified. The transmitter will provide an unmodulated RF carrier output during this interval. Data transmission is commenced by activation of the data waveform at the transmitter modulation input. The receiver demodulates the transmitted carrier and provides a replica of the data waveform for retransmission from the host Spacecraft. The data transmission must be timed to coincide with antenna line-of-sight continuity between penetrator and host Spacecraft, considering the rotational period of the comet and location of the penetrator with respect

to the axis of rotation. The impact of a two-way communications link, as suggested by Figure E-1(b) is undesirable in terms of penetrator lifetime. An additional receiver on the penetrator must operate continuously in order to provide the two-way paging function, an enormous power consumption impact compared to the low-duty cycle transmissions required for baseline performance.

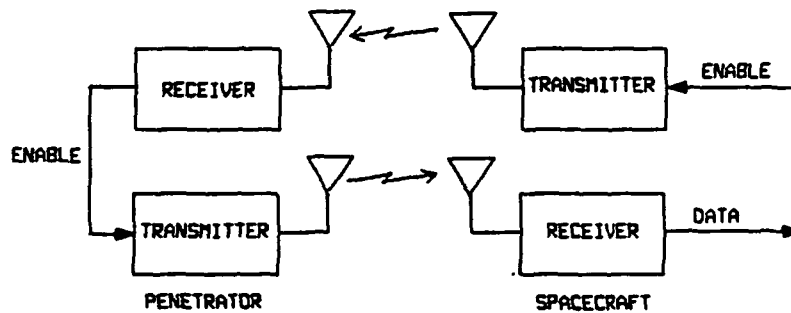


Figure E-1(b) Two Way Link

E 2.1 Operating Frequency Selection

Established hardware availability and acceptable soil/ice attenuation characteristics lead to selection of 1435-1545 MHz as the most practical operating frequency range. Table E-1 illustrates several factors involved in the choice.

Table E-1 Operating Frequency Selection Parameters

(-)	Increasing Path Loss	
(-)	Increasing Soil/Ice Attenuation	
(+)	Decreasing Antenna Size	- 2300 MHz
		- 2200 MHz S-Band Std Telemetry
		- 1850 MHz
		- 1710 MHz
		- 1545 MHz
		- 1435 MHz L-Band Std Telemetry
(+)	Decreasing Path Loss	
(+)	Decreasing Soil/Ice Attenuation	
(-)	Increasing Antenna Size	

Standard L-Band telemetry receivers and transmitters are readily available in the 1435-1545 MHz frequency range, at very low cost in comparison to semi-custom developed hardware. While operating at a somewhat lower frequency (1000 MHz) may offer a slight performance advantage, with approximately 3.6 dB lower path loss ($20 \log f_2/f_1$) and perhaps 1.0 dB lower soil/ice

attenuation, it is unfortunate to note that candidate suppliers indicate a major design impact in modifying the existing L-Band transmitter for 1000 MHz operation. Although it is not appropriate to baseline a 1000 MHz operating frequency, it is appropriate to identify the design impact assessment as a further study item.

E 2.2 Link Analysis

Link analyses have been performed to evaluate candidate modulation parameters, providing assessments of link data quality. Modulation types considered are Binary PSK (Phase Shift Keying), PM (Phase Modulation), and FM (Frequency Modulation). All the modulation types provide adequate link data quality margin; the best performance is obtained from PSK, with 20 dB link margin, followed by PM and FM. As detailed in Tables E-2, E-3 and E-4, transmitter power is assumed to be +23dBm (200 mW) for all cases. Other common parameters such as antenna gains, system losses and soil/ice attenuation, result in Received Signal Strength of -107.5 dBm and a receiver noise floor density of -168 dBm/Hz. The data bit rate is assumed to be 1 Kbps, which allows for growth in the length of the data stream and/or addition of error detection/correction bits, or reduction of the data transmission duration. The minimum required data rate is approximately 100 bps based on transmission of spectrometer data in a ten-minute interval.

Table E-2 Link Analysis (PSK) 1500 MHz

Transmit Power	+23 dBm
Cable Loss	-0.5
Antenna Gain, Transmit	6.0
Pointing Loss	-3.0
Soil/Ice Attenuation	-6.0
Space Loss 55 km	-131.5
Antenna Gain RCV	6.0
Pointing Loss	-0.5
Polarization Loss	-0.5
Cable Loss	-0.5
Received Signal Strength	-107.5 dBm
Noise Spectral Density	-174 dBm/Hz
Receiver Noise Figure	6.0 dB
Receiver Noise Floor, N_0	-168 dBm/Hz
Bit Bandwidth (1000 bps)	30 dB Hz
E_b/N_0	30.5 dB
E_b/N_0 for 10^5 BER	10.5 dB
Link Margin	20 dB

Table E-3 Link Analysis (PSK/PM) 1500 MHz

Transmit Power	+23 dBm
Cable Loss	-0.5
Antenna Gain, Transmit	6.0
Pointing Loss	-3.0
Soil/Ice Attenuation	-6.0
Space Loss 55 km	-131.5
Antenna Gain RCV	6.0
Pointing Loss	-0.5
Polarization Loss	-0.5
Cable Loss	-0.5
Received Signal Strength	-107.5 dBm
Receiver Noise Density (KT)	-174 dBm/Hz
Receiver Noise Figure	6.0 dB
Receiver Noise Floor Density	-168 dBm/Hz
Signal-to-Noise Density Ratio	60.5 dBm Hz
Modulation Loss, $B^2/2 = 1.0$	-3.0
Reciprocal Bit Rate (1 KBps)	-30 dB Hz
Subcarrier to Noise Ratio	27.5 dB
Required E_B/N_O , 10^{-5} BER (PSK)	10.5 dB
Link Margin	17 dB

Table E-4 Link Analysis (PCM/FM) 1500 MHz

Transmit Power	+23
Cable Loss	-0.5
Antenna Gain, Transmit	+6.0
Pointing Loss	-3.0
Ice Attenuation	-6.0
Space Loss 55 km	-131.5
Antenna Gain RCV	+6.0
Pointing Loss	-0.5
Polarization Loss	-0.5
Cable Loss	-0.5
Received Signal Strength	-107.5 dBm
Receiver Noise Floor Density	-168 dBm/Hz
Signal-to-Noise Density Ratio	60.5 dB/Hz
Bit Bandwidth 1 KHz	30.0 db Hz
E_B/N_O Input	30.5 dB
Required E_B/N_O Output, $P(E) = 1E-5^*$	13.5 dB
Required E_B/N_O Input, $P(E) = 1E-5$	20.5 dB
IF Bandwidth = 200 KHz	
$f = 20$ KHz	
Link Margin	10.0 dB
*Estimated for Non-Gaussian Noise	

Table E-2 shows the PSK link analysis. The signal-to-noise density in the bit bandwidth, E_b/N_0 , determines the output data bit error rate. Non-coherent detection is assumed in this case, with E_b/N_0 of 10.5 dB required for a 1 in 10^5 bit error rate. The resulting 20 dB link margin is an indication that extremely high quality data will be obtained. This link is capable of much higher data rates, as the bit bandwidth determines the required signal-to-noise ratio.

In Table E-3, the PM implementation is shown to provide a link margin of 17 dB. The modulation scheme considered here is truly PSK/PM, whereby an audio subcarrier, at typically 10 to 100 KHz, is PSK-modulated by the data stream. The data subcarrier is then phase-modulated onto the RF carrier. Link performance is the same as the PSK link, except for 3 dB modulation loss incurred in the phase modulation process. This type of modulation is typically used for coherent-transponder data transmission, whereby multiple subcarriers may be used to transmit different data streams.

FM link performance is analyzed in Table E-4. The modulation scheme considered here is PCM/FM, where the data waveform directly frequency-modulates the transmitted RF carrier. Analysis of an FM link is considerably more complex than that of PM or PSK, because the signal-to-noise performance of the FM discriminator used to recover the data waveform exhibits threshold behavior, dependent on input noise bandwidth, i.e., the RF bandwidth, and FM deviation. FM is capable of providing modulation gain when the signal-to-noise ratio is sufficiently high, as FM deviation is increased. However, if the input noise bandwidth is in excess of what is required to pass the RF spectrum of the modulated signal, rapid degradation results. For a given RF bandwidth, FM deviation is chosen to provide the best overall performance, a compromise between excessive RF bandwidth for low values of FM deviation, and below-threshold behavior at low signal-to-noise ratios for high values of FM deviation. The minimum practical RF bandwidth, actually the IF bandwidth of the FM receiver, has been determined to be 200 KHz based on standard availability. In addition to the associated filter design difficulty, narrower bandwidths should not be considered due to the needed allowance for frequency drift and aging effects. The 200 KHz bandwidth corresponds to ± 100 KHz frequency tolerance between transmitter and receiver. At 1500 MHz, the ± 100 KHz tolerance is ± 67 ppm, which is on the order of achievable crystal oscillator frequency stability. A series of computations of output signal-to-noise, for various values of RF bandwidth and FM deviation index, have shown the best value of FM deviation to be approximately 20 KHz. The resulting link margin, 10 dB, reflects the fact that the RF signal input to the receiver could be reduced by 10 dB, still yielding a 1 in 10^5 bit error rate. However, this is a somewhat pessimistic margin. Because the FM output signal-to-noise performance is nonlinear with respect to input signal-to-noise, the 10 dB RF signal strength margin corresponds to, in this case, approximately 20 dB of output signal-to-noise ratio margin. The data quality is equivalent, then, to that of the PSK link, although more sensitive to reductions in signal strength.

The link analyses show PSK, PM, and FM all to be viable for the CNPS data link implementation, as summarized in Table E-5.

Table E-5 Link Analysis Summary

Modulation Type	RF Signal Strength Margin	Data Quality Margin
PSK	20 db	20 db
PCM/FM	10 db	20 db
PSK/PM	17 db	17 db

Based on link performance, hardware considerations, and cost/risk factors, the FM data link was ultimately chosen as a result of the modulation trade study presented in a following section.

E 2.3 Antenna Design

The CNPS antenna design baseline continues to be the rectangular microstrip patch antenna, as presented in the study proposal. Originally, however, a four-element array was presented as the receive antenna on the supporting Spacecraft. This is presently not being considered necessary, as the link analysis considered a single microstrip patch on either end of the link, i.e., the same antenna on penetrator and Spacecraft. The four-element array provides a fallback, should additional gain requirements be identified in subsequent definition phases. Antenna performance characteristics are shown in Table E-6.

Table E-6 Antenna Performance Characteristics

Center Frequency	1500 MHz
Gain, 50 ohm System	Greater than 6.0 dBi
Half Power Beamwidth	Greater than 90°
Polarization	Circular
Bandwidth	1 to 2%
VSWR	Less than 2.0:1

It is anticipated that the antenna will be constructed from a Duroid laminate material and installed with a thin radome covering of appropriate RF transparent material.

E 2.4

Transmitter-Receiver Design

Trade study considerations of hardware availability, growth capability, cost, performance, and technical risk show FM to be the best selection for the CNPS application. In choosing the transmitter and receiver designs, the "must" characteristics are current hardware availability and growth capability. As shown in the table below, available hardware has been identified for all three types of modulations being considered. Although the use of PSK in data communications applications is well established, offering excellent performance, it is unfortunate that there is an absence of cost-effective general purpose PSK transmitters and receivers on the market. Existing hardware is identifiable, but not truly suited to the CNPS application. The PSK transmitter and receiver presented in the table were developed for the Galileo program, and in general are too costly, too heavy, too large, and consume too much power to compete successfully with the FM hardware. The PM hardware presented in the table consists of transmitter and receiver sections of a SGLS coherent data transponder, which operates with data subcarriers, as treated in the PM link analysis. This hardware would provide a great deal of unused capability in the CNPS application, but is yet a competitive alternative to FM, particularly in terms of functional growth. Low-power, linear PM transmitters and receivers are available in virtual counterpart form to the FM hardware presented in Table E-7, as well, but FM is capable of better ultimate data quality performance.

Table E-7 Transmitter-Receiver Hardware Characteristics

	FM	PM	PSK
Transmitter			
Part No.	TM-502	CXS-800	01-P07010R
Manufacturer	Aydin Vector	Loral	Motorola
Size	2.5 in Dia x 1.25 in	4 x 8 x 2 in.	4.7 x 4.8 x 3.4 in.
Weight	7 oz	3 lb (est)	3.5 lb
Input Power	5.6 W	18.5 W	3.7 W
Frequency	1435-1540 MHz	TBD	1387 MHz
Output Power	+23 dBm	+23 dBm	+21 to +23 dBm
Data Interface	Analog	Digital	Digital
Receiver			
Part No.	RCC 201-1	CXS-800	3648900-100-X
Manufacturer	Aydin Vector	Loral	Hughes
Size	3.25 x 6 x 1.3 in.	4 x 8 x 4 in.	16.1 x 7 x 6.5 in.
Weight	26 oz	6 lb (est)	20 lb
Input Power	2.8 W	3.6 W	23.5 W
Data Interface	Analog	Digital	Digital

There is an abundance of proven, qualified FM transmitter and receiver designs available for consideration. The transmitter presented here was originally developed for telemetry transmission during artillery projectile flight. The receiver has not been formally flight-qualified, but is similar to qualified designs, and will be qualified on an existing contract in the near future. Some qualification costs would be incurred for the CNPS application, however. The transmitter-receiver design selection trade study is presented in the following table. The various "want" characteristics are weighted by degree of importance, and scores contribute accordingly to the overall total. The FM transmitter-receiver scores highest on the basis of strengths in the areas of cost and configuration (size/power/weight). The FM circuitry is less complex than the PSK and PM counterparts, providing an advantage in another category. As discussed previously, FM link margin should perhaps be increased to more accurately reflect data quality performance, but in this case, the other advantages of the FM implementation are able to offset the apparent disadvantage of a lower link margin. On the interface characteristics category, the digital logic data interface offered by the PSK and PM hardware is considered superior to the analog interface of the FM transmitter and receiver. The trade study summary is shown in Table E-8.

Table E-8 Transmitter-Receiver Design Selection Trade Study

Item	Weight	Score = Weight x (0-10 Possible)		
		FM	PSK	PM
Cost	3	30	15	15
Link Margin	2	10	20	17
Configuration (Size/Power/Weight)	2	14	8	6
Interface Characteristics	1	5	10	10
Complexity/Reliability	1	7	5	4
Qualification History	1	5	6	6
Total	10	71	64	58

The CNPS data RF link can be implemented at a minimum cost with currently-available FM transmitter and receiver hardware. In order to ensure satisfaction of all CNPS program requirements, the transmitter and receiver should be procured according to a system-level specification tailored to the existing hardware designs, but also establishing CNPS reliability, test, analysis, and documentation requirements. Transmitter and receiver performance characteristics critical to the system-level specification appear in Table E-9.

Table E-9
Transmitter and Receiver Critical Performance Specifications

a) Transmitter Performance Characteristics	Unit
Operating Frequency	TBD
Operating Frequency Range	1435-1540 MHz
Output Power	+23 dBm Minimum
Modulation Type	FM
Modulation Frequency Response	DC-500 KHz
Deviation Sensitivity	100 KHz/V Maximum
Input Power	5.6 W Maximum
Warmup Time	1 min
Frequency Stability	Matched Crystal
Temperature Range	TBD
b) Receiver Performance Characteristics	
Operating Frequency	TBD
Operating Frequency Range	1435-1540 MHz
Noise Figure	6 dB Maximum
IF Bandwidth	200 KHz
Demodulation Type	FM
Frequency Response	DC-50 KHz
FM Output Sensitivity	1 V/100 KHz Minimum
Input Power	2.8 W Maximum
Warmup Time	1 min
Frequency Stability	Matched Crystal/AFC
Temperature Range	TBD

E 3.0 Conclusions

The CNPS RF Subsystem design presents low development risk due to the utilization of existing-design hardware. Predicted performance shows high data quality will be maintained by a greater than 10 dB link margin.

We recommend that two special test activities be undertaken early in the CNPS design development phase, in order to characterize link performance and further minimize risk. First, a series of tests should be conducted to verify soil/ice attenuation behavior, including antenna pattern measurements. Second, the RF link should be simulated for design selection of transmitter modulation parameters, and verification of link margin.

Appendix F - FLIGHT SOFTWARE TOP-LEVEL VCLR'S

Although the penetrator system's mission can be divided into numerous phases, three major phases were chosen (Prerelease, Flight, and Postimpact) in order to simplify flight software design.

The goal was to make the programs in the penetrator and in the PSM as similar as possible. Therefore the top-level VCLR's (Visual Control Logic Representations) for both are identical.

F 1.0 PSM TOP-LEVEL VCLR

PERFORM MICROCOMPUTER SELF TEST & SAVE STATUS		
READ RE-START DATA FROM RAM		
PERFORM POWER-ON INITIALIZATION		
DOWHILE POWER ON		
PHASE ?		
PRERELEASE	FLIGHT	POST IMPACT
PERFORM PRERELEASE OPERATIONS	PERFORM FLIGHT OPERATIONS	PERFORM POST IMPACT OPERATIONS

F 2.0 PSM PRERELEASE VCLR

PERFORM PRERELEASE INITIALIZATION						
PERFORM MICROCOMPUTER SELF-TEST & SAVE STATUS						
RESET WATCHDOG TIMER						
CONTROL HEATER						
DOUNTIL INTERRUPT OR PHASE = FLIGHT						
INTERRUPT TYPE ?						
HARDLINE CTLR		RTI				
READ DATA FROM PEN		T	COMMAND PENDING ?			F
PROCESS PENETRATOR DATA		RESET COMMAND-PENDING FLAG				STORE COMMAND FOR EXECUTION ON NEXT RTI
		COMMAND TYPE ?				
		DATA DUMP	EJECT	PENETRATOR	OTHER	SET COMMAND- PENDING FLAG
		SEND PACKET TO CDS	TURN OFF PENETRA- TOR HARD- LINE PWR	SEND CMD TO PENETRATOR VIA HARDLINE CONTROLLER	TBD	
			RESET ELAPSED TIMER			
	SET PHASE = FLIGHT					
RETURN TO POINT OF INTERRUPTION						

F 3.0 PSM FLIGHT VCLR

PERFORM FLIGHT INITIALIZATION				
PERFORM MICROCOMPUTER SELF-TEST & SAVE STATUS				
RESET WATCHDOG TIMER				
CONTROL HEATER				
READ ELAPSED TIMER				
T	TIME CALCULATED FLIGHT TIME ?			F
SET PHASE = POSTIMPACT		NULL		
DOUNTIL INTERRUPT OR PHASE = POSTIMPACT				
INTERRUPT TYPE ?				
RECEIVER		RTI		
READ RECEIVER DATA		T	COMMAND PENDING ?	
T	IMPACT MSG ?	F	RESET COMMAND-PENDING FLAG	
SET PHASE = POST-IMPACT		SEND DATA TO PACK-ETIZER		STORE COMMAND FOR EXECUTION ON NEXT RTI
		COMMAND TYPE ?		
		DATA DUMP		OTHER
		SEND PACKET TO CDS		TBD
				SET COMMAND-PENDING FLAG
RETURN TO POINT OF INTERRUPTION				

F 4.0 PSM POST IMPACT VCLR

PERFORM POST IMPACT INITIALIZATION			
PERFORM MICROCOMPUTER SELF-TEST & SAVE STATUS			
RESET WATCHDOG TIMER			
CONTROL HEATER			
DOUNTIL INTERRUPT			
INTERRUPT TYPE ?			
RECEIVER	RTI		
READ RECEIVER DATA	T	COMMAND PENDING ?	F
SEND DATA TO PACKETIZER	RESET COMMAND-PENDING FLAG		STORE COMMAND FOR EXECUTION ON NEXT RTI
	COMMAND TYPE ?		
	DATA DUMP	OTHER	SET COMMAND- PENDING FLAG
	SEND PACKET TO CDS	TBD	
RETURN TO POINT OF INTERRUPTION			

F 5.0 PENETRATOR TOP-LEVEL VCLR

PERFORM MICROCOMPUTER SELF TEST & SAVE STATUS		
READ RE-START DATA FROM RAM		
PERFORM POWER-ON INITIALIZATION		
DOWHILE POWER ON		
PHASE ?		
PRERELEASE	FLIGHT	POST IMPACT
PERFORM PRERELEASE OPERATIONS	PERFORM FLIGHT OPERATIONS	PERFORM POST IMPACT OPERATIONS

F 6.0 PENETRATOR PRERELEASE VCLR

PERFORM PRERELEASE INITIALIZATION				
PERFORM MICROCOMPUTER SELF-TEST & SAVE STATUS				
RESET WATCHDOG TIMER				
CONTROL HEATERS				
DOUNTIL INTERRUPT OR PHASE = FLIGHT				
INTERRUPT TYPE ?				
HARDLINE CONTROLLER				OTHER
READ COMMAND FROM PSM				
COMMAND TYPE ?				
PARAMETER UPDATE	EJECT- PENDING	PRERELEASE CHECKOUT	OTHER	TBD
STORE NEW PARAMETER	PERFORM EJECT- DETECT ALGORITHM	COLLECT DATA FROM SCIENCE	TBD	
	RESET ELAPSED TIMER			
	SET PHASE = FLIGHT	SEND DATA TO PSM		
RETURN TO POINT OF INTERRUPTION				

F 7.0 PENETRATOR FLIGHT VCLR

PERFORM FLIGHT INITIALIZATION			
COLLECT EJECT-ACCELERATION DATA			
TRANSMIT EJECT-ACCELERATION DATA			
PERFORM MICROCOMPUTER SELF-TEST & SAVE STATUS			
RESET WATCHDOG TIMER			
CONTROL HEATERS			
DEQUE NEXT TASK			
READ ELAPSED TIMER (COUNTS UP)			
SET EVENT TIMER (COUNTS DOWN)			
SWITCH TO LOW-POWER MODE			
NULL			
DOUNTIL EVENT TIMER INTERRUPT			
SWITCH TO HIGH-POWER MODE			
EVENT ?			
	PRE MOTOR BURN	MOTOR BURN	OTHER
	TURN OFF HIGH VOLTAGE SUPPLY	IGNITE MOTOR	TBD
		COLLECT MOTOR-BURN ACCELERATION DATA	
		SET BURN FLAG	
DOUNTIL BURN FLAG SET			
SET EVENT TIMER = ____ SEC			
SAMPLE ACCELEROMETERS AT HIGH RATE			
DOUNTIL IMPACT OR TIMEOUT			
SET PHASE = POSTIMPACT			

F 8.0 PENETRATOR POST-IMPACT VCLR

PERFORM POST IMPACT INITIALIZATION	
PERFORM MICROCOMPUTER SELF-TEST & SAVE STATUS	
RESET WATCHDOG TIMER	
CONTROL HEATERS	
TRANSMIT IMPACT MESSAGE	
	SET EVENT TIMER = 1 SEC
	TRANSMIT MOTOR-BURN ACCELERATION DATA
	TRANSMIT IMPACT DECELERATION DATA
	DO UNTIL EVENT TIMER INTERRUPT OR TRANSMISSION COMPLETE
TRANSMISSION COMPLETE	EVENT TIMER INTERRUPT
NULL	RESET WATCHDOG TIMER
	COLLECT TEMPERATURE PROBES DATA
	SET EVENT TIMER = 1 SEC
	RETURN TO POINT OF INTERRUPTION
	SET EVENT TIMER = 1 SEC
	TRANSMIT TEMPERATURE PROBES DATA (IMPACT TRANSIENT)
	TRANSMIT ALPHA DATA
	TRANSMIT GAMMA DATA
DO UNTIL EVENT TIMER INTERRUPT OR TRANSMISSION COMPLETE	
TRANSMISSION COMPLETE	EVENT TIMER INTERRUPT
NULL	RESET WATCHDOG TIMER
	COLLECT TEMPERATURE PROBES DATA
	SET EVENT TIMER = 1 SEC
	RETURN TO POINT OF INTERRUPTION

(Continued on next page)

PENETRATOR POST-IMPACT VCLR (CONT'D)

TRANSMIT TEMPERATURE PROBES DATA (STEADY-STATE)	
RE-TRANSMIT ACCELERATION & DECELERATION DATA	
SET COUNT = 0	
SET EVENT TIMER = ____ MIN	
PERFORM MICROCOMPUTER SELF-TEST AND SAVE STATUS	
RESET WATCHDOG TIMER	
CONTROL HEATERS	
SWITCH TO LOW-POWER MODE	
NULL	
DUNTIL EVENT TIMER INTERRUPT	
SWITCH TO HIGH-POWER MODE	
COLLECT TEMPERATURE PROBES DATA	
COUNT = COUNT + 1	
DUNTIL COUNT = ____ (NUCLEUS ROTATIONAL PERIOD)	
TRANSMIT ALPHA DATA	
TRANSMIT GAMMA DATA	
TRANSMIT TEMPERATURE PROBES DATA (PERIODIC)	
DUNTIL ELAPSED TIME = 7 DAYS	
PERFORM LONG-TERM SCIENCE OPERATIONS	
DUNTIL BATTERY DIES	

Appendix G - MICROCOMPUTER MEMORY & TELEMETRY ESTIMATES

G 1.0 GROUND RULES

- (1) DECOMPOSE MODULES TO APPROXIMATELY 100 INSTRUCTIONS PER MODULE.
- (2) USE SCALED GIBSON MIX TO CALCULATE AVERAGE BYTES PER INSTRUCTION; SCALED TO COMPENSATE FOR LACK OF FLOATING POINT INSTRUCTIONS IN 80C86; SCALED BY $1/1-(.069+.038+.015)$.
- (3) CALCULATE TOTAL BYTES PER PROGRAM AND ADD 50% MARGIN.

<u>INSTRUCTIONS</u>	<u>BYTES/ INSTR</u>	<u>SCALED GIBSON MIX</u>	<u>PRODUCT</u>
LOAD & STORE	2.71	.355	.962
FIXED PT ADD, SUB	3.00	.069	.207
COMPARES	3.00	.043	.129
BRANCHES	2.14	.189	.404
FLT PT ADD, SUB	0	0	0
FLT PT MULT	0	0	0
FIXED PT MULT	2.00	.007	.014
FLT PT DIV	0	0	0
FIXED PT DIV	2.00	.002	.004
SHIFT	2.00	.050	.100
LOGICAL	3.00	.018	.054
NON-REG INSTRUCTIONS	1.06	.060	.064
INDEXING	2.00	.205	.410
			<u>2.35 BYTES / INSTR AVERAGE</u>

G 2.0 PSM PROM ESTIMATE

<u>MODULE</u>	<u>PHASE-USAGE</u>		
	<u>PRERELEASE</u>	<u>FLIGHT</u>	<u>POST IMPACT</u>
EXEC	X	X	X
INIT	X		
SELFTTEST	X	X	X
HARDLINE	X		
BIUCMDS	X	X	X
BIUTLM	X	X	X
THERMAL	X	X	X
TIMERS	X	X	X
RECEIVER		X	X
PACKETIZER	X	X	X
INTERRUPT	X	X	X

(11 MODULES) (100 INSTR/MODULE) (2.35 BYTES/INSTR) = 2585 BYTES

2585 BYTES + 50% MARGIN = 3878 BYTES

G 3.0 PENETRATOR PROM ESTIMATE

<u>MODULE</u>	<u>PHASE-USAGE</u>		
	<u>PRERELEASE</u>	<u>FLIGHT</u>	<u>POST IMPACT</u>
EXEC	X	X	X
INIT	X		
SELFTEST	X	X	X
HARDLINE	X		
THERMAL	X	X	X
POWERMGMT		X	X
TIMERS	X	X	X
TRANSMITTER		X	X
GAMMA-SPEC	X	X	X
ALPHA-BACK	X	X	X
ACCELS		X	
TEMPROBES			X
MOTOR		X	
PACKETIZER		X	X
IMPACTDET		X	
DATA COMP		X	X
INTERRUPT	X	X	X

(17 MODULES) (100 INSTR/MODULE) (2.35 BYTES/INSTR) = 3995 BYTES

3995 BYTES + 50% MARGIN = 5993 BYTES

Following are the RAM and data estimates. The tables also show the beneficial effects of data compression on RAM size and data length. The JPL data compression algorithm referenced in Appendix I of the CRAF document will be used to achieve a typical 8:1 reduction in gamma ray spectrometer data. The reduction in data length from 100,000 bits to 40,000 bits is the result of data compression. Using the current transmission rate projection of 1000 bits per second, this gives a link time of 40 seconds.

The RAM tables, with gamma data compression, show a requirement of approximately 16 kbytes, given a margin of slightly less than 10%. This number will be used to determine the chip count.

G 4.0 PENETRATOR RAM ESTIMATE

<u>BYTES</u>	<u>FUNCTION</u>	<u>COMMENTS</u>
8192	ALPHA	4 ACCUMULATIONS OF X-RAY DATA
16384	GAMMA	8192, 16-BIT WORDS
3750	ACCELEROMETERS	30000 BITS
200	TEMP PROBES	1600 BITS
64	HOUSEKEEPING	
256	STACK	
64	SCRATCHPAD	
64	PARAMETERS TABLE	

28974 TOTAL

IF COMPRESS GAMMA DATA 8:1,
TOTAL = 14638 + 10% = 16102 BYTES.

* ASSUMES ALPHA/PROTON DATA WILL OVERLAY X-RAY DATA.

G 5.0 PSM RAM ESTIMATE *

<u>BYTES</u>	<u>FUNCTION</u>	<u>COMMENTS</u>
28590	TELEMETRY	ONE SET OF PENETRATOR SCIENCE AND H/K DATA
128	HOUSEKEEPING	
256	STACK	
64	SCRATCHPAD	

29038 TOTAL

IF COMPRESS GAMMA DATA 8:1,
TOTAL = 14702 + 10% = 16173 BYTES.

* ASSUMES PSM MUST BUFFER ONE SET OF PENETRATOR DATA BEFORE
SENDING IT TO SPACECRAFT CDS.

G 6.0 PENETRATOR DATA LENGTH *

<u>BITS</u>	<u>DATA SOURCE</u>	<u>COMMENTS</u>
16384	ALPHA	1 ACCUMULATION OF X-RAY DATA **
131072	GAMMA	8192 16-BIT WORDS
30000	ACCELEROMETERS	IMPACT DATA
1600	TEMP PROBES	IMPACT DATA
512	HOUSEKEEPING	

179568 TOTAL

IF COMPRESS GAMMA DATA 8:1,
TOTAL = 64880 BITS WITH ACCELEROMETER DATA, OR
TOTAL = 34880 BITS WITHOUT ACCELEROMETER DATA.
(ROUND TO 40000 BITS FOR POWER CALCULATIONS.)

* THIS DATA WILL BE CONTAINED IN THE "SOURCE DATA" FIELD OF THE
CNPS SOURCE PACKET.

** ASSUMES X-RAY AND ALPHA/PROTON DATA WILL NOT BE TRANSMITTED IN
SAME PACKET.

Appendix H - ERROR DETECTION & CORRECTION

The attached trade matrix addresses the issue of Error Detection and Correction (EDAC) of the data transmitted from the penetrator to the PSM. Error detection-only is relatively easy to implement and should be the minimum requirement for this mission. However, given the desirability of compressing part of the science data in order to reduce RAM buffer requirements, use of an error-correcting code must also be considered, since each bit of compressed data will contain more information and thus be more vulnerable to bit-errors.

A good compromise may be to use EDAC only for the compressed data and CRC detection-only for the remaining data. If the gamma-ray spectrometer data is compressed 8:1, then 87.5% of the raw data will not be transmitted. Using an error-correcting code such as Reed-Solomon on this data would add approximately 15% of the bits back into the transmission. This approach may be acceptable for both the alpha and gamma data since the baseline position is to continually integrate the data from these instruments so that each set of data is inherently redundant.

PENETRATOR DATA EDAC TRADE

CANDIDATE	ADVANTAGES	DISADVANTAGES
PARITY	EASIEST TO IMPLEMENT.	ERROR DETECTION ONLY. SUSCEPTIBLE TO MULTIPLE ERRORS.
16-BIT CRC	EASY TO IMPLEMENT.	ERROR DETECTION ONLY.
HAMMING OR BCH	DOUBLE-BIT DETECTION AND SINGLE OR DOUBLE-BIT CORRECTION.	HARDER TO IMPLEMENT.
REED SOLOMON (n,n-32)	CORRECTS UP TO 16 ERRORS	HARDER TO IMPLEMENT. APPROXIMATELY 15% OVERHEAD.

Appendix I - PENETRATOR ACCELEROMETER SAMPLING

Penetrator deceleration vs. time plots were used to determine: (1) the need for a sample/hold amplifier in the penetrator data acquisition system, (2) the accelerometer RAM requirements, and (3) the impact-detection strategy.

I 1.0 Sample/Hold Amplifier

Assuming use of an AD574 12-bit ADC short-cycled to 10-bit resolution, the conversion time is

$$t = (10/12) (25 \mu s) = 21 \mu s.$$

The maximum input signal slew rate that the ADC can handle is

$dv/dt = (2^{-n})(V_{fullscale})/t_{conv} = (2^{-10})(10v)/21 \mu s = 465 V s^{-1}$
The plot for penetrability = 10 shows that the axial accelerometer slew rate could be as high as 7 V in 10 ms, or $700 V s^{-1}$. Therefore, the penetrator data acquisition system will require a sample/hold amplifier, such as the AD346.

The maximum throughput for the combination of AD574 ADC and AD346 sample/hold amp is the inverse of the sum of ADC conversion time, S/H acquisition time, and S/H settling time:

$$1 \text{ sample}/(21 + 2 + 2) \mu s = 40,000 \text{ samples per second.}$$

This meets the requirement, shown in (3) below, to take data at 20,000 samples per second.

I 2.0 Accelerometer RAM Requirements

Analysis of the penetration vs. time plots from penetrability = 2 to 100 shows the following:

- (a) Max pulse width = 75 ms at penetrability = 100.
- (b) 30 g is a good threshold value for impact-detection purposes.
- (c) Max delay to the 30 g point = 19 ms at penetrability = 100.
- (d) Min delay to the 30 g point = 1 ms at penetrability = 2.

To assure bracketing the maximum pulsewidth with the 30 g thresholds, it is necessary to freeze the accelerometer data from 25 ms before the threshold for 100 ms total.

Using 10-bit resolution and taking 1 sample per 50 μs , as shown in (3) below, gives a RAM storage requirement of:

$$100 \text{ ms} \times 20 \text{ bits}/100 \mu s = 20,000 \text{ bits.}$$

I 3.0 Impact-Detection

The strategy for detection of impact is to monitor one high-g axial accelerometer output, starting at the burn of the solid rocket motor, for a value in excess of -30 g. While monitoring the high-g output, the values from all seven accelerometers will be read and stored for subsequent transmission.

The following sampling sequence was devised to sample the low-g accelerometer at 6 times the rate used for the two high-g triads. The low-g accelerometer is designated A ; one triad is designated B, C, and D; and the other triad is designated E, F, and G. The sampling sequence is as follows, with 50 μ s between samples:

A B A C A D A E A F A G A B A C A D A E A...

Given the above sampling sequence, the required throughput is 1 sample/50 μ s = 20,000 samples per second, well within the 40,000 samples per second capability of the system, as calculated in (1) above.

The next question was whether the microcomputer could read/store the data and perform an impact-detection algorithm on the data in realtime. The attached timing analysis shows that the 80C86 operating at 5 MHz can not read/store the data within the required 50 μ s per sample. Therefore the high-rate sampling of accelerometer data will be handled by the hardware shown in Figure 5.6-22, (Penetrator Data Handling Data Acquisition System.)

When the microcomputer sets the HIRATE signal, the logic will sample the seven accelerometers in the sequence shown above, at 50 μ s per channel and store the data in a RAM in wraparound fashion.

The "Code Conversion Logic" consists of five two-input gates and three inverters which convert the output of the four-bit HC161 counter to three HC4051 mux address signals in the previously indicated sequence.

When the logic detects that a high-g axial value has exceeded, n times in a row, a threshold value preloaded into the 82C82 register by the microcomputer, the logic will store enough additional words into the RAM to ensure bracketing the axial pulse. The logic will then send the FREEZERUPT signal to the microcomputer to indicate that the impact transient is complete. The microcomputer will reset the HIRATE signal, freezing the data and putting the data acquisition system back into its normal low-rate mode. The microcomputer will then read the data from the RAM for transmission to the spacecraft.

I 4.0 DAS Interrupt Service Routine

T	MUX ADDRESS = 7 ?	F
SET MUX ADDRESS = 1	INCREMENT MUX ADDRESS	
READ ADC WORD		
STORE ADC WORD		
T	RAM ADDRESS = MAX LIMIT ?	F
RE-INITIALIZE POINTER TO TOP OF RAM BUFFER	T IMPACT FLAG SET ? F	
	T RAM ADDRESS = END ? F	N
	SET FREEZE FLAG NULL	U
		L

I 5.0 DAS INTERRUPT SERVICE ROUTINE (CRITICAL PATH)

uC CLOCKS	INSTRUCTIONS	OPERATION
54	PUSH regs	Interrupt overhead
14	CMP imm to mem	Mux address = 7 ?
8	JNE	
19	INC mem	Incr mux address
12	MOV mem to reg	Read ADC word
13	MOV reg to mem	Store ADC word
14	CMP imm to mem	RAM address = max limit ?
8	JNE	
14	CMP imm to mem	Impact flag set ?
8	JE	
14	CMP imm to mem	RAM address = end ?
8	JE	
14	MOV imm to mem	Set freeze flag
54	POP regs	Interrupt overhead

254 Clocks X 0.2 μ s/clock = 50.8 μ s

Appendix J - POWER CONSUMPTION

The following pages show the methods used to minimize CNPS power and the groundrules used to calculate maximum and average power for the PSM and the penetrator.

J 1.0 CNPS POWER MANAGEMENT

J 1.1 PSM

- a. POWER SWITCHES
 - 1. DATA ACQUISITION SYSTEM
 - 2. PENETRATOR
- b. CONTROL CLOCK RATE (82C85)
 - 1. MICROCOMPUTER
 - 2. HARDLINE CONTROLLER

J 1.2 PENETRATOR

- a. POWER SWITCHES
 - 1. DATA ACQUISITION SYSTEM
 - 2. TRANSMITTER
- b. CONTROL CLOCK RATE (82C85)
 - 1. MICROCOMPUTER
 - 2. ALPHA (AFTER PRIMARY MISSION)
 - 3. GAMMA (AFTER PRIMARY MISSION)
 - 4. HARDLINE CONTROLLER

J 1.3 GENERAL

- a. USE 4000 SERIES CMOS INSTEAD OF HC SERIES IN SLOW CIRCUITS

J 2.0 POWER CALCULATION GROUND RULES

J 2.1 PRERELEASE

- a. INTEGRATE SCIENCE DATA FOR 1 HR.
- b. SEND 40,000 BIT PACKET TO S/C CDS @ 201.6 Kbps = 0.2 SEC.
BIU DUTY CYCLE = (0.2 SEC) / (3600 SEC) = 0.
- c. EJECT PENETRATOR.

J 2.2 FLIGHT

- a. MIN FLIGHT TIME = (3500 M @ 1 M/SEC) + (1000 M @ 44 M/SEC) = 3523 SEC
- b. INTEGRATE ALPHA & GAMMA DATA FOR 10 MINUTES.
(600) / (3523) = 0.17 SCIENCE INSTRUMENT DUTY CYCLE
- c. LET MICROCOMPUTER DUTY CYCLE = .009 + .026 OVERHEAD = .035
- d. ASSUME PSM RECEIVER IS CONTINUOUSLY POWERED.

J 2.3 POST-IMPACT

- a. $(40,000 \text{ BITS/XMISSION}) / (1000 \text{ BITS/SEC}) = 40 \text{ SEC/XMISSION}$
- b. XMIT ONCE/HR WORST CASE
 $(40 \text{ SEC}) / (3600 \text{ SEC}) = .009 \text{ XMISSION DUTY CYCLE}$
- c. LET MICROCOMPUTER DUTY CYCLE = $.009 + .026 \text{ OVERHEAD} = .035$
- d. ASSUME 1 MSEC TO SAMPLE TEMP SENSORS EVERY 10 MIN.
 $(.001 \text{ SEC}) / (600 \text{ SEC}) = 0 \text{ DAS DUTY CYCLE}$
- e. ASSUME PSM RECEIVER IS POWERED CONTINUOUSLY.

J 3.0 GENERAL

- a. USE POWER DATA FROM PARTS LIST FOR HIGH-POWER PARTS AND ESTIMATE LOW-POWER PARTS.

J 4.0 PENETRATOR POWER

<u>LOAD</u>	<u>PMAX (WATTS)</u>
ALPHA	0.5
GAMMA	0.5
MICROCOMPUTER	1.2
DAS	1.4
HARDLINE CONTROLLER	0.2
TRANSMITTER	5.6
CRYSTAL HEATER	37.0
GAMMA FSE HEATER	0.5
BATTERY HEATERS	2.0
ELECTRONICS HEATER	1.0
ROCKET MOTOR HEATER	0.6

THE POWER PROFILES ARE SHOWN IF TABLE J-1.

J 5.0 PSM POWER

<u>LOAD</u>	<u>PMAX (WATTS)</u>
BIU	1.0
MICROCOMPUTER	1.2
DAS	0.9
HARDLINE CONTROLLER	0.2
RECEIVER	2.8
ELECTRONICS HEATER	1.0

THE POWER PROFILES ARE SHOWN IN TAQBLE J-2.

Table J-1 Penetrator Average Power, watts

Load	Prelease				Flight				Post Impact			
	P _{max}	Cycle	P _{stdby}	P _{avg}	P _{max}	Cycle	P _{stdby}	P _{avg}	P _{max}	Cycle	P _{stdby}	P _{avg}
Alpha	0.5	1.0	0.1	0.5	0.5	0	0.1	0.1	0.5	1.0	0.1	0.5
Gamma	0.5	1.0	0.1	0.5	0.5	0	0.1	0.1	0.5	1.0	0.1	0.5
μC	1.2	0	0.2	0.2	1.2	.035	0.2	.24	1.2	.035	0.2	0.24
DAS	1.4	0	0	0	1.4	0	0	0	1.4	0	0	0
Hardline Ctlr	0.2	0	0	0	0.2	0	0	0	0.2	0	0	0
Transmitter	5.6	0	0	0	5.6	0	0	0	5.6	.009	0	.05
Xtal Heater	37	0	0	0	37	0	0	0	37	0	0	0
Gamma FSE Heater	0.5	0.5	0	0.25	0.5	0	0	0	0.5	0.5	0	0.25
Battery Heaters	2.0	1.0	0	2.0	2.0	1.0	0	2.0	2.0	1.0	0	2.0
Electronics Heater	1.0	0.5	0	0.5	1.0	0.5	0	0.5	1.0	0.5	0	0.5
Rocket Motor Heater	0.6	1.0	0	0.6	0.6	1.0	0	0.6	0.6	0	0	0

P_{avg} = (P_{max}) (Cycle) + (P_{stdby}) (1-Cycle)

Table J-2 PSM Average Power, watts

Load	Prelease				Flight				Post Impact			
	P _{max}	Cycle	P _{stdby}	P _{avg}	P _{max}	Cycle	P _{stdby}	P _{avg}	P _{max}	Cycle	P _{stdby}	P _{avg}
BIU	1.0	0	0.1	0.1	1.0	0	0.1	0.1	1.0	0	0.1	0.1
μC	1.2	0	0.2	0.2	1.2	.010	0.2	0.2	1.2	.010	0.2	0.2
DAS	0.9	0	0	0	0.9	0	0	0	0.9	0	0	0
Hardline Ctr	0.2	0	0	0	0.2	0	0	0	0.2	0	0	0
Receiver	2.8	1	0	2.8	2.8	1.0	0	2.8	2.8	1.0	0	2.8
Electronics Heater	1.0	0.5	0	0.5	1.0	0.5	0	0.5	1.0	0.5	0	0.5

P_{avg} = (P_{max}) (Cycle) + (P_{stdby}) (1-Cycle)

J 6.0 PENETRATOR BATTERY REQUIREMENTS

- GROUND RULES:
- (1) USE THE PENETRATOR AVERAGE POWER NUMBERS FOR THE FLIGHT AND POSTIMPACT PHASES ONLY.
 - (2) PENETRATOR HEATER AND TRANSMITTER POWER IS PROVIDED DIRECTLY FROM THE PENETRATOR BATTERY DURING FLIGHT AND POSTIMPACT.
 - (3) OTHER POWER IS PROVIDED BY THE POWER CONVERTER AT 70% EFFICIENCY.
 - (4) THE FLIGHT PHASE IS 2 HOURS; THE POSTIMPACT PHASE IS 120 HOURS.
 - (5) POWER CONVERTER INPUT RANGE = 24 - 32 VDC.
 - (6) Li/SOCl₂ BATTERY:
3.0 - 3.6 VDC PER D-CELL
12 - 15 AMPERE-HOURS PER D-CELL

USE 9 SERIES CELLS TO PROVIDE APPROXIMATELY 30 VDC TO THE POWER CONVERTER.

FLIGHT ENERGY = $(0.44 \text{ WATTS}/0.7 + 3.1 \text{ WATTS}) (2 \text{ HOURS}) = 7.5 \text{ WATT-HOURS}$

POSTIMPACT ENERGY = $(1.24 \text{ WATTS}/0.7 + 2.8 \text{ WATTS}) (120 \text{ HOURS}) = 548.6 \text{ WATT-HOURS}$

TOTAL ENERGY = 556.1 WATT-HOURS

$(556.1 \text{ WATT-HOURS}) / (3.0 \text{ VDC/CELL}) (9 \text{ CELLS}) = 20.6 \text{ AMPERE-HOURS}$

20.6 AMPERE-HOURS REQUIRES TWO PARALLEL STACKS OF THE 9 SERIES CELLS.

CNPS PSM ELECTRONICS PARTS LIST

SUBSYSTEM/CIRCUIT: PENETRATOR SUPPORT MODULE/MICROCOMPUTER

QTY	MANUFACTURER	PART NUMBER	DESCRIPTION	POWER	PACKAGE	COMMENTS
1			CRYSTAL		.5 X .75	
1	HARRIS	80C86	MICROPROCESSOR	500	40-PIN DIP	20 MA/MHZ X 5 MHZ X 5V
1	HARRIS	82C54	TIMERS	0	24-PIN DIP	58594 HZ/8MHZ X 10MA X 5.5V
1	HARRIS	82C55	PROG'BLE PERIPH I/F		40-PIN DIP	
1	HARRIS	82C59	PRIORITY INT' RUPT CTLR		28-PIN DIP	
2	HARRIS	82C82	LATCH		20-PIN DIP	
1	HARRIS	82C85	CLOCK CONTROLLER	150	24-PIN DIP	PWR @ 5 MHZ FROM 8-1-85 EP ARTICLE
2	HARRIS	82C86	TRANSCEIVER		20-PIN DIP	
2	HARRIS	6616	PROM, 2K X 8	164	24-PIN DIP	13 MA/MHZ X 1.25 MHZ X 5V/CHIP X 2 CHIPS
8	HARRIS	6516	RAM, 2K X 8	69	24-PIN DIP	55 MA/MHZ X 0.125 MHZ X 5V/CHIP X 2 CHIPS
1		54HC00	QUAD NAND		14-PIN FP	
1		54HC02	QUAD NOR		14-PIN FP	
1		54HC04	HEX INVERTER		14-PIN FP	
2		54HC10	TRIPLE NAND		14-PIN FP	
1		54HC27	TRIPLE NOR		14-PIN FP	
1		54HC30	8-IN NAND		14-PIN FP	
1		54HC32	QUAD OR		14-PIN FP	
2		54HC138	3-8 DECODER		16-PIN FP	
2		54HC4020	14-BIT COUNTER	38	16-PIN FP	100 PF X 5V ² X (15 MHZ + 15/2 ¹⁴ MHZ)
10		RNCXX	1/4 W RESISTOR			
10		CKRXX	CERAMIC CAP			

CNPS PSM ELECTRONICS PARTS LIST (Cont'd)

SUBSYSTEM/CIRCUIT: PENETRATOR SUPPORT MODULE/DATA ACQUISITION SYSTEM

QTY	MANUFACTURER	PART NUMBER	DESCRIPTION	POWER	PACKAGE	COMMENTS
2		54HC4051	8-CHANNEL ANALOG MUX		16-PIN FP	
1		LM108	OP AMP		10-PIN FP	
1	ANAL DEVICES	AD574	A/D CONVERTER	725	28-PIN DIP	
2		82C82	LATCH		20-PIN DIP	
10		RNCXX	1/4 W RESISTOR			
10		CKRXX	CERAMIC CAP			
4		CSRXX	TANT CAP			

SUBSYSTEM/CIRCUIT: PENETRATOR SUPPORT MODULE/BUS INTERFACE UNIT & I/F

QTY	MANUFACTURER	PART NUMBER	DESCRIPTION	POWER	PACKAGE	COMMENTS
1	JPL		BUS INTERFACE UNIT	1000	3 X 3	GFE
2		82C86	TRANSCEIVER		20-PIN DIP	
1		54HC241	OCTAL BUFFER		20-PIN FP	

SUBSYSTEM/CIRCUIT: PENETRATOR SUPPORT MODULE/HARDLINE CONTROLLER

QTY	MANUFACTURER	PART NUMBER	DESCRIPTION	POWER	PACKAGE	COMMENTS
1	HARRIS	15530	MANCHESTER ENC/DEC	50	24-PIN DIP	
2		82C86	TRANSCEIVER		20-PIN DIP	
2		54HC00	QUAD NAND		14-PIN FP	
2		54HC164	SIPO SHIFT REG		14-PIN FP	
2		54HC165	PISO SHIFT REG		16-PIN FP	
1		78C30	LINE DRIVER	10	14-PIN FP	1 MHZ X 200 PF X 5V ² + LOAD
1		78C20	LINE RECEIVER	83	14-PIN FP	15 MA X 5.5V
5		RNCXX	1/4 W RESISTOR			
5		CKRXX	CERAMIC CAP			

SUBSYSTEM/CIRCUIT: PENETRATOR SUPPORT MODULE/SPIN-EJECT MECHANISM DRIVER

QTY	MANUFACTURER	PART NUMBER	DESCRIPTION	POWER	PACKAGE	COMMENTS
			DRIVEN BY SPACECRAFT			

CNPS PSM ELECTRONICS PARTS LIST (CONT'D)

SUBSYSTEM/CIRCUIT: PENETRATOR SUPPORT MODULE/RECEIVER & INTERFACE

QTY	MANUFACTURER	PART NUMBER	DESCRIPTION	POWER	PACKAGE	COMMENTS
1	AYDIN VECTOR	RCC201-1	RECEIVER	2800	3.25X6X1.3	
1	NATL	LM108	OP AMP	12	10-PIN FP	
1	NATL	LM111	COMPARATOR	18	10-PIN FP	
1	HARRIS	15530	MANCHESTER ENC/DEC		24-PIN DIP	
2		54HC164	SIPO REG		14-PIN FP	
2		54HC241	OCTAL BUFFER		20-PIN FP	
1		CD4516	4-BIT COUNTER		16-PIN FP	
12		RNCXX	1/4 W RESISTOR			
10		CKRXX	CERAMIC CAP			
1		4N49	OPTO-ISOLATOR		6-PIN DIP	

SUBSYSTEM/CIRCUIT: PENETRATOR SUPPORT MODULE/ANTENNA

QTY	MANUFACTURER	PART NUMBER	DESCRIPTION	POWER	PACKAGE	COMMENTS
1			MICROSTRIP PATCH			
A/R			50-OHM COAX			

SUBSYSTEM/CIRCUIT: PENETRATOR SUPPORT MODULE/POWER CONVERTER (LVPS)

QTY	MANUFACTURER	PART NUMBER	DESCRIPTION	POWER	PACKAGE	COMMENTS
1	MOTOROLA	SG1526	PWM CONTROLLER			
1	NATL	LM124	QUAD OP-AMP		14-PIN DIP	
2	MMDA		TRANSFORMER			
2		2NXXXX	TRANSISTOR		TO-18	
1		2NXXXX	TRANSISTOR		TO-3	
5	MMDA		CHOKER			
20		RNCXX	1/4 W RESISTOR			
6		RXXXX	1 W RESISTOR			
19		CXRXX	CERAMIC CAP			
5		CSRXX	TANTALUM CAP			
16		1MXXXX	DIODE			

CNPS PSM ELECTRONICS PARTS LIST (CONT'D)

SUBSYSTEM/CIRCUIT: PENETRATOR SUPPORT MODULE/POWER SWITCHES

QTY	MANUFACTURER	PART NUMBER	DESCRIPTION	POWER	PACKAGE	COMMENTS
2	TELEDYNE	421	SPDT MAGLATCH RELAY	PULSE	TO-5	FOR DAS & PENETRATOR
4		4N49	OPTO-ISOLATOR	PULSE	6-PIN DIP	
1		54HC04	HEX INVERTER		14-PIN FP	
4		RNCXX	1/4 W RESISTOR			
4		CKRXX	CERAMIC CAP			

SUBSYSTEM/CIRCUIT: PENETRATOR SUPPORT MODULE/ELECTRONICS HEATER

QTY	MANUFACTURER	PART NUMBER	DESCRIPTION	POWER	PACKAGE	COMMENTS
1			HEATER			
1		2NXXXX	TRANSISTOR		TO-18	
1			THERMOCOUPLE			
1	PMI	OP-20	OP AMP		8-PIN DIP	
2			PLATINUM RESISTOR			
6		RBRXX	W/W RESISTOR			
5		RNCXX	1/4 W RESISTOR			
2		CKRXX	CERAMIC CAP			

CNPS PENETRATOR ELECTRONICS PARTS LIST

SUBSYSTEM/CIRCUIT: PENETRATOR/MICROCOMPUTER

QTY	MANUFACTURER	PART NUMBER	DESCRIPTION	POWER	PACKAGE	COMMENTS
1			CRYSTAL		.5 X .75	
1	HARRIS	80C86	MICROPROCESSOR	500	40-PIN DIP	20 MA/M Z X 5 MHZ X 5V
2	HARRIS	82C54	TIMERS	0	24-PIN DIP	58594 HZ/8MHZ X 10MA X 5.5V
2	HARRIS	82C55	PROG'BLE PERIPH I/F		40-PIN DIP	
1	HARRIS	82C59	PRIORITY INT'RUPT CTLR		28-PIN DIP	
2	HARRIS	82C82	LATCH		20-PIN DIP	
1	HARRIS	82C85	CLOCK CONTROLLER	150	24-PIN DIP	PWR @ 5 MHZ FROM 8-1-85 EP ARTICLE
2	HARRIS	82C86	TRANSCEIVER		20-PIN DIP	
4	HARRIS	6616	PROM, 2K X 8	164	24-PIN DIP	13 MA/MHZ X 1.25 MHZ X 5V/CHIP X 2 CHIPS
8	HARRIS	6516	RAM, 2K X 8	69	24-PIN DIP	55 MA/MHZ X 0.125 MHZ X 5V/CHIP X 2 CHIPS
1		54HC00	QUAD NAND		14-PIN FP	
1		54HC02	QUAD NOR		14-PIN FP	
1		54HC04	HEX INVERTER		14-PIN FP	
2		54HC10	TRIPLE NAND		14-PIN FP	
1		54HC27	TRIPLE NOR		14-PIN FP	
1		54HC30	8-IN NAND		14-PIN FP	
1		54HC32	QUAD OR		14-PIN FP	
2		54HC138	3-8 DECODER		16-PIN FP	
2		54HC4020	14-BIT COUNTER	38	16-PIN FP	100 PF X 5V ² X (15 MHZ + 15/2 ¹⁴ MHZ)
10		RNCXX	1/4 W RESISTOR			
10		CKRXX	CERAMIC CAP			

CNPS PENETRATOR ELECTRONICS PARTS LIST (Cont'd)

SUBSYSTEM/CIRCUIT: PENETRATOR/DATA ACQUISITION SYSTEM

QTY	MANUFACTURER	PART NUMBER	DESCRIPTION	POWER	PACKAGE	COMMENTS
1		54HC00	QUAD NAND		14-PIN FP	
1		54HC02	QUAD NOR		14-PIN FP	
2		54HC04	HEX INVERTER		14-PIN FP	
2		54HC08	QUAD AND		14-PIN FP	
1		54HC20	DUAL 4-IN NAND		14-PIN FP	
1		54HC32	QUAD OR		14-PIN FP	
1		54HC74	DUAL D FF		14-PIN FP	
3		54HC85	DIGITAL COMPARATOR		16-PIN FP	
1		54HC153	DIGITAL MUX		16-PIN FP	
5		54HC161	14-BIT COUNTER		16-PIN FP	
4		54HC193	UP/DOWN COUNTER		16-PIN FP	
8		54HC241	OCTAL BUFFER		20-PIN FP	
3		54HC4051	8-CHANNEL ANALOG MUX		16-PIN FP	
1	NATL	LM108	OP AMP	12	10-PIN FP	
1	ANAL DEVICES	AD346	S & H AMP	500	14-PIN DIP	
1	ANAL DEVICES	AD574	A/D CONVERTER	725	28-PIN DIP	
4	HARRIS	6516	RAM, 2Kx8		24-PIN DIP	FOR IMPACT DECELERATION DATA
2		82C82	LATCH		20-PIN DIP	
10		RNCXX	1/4 W RESISTOR			
10		CKRXX	CERAMIC CAP			
4		CSRXX	TANT CAP			

SUBSYSTEM/CIRCUIT: PENETRATOR/HARDLINE CONTROLLER

QTY	MANUFACTURER	PART NUMBER	DESCRIPTION	POWER	PACKAGE	COMMENTS
1	HARRIS	15530	MANCHESTER ENC/DEC		24-PIN DIP	
2		82C86	TRANSCEIVER		20-PIN DIP	
2		54HC00	QUAD NAND		14-PIN FP	
2		54HC164	SIPO SHIFT REG		14-PIN FP	
2		54HC165	PISO SHIFT REG		16-PIN FP	
1	NATL	78C30	LINE DRIVER		14-PIN FP	
1	NATL	78C20	LINE RECEIVER		14-PIN FP	
5		RNCXX	1/4 W RESISTOR			
5		CKRXX	CERAMIC CAP			

CNPS PENETRATOR ELECTRONICS PARTS LIST (CONT'D)

SUBSYSTEM/CIRCUIT: PENETRATOR/GAMMA-RAY SPECTROMETER

QTY	MANUFACTURER	PART NUMBER	DESCRIPTION	POWER	PACKAGE	COMMENTS
1			GE XTAL SENSOR ASSY			
1	AMPTEK	A-203	CHARGE/SHAPING AMP		.5 X .97	FRONT-END
2	NATL	LM108	OP AMP		10-PIN FP	"
1	NATL	LM111	COMPARATOR	18	10-PIN FP	"
1		54HC4051	ANALOG MUX		16-PIN FP	"
0.5	INTERSIL	7641	QUAD OP AMP		14-PIN DIP	"
0.5	MOTOROLA	MC14574	DUAL COMP/OP AMP		14-PIN DIP	"
16		RNCXX	1/4 W RESISTOR			"
2		CKRXX	CERAMIC CAP			"
0.75	INTERSIL	7641	QUAD OP AMP		14-PIN DIP	WILKINSON ADC
1	HARRIS	2425	SAMPLE & HOLD		14-PIN DIP	"
0.75	MOTOROLA	MC14574	DUAL COMP/OP AMP		14-PIN DIP	"
1	INTERSIL	7660	VOLTAGE CONVERTER		8-PIN DIP	"
2		54HC74	DUAL D FF		14-PIN FP	"
1		54HC00	QUAD NAND		14-PIN FP	"
4		CD4516	4-BIT COUNTER		16-PIN FP	"
2		2N5089	TRANSISTOR		TO-18	"
21		RNCXX	1/4 W RESISTOR			"
7		CKRXX	CERAMIC CAP			"
7		CSRXX	TANTALUM CAP			"
5		1NXXXX	DIODES			"
2		82C86	TRANSCEIVER		20-PIN DIP	READ-INCREMENT-WRITE LOGIC
1		54HC00	QUAD NAND		14-PIN FP	"
1		54HC04	HEX INVERTER		14-PIN FP	"
1		54HC27	TRIPLE NOR		14-PIN FP	"
2		54HC74	DUAL D FF		14-PIN FP	"
1		54HC164	SIPO REG		14-PIN FP	"
5		54HC241	OCTAL BUFFER		20-PIN FP	"
1		54HC4040	12-BIT COUNTER		16-PIN FP	"
4		CD4516	4-BIT COUNTER		16-PIN FP	"
8	HARRIS	6516	RAM, 2K X 8		24-PIN DIP	FOR 1 SPECTRUM OF 8K CHANNELS @ 16 BITS/CHANNEL

-K7-

CNPS PENETRATOR ELECTRONICS PARTS LIST (CONT'D)

SUBSYSTEM/CIRCUIT: PENETRATOR/ALPHA-BACKSCATTER

QTY	MANUFACTURER	PART NUMBER	DESCRIPTION	POWER	PACKAGE	COMMENTS
1	UNIV OF CHI		SENSOR HEAD			SENSOR HEAD WITH AMPS
3	AMPTEK	A-203	CHARGE/SHAPING AMP		.5 X .97	PREAMPS
3	TIATL	LM108	OP AMP		10-PIN FP	POSTAMPS
4	NATL	LM111	COMPARATOR		10-PIN FP	COINCIDENCE LOGIC
6	NATL	LM108	OP AMP		10-PIN FP	
2			DELAY LINE			
8			ANALOG SWITCH			
1			XTAL		.5 X .75	
5		54HCXX	MISC SSI		14/16-PIN FP	
3	INTERSIL	7641	QUAD OP AMP		14-PIN DIP	WILKINSON ADC (3 EACH)
3	HARRIS	2425	SAMPLE & HOLD		14-PIN DIP	"
3	MOTOROLA	MC14574	DUAL COMP/OP AMP		14-PIN DIP	"
3	INTERSIL	7660	VOLTAGE CONVERTER		8-PIN DIP	"
6		54HC74	DUAL D FF		14-PIN FP	"
3		54HC00	QUAD NAND		14-PIN FP	"
12		CD4516	4-BIT COUNTER		16-PIN FP	"
6		2N5089	TRANSISTOR		TO-18	"
87		RNCXX	1/4 W RESISTOR			"
24		CKRXX	CERAMIC CAP			"
21		CSRXX	TANTALUM CAP			"
15		1NXXXX	DIODES			"
3		82C86	TRANSCEIVER		20-PIN DIP	READ-INCREMENT-WRITE LOGIC (3 SETS)
3		54HC00	QUAD NAND		14-PIN FP	"
3		54HC04	HEX INVERTER		14-PIN FP	"
3		54HC27	TRIPLE NOR		14-PIN FP	"
6		54HC74	DUAL D FF		14-PIN FP	"
3		54HC164	SIPO REG		14-PIN FP	"
12		54HC241	OCTAL BUFFER		20-PIN FP	"
3		54HC4040	12-BIT COUNTER		16-PIN FP	"
6		CD4516	4-BIT COUNTER		16-PIN FP	"
4	HARRIS	6516	RAM, 2K X 8		24-PIN DIP	FOR 2 SPECTRA OF 512 CHANNELS EACH @ 8 BITS/CHANNEL AND 1 SPECTRUM OF 1024 CHANNELS @ 16 BITS/CHANNEL
10		54HCXXX	MISC SSI & MSI		14/16-PIN FP	STATUS & CONTROL LOGIC

CNPS PENETRATOR ELECTRONICS PARTS LIST (CONT'D)

SUBSYSTEM/CIRCUIT: PENETRATOR/ACCELEROMETERS & INTERFACE

QTY	MANUFACTURER	PART NUMBER	DESCRIPTION	POWER	PACKAGE	COMMENTS
2	PCB	306A06	ACCELEROMETER, 500 g		.625 CUBE	
1			ACCELEROMETER, 20 g			
1			ACCELEROMETER, 1g			
4			CONSTANT-CURRENT DIODE			
4		RNCXX	1/4 W RESISTOR			
4		CKRXX	CERAMIC CAP			

SUBSYSTEM/CIRCUIT: PENETRATOR/TEMPERATURE PROBES & INTERFACE

QTY	MANUFACTURER	PART NUMBER	DESCRIPTION	POWER	PACKAGE	COMMENTS
4			THERMOCOUPLE			
4	PMI	OP-20	OP AMP		8-PIN DIP	
8			PLATINUM RESISTOR			
24		RBRXX	W/W RESISTOR			
12		RNCXX	1/4 W RESISTOR			
8		CKRXX	CERAMIC CAP			

SUBSYSTEM/CIRCUIT: PENETRATOR/CRYSTAL-ANNEAL HEATER

QTY	MANUFACTURER	PART NUMBER	DESCRIPTION	POWER	PACKAGE	COMMENTS
1			HEATER			
1		2NXXXX	TRANSISTOR		TO-18	
1			THERMOCOUPLE			
1	PMI	OP-20	OP AMP		8-PIN DIP	
2			PLATINUM RESISTOR			
6		RBRXX	W/W RESISTOR			
5		RNCXX	1/4 W RESISTOR			
2		CKRXX	CERAMIC CAP			

CNPS PENETRATOR ELECTRONICS PARTS LIST (CONT'D)

SUBSYSTEM/CIRCUIT: PENETRATOR/ELECTRONICS HEATER

QTY	MANUFACTURER	PART NUMBER	DESCRIPTION	POWER	PACKAGE	COMMENTS
1			HEATER			
1		2NXXXX	TRANSISTOR		TO-18	
1			THERMOCOUPLE			
1	PMI	OP-20	OP AMP		8-PIN DIP	
2			PLATINUM RESISTOR			
6		RBRXX	W/W RESISTOR			
5		RNCXX	1/4 W RESISTOR			
2		CKRXX	CERAMIC CAP			

SUBSYSTEM/CIRCUIT: PENETRATOR/GAMMA-SPEC FSE HEATER

QTY	MANUFACTURER	PART NUMBER	DESCRIPTION	POWER	PACKAGE	COMMENTS
1			HEATER			
1		2NXXXX	TRANSISTOR		TO-18	
1			THERMOCOUPLE			
1	PMI	OP-20	OP AMP		8-PIN DIP	
2			PLATINUM RESISTOR			
6		RBRXX	W/W RESISTOR			
5		RNCXX	1/4 W RESISTOR			
2		CKRXX	CERAMIC CAP			

SUBSYSTEM/CIRCUIT: PENETRATOR/BATTERY HEATERS

QTY	MANUFACTURER	PART NUMBER	DESCRIPTION	POWER	PACKAGE	COMMENTS
2			HEATER			
2		2NXXXX	TRANSISTOR		TO-18	
2			THERMOCOUPLE			
2	PMI	OP-20	OP AMP		8-PIN DIP	
4			PLATINUM RESISTOR			
12		RBRXX	W/W RESISTOR			
10		RNCXX	1/4 W RESISTOR			
4		CKRXX	CERAMIC CAP			

CNPS PENETRATOR ELECTRONICS PARTS LIST (CONT'D)

SUBSYSTEM/CIRCUIT: PENETRATOR/ROCKET MOTOR HEATER & I/F

QTY	MANUFACTURER	PART NUMBER	DESCRIPTION	POWER	PACKAGE	COMMENTS
1			HEATER			HEATER & INITIATOR PARTS
3		2HXXX	TRANSISTOR		TO-18	
1			THERMOCOUPLE			
1	PMI	OP-20	OP AMP		8-PIN DIP	
2			PLATINUM RESISTOR			
6		RBRXX	W/W RESISTOR			
9		RNCXX	1/4 W RESISTOR			
2		CKRXX	CERAMIC CAP			
8		CSRXX	TANTALUM CAP, 68 uF, 35V		.351 X .786	

SUBSYSTEM/CIRCUIT: PENETRATOR/TRANSMITTER & INTERFACE

QTY	MANUFACTURER	PART NUMBER	DESCRIPTION	POWER	PACKAGE	COMMENTS
1	AYDIN VECTOR	TM-502/L	TRANSMITTER	5600	2.5 DIA X .25	
1		54HC165	PISO REG		16-PIN FP	
1		CD4516	4-BIT COUNTER		16-PIN FP	
1	HARRIS	15530	MANCH ENC/DEC		24-PIN DIP	
4		RNCXX	1/4 W RESISTORS			
1		4H49	OPTO-ISOLATOR		6-PIN DIP	

SUBSYSTEM/CIRCUIT: PENETRATOR/ANTENNA

QTY	MANUFACTURER	PART NUMBER	DESCRIPTION	POWER	PACKAGE	COMMENTS
1			PATCH ANTENNA			
A/R			50-ohm COAX			

CNPS PENETRATOR ELECTRONICS PARTS LIST (CONT'D)

SUBSYSTEM/CIRCUIT: PENETRATOR/POWER CONVERTER (LVPS)

QTY	MANUFACTURER	PART NUMBER	DESCRIPTION	POWER	PACKAGE	COMMENTS
1	MOTOROLA	SG1526	PWM CONTROLLER			FROM 0550
1	NATL	LM124	QUAD OP-AMP		14-PIN DIP	
2	MMDA		TRANSFORMER			
2		2NXXXX	TRANSISTOR		TO-18	
1		2NXXXX	TRANSISTOR		TO-3	
5	MMDA		CHOKER			
20		RNCXX	1/4 W RESISTOR			
6		RXXXX	1 W RESISTOR			
19		CXRXX	CERAMIC CAP			
5		CSRXX	TANTALUM CAP			
16		1NXXXX	DIODE			

SUBSYSTEM/CIRCUIT: PENETRATOR/POWER CONVERTER (HVPS)

QTY	MANUFACTURER	PART NUMBER	DESCRIPTION	POWER	PACKAGE	COMMENTS
1	PMI	DAC-08	D/A CONVERTER	48	16-PIN DIP	MODIFIED UAMS CIRCUIT (U OF MINN)
1	NATL	LM108	OP AMP	12	10-PIN FP	
2	MMDA		TRANSFORMER			
1	HARRIS	HA-OP07	OP AMP		8-PIN DIP	CONTROL LOOP
2	NATL	LM108	OP AMP	12	10-PIN FP	V/I MONITORS
3		2NXXXX	TRANSISTOR		TO-18	
11		1NXXXX	DIODE			
24		RXXXX	1/4 W RESISTOR			
14		CKRXX	CERAMIC CAP			
6		CSRXX	TANTALUM CAP			

SUBSYSTEM/CIRCUIT: PENETRATOR/BATTERY

QTY	MANUFACTURER	PART NUMBER	DESCRIPTION	POWER	PACKAGE	COMMENTS
2			BATTERY MODULES			

CHIPS PENETRATOR ELECTRONICS PARTS LIST (CONT'D)

SUBSYSTEM/CIRCUIT: PENETRATOR/POWER SWITCHES

QTY	MANUFACTURER	PART NUMBER	DESCRIPTION	POWER	PACKAGE	COMMENTS
3	TELEDYNE	421	SPDT MAGLATCH RELAY	PULSE	TO-5	FOR DAS & TRANSMITTER & BATTERY
6		4N49	OPTO-ISOLATOR	PULSE	6-PIN DIP	
1		54HC04	HEX INVERTER		14-PIN FP	
6		RNCXX	1/4 W RESISTOR			
6		CKRXX	CERAMIC CAP			

SUBSYSTEM/CIRCUIT: PENETRATOR/ALPHA DEVICE DRIVERS

QTY	MANUFACTURER	PART NUMBER	DESCRIPTION	POWER	PACKAGE	COMMENTS
2		2NXXXX	TRANSISTOR		TO-18	DOOR DRIVER (PIN-PULLER)
4		RNCXX	RESISTOR			
6		2NXXXX	TRANSISTOR		TO-18	SHUTTER DRIVERS (FUSE-LINK/ SPRINGS; 2 INHIBITS)
12		RNCXX	RESISTOR			

SUBSYSTEM/CIRCUIT: PENETRATOR/GAMMA DEVICE DRIVER

QTY	MANUFACTURER	PART NUMBER	DESCRIPTION	POWER	PACKAGE	COMMENTS
2		2NXXXX	TRANSISTOR		TO-18	XTAL CAGING MECHANISM (PIN-PULLER)
4		RNCXX	1/4 W RESISTOR			

Appendix L: CABLE SIGNALS

PEM = PENETRATOR ELECTRONICS MODULE.

<u>INTERFACE</u>	<u>SIGNALS</u>	<u>WIRES</u>
ALPHA/PEM J1	ALPHA OUT	2
ALPHA/PEM J1	PROTON OUT	2
ALPHA/PEM J1	X-RAY OUT	2
ALPHA/PEM J1	THERMOCOUPLE 1	2
ALPHA/PEM J1	THERMOCOUPLE 2	2
ALPHA/PEM J1	SHUTTER FUSE 1	1
ALPHA/PEM J1	SHUTTER FUSE 2	1
ALPHA/PEM J1	SHUTTER FUSE 3	1
ALPHA/PEM J1	DOORPULLER	1
ALPHA/PEM J1	SHUTTER STATUS 1	1
ALPHA/PEM J1	SHUTTER STATUS 2	1
ALPHA/PEM J1	SHUTTER STATUS 3	1
ALPHA/PEM J1	DOOR STATUS	1
ALPHA/PEM J1	+5 V	1
ALPHA/PEM J1	+12 V	1
ALPHA/PEM J1	-12 V	1
ALPHA/PEM J1	RETURN	1
ALPHA PEM J2	200 V	2
GE XTAL/GAMMA	XTAL SIG	2
GE XTAL/PEM J3	XTAL HEATER	2
GE XTAL/PEM J3	THERMOCOUPLE	2
GAMMA/PEM J3	GAMMA OUT	2
GAMMA/PEM J3	FSE HEATER	2
GAMMA/PEM J3	FSE THERMOCOUPLE	2
GAMMA/PEM J3	+12 V	1
GAMMA/PEM J3	-12 V	1
GAMMA/PEM J3	RETURN	1
GAMMA/PEM J2	3000 V	2
ACCELEROMETERS/PEM J3	ACCELEROMETER 1	2
ACCELEROMETERS/PEM J3	ACCELEROMETER 2	2
ACCELEROMETERS/PEM J3	ACCELEROMETER 3	2
ACCELEROMETERS/PEM J3	ACCELEROMETER 4	2
ACCELEROMETERS/PEM J3	ACCELEROMETER 5	2
ACCELEROMETERS/PEM J3	ACCELEROMETER 6	2
ACCELEROMETERS/PEM J3	ACCELEROMETER 7	2
TEMPERATURE PROBES/PEM J3	TEMPERATURE PROBE 1	2
TEMPERATURE PROBES/PEM J3	TEMPERATURE PROBE 2	2
TEMPERATURE PROBES/PEM J3	TEMPERATURE PROBE 3	2
TEMPERATURE PROBES/PEM J3	TEMPERATURE PROBE 4	2

TRANSMITTER/PEM J4	+28 V	1
TRANSMITTER/PEM J4	RETURN	1
TRANSMITTER/PEM J4	MODULATION	2
TRANSMITTER/PATCH ANTENNA	RF OUT	2
ROCKET MOTOR/PEM J4	INITIATOR	2
ROCKET MOTOR/PEM J4	ROCKET MOTOR HEATER	2
ROCKET MOTOR/PEM J4	THERMOCOUPLE	2
PSM CONN/PEM J4	DATA TO PSM	2
PSM CONN/PEM J4	DATA TO PENETRATOR	2
PSM CONN/PEM J4	SECONDARY RETURN	1
PSM CONN/PEM J4	INITIATOR INTERLOCK	2
PSM CONN/PEM J1	+30 V	1
PSM CONN/PEN J1	PRIMARY RETURN	1
BATTERY MODULE 1/PEM J1	+30 V	1
BATTERY MODULE 1/PEM J1	RETURN	1
BATTERY MODULE 1/PEM J1	BATTERY MODULE 1 HEATER	2
BATTERY MODULE 1/PEM J1	THERMOCOUPLE	2
BATTERY MODULE 2/PEM J1	+30 V	1
BATTERY MODULE 2/PEM J1	RETURN	1
BATTERY MODULE 2/PEM J1	BATTERY MODULE 2 HEATER	2
BATTERY MODULE 2/PEM J1	THERMOCOUPLE	2

PSM CABLE SIGNALS

PSMEM = PSM ELECTRONICS MODULE

<u>INTERFACE</u>	<u>SIGNALS</u>	<u>WIRES</u>
PSMEM J1/SEPARATION CONN	DATA TO PENETRATOR	2
PSMEM J1/SEPARATION CONN	DATA TO PSM	2
PSMEM J1/SEPARATION CONN	SECONDARY RETURN	1
PSMEM J1/SEPARATION CONN	+30 V	1
PSMEM J1/SEPARATION CONN	PRIMARY RETURN	1
PSMEM J1/RECEIVER J1	+30 V	1
PSMEM J1/RECEIVER J1	RETURN	1
PSMEM J1/RECEIVER J1	RECEIVER OUTPUT	2
PSMEM J2/CDS	CDS BUS	2
PSMEM J2/CDS	RTI	2
PSMEM J3/POWER	+30 V	1
PSMEM J3/POWER	RETURN	1
RECEIVER J2/ANTENNA	RECEIVER INPUT	2
SPIN-EJECT MECH/PYRO	SPIN-EJECT	2

MORTON THIOKOL INC.

Elkton Division

June 27, 1985

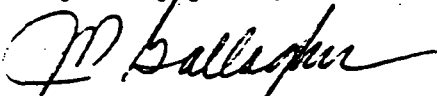
Mr. James McKinnis
Martin Marietta Aerospace
Denver Division
P.O. Box 179
Denver, CO 80201

Dear Jim:

Enclosed are copies of pressure vs. time traces for four static tests conducted in an end burning grain in a motor similar to the one we suggested for the Comet Penetrator. As you can see, these traces are fairly flat.

If you need additional information, give me a call.

Very truly yours,



John P. Gallagher
New Product Manager

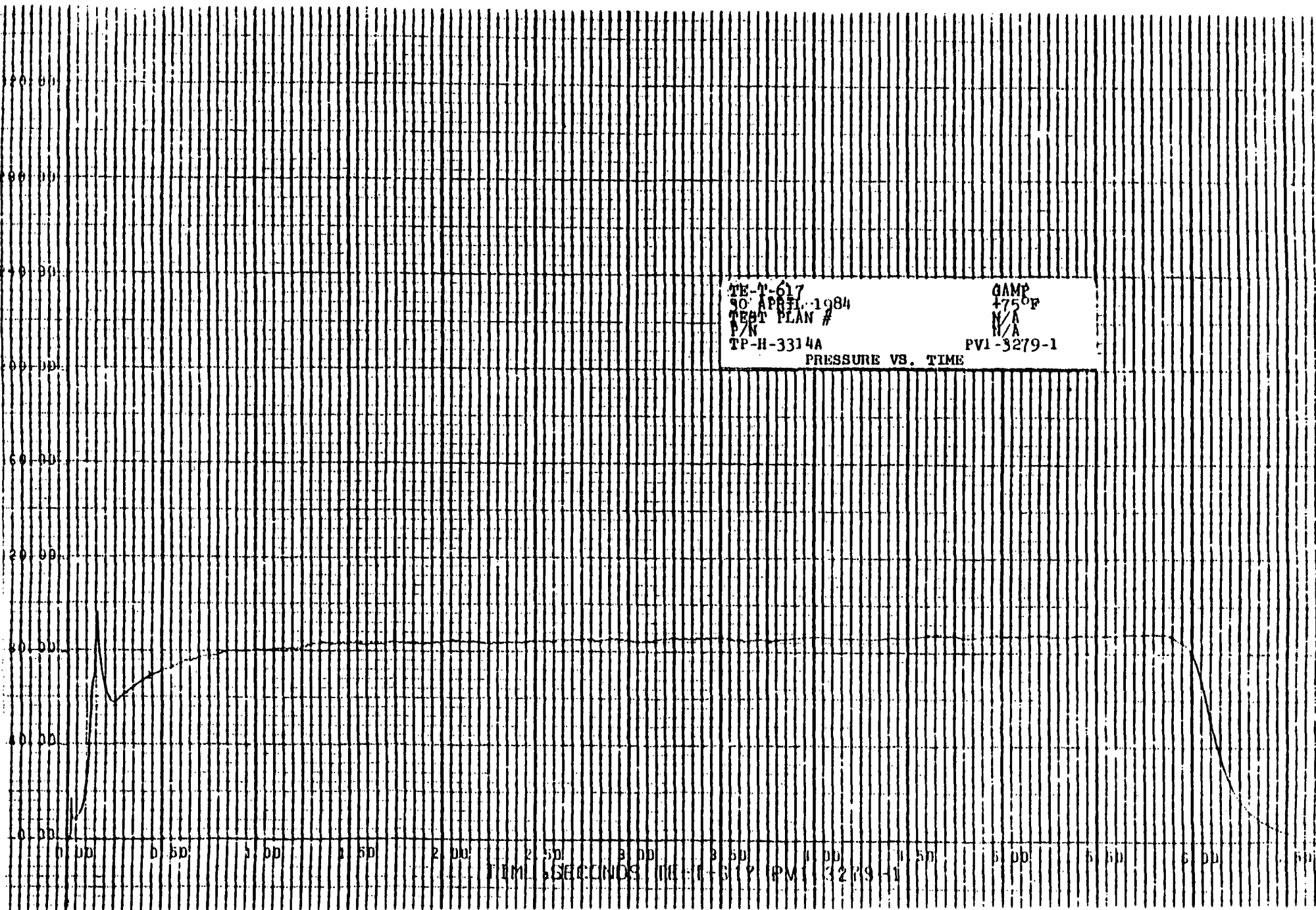
JPG:lh
Enclosure

DISTRIBUTION

J. Sterhardt	D6700
D. Gray	D6700
J. Donathan	D6700
R. Cooke	D6700
J. Marcus	D6700
D. Devers	D6710
G. Mason	D6710
948 J. McKinnis w/Encl.	D6710
C. McClure	D6740
T. Knight (Tech Opts - Info)	0550
Corres. Control (2)	D6740

ORIGINAL PAGE IS
OF POOR QUALITY

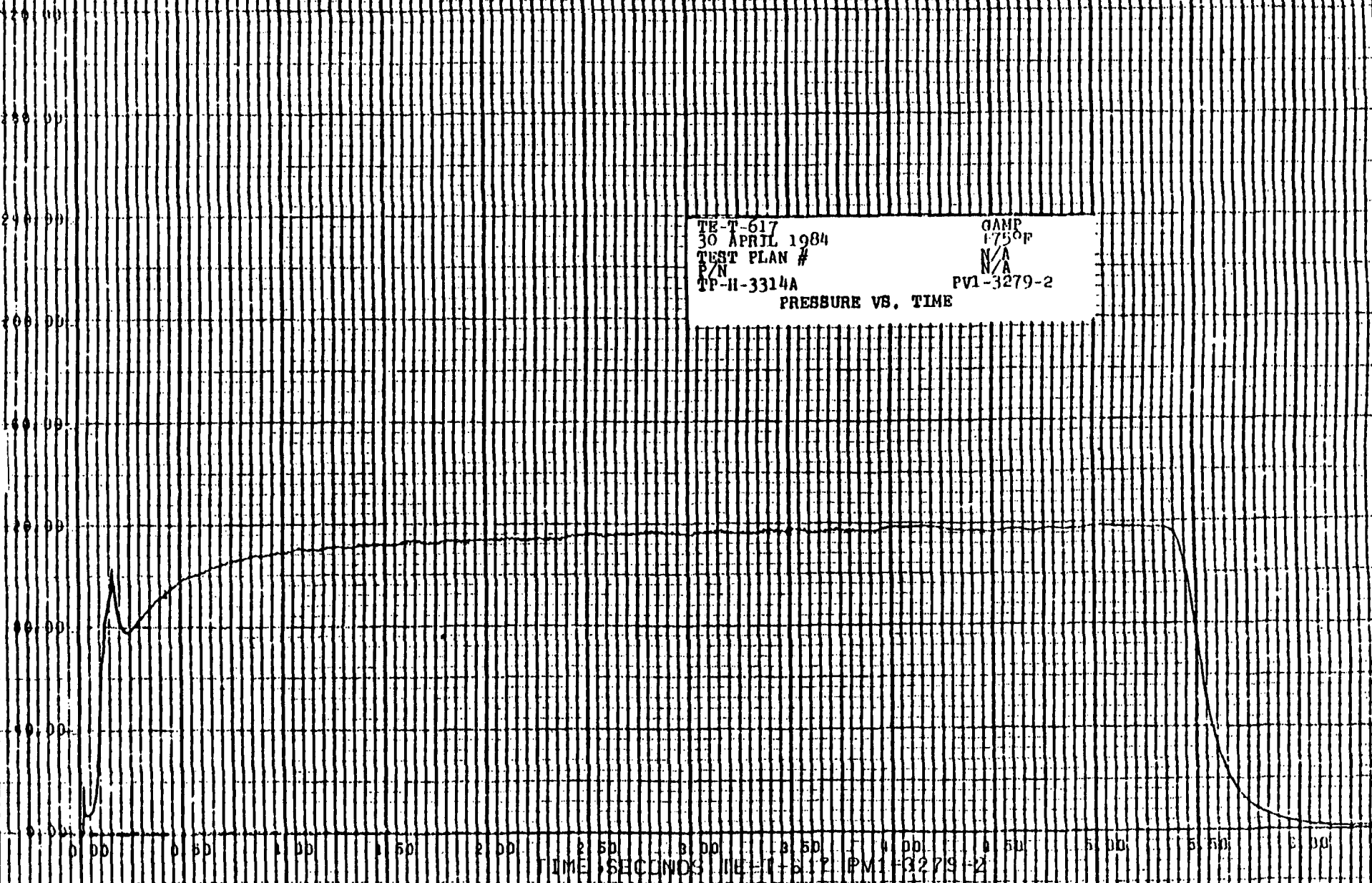
-M2-



ORIGINAL PAGE IS
OF POOR QUALITY

-M3-

TE-T-617
30 APRIL 1984
TEST PLAN #
B/N
TP-II-3314A
GAMP
1750F
N/A
PV1-3279-2
PRESSURE VS. TIME

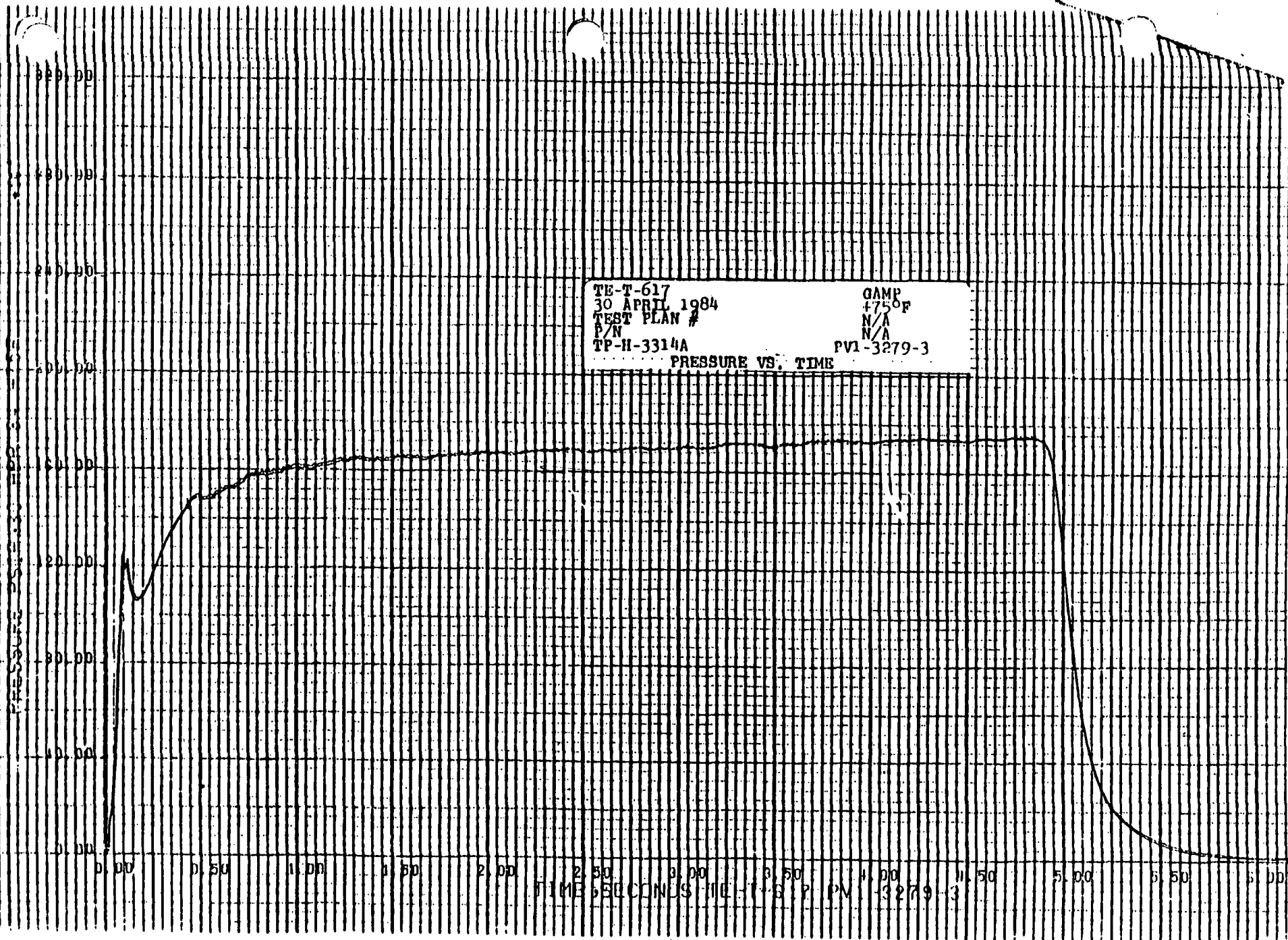


TE-T-617
PV1-3279-2

TE-T-617
30 APRIL 1984
TEST PLAN #
P/N
TP-H-3314A

GAMP
+75°F
N/A
N/A
PV1-3279-3

PRESSURE VS. TIME



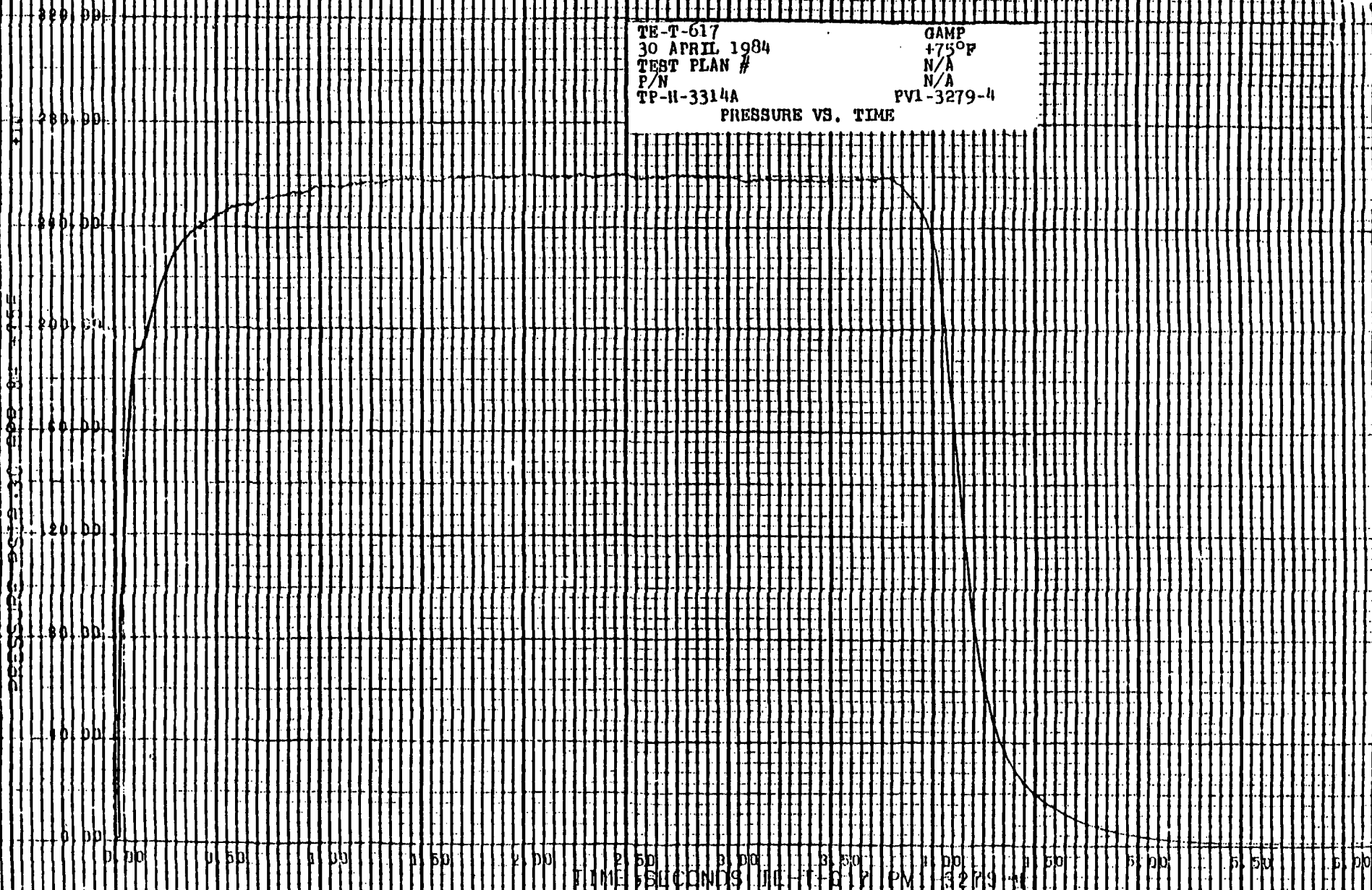
-M4-

ORIGINAL PAGE IS
OF POOR QUALITY

TE-T-617
30 APRIL 1984
TEST PLAN #
P/N
TP-H-3314A

GAMP
+75°F
N/A
N/A
PV1-3279-4

PRESSURE VS. TIME



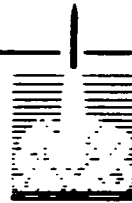
TIME IN SECONDS TE-T-617 PM 3279-4

-M5-

ORIGINAL PAGE IS
OF POOR QUALITY

MORTON THIOKOL, INC.

Elkton Division



Mr. Jim McKinnis
Martin Marietta Aerospace
1600 Jefferson Plaza
Lakewood, CO 80201

Subject: Comet Penetrator Program

Reference: Telecon Discussion, Mr. J. McKinnis, MMA/Denver and
J. Reardon, Morton Thiokol, Inc./Elkton Division on
October 15, 1986

Gentlemen:

The Elkton Division of Morton Thiokol, Inc. is pleased to provide support to Martin Marietta/Denver Aerospace on the Comet Penetrator program.

We estimate that the program can easily be performed within the 15-month period that is required to meet the MMA-specified testing in the second and third quarter of 1988 with deliveries in the first quarter of 1989.

The thruster concept is shown in Figure 1. The program would consist of design, hardware fabrication, test, and delivery. A total of six units would be fabricated; four would be static tested at Elkton and two would be delivered for flight.

The four test units would consist of an initial ballistic verification round followed by three units that would be subjected to environmental testing (shock, vibration, and thermal cycling). Radiographic inspection would follow this exposure and then the units would be static tested in an altitude simulation cell that will provide an initial simulation of 30,000 feet.

October 22, 1985

Program Event	Approximate Time Frame
Program ATP	Fourth quarter '87
Conduct ballistic test (1) at Elkton	Second quarter '88
Conduct environmental tests at Elkton (3) that include: <ol style="list-style-type: none"> 1. Shock testing 2. Vibration testing 3. Temperature cycling 4. Altitude simulation at approx. 80,000 ft at beginning of static test 	Third quarter '88
Deliver 2 flight motors	First quarter '89

The separate issue of initiation systems for use on the shuttle with MIL-STD-1512 compliance is best addressed by a fully qualified safe-and-arm device qualified for use on the space shuttle and identified as our Model 2134A. A brochure describing this unit is enclosed for your information.

The safe-and-arm and ordnance requirements for the program are as follows:

Item	Quantity	Remarks
Safe-and-arm device, Model 2134A	2	Flight units
Explosive transfer assemblies (ETAs)	4	Flight units
Elkton test ETA lines	8	Support motor test units; will be initiated by blasting caps
Through bulkhead initiators	12	Two units per motor; all configurations

If a MIL-STD-1512 compliant squib can be baselined, the design will easily adapt to it.

EP917-86

October 22, 1985

If there are any questions, please contact
John Gallagher, product manager or Joseph E. Reardon, program manager.

Very truly yours,

A handwritten signature in cursive script, appearing to read "Richard L. Davis".

Richard L. Davis
Vice President and General Manager

JER/rld

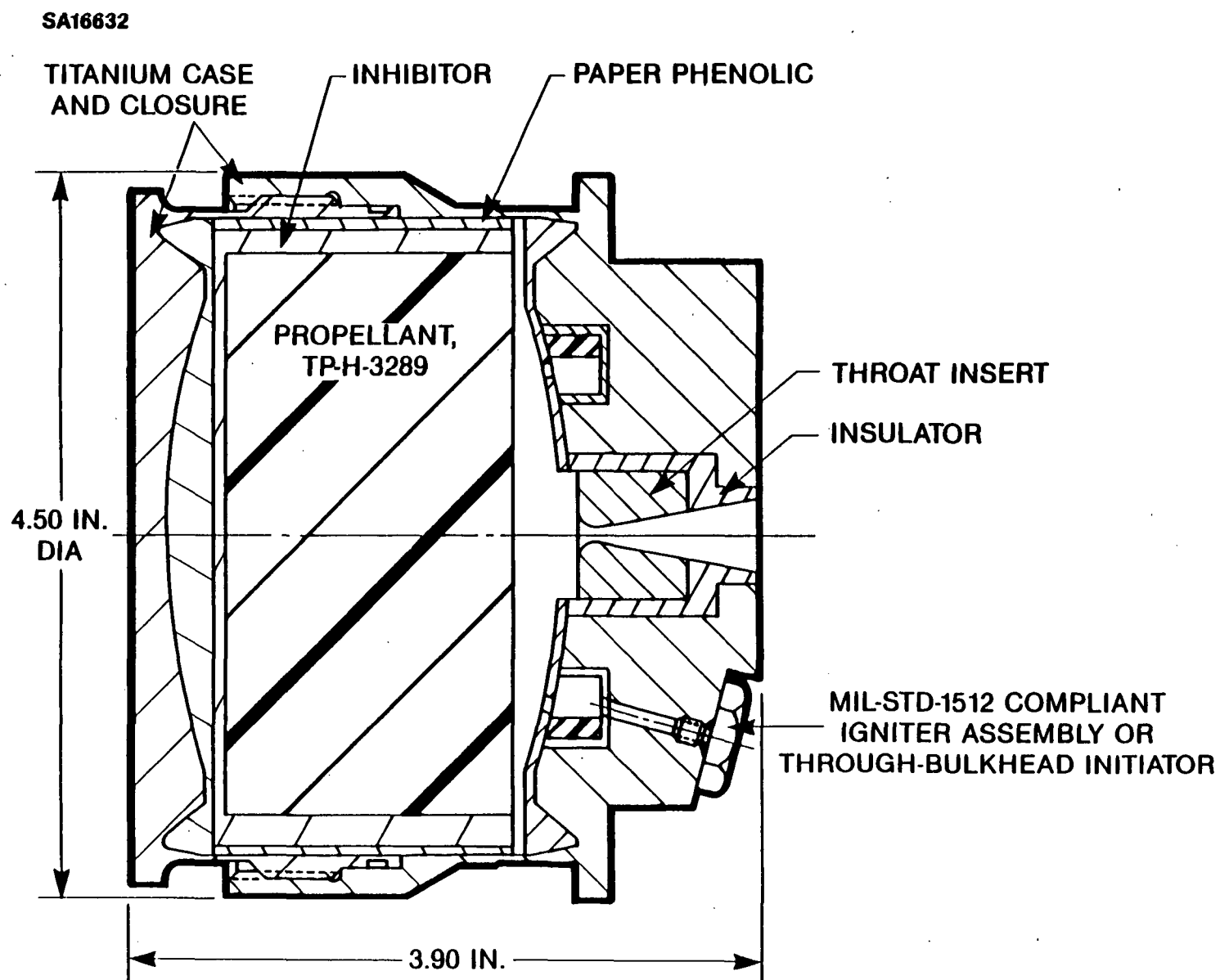


FIGURE 1. COMET PENETRATOR ASSEMBLY